Investigation of Interaction and Dynamics in Complex Liquids: Theory and Computer Simulations

Thesis Submitted for the Degree of

Doctor of Philosophy (Science)

of

Jadavpur University

by

Dhrubajyoti Maji

Department of Chemical, Biological and Macromolecular Sciences

S. N. Bose National Centre for Basic Sciences

Block-JD, Sector-III, Salt Lake

Kolkata-700106, India

April 2024

S.N. Bose National Centre for Basic Sciences
Sector - III, Block - JD, Salt Lake, Kolkata - 700098

Dr. Ranjit Biswas
Senior Professor
Chemical and Biological Sciences

Phone: 033 2335 5706-08 (O)
Email: ranjit@bose.res.in
Fax: 033 2335 3477

CERTIFICATE FROM THE SUPERVISOR

This is to certify that the thesis entitled "**Investigation of Interaction and Dynamics in Complex Liquids: Theory and Computer Simulations**" submitted by Sri **Dhrubajyoti Maji** (Index no.: 30/19/Chem./26) who got his name registered on 21/08/2019 for the award of Ph. D. (Science) degree of Jadavpur University, is absolutely based upon his own work under the supervision of Prof. Ranjit Biswas and that neither this thesis nor any part of it has been submitted for either any degree / diploma or any other academic award anywhere before.

Ranjit Biswas
15.04.24

DR. RANJIT BISWAS
Senior Professor
Dept. of Chemical, Biological & Macromolecular Sciences
S. N. Bose National Centre for Basic Sciences
Block - JD, Sector-III, Salt Lake, Kolkata - 700 106, India

Dedicated to

my parents

Bholanath Maji

and

Keya Maji

Acknowledgement

After spending almost six years as a research scholar in the department of Chemical, Biological and Macromolecular Science (CBMS) at S. N. Bose National Centre for Basic Sciences, I feel it is important to express my gratitude towards all the individuals who have supported me throughout my academic journey.

I am incredibly grateful and honoured to express my sincere appreciation and heartfelt gratitude to my supervisor, Prof. Ranjit Biswas, for his unwavering encouragement and support throughout my academic journey. Having the privilege of working under his guidance has been a truly enriching and invaluable experience, and I consider myself very fortunate to have him as my mentor. Under his supervision, I have had the opportunity to develop my critical thinking skills and work independently, while also learning to approach problems from multiple perspectives. His vast knowledge, dedication to his work, and enthusiasm for exploring new ideas have been a constant source of inspiration for me, and I am deeply grateful for his mentorship. Moreover, His kind and caring demeanour towards me has been a source of comfort and encouragement, and I will always cherish his affectionate attitude. His guidance has not only enriched my academic pursuits but also imparted invaluable life lessons that will stay with me forever.

I am immensely grateful to Prof. Pradip Kr. Ghorai, IISER Kolkata, for collaborating with me. I would also like to express my sincere gratitude to the faculty members of the Centre who have played an integral role in my personal and academic growth.

My sincere thanks to all of the members of my thesis committee and research advisory committee (RAC), Prof. Manik Pradhan, SNBNCBS, Dr. Suman Chakrabarty, SNBNCBS and Prof. Subratanath Koner, Jadavpur University, for generously sharing their valuable time with me despite their demanding schedules.

I express my gratitude to all the individuals who have been involved in procuring and maintaining the computational facility at SNBNCBS. Their hard work and dedication have ensured that I have had access to the resources necessary to conduct my research effectively, and I am deeply appreciative of their efforts. Furthermore, I would like to extend my thanks to the Dean (Academic Programme)'s office for their support throughout my time at SNBNCBS. Their assistance has been invaluable, and I am grateful for their help and guidance over the years.

I would like to express my sincere appreciation to all of my labmates Jayanta, Narayan, Amrita, Sudipta, Rik and Aziz and, Dr. Tonima Nandy and Dr. Joyeeta Banerjee from PCCP Lab. Their presence has been akin to having an extended family here, as they have provided a welcoming and supportive atmosphere that has been invaluable to me. Regardless of the situation, they have always been by my side, and I am deeply grateful for their unwavering companionship. I am grateful to Dr. Ejaj Tarif, Dr. Kajal Kumbhakar, Dr. Atanu Baksi and Dr. Juriti Rajbangshi for their invaluable contributions towards my personal and academic growth. Their guidance and support have been instrumental in helping me learn a range of academic and non-academic skills, and I am deeply appreciative of their efforts. Here, I would like to specially mention and thank my seniors Dr. Sandipa Indra, Dr. Tamisra Pal and Dr. Suman Das for their collaborative works with me.

I extend my cordial appreciation to all the academic and non-academic staffs of SNBNCBS for their assistance.

I convey my sincere regards to Dr. Parijat Das for her affectionate and tender nature during my visit. I will cherish the loving memories spent with the dynamic duo of Rik and Sam.

I would like to convey my sincere thanks to the educators who have guided me at various stages of my academic path: Prof. Prasanna Duley, Dr. Samrajni Dewan, Dr. Pradipta Ghosh, and Dr. Nabakumar Bera. Their unwavering support and enthusiasm have been invaluable to me.

I will forever be thankful to my maternal grandparents and other family members who have played a pivotal role in shaping my life.

Finally, I want to extend my heartfelt gratitude to the two most important individuals in my life, my parents, for their love, blessings, and invaluable lessons.

Abstract

This thesis entitled, "**Investigation of Interaction and Dynamics in Complex Liquids: Theory and Computer Simulations**" investigates the structural and dynamical aspects of a variety of liquid systems, ranging from simple to complex, using molecular dynamics simulations. The studied systems include deep eutectic solvents (DES) and binary mixtures, such as, neat molten amide, amide-based ionic DESs, glucose-based naturally abundant DESs (NADESs), binary mixtures of ethylene glycol (EG) and glucose, and choline chloride-based DESs. The molecular arrangements of the systems at the molecular level have been investigated, including discussions on the possible formation of deep eutectic systems of binary mixtures. Additionally, the solubility of drug molecules in DESs was investigated and the importance of non-polar interaction in controlling solubility analysed. A major aspect of this thesis is the comprehensive computation of dielectric relaxation (DR) spectra from molecular dynamics (MD) simulations for a number of ionic and non-ionic DESs, which successfully explained in molecular terms the relevant experimental data. This computational framework was further expanded to study DR in binary mixtures and neat liquids and provide microscopic explanations to experiments. With a focus on exploring the application potential of these liquids in industrial and technological sectors, the simulation protocols have been critically examined for accuracy and validity by extensively comparing the simulated data with those from experiments.

The first part of the thesis deals with a debate over the mega-value of the static dielectric constant of acetamide-based ionic DESs and provides a satisfactory resolution. New dielectric relaxation data measured in the frequency range $0.2 \leq \upsilon/\mathrm{GHz} \leq 50$ suggests a significant electrolyte-induced reduction of the static dielectric constant of the host acetamide (ε_s), which differ dramatically from earlier experimental data measured in the $0.1\ \mathrm{Hz} - 100\ \mathrm{MHz}$ frequency range. Simulation studies of dielectric relaxation shed light on the origin of the decrease of the static dielectric constant of such ionic systems. Dissection of total dielectric spectra into rotational, translational and ro-translational components indicate major contribution to DR arises from the rotational dynamics of the fluctuating host dipolar solvent molecules. The origin of the ion-induced dielectric decrement was traced to a frustration of the local orientational dipolar order brought out by a partial damage of the H-bond network of acetamide.

The structure and dynamics of a glucose-based NADES have been extensively explored employing temperature dependent MD simulations. Real-space pair correlations, depicted by radial distribution functions (RDFs) and the three-dimensional spatial arrangements, revealed size-dependent interactions between glucose, urea and water. Relaxation times of structural hydrogen bonds get incrementally faster with temperature. Computation of DR reveals the complex interplay of molecular motions within the system. Component-wise decomposition of total DRS reveals dominant contributions from self- and cross-interactions involving glucose and urea.

Drug solubilization is an important aspect of the potential use of DESs. The solvation efficiency of two choline chloride (ChCl) based DESs where ethylene glycol (EG) and propylene glycol (PG) are the hydrogen bond donors (HBDs) to solubilize a drug- paracetamol, has been extensively investigated. Predicted solubilities from simulations agree well with the experimental results. Roles of hydrogen bonding and non-polar interactions have been studied which may help designing new and more useful DESs for this purpose.

The definition of DES becomes somewhat flaccid when one groups both solid-solid and solid-liquid combinations under one name, that is, DES. An example of a solid-liquid mixture being branded as DES is ChCl-EG DES or ethaline. We have studied mixtures of ChCl and EG at different compositions to look into this problem computationally. We haven't detected any 'magic composition' that accompanies anomalous changes in structural and/or dynamical properties which may indicate formation of a DES.

Beyond DESs, we explored another class of liquids – the cryoprotectants. Sugars and polyols are well-known cryoprotecting agents (CPAs). We have computationally investigated mixtures of glucose (sugar) and ethylene glycol (polyol) at different compositions to monitor the changes in their structural and dynamical properties, with a focus on correlating relaxation processes with the solution structure. The study has revealed that increasing glucose content damages the hydrogen bond network of ethylene glycol while enhancing interactions among glucose molecules. This has a deep implication on the over-all polarization relaxation in the system. Coordination number analysis indicates a rise in glucose population around both ethylene glycol and glucose. The slowing down of molecular migration and multi-exponential relaxations in reorientational and hydrogen bond correlation functions suggest the formation of a glucose domain, offering insights into the cryoprotection mechanism.

সারমর্ম

এই থিসিসে আণবিক গতিবিদ্যা সিমুলেশন ব্যবহার করে বিভিন্ন ধরনের সরল থেকে জটিল তরল পদার্থের কাঠামোগত ও গতিশীলতা সংক্রান্ত ধর্মগুলি নিয়ে আলোচনা করা হয়েছে। মূলত বিভিন্ন প্রকারের ডিপ ইউটেকটিক দ্রাবক এবং দ্বি-মিশ্রণ নির্ভর সিস্টেম যেমন গলিত অ্যাসিটামাইড, অ্যামাইড-ভিত্তিক ডীপ ইউটেকটিক দ্রাবক, গ্লুকোজ-ভিত্তিক প্রাকৃতিক ডিপ ইউটেকটিক দ্রাবক, কোলিন ক্লোরাইড-ভিত্তিক ডীপ ইউটেকটিক দ্রাবক, গ্লুকোজ এবং ইথিলিন গ্লাইকলের দ্বিমিশ্রণ অধ্যয়ন করা হয়েছে। আণবিকস্তরে প্রতিটি সিস্টেমের গঠন কাঠামো ও গতিবিদ্যা অনুসন্ধান করা হয়েছে, যেমন বিভিন্ন আয়নীয় ও অ-আয়নীয় ডীপ ইউটেকটিক দ্রাবকের ডাইইলেকট্রিক রিলাক্সেশন স্পেক্ট্রোস্কোপি, মিশ্রণের ক্ষেত্রে সম্ভাব্য ডীপ ইউটেকটিক গঠন। এছাড়াও একটি ঔষধি ড্রাগের দুই প্রকার ডীপ ইউটেকটিক দ্রাবকে দ্রাব্যতা আলোচনা করা হয়েছে। এই থিসিসের একটি গুরুত্বপূর্ণ দিক হলো আণবিক গতিবিদ্যা সিমুলেশন ব্যবহার করে ডাইইলেকট্রিক রিলাক্সেশন স্পেক্ট্রোস্কোপি গণনা এবং এটিকে বিভিন্ন তরল সিস্টেমের জন্য সফলভাবে প্রয়োগ করা। এই ধরনের সিস্টেমগুলির সম্ভাব্য প্রয়োগগুলি নিয়েও কথা বলা হয়েছে। সিমুলেশন থেকে প্রাপ্ত ফলাফল যেখানে সম্ভব সেখানে পরীক্ষালব্ধ তথ্যের সঙ্গে তুলনা করা হয়েছে।

এই থিসিসের প্রথম ভাগে বিশুদ্ধ গলিত অ্যাসিটামাইড এবং তিন প্রকারের অ্যাসিটামাইড-ভিত্তিক আয়নীয় ডীপ ইউটেকটিক দ্রাবকের ডাইইলেকট্রিক রিলাক্সেশন স্পেক্ট্রোস্কোপি গণনা করা হয়েছে এবং পরীক্ষালব্ধ তথ্যের সঙ্গে তুলনা করে সিস্টেমসমূহের আণবিকস্তরে ডাইপোল রিলাক্সেশন আরো গভীরভাবে অধ্যয়ন করা হয়েছে।

আয়নীয় ডীপ ইউটেকটিক দ্রাবকের পর একটি গ্লুকোজ-ভিত্তিক প্রাকৃতিক অ-আয়নীয় ডিপ ইউটেকটিক দ্রাবকের কাঠামোগত ও গতিশীলতা সংক্রান্ত ধর্মগুলি গভীরভাবে বিশ্লেষণ করা হয়েছে। ডীপ ইউটেকটিক দ্রাবকের উপাদানগুলি কিভাবে অন্তঃ এবং আন্তঃ মিথস্ক্রিয়ার মাধ্যমে দ্রাবকটির সার্বিক প্রকৃতি নির্ধারণ করে সে বিষয়ে বিস্তারিত আলোচনা করা হয়েছে।

ডীপ ইউটেকটিক দ্রাবকের একটি সম্ভাব্য প্রায়োগিক উপযোগিতা হলো বিভিন্ন ঔষধি ড্রাগকে দ্রবীভূত করা। এখানে প্যারাসিটামল নামক ঔষধি ড্রাগের দুই প্রকার ডীপ ইউটেকটিক দ্রাবকে দ্রাব্যতা আলোচনা করা হয়েছে। এই আলোচনায় প্রথমে সিমুলেশনের মাধ্যমে দ্রাব্যতা নির্ণয় ও পরে যে সম্ভাব্য কারকগুলি দায়ী সেগুলিকে চিহ্নিত করা হয়েছে। এর ফলে ঔষধি ড্রাগের দ্রাব্যতার জন্য উপযুক্ত ডীপ ইউটেকটিক দ্রাবকের পরিকল্পনা করা সহজ হবে।

ইথালিন একটি সুপরিচিত ডীপ ইউটেকটিক দ্রাবক যেখানে কোলিন ক্লোরাইড এবং ইথিলিন গ্লাইকল ১:২ মোল অনুপাতে মিশ্রিত থাকে। আমরা এই ১:২ থেকে ১:৬ মোল অনুপাত পর্যন্ত বিভিন্ন মিশ্রণের কাঠামোগত ও গতিশীলতা সংক্রান্ত ধর্মগুলি অধ্যয়ন করেছি কিন্তু কোন আকস্মিক পরিবর্তন খুঁজে পাইনি যেটি একটি নির্দিষ্ট মিশ্রণকে ডীপ ইউটেকটিক বলে চিহ্নিত করতে পারে।

ডীপ ইউটেকটিক দ্রাবক ছাড়া আমরা আর এক প্রকার তরল মিশ্রণের ধর্ম অনুসন্ধান করেছি - ক্রাইওপ্রোটেক্ট্যান্ট। আমরা গ্লুকোজ এবং ইথিলিন গ্লাইকল দ্বি-মিশ্রণের গঠনগত এবং গতিশীল বৈশিষ্ট্যগুলির পরিবর্তন অধ্যয়নের জন্য বিভিন্ন ঘনত্বে সিমুলেশন করেছি। দেখা গেছে যে যে মিশ্রণে গ্লুকোজের পরিমাণ বাড়লে ইথিলিন গ্লাইকলের হাইড্রোজেন বন্ড নেটওয়ার্ক ক্ষতিগ্রস্ত হয় এবং গ্লুকোজ অণুর মধ্যে মিথস্ক্রিয়া বেড়ে যায়। সেই সঙ্গে আণবিক চলন এবং ঘূর্ণণও ক্রমশ মন্দীভূত হতে থাকে। এর দ্বারা বোঝা যায় যে মিশ্রণে ক্রমশ গ্লুকোজ ডোমেইন তৈরি হচ্ছে যা এই মিশ্রণের ক্রাইওপ্রোটেক্ট্যান্ট ক্ষমতাকে প্রভাবিত করে।

List of Publications

1. "Dielectric Relaxations of Molten Acetamide: Dependence on the Model Interaction Potentials and the Effects of System Size" **Dhrubajyoti Maji**, Sandipa Indra and Ranjit Biswas, *J. Chem. Sci.* 2021, **133** (**4**), 104.

2. "Dielectric Relaxation and Dielectric Decrement in Ionic Acetamide Deep Eutectic Solvents: Spectral Decomposition and Comparison with Experiments" **Dhrubajyoti Maji** and Ranjit Biswas, *J. Chem. Phys.,* 2023, **158**, 104503.

3. "Structure and Dynamics of a Glucose-Based Cryoprotectant Mixture: A Computer Simulation Study" **Dhrubajyoti Maji**, Narayan Chandra Maity and Ranjit Biswas, *Theor. Chem. Acc.* 2023, **142** (**5**), 43.

4. "Enhanced solubility of paracetamol in (ChCl + polyol) deep eutectics: A novel interplay between non-polar and H-bond interactions" **Dhrubajyoti Maji** and Ranjit Biswas, *Phys. Chem. Chem. Phys.* (under review).

5. "Exploring the structural and dynamic behavior of a glucose-urea-water deep eutectic solvent via molecular dynamics simulations" **Dhrubajyoti Maji** and Ranjit Biswas, *J. Phys. Chem. B* (to be submitted).

6. "Can the structural and dynamical behaviours of ChCl:EG mixtures provide insight into deep eutectic formation?" **Dhrubajyoti Maji** and Ranjit Biswas, *J. Phys. Chem. B* (to be submitted).

7. ***"Difference in "Supercooling" Affinity between (Acetamide + Na/KSCN) Deep Eutectics: Reflections in the Simulated Anomalous Motions of the Constituents and Solution Microheterogeneity Features" by Swarup Banerjee, Pradip Kr. Ghorai, **Dhrubajyoti Maji** and Ranjit Biswas, *J. Phys. Chem. B* 2022, **126**, 10146-10155.

8. ***"Validity of the Onsager-Glarum Relation in a Molecular Coulomb Fluid: Investigation via Temperature-dependent Molecular Dynamics Simulations of a Representative Ionic Liquid, [BMIM][PF6]" by Tamisra Pal, Suman Das, **Dhrubajyoti Maji** and Ranjit Biswas, *New J. Chem*. 2023, **47**, 14906-14920.

9. ***"Temperature-dependent dielectric relaxation measurements of (acetamide + K/Na SCN) deep eutectic solvents: Decoding the impact of cation identity via computer simulations" Jayanta Mondal, **Dhrubajyoti Maji** and Ranjit Biswas, *J. Chem. Phys.* 2024, **160**, 084506.

*** Not included in this thesis

Contents

Chapter 1

Introduction

Solvents play a crucial role in a wide range of chemical processes, from laboratory experiments to industrial manufacturing. A solvent is a substance that dissolves a solute to form a homogeneous mixture, and it is often used to extract, purify, or separate different compounds.[1–4] Solvents are essential in many industrial processes, such as oil refining,[5] polymer production,[6,7] and paint manufacturing.[8] They are used to dissolve and transport materials,[9,10] to clean equipment and surfaces,[11–13] and to control the viscosity and other properties of the final products.[14,15] In addition, solvents are often used as reaction media, allowing chemical reactions to occur in a homogeneous and controlled environment.[16,17] One of the most important applications of solvents is in the pharmaceutical industry.[18,19] Many drugs are made by dissolving active ingredients in solvents, which are then purified and formulated into tablets, capsules, or other dosage forms.[20] Solvents can also be used to extract natural products from plants and other sources, which can then be used as drugs or as starting materials for chemical synthesis.[21,22] However, the use of solvents also presents some challenges and risks. Many solvents are toxic,[23,24] flammable,[25] or environmentally hazardous,[26,27] and their disposal can pose a serious problem. Therefore, it is important to use solvents judiciously and to select the appropriate solvent for each application, taking into account its properties, cost, and environmental impact.[28,29]

Deep eutectic solvents (DESs) are a type of solvent system that has gained significant attention in recent years due to their unique properties and potential applications.[30–32] DESs are formed by the combination of two or more solid or liquid components, usually a hydrogen bond donor (HBD) and a hydrogen bond acceptor (HBA), at a specific ratio.[33,34] The resulting mixture has a lower melting point than either of the individual components and exhibits a liquid-like behaviour, allowing it to function as a solvent.[33,34] Some of the main advantages of DESs are their low toxicity and, biodegradability compared to conventional organic solvents.[31] This makes them a more environmentally friendly alternative for a wide range of applications, from chemical synthesis and extraction to electrochemistry and catalysis.[35–41] Additionally, DESs can be easily synthesized from inexpensive and renewable starting materials, which makes them cost-effective and sustainable.[42–44] Another important characteristic of DESs is their

ability to dissolve a wide range of compounds, including polar and nonpolar species, with high selectivity and efficiency.[45,46] This makes them a versatile media for applications in both basic science research and industry sectors. DESs have been used, for example, as reaction media for various chemical transformations,[47,48] as extraction solvents for natural products,[49,50] and as electrolytes in electrochemical devices.[51,52] However, despite their potential advantages, DESs are still a relatively new and unexplored field of research, and many questions remain unanswered regarding their properties, behaviour, and potential applications. Further studies are needed to fully understand the unique characteristics of DESs and to optimize their synthesis and use for different purposes.

Ionic DESs are a specific type of deep eutectic solvent that has recently gained attention in the scientific community due to their unique properties and potential applications.[53,54] Ionic DESs are made up of hydrogen bond donors and ions generated from the dissociation of added electrolytes, and their extensive interspecies H-bond interactions cause frustrations in the ionic lattices that provide enthalpic support for their formation. They also gain entropy for being in the liquid phase. One of the main advantages of ionic deep eutectic solvents is their high ionic conductivity, which makes them useful as electrolytes in electrochemical devices, such as, batteries, fuel cells, and supercapacitors.[55–57] Their unique polarity and solvation properties can facilitate the formation of specific molecular assemblies and stabilize reactive intermediates, leading to increased selectivity and yield in chemical reactions. Moreover, these are considered to be more environmentally friendly and sustainable than common organic solvents, as they can be synthesized from renewable and biodegradable starting materials.

Various experimental techniques have been used to study the micro heterogeneous relaxation dynamics of ionic DESs, including time-resolved fluorescence experiments,[58–60] dielectric relaxation and conductivity measurements,[61–63] and femtosecond Raman induced Kerr effect spectroscopic measurements.[64] Computer simulations have also been carried out to generate microscopic understanding of the experimentally measured relaxation dynamics.[65–69] Recent dielectric relaxation data accessed via measurements in a frequency window ($0.2 \leq \upsilon/\mathrm{GHz} \leq 50$) indicates a dramatic difference between the static dielectric constant (ε_s) of ionic acetamide DES and what was concluded from earlier experiments.[62,70] This triggers a debate on the true impact of electrolyte ions on the ε_s of the host acetamide, motivating further theoretical and/or experimental investigation employing different techniques for providing a resolution to this debate. Dielectric relaxation spectroscopy (DRS) measures the collective polarization fluctuations of a given medium in the presence of a time-dependent electric field, and computer

simulations offer a necessary framework to computationally examine the component contributions to the measured DR spectra. This inter-relationship between theory and experiments provides the necessary avenue to deal with debate over the impact of electrolyte on ε_s of ionic DESs.[65,71,72]

Naturally abundant deep eutectic solvents (NADESs) are a type of deep eutectic solvent that can be formed from naturally occurring substances, such as sugars, organic acids, and amino acids.[73,74] NADESs are formed by the combination of two or more components in a specific mole ratio, resulting in a liquid-like mixture that exhibits solvent properties. One of the main advantages of NADESs is their natural abundance and low cost compared to synthetic deep eutectic solvents.[75,76] The components used to form NADESs are often readily available from natural sources, such as fruits, vegetables, and plant extracts, which makes them an attractive alternative to synthetic solvents for various applications, including extraction, synthesis, and separation.[76] Additionally, NADESs have been found to have unique physical and chemical properties, such as high viscosity, low volatility, and high stability, which make them useful for various applications in material science and biotechnology.[76,77] Furthermore, NADESs are considered to be more environmentally friendly and sustainable than traditional organic solvents, as they are biodegradable, non-toxic, and renewable.[78] NADESs can also be easily synthesized and recycled, which makes them a more sustainable alternative for various applications in research and industry.[79] Investigating the structure and dynamics of NADESs is critical to understand their properties and potential applications.

Several experimental techniques have been employed to investigate the structure and dynamics of NADESs. X-ray diffraction (XRD) and neutron diffraction have been used to study the structure of NADESs.[80–83] These studies have revealed that NADESs consist of complex networks of hydrogen bonds between the constituents, and that the network structure changes significantly as the temperature and composition of the solvent is varied. Vibrational spectroscopic techniques, such as infrared (IR) and Raman spectroscopy, have also been used to study the interactions between the constituents in NADESs.[84–86] These studies have revealed that hydrogen bonding interactions are the dominant intermolecular forces in NADESs. Finally, NMR spectroscopy has been used to study the dynamics of NADESs, revealing that the solvent exhibits highly heterogeneous dynamics at the molecular level.[87,88] DRS has been proven to be a powerful tool in investigating the structure and dynamics of NADESs.[73,74] The dielectric properties of NADESs have been found to be strongly influenced by the nature of the constituents and the degree of hydrogen bonding between them. Experimentally, it can be

challenging to interpret the dielectric behaviour of complex systems such as NADESs, in terms of individual responses. However, MD simulations can be used as a complementary technique to experiment and provide insight into the species-specific interactions that are often difficult to obtain from experiments alone. In previous studies, molecular dynamics simulations have been used to investigate the dielectric properties of NADESs, and the results have been found to agree well with experimental data.

The solubility of drugs is a critical parameter in the development of pharmaceutical formulations.[89,90] Poor solubility can limit the bioavailability and efficacy of a drug, leading to potential issues in drug delivery and patient treatment.[91] DES have been shown to enhance the solubility and dissolution rate of various drugs, thereby improving their therapeutic efficacy.[92,93] However, despite their potential, there is a lack of understanding of the underlying mechanisms governing drug solubility in DESs. We aim to investigate the solubility behaviour of drugs in different DESs and to elucidate the factors that influence drug solubility in these solvents. The findings from this study may provide insight into the use of DESs as solvents for drug delivery and formulation, and can have implications for the development of new and improved pharmaceutical products.

Characterizing a solution as a deep eutectic solvent requires a comprehensive understanding of the thermodynamics and kinetics involved in their formation, as well as their physical and chemical properties.[87,94] The system is expected to show some unique structural and dynamical properties at eutectic composition which is different from simple mixtures. MD simulation can analyse different kinds of such properties to predict possible formation of DESs.[95]

Cryopreservation is a critical process used in the storage and transportation of biological samples, including cells, tissues, and organs.[96–98] The use of cryoprotectants is essential to prevent damage to biological samples during freezing and thawing.[99,100] Binary mixtures have shown promises as potential cryoprotectants due to their ability to reduce the formation of ice crystals and minimize damage to biological samples.[101,102] However, a fundamental understanding of the structure and dynamics of these mixtures is essential to optimize their cryoprotective properties. Hence, it is worth studying the structure and dynamics of binary mixtures that can potentially act as cryoprotectants to gain a deeper understanding of their properties and improve their effectiveness in preserving biological samples. The ability to preserve biological samples is of great importance in various fields such as medicine, biotechnology, and agriculture. Cryopreservation allows for long-term storage of biological

materials, enabling access to these resources for future research and application. Moreover, a better understanding of the structure and dynamics of binary mixtures can lead to the development of new and improved cryoprotectants that are more effective and have fewer adverse effects on biological samples.

It is known that DRS could provide important insights regarding designing and developing of materials for a variety of technological applications, including energy storage, electronic devices, and biological systems.[103–105] Understanding dielectric relaxation requires a detailed understanding of the dynamics of polar molecules and their interactions with surrounding environments. MD simulation is a powerful computational technique that allows for the study of molecular dynamics at a microscopic level, including dielectric relaxation. MD simulation has become an increasingly popular tool for investigating dielectric relaxation due to its ability to provide detailed information about the dynamics and structure of complex systems. The use of MD simulation has several advantages over experimental methods, including the ability to study molecular-level details and the ability to control the system conditions precisely.[106–108]

Simulation techniques offer a framework to split the total relaxation into contributions arising from the self- and cross-interactions of system constituents. This decomposition approach has found application in various systems, including aqueous solutions of ions,[71,72,109–112] ionic liquids,[113–121] and aqueous solutions of biomolecules.[122–124] Importantly, it can be further extended to cover both ionic and non-ionic DESs. The application of a component-wise decomposition of DRS not only aids in comprehending the complex dynamics of these systems but also plays an important role in unraveling changes in the static dielectric constant. By isolating the contributions of individual components, we can gain insights into the interactions within the system, providing a detailed understanding of its behaviour. This approach proves particularly valuable in studying DESs, where the unique combination of components requires a nuanced analysis to decipher the complex interplay of self- and cross-interactions. When dealing with ionic systems, experimental techniques encounter challenges such as electrode polarization[125–127] and Maxwell-Wagner effects,[128,129] particularly at lower frequencies. These issues hinder the accurate measurements of dielectric response in this frequency range. In contrast, simulation techniques offer a solution by avoiding these difficulties altogether. Moreover, MD simulations can provide insight into the dynamics of polar molecules in various environments, including non-equilibrium conditions that are challenging to achieve experimentally.[130,131] However, MD simulations also have certain limitations, including the

availability of accurate force fields, computational resources, and possible artifacts arising from the finite size of the simulation box.[131,132]

This thesis is comprised of a total of 8 chapters, with the introductory chapter being the first one. In chapter 2, we used molecular dynamics simulations to investigate the properties of molten acetamide at a temperature of 358.15 K. Our goal was to interpret available dielectric relaxation (DR) data from experiments.[62] We used two different models of interaction potentials based on optimised potential for liquid simulations (OPLS) force fields: the united-atom (OPLS-UA)[133] and the all-atom (OPLS-AA)[134] interaction potentials. Interestingly, the OPLS-UA model predicted a value of static dielectric constant (ε_s) for molten acetamide that agreed well with experimental results, but predicted a DR dynamics that were much slower than observed in experiments. On the other hand, the OPLS-AA model provided a much better description of the experimental DR dynamics but severely underestimated the ε_s value. To ensure the accuracy of our results, we also varied the size of the simulated systems, testing them with 250, 500, and 1000 molecules. We directly compared our simulated results with experimental data and explored the role of single dipole rotation in molten acetamide. Our findings provide valuable insights into the properties of this material and shed light on the limitations and advantages of different models used to study its behaviour.[135]

In chapter 3 the frequency-dependent dielectric relaxation in three ionic DESs- (acetamide+$LiClO_4$/NO_3/Br) - were investigated using MD simulations in a temperature range of $329 \leq T/K \leq 358$.[65] The dielectric spectra obtained from the simulations were decomposed to identify the rotational, translational, and ro-translational contributions. As expected, the dipolar contributions dominated the dielectric spectra across all frequencies, while the translational and ro-translational contributions were relatively small. Interestingly, the translational and cross ro-translational contributions only appeared in the THz regime, in contrast to the dipolar relaxations, which dominated the MHz-GHz frequency window and were dependent on viscosity. The simulations also revealed an anion-dependent decrement of the static dielectric constant ($\varepsilon_s \sim$ 20 - 30) for acetamide in these ionic DESs, consistent with experimental observations. Additionally, dipole-correlations (Kirkwood g factor) indicated significant orientational frustrations, which were associated with the anion-dependent damage of the acetamide H-bond network. However, the single dipole reorientation time distributions did not indicate the presence of any 'rotationally frozen' molecules, suggesting that the dielectric decrement is largely static in origin.

In chapter 4, We investigated the structural and dynamic behaviour of a deep eutectic solvent made up of glucose, urea, and water[73] using molecular dynamics simulations. We analysed the centre-of-mass radial distribution functions and hydrogen-bond site-site radial distribution functions and found that the least intense interaction was between glucose molecules, while water molecules had the most intense interaction. As temperature increased, the peak heights slightly decreased, and the number of hydrogen bonds between different species decreased as well. We then decomposed the dielectric relaxation spectra into six individual spectra, which cannot be done in experiments. The static dielectric constant is found to get mitigated with increasing temperature demonstrating the effect of thermal energy to randomize dipole orientations. Almost all components collectively contributed to the origin of the timescales, where the relaxation times involving glucose molecules appear at lower frequencies.

In chapter 5, we discuss the solubility of a drug molecule in DESs. Our MD simulation study aimed to calculate the solubility of paracetamol in two choline chloride-based deep eutectic solvents, with varying hydrogen bond donor (HBD) molecules: ethylene glycol (EG) and propylene glycol (PG). We analysed coordination numbers and number of hydrogen bonds and, plotted them against paracetamol concentrations to determine the maximum solubility limit. We defined maximum solubility as the concentration where the coordination of other species around paracetamol is at its highest and that of paracetamol around paracetamol is at its lowest, and where the number of hydrogen bonds per paracetamol with other species is at its maximum and that of paracetamol with paracetamol is at its minimum. Our simulations revealed that both hydrogen bonding and non-polar interactions played critical roles in the solubilisation of paracetamol, and PG-DES was a better solvent due to the presence of an extra non-polar methyl group. Our results were in line with available experimental data, showing that in these deep eutectics, the solubility of paracetamol increases significantly compared to water. Additionally, PG-DES demonstrated higher solubilisation compared to EG-DES. These findings may be useful for designing more effective solvents for drug delivery applications.

Chapter 6 investigates the deep eutectic behaviour of choline chloride-ethylene glycol mixtures. Recent studies have shown that the behaviour of the choline chloride-ethylene glycol mixture is better described as a normal binary mixture, rather than forming a deep eutectic at a 1:2 mole ratio.[95,136,137] In a molecular dynamics simulation study covering a composition range from 1:2 to 1:6, we found that the structural and dynamical properties of the mixtures vary significantly with composition, essentially indicating the impact of solute concentration. The numbers of different type of hydrogen bonds monotonically change and, hydrogen bond

relaxation times increase with increasing choline chloride composition, while viscosity and density increase. These findings have important implications for designing deep eutectic solvents.

Chapter 7 provides an in-depth analysis of the structural and dynamical properties of glucose-based cryoprotectant mixtures. By using molecular dynamics simulations, the study sheds light on how different weight percentages of glucose and ethylene glycol affect the H-bond network, coordination numbers, and thermo-physical properties of the solutions.[138] The results suggest that as glucose concentration increases, the H-bond network among glucose molecules becomes more prevalent, leading to a partially damaged H-bond network in ethylene glycol. Moreover, the simulations reveal that the migration of molecules slows down as glucose concentration increases in the mixture, with ethylene glycol molecules showing relatively more mobility than glucose. The study also hints at the formation of glucose domains through intraspecies H-bonding, which might be a key feature for the cryoprotection ability of these mixtures.

The final chapter of this thesis is chapter 8, which includes a summary of the findings as well as possible areas for future research.

References

1 P. S. Corrêa, W. G. Morais Júnior, A. A. Martins, N. S. Caetano and T. M. Mata, *Processes*, 2020, **9**, 10.

2 A. Wüst Zibetti, A. Aydi, M. Arauco Livia, A. Bolzan and D. Barth, *J. Supercrit. Fluids*, 2013, **83**, 133–145.

3 N. V. THAKUR, *Miner. Process. Extr. Metall. Rev.*, 2000, **21**, 277–306.

4 C. Reichardt, *Org. Process Res. Dev.*, 2007, **11**, 105–113.

5 R. N. Magomedov, A. V. Pripakhaylo, T. A. Maryutina, A. I. Shamsullin and T. S. Ainullov, *Russ. J. Appl. Chem.*, 2019, **92**, 1634–1648.

6 M. E. Schimpf and S. N. Semenov, *J. Phys. Chem. B*, 2000, **104**, 9935–9942.

7 C. J. Luo, M. Nangrejo and M. Edirisinghe, *Polymer (Guildf)*, 2010, **51**, 1654–1662.

8 D. C. Glass, A. Spurgeon, I. A. Calvert, J. L. Clark and J. M. Harrington, *Occup. Environ. Med.*, 1994, **51**, 617–625.

9 J. S. Wang and C. M. Wai, *J. Supercrit. Fluids*, 2007, **40**, 176–182.

10 L. E. Bromberg and A. M. Klibanov, *PNAS*, 1995, **92**, 1262–1266.

11 J. Durkee, *Cleaning with Solvents: Science and Technology*, Elsevier Science, United Kingdom, 2013.

12 D. B. McGregor, E. Heseltine and H. Møller, *Scand. J. Work Environ. Health*, 1995, **21**, 310–312.

13 J. B. Durkee, in *Developments in Surface Contamination and Cleaning*, Elsevier, 2008, pp. 759–871.

14 E. P. G. Arêas, J. A. G. Arêas, J. Hamburger, W. L. Peticolas and P. S. Santos, *J. Colloid Interface Sci.*, 1996, **180**, 578–589.

15 A. Almagor, S. Yedgar and B. Gavish, *Biorheology*, 1990, **27**, 605–610.

16 S. Santoro, F. Ferlin, L. Luciani, L. Ackermann and L. Vaccaro, *Green Chem.*, 2017, **19**, 1601–1612.

17 T. Hamada, Y. Sameshima, K. Honda, T. Omasa, J. Kato and H. Ohtake, *J. Biosci. Bioeng.*, 2008, **106**, 357–362.

18 P. Kolář, J.-W. Shen, A. Tsuboi and T. Ishikawa, *Fluid Phase Equilib.*, 2002, **194–197**, 771–782.

19 K. Grodowska and A. Parczewski, *Acta. Pol. Pharm.*, 2010, **67**, 3–12.

20 D. K. Sahana, G. Mittal, V. Bhardwaj and M. N. V. R. Kumar, *J. Pharm. Sci.*, 2008, **97**, 1530–1542.

21 S. Visht and S. Chaturvedi, *J. Curr. Pharm. Res.*, 2012, **2**, 584.

22 M. A. Rostagno and J. M. Prado, *Natural product extraction: principles and applications*, The Royal Society of Chemistry, 2013.

23 J. V Bruckner, S. S. Anand and D. A. Warren, *Casarette and Doull's Toxicology: The Basic Science of Poison, 7th Ed. Klaassen CD (Eds.)*, 2008, 981–1051.

24 D. R. Joshi and N. Adhikari, *J. Pharm. Res. Int.*, 2019, **28**, 1–18.

25 F. Guo, W. Hase, Y. Ozaki, Y. Konno, M. Inatsuki, K. Nishimura, N. Hashimoto and O. Fujita, *Exp. Therm. Fluid Sci.*, 2019, **109**, 109858.

26 W.-T. Tsai, *J. Loss Prev. Process Ind.*, 2002, **15**, 147–157.

27 A. D. Curzons, D. C. Constable and V. L. Cunningham, *Clean Products and Processes*, 1999, **1**, 82–90.

28 I. T. Horváth, *Green Chem.*, 2008, **10**, 1024–1028.

29 J. Płotka-Wasylka, M. Rutkowska, K. Owczarek, M. Tobiszewski and J. Namieśnik, *TrAC, Trends Anal. Chem.*, 2017, **91**, 12–25.

30 E. L. Smith, A. P. Abbott and K. S. Ryder, *Chem. Rev.*, 2014, **114**, 11060–11082.

31 F. M. Perna, P. Vitale and V. Capriati, *Curr. Opin. Green Sustain. Chem.*, 2020, **21**, 27–33.

32 B. B. Hansen, S. Spittle, B. Chen, D. Poe, Y. Zhang, J. M. Klein, A. Horton, L. Adhikari, T. Zelovich, B. W. Doherty, B. Gurkan, E. J. Maginn, A. Ragauskas, M. Dadmun, T. A. Zawodzinski, G. A. Baker, M. E. Tuckerman, R. F. Savinell and J. R. Sangoro, *Chem. Rev.*, 2021, **121**, 1232–1285.

33 A. P. Abbott, K. J. Edler and A. J. Page, *J. Chem. Phys*., 2021, **155**, 150401.

34 T. El Achkar, H. Greige-Gerges and S. Fourmentin, *Environ. Chem. Lett.*, 2021, **19**, 3397–3408.

35 L. I. N. Tomé, V. Baião, W. da Silva and C. M. A. Brett, *Appl. Mater. Today*, 2018, **10**, 30–50.

36 Y. Marcus and Y. Marcus, *Applications of deep eutectic solvents*, Springer, 2019.

37 A. Shishov, A. Bulatov, M. Locatelli, S. Carradori and V. Andruch, *Microchem. J.*, 2017, **135**, 33–38.

38 T. El Achkar, H. Greige-Gerges and S. Fourmentin, *Environ. Chem. Lett.*, 2021, **19**, 3397–3408.

39 L. I. N. Tomé, V. Baião, W. da Silva and C. M. A. Brett, *Appl. Mater. Today*, 2018, **10**, 30–50.

40 Q. Zhang, K. D. O. Vigier, S. Royer and F. Jérôme, *Chem. Soc. Rev.*, 2012, **41**, 7108–7146.

41 A. Abo-Hamad, M. Hayyan, M. A. AlSaadi and M. A. Hashim, *Chem. Eng. J.*, 2015, **273**, 551–567.

42 K. M. Jeong, M. S. Lee, M. W. Nam, J. Zhao, Y. Jin, D. K. Lee, S. W. Kwon, J. H. Jeong and J. Lee, *J. Chromatogr. A*, 2015, **1424**, 10–17.

43 P. Liu, J. W. Hao, L. P. Mo and Z. H. Zhang, *RSC Adv.*, 2015, **5**, 48675–48704.

44 J. Liu, X. Li and K. H. Row, *J. Mol. Liq.*, 2022, **362**, 119654.

45 A. P. Abbott, G. Capper, D. L. Davies, K. J. McKenzie and S. U. Obi, *J. Chem. Eng. Data*, 2006, **51**, 1280–1282.

46 F. P. Pelaquim, A. M. Barbosa Neto, I. A. L. Dalmolin and M. C. da Costa, *Ind. Eng. Chem. Res.*, 2021, **60**, 8607–8620.

47 G. Di Carmine, A. P. Abbott and C. D'Agostino, *React. Chem. Eng.*, 2021, **6**, 582–598.

48 D. A. Alonso, A. Baeza, R. Chinchilla, G. Guillena, I. M. Pastor and D. J. Ramón, *European J. Org. Chem.*, 2016, **2016**, 612–632.

49 X. Li and K. H. Row, *J. Sep. Sci.*, 2016, **39**, 3505–3520.

50 L. Duan, L.-L. Dou, L. Guo, P. Li and E.-H. Liu, *ACS Sustain. Chem. Eng.*, 2016, **4**, 2405–2411.

51 L. Millia, V. Dall'Asta, C. Ferrara, V. Berbenni, E. Quartarone, F. M. Perna, V. Capriati and P. Mustarelli, *Solid State Ion*, 2018, **323**, 44–48.

52 H. Cruz, N. Jordão and L. C. Branco, *Green Chem.*, 2017, **19**, 1653–1658.

53 L. C. Tomé and D. Mecerreyes, *J. Phys. Chem. B*, 2020, **124**, 8465–8478.

54 J. Huang, X. Guo, T. Xu, L. Fan, X. Zhou and S. Wu, *J. Chromatogr. A*, 2019, **1598**, 1–19.

55 Y. Ji, H. Zhou, P. Sun, J. Liu, Q. Li, P. Lu and Q. Xu, *Int. J. Green Energy*, 2022, 1–11.

56 M. J. Roldán-Ruiz, M. L. Ferrer, M. C. Gutiérrez and F. del Monte, *ACS Sustain. Chem. Eng.*, 2020, **8**, 5437–5445.

57 A. Zhu, X. Bian, W. Han, D. Cao, Y. Wen, K. Zhu and S. Wang, *Resour. Conserv. Recycl.*, 2023, **188**, 106690.

58 A. Das and R. Biswas, *J. Phys. Chem. B*, 2015, **119**, 10102–10113.

59 N. Subba, E. Tarif, P. Sen and R. Biswas, *J. Phys. Chem. B*, 2020, **124**, 1995–2005.

60 S. Dinda, A. Sil, A. Das, E. Tarif and R. Biswas, *J. Mol. Liq.*, 2022, **349**, 118126.

61 K. Kumbhakar, E. Tarif, K. Mukherjee and R. Biswas, *J. Mol. Liq.*, 2019, **290**, 111225.

62 K. Mukherjee, A. Das, S. Choudhury, A. Barman and R. Biswas, *J. Phys. Chem. B*, 2015, **119**, 8063–8071.

63 K. Mukherjee, S. Das, J. Rajbangshi, E. Tarif, A. Barman and R. Biswas, *J. Phys. Chem. B*, 2021, **125**, 12552–12567.

64 R. Biswas, A. Das and H. Shirota, *J. Chem. Phys.*, 2014, **141**, 134506.

65 D. Maji and R. Biswas, *J. Chem. Phys.*, 2023, **158**, 174503.

66 S. Banerjee, P. Kr. Ghorai, D. Maji and R. Biswas, *J. Phys. Chem. B*, 2022, **126**, 10146–10155.

67 B. Guchhait, S. Das, S. Daschakraborty and R. Biswas, *J. Chem. Phys.*, 2014, **140**, 104514.

68 A. Das, S. Das and R. Biswas, *J. Chem. Phys.*, 2015, **142**, 034505.

69 A. Das, S. Das and R. Biswas, *Chem. Phys. Lett.*, 2013, **581**, 47–51.

70 G. Berchiesi, M. De Angelis, G. Rafaiani and G. Vitali, *J. Mol. Liq.*, 1992, **51**, 11–38.

71 A. Chandra, *J. Chem. Phys.*, 2000, **113**, 903–905.

72 A. Chandra and G. N. Patey, *J. Chem. Phys.*, 1994, **100**, 8385–8391.

73 E. Tarif, J. Mondal and R. Biswas, *J. Phys. Chem. B*, 2019, **123**, 9378–9387.

74 E. Tarif, J. Mondal and R. Biswas, *J. Mol. Liq.*, 2020, **303**, 112451.

75 A. Paiva, R. Craveiro, I. Aroso, M. Martins, R. L. Reis and A. R. C. Duarte, *ACS Sustain. Chem. Eng.*, 2014, **2**, 1063–1071.

76 Y. Dai, J. van Spronsen, G.-J. Witkamp, R. Verpoorte and Y. H. Choi, *Anal. Chim. Acta.*, 2013, **766**, 61–68.

77 H. Vanda, Y. Dai, E. G. Wilson, R. Verpoorte and Y. H. Choi, *Comptes. Rendus. Chimie.*, 2018, **21**, 628–638.

78 Y. Liu, J. B. Friesen, J. B. McAlpine, D. C. Lankin, S.-N. Chen and G. F. Pauli, *J. Nat. Prod.*, 2018, **81**, 679–690.

79 P. Pollet, E. A. Davey, E. E. Ureña-Benavides, C. A. Eckert and C. L. Liotta, *Green Chem.*, 2014, **16**, 1034–1055.

80 W.-C. Huang, D. Zhao, N. Guo, C. Xue and X. Mao, *J. Agric. Food Chem.*, 2018, **66**, 11897–11901.

81 C. Yuan, K. Chu, H. Li, L. Su, K. Yang, Y. Wang and X. Li, *Chem. Phys. Lett.*, 2016, **661**, 240–245.

82 O. S. Hammond, R. Atri, D. T. Bowron and K. J. Edler, *Chem. Eur. J.*, 2022, **28**, e2022005.

83 C. F. Araujo, J. A. P. Coutinho, M. M. Nolasco, S. F. Parker, P. J. A. Ribeiro-Claro, S. Rudić, B. I. G. Soares and P. D. Vaz, *Phys. Chem. Chem. Phys.*, 2017, **19**, 17998–18009.

84 R. Xin, S. Qi, C. Zeng, F. I. Khan, B. Yang and Y. Wang, *Food Chem.*, 2017, **217**, 560–567.

85 S. Elderderi, L. Wils, C. Leman-Loubière, S. Henry, H. J. Byrne, I. Chourpa, E. Munnier, A. A. Elbashir, L. Boudesocque-Delaye and F. Bonnier, *Anal. Bioanal. Chem.*, 2021, **413**, 4785–4799.

86 T. Jurić, D. Uka, B. B. Holló, B. Jović, B. Kordić and B. M. Popović, *J. Mol. Liq.*, 2021, **343**, 116968.

87 P. L. Pisano, M. Espino, M. de los Ángeles Fernández, M. F. Silva and A. C. Olivieri, *Microchem. J.*, 2018, **143**, 252–258.

88 I. Delso, C. Lafuente, J. Muñoz-Embid and M. Artal, *J. Mol. Liq.*, 2019, **290**, 111236.

89 N. J. Babu and A. Nangia, *Cryst. Growth Des.*, 2011, **11**, 2662–2679.

90 K. T. Savjani, A. K. Gajjar and J. K. Savjani, *ISRN Pharm.*, 2012, **2012**, 1–10.

91 C. Lipinski and others, *Am. Pharm. Rev*, 2002, **5**, 82–85.

92 I. M. Aroso, J. C. Silva, F. Mano, A. S. D. Ferreira, M. Dionìsio, I. Sá-Nogueira, S. Barreiros, R. L. Reis, A. Paiva and A. R. C. Duarte, *Eur. J. Pharm. Biopharm.*, 2016, **98**, 57–66.

93 S. Golgoun, M. Mokhtarpour and H. Shekaari, *Pharm. Sci.*, 2020, **27**, 86–101.

94 L. P. Silva, L. Fernandez, J. H. F. Conceição, M. A. R. Martins, A. Sosa, J. Ortega, S. P. Pinho and J. A. P. Coutinho, *ACS Sustain. Chem. Eng.*, 2018, **6**, 10724–10734.

95 V. Alizadeh, F. Malberg, A. A. H. Pádua and B. Kirchner, *J. Phys. Chem. B*, 2020, **124**, 7433–7443.

96 E. E. Benson, in *Plant conservation biotechnology*, CRC Press, 1999, pp. 109–122.

97 F. Engelmann, *In Vitro Cellular & Developmental Biology-Plant*, 2004, **40**, 427–433.

98 D. E. Pegg, *Semin Reprod. Med.*, 2002, **20**, 005–014.

99 B. J. Fuller, *CryoLetters*, 2004, **25**, 375–388.

100 G. D. Elliott, S. Wang and B. J. Fuller, *Cryobiology*, 2017, **76**, 74–91.

101 A. C. Drake, Y. Lee, E. M. Burgess, J. O. M. Karlsson, A. Eroglu and A. Z. Higgins, *PLoS One*, 2018, **13**, e0190713.

102 B. J. Finkle and J. M. Ulrich, *Plant Physiol.*, 1979, **63**, 598–604.

103 G. Smith, A. P. Duffy, J. Shen and C. J. Olliff, *J. Pharm. Sci.*, 1995, **84**, 1029–1044.

104 W. E. Vaughan, *Annu. Rev. Phys. Chem.*, 1979, **30**, 103–124.

105 C. Wu, Z. Li, G. M. Treich, M. Tefferi, R. Casalini, R. Ramprasad, G. A. Sotzing and Y. Cao, *Appl. Phys. Lett*., 2019, **115**, 163901.

106 L. Boldon, F. Laliberte and L. Liu, *Nano Rev.*, 2015, **6**, 25661.

107 A. Hospital, J. R. Goñi, M. Orozco and J. L. Gelp, *Adv. Appl. Bioinform. Chem.*, 2015, **8**, 37–47.

108 K. Zhou and B. Liu, *Molecular dynamics simulation: Fundamentals and Applications*, Academic Press, 2022.

109 J. M. Caillol, D. Levesque and J. J. Weis, *J. Chem. Phys.*, 1986, **85**, 6645–6657.

110 S. Chowdhuri and A. Chandra, *J. Chem. Phys.*, 2001, **115**, 3732–3741.

111 A. Chandra, D. Wei and G. N. Patey, *J. Chem. Phys.*, 1993, **98**, 4959–4966.

112 G. Löffler, H. Schreiber and O. Steinhauser, *J. Chem. Phys.*, 1997, **107**, 3135–3143.

113 C. Schröder and O. Steinhauser, *J. Chem. Phys.*, 2010, **133**, 154511.

114 C. Schröder and O. Steinhauser, *J. Chem. Phys.*, 2009, **131**, 114504.

115 C. Schröder and O. Steinhauser, *J. Chem. Phys.*, 2010, **132**, 244109.

116 C. Schröder, M. Haberler and O. Steinhauser, *J. Chem. Phys.*, 2008, **128**, 134501.

117 C. Schröder, T. Rudas and O. Steinhauser, *J. Chem. Phys.*, 2006, **125**, 244506.

118 C. Schröder, C. Wakai, H. Weingärtner and O. Steinhauser, *J. Chem. Phys.*, 2007, **126**, 084511.

119 C. Schröder, J. Hunger, A. Stoppa, R. Buchner and O. Steinhauser, *J. Chem. Phys.*, 2008, **129**, 184501.

120 C. Schröder, T. Rudas, G. Neumayr, S. Benkner and O. Steinhauser, *J. Chem. Phys.*, 2007, **127**, 234503.

121 C. Schröder, M. Sega, M. Schmollngruber, E. Gailberger, D. Braun and O. Steinhauser, *J. Chem. Phys.*, 2014, **140**, 204505.

122 T. Rudas, C. Schröder, S. Boresch and O. Steinhauser, *J. Chem. Phys.*, 2006, **124**, 234908.

123 S. Boresch, P. Höchtl and O. Steinhauser, *J. Phys. Chem. B*, 2000, **104**, 8743–8752.

124 S. Boresch, M. Willensdorfer and O. Steinhauser, *J. Chem. Phys.*, 2004, **120**, 3333–3347.

125 S. Emmert, M. Wolf, R. Gulich, S. Krohns, S. Kastner, P. Lunkenheimer and A. Loidl, *Eur. Phys. J. B*, 2011, **83**, 157–165.

126 P. Ben Ishai, M. S. Talary, A. Caduff, E. Levy and Y. Feldman, *Meas. Sci. Technol.*, 2013, **24**, 102001.

127 F. Pizzitutti and F. Bruni, *Rev. Sci. Instrum.*, 2001, **72**, 2502–2504.

128 C. C. Wang, H. B. Lu, K. J. Jin and G. Z. Yang, *Mod. Phys. Lett. B*, 2008, **22**, 1297–1305.

129 M. Samet, A. Kallel and A. Serghei, *J. Compos. Mater.*, 2022, **56**, 3197–3217.

130 M. P. Allen and D. J. Tildesley, *Computer Simulations of Liquids*, Oxford University Press, New York, 1987.

131 W. F. Van Gunsteren and H. J. C. Berendsen, *Angew. Chem., Int. Ed. Engl.*, 1990, **29**, 992–1023.

132 E. Krieger and G. Vriend, *J. Comput. Chem.*, 2015, **36**, 996–1007.

133 J. A. Aguilar-Pineda, G. A. Méndez-Maldonado, E. Núñez-Rojas and J. Alejandre, *Mol. Phys.*, 2015, **113**, 2716–2724.

134 C. Caleman, P. J. Van Maaren, M. Hong, J. S. Hub, L. T. Costa and D. van der Spoel, *J. Chem. Theory Comput.*, 2012, **8**, 61–74.

135 D. Maji, S. Indra and R. Biswas, *J. Chem. Sci.*, 2021, **133**, 104.

136 V. Agieienko and R. Buchner, *Phys. Chem. Chem. Phys.*, 2022, **24**, 5265–5268.

137 V. Agieienko, V. Neklyudov and R. Buchner, *J. Phys. Chem. Lett.*, 2022, **13**, 10805–10809.

138 D. Maji, N. C. Maity and R. Biswas, *Theor. Chem. Acc.*, 2023, **142**, 43.

Chapter 2

Dielectric relaxations of molten acetamide: Dependence on the model interaction potentials and the effects of system size

2.1 Introduction

Amide systems are an exciting class of molecules because of their proximity to the world of proteins and peptides in terms of functional groups.[1,2] The existence of the peptide bond (-CO-NH-) in amides, which is also the linkage unit in polypeptides and proteins, makes amides biologically relevant. Acetamide (CH_3CONH_2) is the smallest amide that contains a methyl group and participates in hydrogen bonding via two amide hydrogens and one carbonyl oxygen.[3–5] As a result, acetamide offers a simple molecular model for studying the effects of hydrogen bonding in peptides and amino acids. This assumes further importance given that the structure and function of a protein are dictated by H-bond interactions. Moreover, liquid acetamide is a useful solvent for its high polarity (static dielectric constant, ε_s ~ 65) and low viscosity (~2.2 cP).[6–10] Therefore, several studies have been performed on acetamide and other small amides.[11–18] In recent years, deep eutectic solvents (DESs) have arrived as better alternatives to conventional organic solvents. Several studies have already explored the dynamics of acetamide in DESs that contain acetamide as one of the main components.[19–27] The orientation jump mechanism and its connection to H-bond dynamics, established for water reorientation dynamics,[28,29] has been investigated for molten acetamide as well.[19,25] Recently, dielectric relaxation measurements of neat molten liquid acetamide in the frequency window, $0.2 \leq \nu/GHz \leq 50$, have been reported for the first time.[26] In contrast, no simulation study on DR of neat, molten acetamide has been performed yet.

An extensive simulation study of neat liquid acetamide examining several aspects, such as the influence of model interaction potential, simulation run time, and simulation system size dependencies, is required to understand the impact of other species on the structure and dynamics of acetamide in a deep eutectic system. Often, electrolytes and other neutral compounds are mixed with acetamide to prepare room-temperature deep eutectic solvents to explore possibilities for applications as synthesis media. Several studies of ionic acetamide deep eutectics have been carried out in the past to characterize the relaxation behavior of

acetamide in those media and to deduce, via interpretation of the measured relaxation parameters, the collective structure of acetamide at that solution condition.[30–34] One of the spectacular yet the most debatable findings of those studies has been the mega value (~10^6) of the ε_s of ionic acetamide DESs determined via DR measurements employing a KHz-MHz frequency window.[30,34] Although a low frequency divergence swamps the dielectric response of conducting solutions as the frequency of the applied electric field approaches zero, the correct value of ε_s must be accessed to understand the ion influence on the macroscopic polarization response of a neat dipolar system. Considering the difficulty of DR measurements for conducting solutions in attaining the plateau for the real part of the complex dielectric spectra in the limit of zero frequency, one can resort to computer simulations where the ionic and non-ionic contributions to the total polarization response could be easily separated out and understood. This separation is critical to examine whether the colossal ε_s of ionic acetamide DESs reported in earlier DR measurements[30,34] is at all real or an experimental artifact due to electrode polarisation.

However, computer simulations with classical interaction potentials have its own limitations too. The most critical of them is the availability of the appropriately coarse-grained classical interaction potentials that can reproduce the experimentally measured structural and dynamical quantities. It has been found in many cases, particularly for solvents participating in an extensive inter- and intra-molecular H-bonding, that the designed model interaction potentials are unable to simultaneously predict the experimentally observed structural and dynamical properties. In such cases, the choice of interaction potential depends on the final goal of the planned study. This means that if properties regulated by the spatial arrangements of medium particles are to be investigated then the interaction parameters that better predict the solvent structural aspects are employed. For a focus on reproducing the relaxation timescales (for example, diffusion and conductivity timescales), potential parameters that are designed to provide a good description of the collective dynamics are used. Although solvent structure represents the spatial particle arrangements arising from averaging of the faster changes (fluctuations) over a certain duration (and thus a function of the averaging timescale), model interaction parameters designed to reproduce solvent dynamics cannot always successfully predict the structural properties. This is a limitation that is a direct consequence of describing collective interactions in terms of classical pair potentials and no explicit treatment of polarizabilities, a trade-off between the quantitative description of the experimental properties and a judicious choice of accessing the computational resources for gaining qualitatively

correct molecular level understanding of the observed phenomena. Temperature transferability and the applicability of a set of potential parameters developed for a neat system to describe interactions in a multicomponent mixture are other critical issues that prevent quantitative interpretation of the simulation results.

In such a scenario, a simulation study of molten acetamide demands a careful consideration of the following aspects: (i) If one of the central foci of a planned study is to examine the mega-value of ε_s of ionic acetamide deep eutectics, then one must start with a model interaction potential that has been designed to reproduce the experimental ε_s of neat molten acetamide, (ii) system size of such simulations must be appropriately decided upon as ε_s is a collective solvent property and connected to the macroscopic (that is, large wavelength) solvent polarisation fluctuations, and (iii) a parallel simulation study must be carried out with another set of interaction potential parameters that have been developed to better describe the relaxation timescales. A judicious juxtaposition of the simulation data obtained via employing these two different sets of model potentials may then provide a qualitatively correct picture of the collective orientational polarisation relaxations of such ionic media. This provides the basic premises for our present study.

Here, we present molecular dynamics simulations of neat molten acetamide at 358.15 K and report results with the aim of interpreting the experimentally available DR data. We have considered two different models of interaction potentials based on the optimized potential for liquid simulations (OPLS) force fields. They are the united-atom (OPLS-UA)[35] and the all-atom (OPLS-AA)[36] interaction potentials. Interestingly, the OPLS-UA model[35] predicts a value of ε_s for molten acetamide that agrees quite well with that reported in experiments[37] but predicts a DR dynamic that is ~3 times slower than found in the relevant experiments. The OPLS-AA model interaction parameters,[36] in contrast, provide a much better description of the experimental DR dynamics but severely underestimate the ε_s value. We have also performed simulations on three systems with 250, 500, and 1000 numbers of molecules to check the impact of system size. A direct comparison between the simulated and experimental dielectric response for neat molten acetamide has been presented and the role of single dipole rotation has been explored.

2.2 Theory and Computational Details

2.2.1 Theory

The dielectric spectrum of a polar system can be calculated by using the total dipole moment of the system. In a polarizable model, electronic polarizability is explicitly considered but at the expense of high computational efficiency. A non-polarizable model deliberately omits the electronic polarizability and set the dielectric function at high frequency (theoretically infinite) (ε_∞) to unity. Static dielectric constant (ε_s) is the value of the frequency-dependent dielectric function, $\varepsilon(\omega)$, in the limit of zero frequency. That is, $\varepsilon_s = \varepsilon(\omega \to 0)$. The numerical value of ε_s can be computed from the fluctuations of the total dipole moment of the system. The total dipole moment $\boldsymbol{M}$ is the summation of the molecular dipole moments ($\boldsymbol{\mu}_i$), $\boldsymbol{M} = \sum_{i=1}^{N} \boldsymbol{\mu}_i$. Dipole moment for each individual molecule can be calculated from the charge (q) and positions ($\boldsymbol{r}$) of the corresponding atoms ($\boldsymbol{\mu}_i = \sum q_i \boldsymbol{r}_i$). The static dielectric constant is then calculated as [38,39]

$$\varepsilon_s = 1 + \frac{\langle \boldsymbol{M}^2 \rangle - \langle \boldsymbol{M} \rangle^2}{3\epsilon_0 V k_B T}, \tag{2.1}$$

where ϵ_0 is vacuum permittivity, V the volume, k_B the Boltzmann constant and T the temperature. Angular brackets represent ensemble averaging. The finite system Kirkwood g-factor (G_K) describes the correlation among the molecular dipoles and connects to the total moment by the following relation[40,41]

$$G_K = \frac{\langle \boldsymbol{M}^2 \rangle - \langle \boldsymbol{M} \rangle^2}{N\boldsymbol{\mu}^2}, \tag{2.2}$$

where $\boldsymbol{\mu}$ is the average dipole moment of a single molecule. Therefore, G_K=1 for an arrangement of totally randomised and uncorrelated dipoles, G_K>1 for configurations with the parallel alignment of dipoles, and G_K<1 for antiparallel orientation of molecular dipoles at the individual level. From this finite system Kirkwood correlation factor, an infinite system Kirkwood factor (g_K) can be evaluated from the following equation[40,41]

$$g_K = \frac{(2\varepsilon_s + 1)}{3\varepsilon_s} G_K, \tag{2.3}$$

Frequency-dependent dielectric spectrum is determined from the Laplace-Fourier transform of the normalized total dipole moment autocorrelation function, $\phi(t)$, which is the pulse-response function of the system.[42]

$$\phi(t) = \frac{\langle \boldsymbol{M}(0).\boldsymbol{M}(t)\rangle}{\langle |\boldsymbol{M}(0)|^2\rangle} \quad . \tag{2.4}$$

Note that $\phi(t)$, by construction, starts from unity at $t = 0$ and decays to zero with time. The multi-exponential or non-exponential character of $\phi(t)$ is then reflected in the experimental DR as multi-Debye, Cole-Cole and Cole-Davidson relaxation processes. Linear response theory[43] approximates the natural dynamics of a given system to its responses in presence of an external weak electric field. Frequency-dependent dielectric spectrum is then obtained as[42]

$$\frac{\varepsilon(\omega)-1}{\varepsilon_s-1} = \mathcal{L}_{i\omega}\left[-\frac{d\phi(t)}{dt}\right] \quad , \tag{2.5}$$

where,

$$\mathcal{L}_{i\omega}[f(t)] = \int e^{i\omega t} f(t) dt. \tag{2.6}$$

In practice, the simulated $\phi(t)$ is fitted with a suitable fit function, $\varphi(t)$, because of the poor converging nature of $\phi(t)$. Then Laplace –Fourier transform of $\varphi(t)$ is performed (instead of $\phi(t)$) to obtain the dielectric spectrum.

Real and imaginary parts of the dielectric spectrum are defined as[44]

$$\varepsilon(\omega) = \varepsilon'(\omega) - i\varepsilon''(\omega) \, . \tag{2.7}$$

There is another correlation function defining the correlation between a molecular dipole with itself. This is self-dipole autocorrelation function and is defined as[44]

$$C_\mu(t) = \frac{\langle \boldsymbol{\mu}_i(t).\boldsymbol{\mu}_i(0)\rangle}{\langle |\boldsymbol{\mu}_i(0)|^2\rangle} \, . \tag{2.8}$$

As for $\phi(t)$ described above, $C_\mu(t)$ is a normalised time autocorrelation function and decays with time from unity to zero.

2.2.2 Computational details

We have already mentioned that two different versions of the OPLS force fields have been employed in the present study. Note that the OPLS-UA model interaction potential employed here is not the same as the united atom version of the original OPLS model.[45] This model is appropriately tweaked to reproduce the experimental ε_s of neat molten acetamide. The functional forms of both the force fields are the same as[35,36]

$$V(r) = \sum_{\text{bonds}} K_r\left(r - r_{eq}\right)^2 + \sum_{\text{angles}} K_\theta(\theta - \theta_{eq})^2$$

$$+ \sum_{\text{torsions}} \left[\frac{V_1}{2}(1+\cos\phi) + \frac{V_2}{2}(1-\cos 2\phi) + \frac{V_3}{2}(1+\cos 3\phi) + \frac{V_4}{2}(1-\cos 4\phi)\right]$$

$$+ \sum_i \sum_{j>i} \left\{\frac{q_i q_j}{4\pi\epsilon_0 r_{ij}} + 4\varepsilon_{ij}\left[\left(\frac{\sigma_{ij}}{r_{ij}}\right)^{12} - \left(\frac{\sigma_{ij}}{\sigma r_{ij}}\right)^{6}\right]\right\} f_{ij} \quad . \tag{2.9}$$

In the above equation, K_r and K_θ are the force constants for bond stretching and angle bending respectively, r_{eq} and θ_{eq} denote the equilibrium bond-length and the angle values, and V represents the Fourier coefficient of torsional angle ϕ. r_{ij} is the distance between two atoms i and j with partial charges q_i and q_j, σ and ε are respectively the van der Waals diameter and the well-depth of the Lennard-Jones potential. Geometric combination rules for the Lennard-Jones parameters are $\sigma_{ij}=(\sigma_{ii}\sigma_{jj})^{1/2}$ and $\varepsilon_{ij}=(\varepsilon_{ii}\varepsilon_{jj})^{1/2}$. The factor $f_{ij}=1$ except for 1-4 interactions where $f_{ij}=0.5$.

All simulations have been performed in the GROMACS-2018.3 MD package.[46] The long-range electrostatic interactions were treated via the Ewald summation technique.[47] Both types of short-range interactions were truncated at 1.1 nm. A particle mesh Ewald method was used with a 0.12 nm grid and a spline of order 4.

Initial structures were built using Packmol.[48] Three systems were simulated for the OPLS-UA model interaction potential containing 250, 500, and 1000 molecules. For the OPLS-AA model also, three systems with the same number of molecules were considered. To check the impact of initial configuration, we have performed another independent MD run containing 500 molecules and using OPLS-UA force field model in same conditions. Periodic boundary conditions were used for all the systems. NPT equilibrations were done for 20 ns (OPLS-UA) and 5 ns (OPLS-AA) at 1 bar and 358.15 K using the leap-frog algorithm with a time step of 1 fs. Note that systems using OPLS-UA potential need much more time to get equilibrated compared to OPLS-AA model. Density, temperature and pressure values are observed thorough the equilibration times. These values get satisfactorily converged within the mentioned equilibration times. Nosé-Hoover thermostat[49] was used for the temperature coupling with time constants 0.2 ps (OPLS-UA) and 1 ps (OPLS-AA). To couple pressure, Parrinello-Rahman barostat[50] was used with time constants 0.5 ps (OPLS-UA) and 5 ps (OPLS-AA). LINCS algorithm[51] was employed to retain all bonds constrained. Thermostat and barostat relaxation times are taken from respective references for OPLS-UA[35] and OPLS-AA.[36]

Production runs (100 ns for OPLS-UA and 60 ns for OPLS-AA) were carried out using the same conditions as equilibration with output files were saving at every 100 fs. Convergence of the value of static dielectric constant with time dictate the goodness of simulation. In case of OPLS-UA interaction potential longer times are required for this type of convergence.

2.3 Results and Discussion

2.3.1 Density and self-diffusion coefficients

To check the reliability of the present simulations liquid densities from different runs have been calculated and these values are compared against the available data[35–37] in Table 2.1.

Table 2.1: Density and self-diffusion coefficient for different potential models. Values are shown for present simulation as well as from existing literatures. Values in parentheses indicate value reported in corresponding paper.

Force Field	Model	No of molecules	T (K)	ρ (kg m^{-3})	D (x10^{-5} cm^{2}s^{-1})
OPLS	UA[35]	250	358.15	994	0.274
		500		995.6 (998.9)	0.285
		1000		996.4	0.274
	AA[36]	1000		1024.3 (1018.7)	0.816
Drude oscillator[62]		64	373	---	---
CHARMM-PIPF[53]		256		---	0.75±0.04
CHARMM[27]		512	365	---	0.91
Experiment[37]			---	998.6	---

For clarity here we have shown only one data set for OPLS-AA model. Density and self-diffusion coefficient values of 250, and 500 molecules for OPLS-AA model are provided in Table 2.A.1 of the Appendix 2.A. Clearly, our simulated density employing the OPLS-UA interaction matches well with the experimental value.[37] In addition, densities predicted here employing the OPLS-UA and OPLS-AA potentials are in very good agreement with the available simulated densities.[35,36] This provides us with the necessary confidence to continue with our proposed study. From the density and self-diffusion coefficient values for two independent MD runs of 500 molecules for OPLS-UA force field (will be denoted as Run 1 and Run 2 hereafter), given in Table 2.A.2 of the Appendix 2.A, no significant effect of initial configuration on these values is observed.

The self-diffusion coefficient is a representative of diffusive dynamics in a given system. The translational mean square displacements (MSDs), $\langle\left|\Delta\overrightarrow{r(t)}\right|^2\rangle = \frac{1}{N}\langle\sum_{i=1}^{N}|\vec{r}_i^c(t) - \vec{r}_i^c(0)|^2\rangle$, have been followed and the diffusion coefficients,[52] $D = \left[\frac{1}{6}(\langle\left|\Delta\overrightarrow{r(t)}\right|^2\rangle\right]_{t\to\infty}$, for molten acetamide have been estimated from the present simulations. The simulated self-diffusion coefficients for our systems and a comparison with the available data are also provided in Table 2.1. D values shown in the last column of Table 2.1 suggest that the system size dependence for the OPLS-UA system is negligible. Also, a minimal system size dependence is observed for OPLS-AA model (Table 2.A.1 of Appendix 2.A). However, the OPLS-UA predicted diffusion coefficient is ~3 times slower than that provided by the OPLS-AA interaction parameters. Interestingly, the OPLS-AA predicted diffusion coefficient for molten acetamide agrees well with those predicted by the CHARMM-PIPF[53] and CHARMM[27] interaction potentials. In addition, the diffusion coefficient predicted here by the OPLS-AA potential (~0.82 x 10^{-5} cm^2s^{-1}) is in good agreement with that (0.92 x 10^{-5} cm^2s^{-1}) reported in the quasi-elastic neutron scattering (QENS) measurements.[27] It is therefore likely that DR time constants obtained by employing the OPLS-AA interaction potential for liquid acetamide would be in better agreement with experiments than those predicted via the OPLS-UA interaction potential.

2.3.2 Radial distribution functions (RDFs)

The structure of liquids in two dimensions can be visualized by the RDFs which describe the probability of finding a particle at a distance *r* from a tagged particle. It is calculated using the following equation:

$$g_{ij}(r) = \frac{1}{\rho N}\langle\sum_{ij}\delta(r - r_{ij})\rangle \tag{2.10}$$

where ρ is the number density, N is the total number of particles and *i* and *j* are particle indices where angular brackets denote ensemble average.

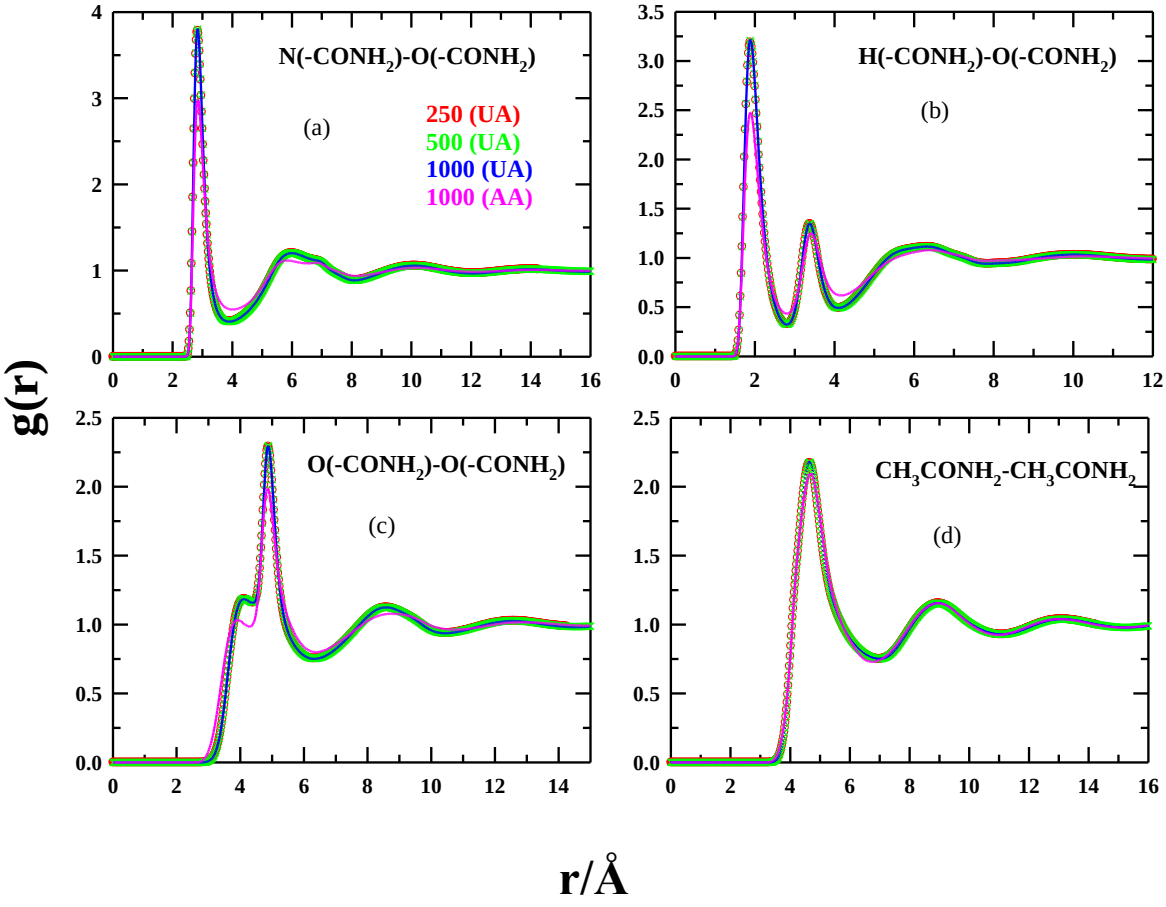

Figure 2.1: Simulated radial distribution functions (RDFs) for different atom-sites of acetamide molecules are shown in four panels. Following site-site RDFs are presented: (a) N(-$CONH_2$)-O(-$CONH_2$), (b) H(-$CONH_2$)-O(-$CONH_2$), (c) O(-$CONH_2$)-O(-$CONH_2$), (d) center-of-mass of acetamide molecules. Representations are color defined as described in panel (a).

Computed RDFs for liquid acetamide are displayed in Figure 2.1 for distributions of different atoms in the system. It has been already suggested that H-bond plays an important role in the structure and dynamics of liquid acetamide.[3,54–58] Calculated RDFs between different types of particles for the present systems depict the liquid structure (in two dimensions though) and provide a scope to compare between the predictions by these two potential models.

The upper-left panel of Figure 2.1 shows the RDF of N (-$CONH_2$)-O (-$CONH_2$). We can see that there is no system size dependence. For both of the models, the first peak appears at ~2.85 Å which is similar to earlier reports.[45,53,59] This peak is mainly the result of hydrogen bonding as explained in Ref 36. The first-peak height is greater for the OPLS-UA model predicted RDF than that by the OPLS-AA model. This may be a reflection of a relatively stronger H-bond

interaction in the OPLS-UA acetamide and can partially explain the relatively lower diffusion coefficient value.

The upper-right panel represents O (-$CONH_2$)-H (-$CONH_2$) RDFs for acetamide. From the X-ray diffraction study,[12,60] O (-$CONH_2$) ---H (-$CONH_2$) bond length is found as 3.03 Å which is comparable with the first peak minimum of the corresponding RDF shown here. The appearances of peak positions are consistent with previous studies,[45,53,59] suggesting that the underlying liquid structure remains the same in the present simulations as found in previous studies. [45,53,59] Here also the first peak height for the OPLS-UA model is greater than that for the OPLS-AA model.

An interesting feature is observed for O (-$CONH_2$)-O (-$CONH_2$) RDFs, shown in the lower-left panel of this figure. Notice that a shoulder appears prior to the main peak. The main peak indicates the configuration where two O atoms of two different molecules approach and a hydrogen atom of one of the two molecules resides between them. The shoulder depicts a spatial arrangement when no hydrogen atom resides between them. The lower-right panel depicts the center-of-mass RDFs of acetamide molecules.

2.3.3 Static dielectric properties

The calculation of the static dielectric constant serves two purposes. Apart from providing insights about the collective orientational structure of the dipolar liquid, convergence for the simulated ε_s with time to a constant value indicates whether the simulation is long enough for calculating the dynamic dielectric properties. We have estimated ε_s for the neat liquid acetamide and the Kirkwood g-factor (for finite and infinite systems). Figure 2.2 depicts the fluctuations of the simulated ε_s with time and its convergence to a certain value after a sufficiently long duration.

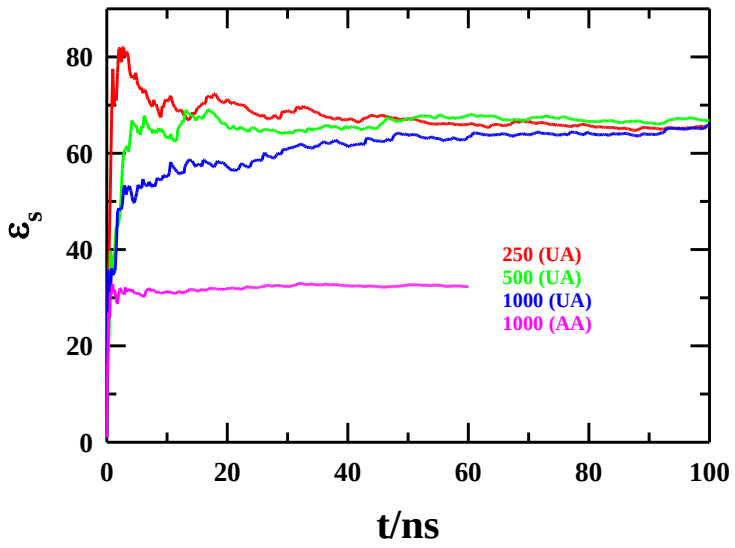

Figure 2.2: Evolutions of static dielectric constant with simulation time for all systems. All systems are fairly converged within the simulation run time. Each system is uniquely color-defined.

Notice that the simulated ε_s fluctuates more when the system size is relatively small. Interestingly, the OPLS-AA model interaction potential predicts an ε_s value nearly half of that by the OPLS-UA model, although the extent of the time-dependent fluctuations is much less for the OPLS-AA predicted ε_s and the convergence is achieved much faster. In addition, a choice of 100 ns production run-time in the present work appears to be logical for simulations of DR in neat molten acetamide.

Table 2.2 summarizes the ε_s values simulated in the present work and compares with those from earlier simulations employing different model interaction potentials[35,36,53,61] and the relevant measurements.[26,37] Comparison of various static dielectric properties among systems with different sizes using OPLS-AA model are provided in Table 2.A.3 of Appendix 2.A. The same properties can be found for Run 1 and Run 2 in Table 2.A.4 of this Appendix.

Table 2.2: Static dielectric properties for different potential models. Values are shown for present simulation as well as from existing literatures.

Force Field	Model	No of molecules	T (K)	ε_s	G_K	g_K	$\langle\mu\rangle$ (D)
OPLS	UA[35]	250	358.15	65.6	2.31	1.55	5.71
		500		66.8	2.34	1.57	
		1000		65.9	2.31	1.55	
	AA[36]	1000		32.3	1.95	1.32	4.26
Drude oscillator[61]		64	373	66±3	2.4±0.2	---	5.80
CHARMM-PIPF[53]		256		154	---	---	5.30
Experiment[26]			354	66	---	---	---
Experiment[37]			---	68.2	---	---	---

Clearly, the OPLS-UA[35] model provides a much better description of the experimental ε_s than by the OPLS-AA[36] (ε_s~32) and the CHARMM-PIPF[53] (ε_s~154) interaction potential. Note the Drude oscillator model[61] is quite successful in predicting the experimental ε_s for liquid acetamide. The estimated values for the average dipole moment and the finite Kirkwood g-factor (G_K) by the Drude oscillator model also corroborate well with the OPLS-UA predictions. The OPLS-AA model, however, substantially underestimates the orientational structure of the liquid acetamide because the estimated ε_s and the Kirkwood factors (G_K and g_K) are significantly lower than those predicted by the other interaction potentials. While stating so we keep in mind that (i) a G_K value greater than unity implies a strong correlation among the molecular dipoles and (ii) the numerical value of ε_s is connected to the macroscopic total orientational pair correlation function (h^{110}) by the relation,[62] $\frac{(\varepsilon_s-1)(2\varepsilon_s+1)}{9\epsilon_0 y} = 1 + \frac{4\pi\rho}{3}\int_0^\infty r^2 h^{110}(r)dr$, where the polarity parameter, $y = 4\pi\mu^2\rho/9\,k_BT$, ρ being the number density. Next, we compare the performance of the OPLS-UA and OPLS-AA interaction potentials in predicting the measured DR timescales.

2.3.4 Dynamic dielectric properties

Monitoring the correlation among dipoles with time, the dipole moment autocorrelation function, provides an insight into the relaxation dynamics of the system. Two different autocorrelation functions have been calculated in this work. They are the total dipole moment autocorrelation function, $\phi(t)$, and the self-dipole moment autocorrelation function, $C_\mu(t)$. While the total dipole moment autocorrelation function tracks the collective orientational relaxations and thus provides a direct theoretical description of the experimentally measured DR data, the self-dipole moment autocorrelation function treats the dipolar orientations at the

single molecule level and explores the connection between the individual dipolar rotational dynamics and the collective orientational polarization relaxations.

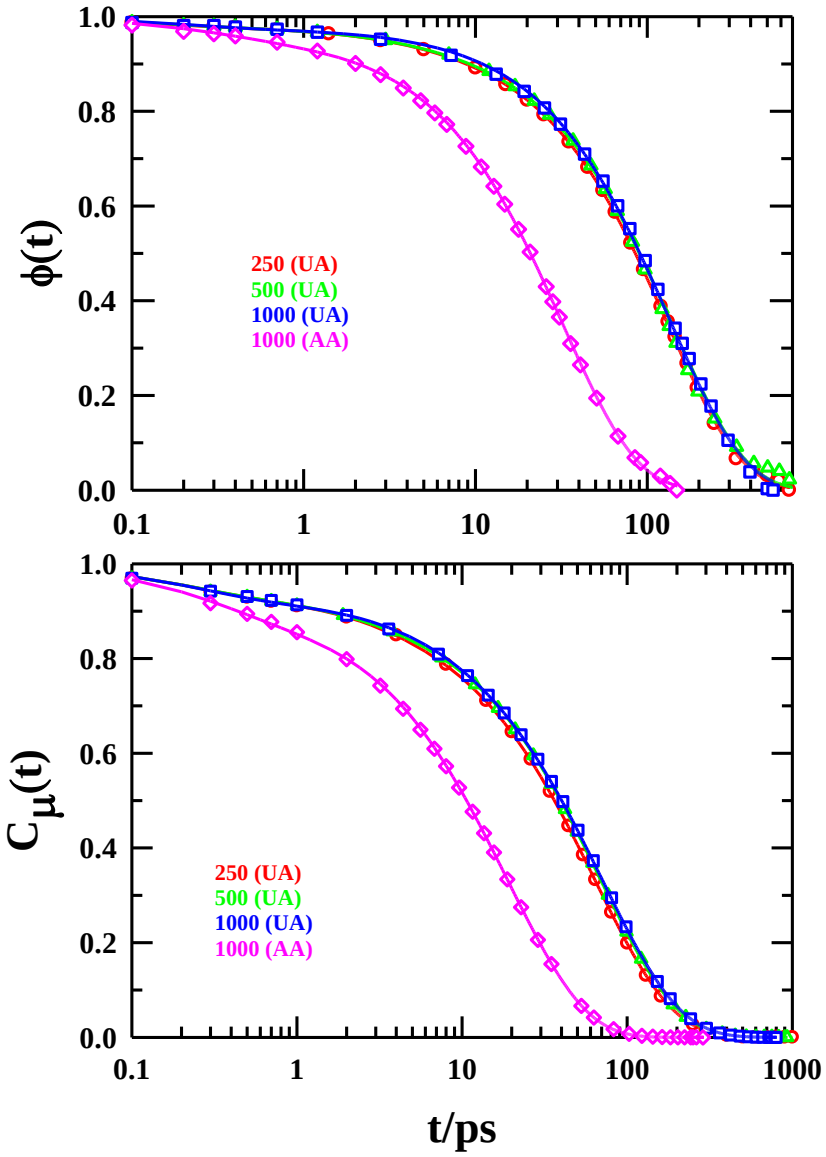

Figure 2.3: Simulated decays of total dipole moment autocorrelation function (upper panel) and dipole moment autocorrelation function for single molecules (lower panel) of all systems. Each system is uniquely color-defined. Open symbols are simulated data points and solid lines denote corresponding fits.

Upper panel of Figure 2.3 presents the time dependence of the simulated total dipole moment autocorrelation function, $\phi(t)$, for the neat liquid acetamide interacting via the OPLS-UA and OPLS-AA potentials. The system size dependence (studied for the OPLS-UA interactions) is negligible. The same plot as Figure 2.3 for OPLS-AA model containing different number of

molecules is shown in Figure 2.A.1 and fit parameters are provided in Tables 2.A.5 and 2.A.6 of the Appendix 2.A. Here also no significant system size dependence is detected. The relaxation for $\phi(t)$ obtained by employing the OPLS-AA potential is much faster than that predicted by the OPLS-UA interactions. Lower panel of Figure 2.3 shows the time dependent decay of the self-dipole moment autocorrelation function, $C_\mu(t)$. The dependence of $C_\mu(t)$ on the interaction potential and the system size is the same as that found for $\phi(t)$. Parameters obtained via multi-exponential fits to the simulated $\phi(t)$ decays are summarized in Table 2.3. Experimentally measured DR times and amplitudes are also shown in this table to facilitate a comparison between simulations and experiments. Table 2.4 summarizes the fit parameters required to adequately describe the simulated $C_\mu(t)$ decays. Plots of $\phi(t)$ and $C_\mu(t)$ for Run 1 and Run 2 are represented in Figure 2.A.2 (Appendix 2.A). Fit parameters are given in Tables 2.A.7 and 2.A.8 of Appendix 2.A, respectively. These results suggest subtle effect of starting structures on final results.

Table 2.3: Fit parameters for total dipole moment autocorrelation functions for all systems. For systems containing 250 and 500 molecules tri-exponential fit functions are used and for systems of 1000 molecules bi-exponential functions are fitted. Experimental results are for two-Debye fitting of experimental DR spectra taken from Ref. 26.

Model	**No of molecules**	a_1	τ_1 **(ps)**	a_2	τ_2 **(ps)**	a_3	τ_3 **(ps)**	$\langle\tau\rangle$ **(ps)**
UA	250	0.96	130.6	0.02	4.4	0.02	0.1	125.5
	500	0.96	138	0.02	4	0.02	0.1	132.6
	1000	0.98	135.5	---	---	0.02	0.2	132.8
AA	1000	0.96	32	---	---	0.04	0.3	30.7
Experiment[26]		0.97	55	0.03	5.5	---	---	53.5

From the data summarized in Table 2.3, it is evident that none of these two model interaction potentials can correctly reproduce the slowest experimental DR time constants, although the amplitude associated with it is predicted nearly quantitatively. The slowest DR time constant predicted by the OPLS-UA model is ~2.5 times slower than that reported in experiments, whereas the OPLS-AA predicted timescale is ~1.7 times faster than in experiments. The degree of disagreement between the predicted slowest DR times by these two versions of the OPLS model potentials (a factor of ~4) is reflective of that already observed between the translational diffusion coefficients. The other slower time constant, which is in the sub-10 ps regime in experiments, is missing for the OPLS-UA interaction when the system size is the largest. In

fact, the OPLS-AA system studied here also does not predict the sub-10 ps timescale. The other sub-picosecond timescale predicted in simulations for both the interactions is absent in experiments. This is because the limited frequency window ($0.2 \leq \nu/GHz \leq 50$) employed in those measurements cannot detect dynamics faster than a couple of picoseconds and thus completely misses the relaxation contributions arising from the collective solvent modes such as the intermolecular vibrations and librations of extensively H-bonded systems of liquids like acetamide.

The self-dipole autocorrelation function, $C_\mu(t)$, maps the correlation between a single dipole with itself at different time lags and therefore tracks the dynamics at the single molecule level. Parameters obtained from fits to $C_\mu(t)$ decays shown in Figure 2.3 (lower panel) are summarized in Table 2.4.

Table 2.4: Fit parameters for dipole moment autocorrelation function for single molecules. In case of UA model systems combination of stretched exponential and bi-exponential is used whereas for AA model system tri-exponential function is fitted.

Model	**No of molecules**	a_1	τ_1 **(ps)**	β	a_2	τ_2 **(ps)**	a_3	τ_3 **(ps)**	τ_{long}* **(ps)**	$\langle\tau\rangle$ **(ps)**
UA	250	0.91	63.3	0.92	0.03	2.8	0.06	0.2	65.8	60
	500	0.91	68.5	0.93	0.03	3.5	0.06	0.2	70.4	64.2
	1000	0.90	71	0.93	0.03	4.3	0.07	0.2	73.4	66.2
AA	1000	0.79	21.4	1.00	0.11	6.2	0.10	0.3	21.4	17.6

*$\tau_{\text{long}} = \tau\Gamma(\beta^{-1})/\beta$

Notice the weakly stretched exponential behavior of the slowest relaxation component of the $C_\mu(t)$ decays. This is a reflection of non-Debye behaviour of liquid acetamide and will emerge again when we show later the dielectric response via Cole-Cole plots. As expected, the slowest decay time constant for $C_\mu(t)$ predicted by the OPLS-UA model is ~3 times slower than that by the OPLS-AA interactions. Interestingly, the sub-10 ps and the sub-picosecond timescales are present in all the $C_\mu(t)$ decays simulated. The similarity in decay amplitudes between the $C_\mu(t)$ and the $\phi(t)$ relaxations strongly suggests that the collective orientational polarization relaxation is intimately connected to the single dipole orientation dynamics. Note this single dipole orientation relaxation ($C_\mu(t)$), although describes orientation dynamics of single molecular dipoles, is collective in nature because this molecular dipole orientational relaxation occurs in a potential created by its surrounding neighbours.

2.3.5 Dielectric spectra

Following the method described in section 2.2.1, dielectric spectra for different systems have been calculated in the frequency range of $0.001 \leq \nu/GHz \leq 10^5$. The existing experimental spectra[26] has been recorded in the frequency window $0.2 \leq \nu/GHz \leq 50$. Therefore, the available experimental DR spectra have been regenerated using the fit functions given in Table 2.3 in order to facilitate a comparison between the simulations and experiments.

Figure 2.4 presents the real (upper panel) and the imaginary (lower panel) components of the simulated dielectric relaxation spectra employing both the model interaction potentials and compares them with those from experiments. As ε_∞ and ε_s vary for different cases, the spectra are compared after appropriate normalization. Notice in both the panels that the experimental spectra are flanked by the simulated counterparts where the OPLS-UA predictions are shifted to lower and OPLS-AA predictions to higher frequencies with respect to the experiments. This means that the relaxation predicted by the OPLS-AA model potential is faster than experiments while the same predicted by the OPLS-UA parameters is slower than what has been found in measurements. This is exactly what we have already seen while comparing $\phi(t)$relaxation timescales with those from experiments. Notice also that there is no significant system size dependence in spectra simulated by employing the OPLS-UA interaction potential.

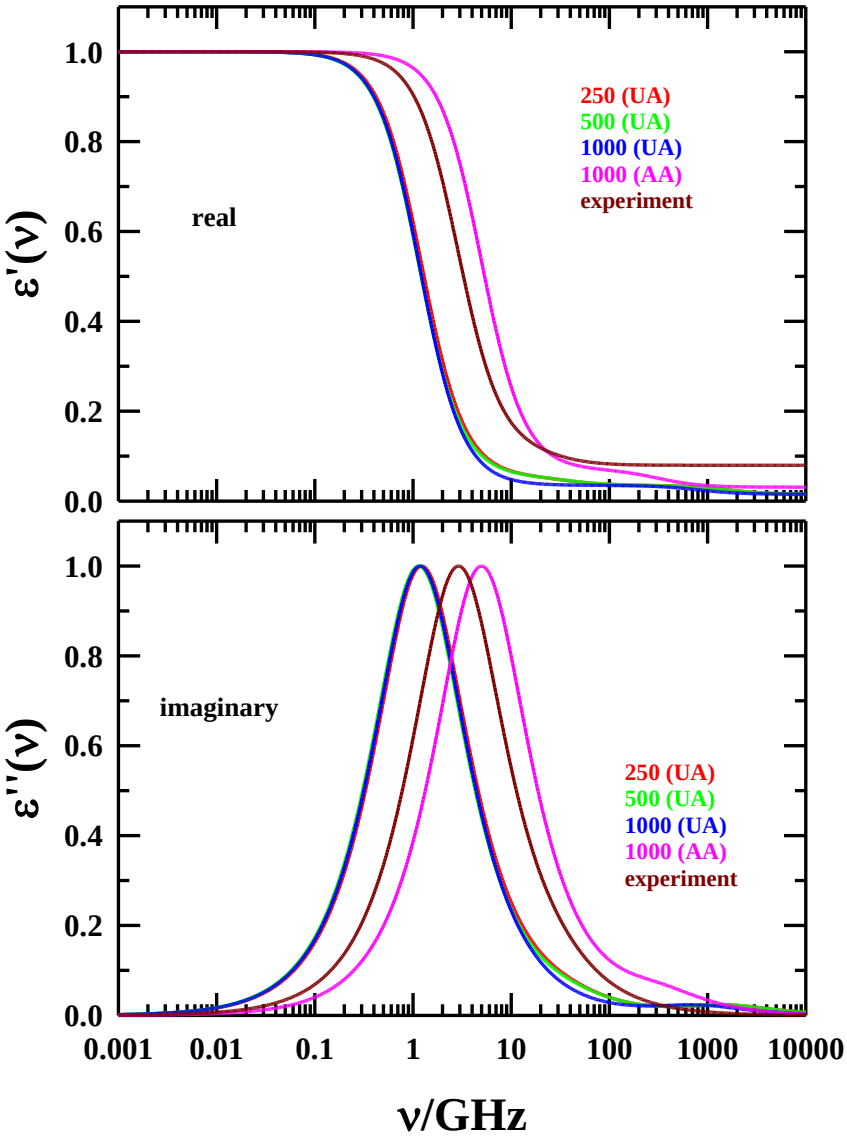

Figure 2.4: Real (upper panel) and imaginary (lower panel) parts of normalized dielectric relaxation spectra obtained from simulation for all acetamide systems are represented along with experimental results (Ref. 26). DRS data for experiment is reproduced using existing fit parameters reported in literature. Each system is uniquely color-defined.

Figure 2.5 displays the Cole-Cole plots for different systems simulated. For Debye liquids, the Cole-Cole plot is a perfect semi-circle.[44] Thus, the non-Debye nature of DR in liquid acetamide is reflected by the small deviation (from being perfect semi-circle) shown by both the simulated and experimental spectra. Tiny semicircles that appeared at the high-frequency region for MD simulation are due to the fast relaxation process which has been missed in the experiments because of the limited frequency window. The non-Debye behavior of molten acetamide has also been found while following the collective single particle reorientational relaxations.[63,64]

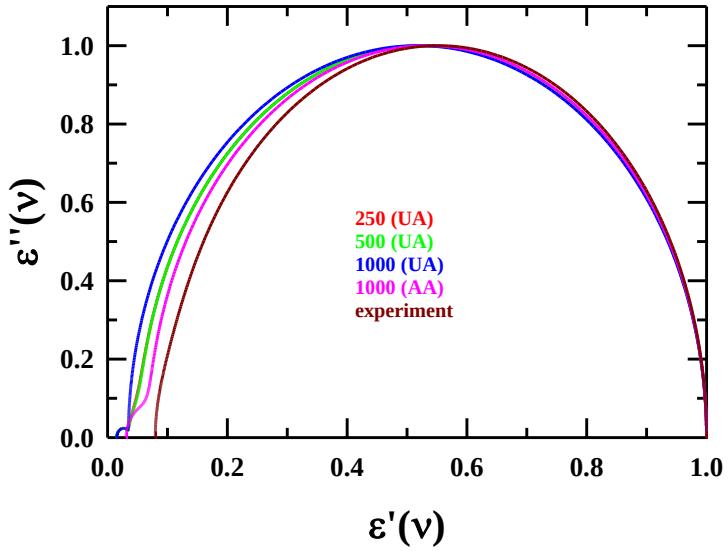

Figure 2.5: Cole-Cole plot of frequency dependent dielectric function. Simulation as well as experimental results (reproduced from fit parameters of Ref. 26) are shown. Each system is uniquely color-defined.

2.4 Conclusion

We present here for the first time a detailed comparison between the experimental and simulated dielectric relaxation spectra of neat molten acetamide where the role of single dipolar orientation dynamics in the collective polarization relaxation has been investigated and understood. This work also assumes importance when one considers that no simulation study of DR in molten acetamide was available although a number of model interaction potentials were developed to predict various solvent properties and translational diffusion coefficients of liquid acetamide. The study of system size dependence of DR for liquid acetamide conducted here, although limited within a model potential, brings out a useful information regarding the sufficiency of system size for performing simulations H-bonded dipolar liquids such as liquid acetamide. The Cole-Cole plot correctly hints at the non-Debye behavior of acetamide already found in simulation studies of reorientational relaxations. The results obtained here will be useful for simulation study DR in acetamide containing deep eutectic solvents, particularly for the investigation of the mega-value of the static dielectric constant of ionic acetamide deep eutectics and the corresponding relaxation time constants reported in the KHz-MHz measurements performed earlier. Moreover, the comparison between the simulation results obtained by employing the OPLS-AA and OPLS-UA potentials shown in this work will be an

important guide for making a logical choice of interaction potential while planning a study on dielectric properties of acetamide containing multi-component mixtures.

Appendix 2.A

Table 2.A.1: Density and self-diffusion coefficient for systems comprised of 250, 500, and 1000 molecules using OPLS-AA interaction potential.

Potential model	No of molecules	T (K)	ρ (kg m^{-3})	D (x10^{-5} cm^{2}s^{-1})
OPLS-AA[36]	250	358.15	1023.4	0.708
	500		1023.4	0.843
	1000		1024.3	0.816

Table 2.A.2: Density and self-diffusion coefficient for systems comprised of 500 molecules and interaction potentials are modelled as OPLS-UA. Results are presented for two independent runs.

Potential model	No of molecules	T (K)	Index of run	ρ (kg m^{-3})	D (x10^{-5} cm^{2}s^{-1})
OPLS-UA[35]	500	358.15	Run 1	995.6	0.285
			Run 2	995.3	0.269

Table 2.A.3: Static dielectric properties for different sized systems using OPLS-AA FF.

Potential Model	No of molecules	T (K)	ε_s	G_K	g_K	$\langle\mu\rangle$ (D)
OPLS-AA[36]	250	358.15	33.6	2.03	1.37	4.26
	500		33.9	2.05	1.39	
	1000		32.3	1.95	1.32	

Table 2.A.4: Static dielectric properties for OPLS-UA potential models. Values are shown for systems comprised of 500 molecules and interaction potentials are modelled as OPLS-UA, and starting with different initial configurations.

Potential Model	No of molecules	T (K)	Index of run	ε_s	G_K	g_K	$\langle\mu\rangle$ (D)
OPLS-UA[35]	500	358.15	Run 1	66.8	2.34	1.57	5.71
			Run 2	67.3	2.36	1.58	

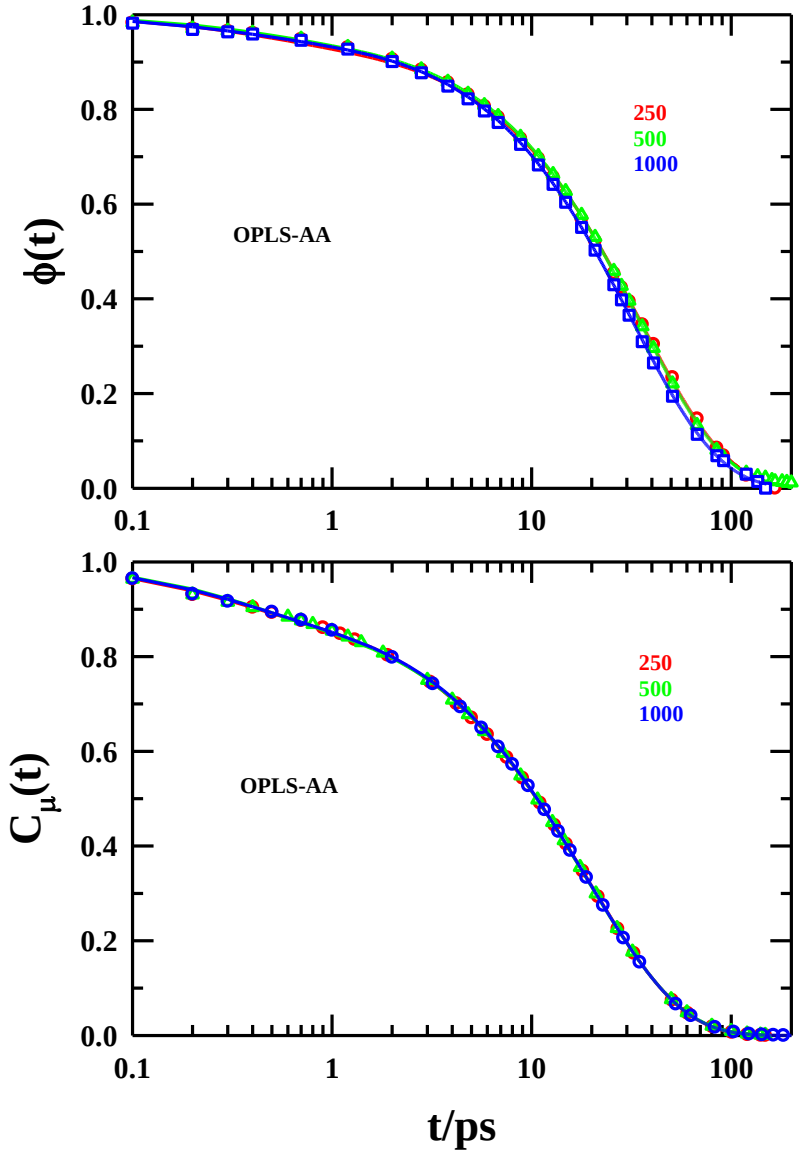

Figure 2.A.1: Simulated decays of total dipole moment autocorrelation function (upper panel) and dipole moment autocorrelation function for single molecules (lower panel) of OPLS-AA systems. Each system is uniquely color-defined. Open symbols are simulated data points and solid lines denote corresponding fits.

Table 2.A.5: Bi-exponential fit parameters for total dipole moment autocorrelation functions for three systems using OPLS-AA FF.

Potential model	No of molecules	a_1	τ_1 (ps)	a_2	τ_2 (ps)	$\langle\tau\rangle$ (ps)
OPLS-AA[36]	250	0.95	35.5	0.05	0.4	33.7
	500	0.96	34.7	0.04	0.4	33.3
	1000	0.96	32	0.04	0.3	30.7

Table 2.A.6: Multi-exponential fit parameters for dipole moment autocorrelation function for single molecules. Results are for three systems containing 250, 500, and 1000 molecules and using OPLS-AA FF.

Potential model	**No of molecules**	a_1	τ_1 **(ps)**	a_2	τ_2 **(ps)**	a_3	τ_3 **(ps)**	$\langle\tau\rangle$ **(ps)**
OPLS-AA[36]	250	0.80	21.2	0.10	4.8	0.10	0.3	17.5
	500	0.76	21.7	0.13	7.2	0.11	0.3	17.5
	1000	0.79	21.4	0.11	6.2	0.10	0.3	17.6

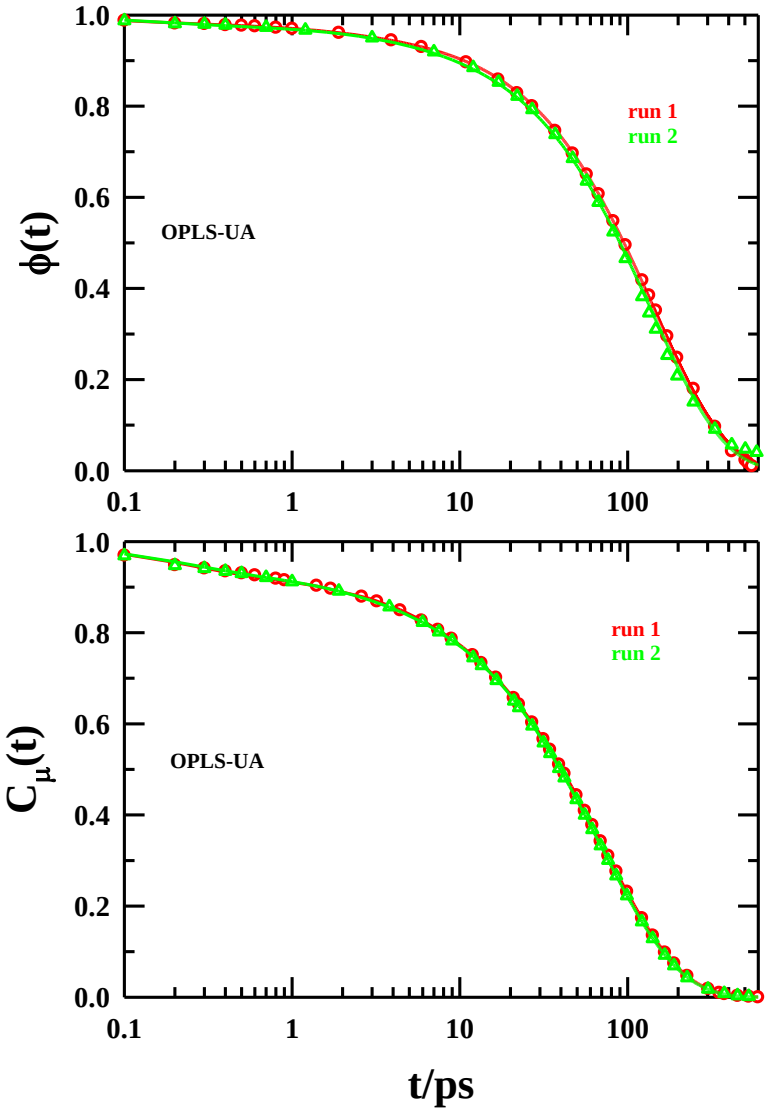

Figure 2.A.2: Simulated decays of total dipole moment autocorrelation function (upper panel) and dipole moment autocorrelation function for single molecules (lower panel) of OPLS-UA systems containing 500 molecules for two independent runs. Each system is uniquely colour-defined. Open symbols are simulated data points and solid lines denote corresponding fits.

Table 2.A.7: Multi-exponential fit parameters for total dipole moment autocorrelation functions for OPLS-UA systems consists of 500 molecules for two independent runs.

Potential model	**No of molecules**	**Index of run**	a_1	τ_1 **(ps)**	a_2	τ_2 **(ps)**	a_3	τ_3 **(ps)**	$\langle\tau\rangle$ **(ps)**
OPLS-UA[35]	500	Run 1	0.96	138	0.02	4	0.02	0.1	132.6
		Run 2	0.97	143	0.02	1.8	0.01	0.1	138.7

Table 2.A.8: Fit parameters for dipole moment autocorrelation function for single molecules for OPLS-UA systems consists of 500 molecules for two independent runs. Combinations of stretched exponential and exponential functions are fitted to the data.

Potential model	**No of molecules**	**Index of run**	a_1	τ_1 (ps)	β	a_2	τ_2 (ps)	a_3	τ_3 (ps)	τ_{long}* (ps)	$\langle\tau\rangle$ (ps)
OPLS-UA[35]	500	Run 1	0.91	68.5	0.93	0.03	3.5	0.06	0.2	70.4	64.2
		Run 2	0.90	71.8	0.94	0.04	5.7	0.06	0.2	73.9	66.8

*$\tau_{\text{long}} = \tau\Gamma(\beta^{-1})/\beta$

References

1 J. B. O. Mitchell and S. L. Price, *Chem. Phys. Lett.*, 1989, **154**, 267–272.

2 D. A. Dixon, K. D. Dobbs and J. J. Valentini, *J. Phys. Chem.*, 1994, **98**, 13435–13439.

3 R. Ludwig, F. Weinhold and T. C. Farrar, *J. Chem. Phy.s*, 1997, **107**, 499–507.

4 M. A. Krestyaninov, E. G. Odintsova, A. M. Kolker and M. G. Kiselev, *J. Mol. Liq.*, 2018, **264**, 343–351.

5 M. W. Wong and K. B. Wiberg, *J. Phys. Chem.*, 1992, **96**, 668–671.

6 R. A. Wallace, *J. Phys. Chem.*, 1971, **75**, 2687–2690.

7 L. R. Dawson, P. G. Sears and R. H. Graves, *J. Am. Chem. Soc.*, 1955, **77**, 1986–1989.

8 L. F. Yntema and L. F. Audrieth, *J. Am. Chem. Soc.*, 1930, **52**, 2693–2698.

9 O. F. Stafford, *J. Am. Chem. Soc.*, 1933, **55**, 3987–3988.

10 D. H. Kerridge, *Chem. Soc. Rev.*, 1988, **17**, 181–227.

11 S. Nasr, M. Ghédira and R. Cortès, *J. Chem. Phys.*, 1999, **110**, 10487–10492.

12 S. Nasr, *J. Chem. Phys.*, 2001, **115**, 6569–6577.

13 S. Trabelsi and S. Nasr, *J. Chem. Phys.*, 2004, **121**, 6380–6385.

14 F. Hammami, S. Nasr and M.-C. Bellissent-Funel, *J. Chem. Phys.*, 2005, **122**, 064505.

15 S. Trabelsi, M. Bahri and S. Nasr, *J. Chem. Phys.*, 2005, **122**, 024502.

16 H. K. Kashyap, T. Pradhan and R. Biswas, *J. Chem. Phys.*, 2006, **125**, 174506.

17 S. K. Pattanayak, N. Prashar and S. Chowdhuri, *J. Chem. Phys.*, 2011, **134**, 154506.

18 R. Biswas and B. Bagchi, *J. Phys. Chem.*, 1996, **100**, 1238–1245.

19 S. Das, R. Biswas and B. Mukherjee, *J. Phys. Chem. B*, 2015, **119**, 274–283.

20 H. Srinivasan, V. K. Sharma, S. Mitra, R. Biswas and R. Mukhopadhyay, *Phys. B: Condens.*, 2019, **562**, 13–16.

21 A. Das, S. Das and R. Biswas, *Chem. Phys. Lett.*, 2013, **581**, 47–51.

22 B. Guchhait, S. Daschakraborty and R. Biswas, *J. Chem. Phys.*, 2012, **136**, 174503.

23 T. Pal and R. Biswas, *Chem. Phys. Lett.*, 2011, **517**, 180–185.

24 K. Mukherjee, S. Das, E. Tarif, A. Barman and R. Biswas, *J. Chem. Phys.*, 2018, **149**, 124501.

25 S. Das, R. Biswas and B. Mukherjee, *J. Phys. Chem. B*, 2015, **119**, 11157–11168.

26 K. Mukherjee, A. Das, S. Choudhury, A. Barman and R. Biswas, *J. Phys. Chem. B*, 2015, **119**, 8063–8071.

27 H. Srinivasan, V. K. Sharma, V. G. Sakai, J. P. Embs, R. Mukhopadhyay and S. Mitra, *J. Phys. Chem. B*, 2020, **124**, 1509–1520.

28 D. Laage and J. T. Hynes, *Science (1979)*, 2006, **311**, 832–835.

29 D. Laage and J. T. Hynes, *J. Phys. Chem. B*, 2008, **112**, 14230–14242.

30 A. Amico, G. Berchiesi, C. Cametti and A. Di Biasio, *J. Chem. Soc., Faraday Trans. 2*, 1987, **83**, 619–626.

31 G. Berchiesi, M. De Angelis, G. Rafaiani and G. Vitali, *J. Mol. Liq.*, 1992, **51**, 11–38.

32 G. Berchiesi, *J. Mol. Liq.*, 1999, **83**, 271–282.

33 R. Płowiec, A. Amico and G. Berchiesi, *J. Chem. Soc., Faraday Trans. 2*, 1985, **81**, 217–224.

34 G. Berchiesi, F. Farhat, M. de Angelis and S. Barocci, *J. Mol. Liq.*, 1992, **54**, 103–113.

35 J. A. Aguilar-Pineda, G. A. Méndez-Maldonado, E. Núñez-Rojas and J. Alejandre, *Mol. Phys.*, 2015, **113**, 2716–2724.

36 C. Caleman, P. J. Van Maaren, M. Hong, J. S. Hub, L. T. Costa and D. van der Spoel, *J. Chem. Theory Comput.*, 2012, **8**, 61–74.

37 D. R. Lide, Ed., *CRC Handbook of Chemistry and Physics*, CRC Press, Boca Raton, 90th edn., 2009.

38 M. Neumann, *Mol. Phys.*, 1983, **50**, 841–858.

39 H. Fröhlich, *Theory of dielectrics: dielectric constant and dielectric loss*, Clarendon Press, Oxford, 2nd edn., 1958.

40 J. G. Kirkwood, *J. Chem. Phys.*, 1939, **7**, 911–919.

41 M. Neumann, *J. Chem. Phys.*, 1986, **85**, 1567–1580.

42 M. Neumann and O. Steinhauser, *Chem. Phys. Lett.*, 1983, **102**, 508–513.

43 R. Kubo, *Reports on Progress in Physics*, 1966, **29**, 306.

44 C. J. F. Bottcher and P. Bordewijk, *Theory of Electric Polarization*, Elsevier, Amsterdam, 2nd edn., 1978, vol. 2.

45 W. L. Jorgensen, D. S. Maxwell and J. Tirado-Rives, *J. Am. Chem. Soc.*, 1996, **118**, 11225–11236.

46 M. J. Abraham, D. van der Spoel, E. Lindahl, B. Hess and the GROMACS development team, GROMACS User Manual version 2018.

47 M. P. Allen and D. J. Tildesley, *Computer Simulations of Liquids*, Oxford University Press, New York, 1987.

48 L. Martínez, R. Andrade, E. G. Birgin and J. M. Martínez, *J. Comput. Chem.*, 2009, **30**, 2157–2164.

49 S. Nosé, *J. Chem. Phys.*, 1984, **81**, 511–519.

50 M. Parrinello and A. Rahman, *J. Appl. Phys.*, 1981, **52**, 7182–7190.

51 B. Hess, H. Bekker, H. J. C. Berendsen and J. G. E. M. Fraaije, *J. Comput. Chem.*, 1997, **18**, 1463–1472.

52 J. P. Hansen and I. R. McDonald, *Theory of Simple Liquids*, Academic, 3rd edn., 2006.

53 W. Xie, J. Pu, A. D. MacKerell and J. Gao, *J. Chem. Theory Comput.*, 2007, **3**, 1878–1889.

54 N. E. Triggs and J. J. Valentini, *J. Phys. Chem.*, 1992, **96**, 6922–6931.

55 T. W. Whitfield, G. J. Martyna, S. Allison, S. P. Bates, H. Vass and J. Crain, *J. Phys. Chem. B*, 2006, **110**, 3624–3637.

56 S. S. Kuduva, D. Bläser, R. Boese and G. R. Desiraju, *J. Org. Chem.*, 2001, **66**, 1621–1626.

57 R. Ludwig, *J. Mol. Liq.*, 2000, **84**, 65–75.

58 M. C. Etter, *Acc. Chem. Res.*, 1990, **23**, 120–126.

59 S. Das, B. Mukherjee and R. Biswas, *J. Chem. Sci.*, 2017, **129**, 939–951.

60 G. A. Jeffrey, J. R. Ruble, R. K. McMullan, D. J. DeFrees, J. S. Binkley and J. A. Pople, *Acta. Crystallogr. B*, 1980, **36**, 2292–2299.

61 E. Harder, V. M. Anisimov, T. Whitfield, A. D. MacKerell and B. Roux, *J. Phys. Chem. B*, 2008, **112**, 3509–3521.

62 C. G. Gray and K. E. Gubbins, *Theory of molecular fluids: Fundamentals*, The Clarendon Press, Oxford University Press, New York, 1984, vol. volume 1.

63 S. Das, R. Biswas and B. Mukherjee, *J. Chem. Phys.*, 2016, **145**, 84504.

64 S. Banerjee, P. Kr. Ghorai, S. Das, J. Rajbangshi and R. Biswas, *J. Chem. Phys.*, 2020, **153**, 234502.

Chapter 3

Dielectric relaxation and dielectric decrement in ionic acetamide deep eutectic solvents: Spectral decomposition and comparison with experiments

3.1 Introduction

Deep eutectic solvents (DESs) constitute a unique class of liquid systems possessing immense potential as less hazardous alternatives to conventional organic solvents for a variety of applications in chemical industries.[1–4] DESs are multicomponent mixtures in molten phase of solid compounds mixed at particular compositions where the liquid phase is accessed through heating at higher temperatures, followed by normal cooling to room temperature or near room temperature. By definition, the liquid phase temperature must be significantly lower than the individual melting temperatures of the mixture components and as a result, is distinctly different from the prediction based on depression of freezing point via colligative effects.[5] Often, the term DESs is used somewhat loosely to encompass the molten phase of the multicomponent mixtures at temperatures and compositions that are away from those corresponding to the eutectic points.[6–12] Several outstanding solvent features, such as, viscosity and polarity turnabilities, relatively lesser environmental footprints, easy to prepare and handle, low vapor pressure, wider thermal and electrochemical windows, etc. have made DESs as popular solvents as reaction media not only for targeted chemical synthesis but also for engineering materials related to technological applications. Naturally therefore, DESs are finding applications in extraction of natural compounds[13], gas absorption[14], synthesis of targeted biopolymers[15] and organic compounds. [16] Recently, ionic DESs have been emerged as potential non-flammable electrolytes for lithium-ion batteries.[17,18]

Ionic deep eutectic solvents act as a bridge between ionic liquids (ILs) and electrolyte solutions. Ionic DESs are comprised of hydrogen bond donors (HBD) and ions generated from the dissociation of the added electrolytes. Substantial charge delocalization induced by the extensive interspecies (ion-amide) H-bond interactions causing frustrations in the ionic lattices

provides the enthalpic support for formation of DESs.[19–22] The entropy gains for being in the liquid phase then completes the driving force behind the stable liquidous regime in DESs, although theoretical/computational investigation for the composition and temperature dependent entropy gain (both rotational and translational) are still unavailable. Different experiments, such as, time-resolved fluorescence experiments,[6,8,9,23–25] dielectric relaxation and conductivity measurements,[11,12,26] and femtosecond Raman induced Kerr effect spectroscopic (fs-RIKES) measurements[27] have been carried out in the last several years and each of these measurements indicated micro heterogeneous relaxation dynamics for the studied ionic DESs. Computer simulations have been carried out in recent times [7,28–30] to generate microscopic understanding of the experimentally measured relaxation dynamics. Fluorescence based measurements among these studies have revealed fractional viscosity dependence for the measured solute rotational and translational timescales, and for the solvation energy relaxation timescales. Average dielectric relaxation times too showed fractional viscosity dependence, while the fs-RIKES experiments detected spectral signatures that were caused by the ion dependent microheterogeneity of these ionic DESs. Anomalous particle motions, such as, orientational[29] and translational[31] jumps have been detected in computer simulations and these might be recognised as heterogeneity markers for these media. Interestingly, these relatively more recent studies have essentially reconfirmed the micro heterogeneous nature of ionic DESs suggested already in several previous studies that reported ultrasonic and other measurements.[32–34]

Recent dielectric relaxation data accessed via measurements in a frequency window $0.2 \leq \nu/\mathrm{GHz} \leq 50$,[11,12] however, indicates a drastic difference between what has been registered now as electrolyte effects on the static dielectric constant (ε_s) of neat molten acetamide and what was concluded from earlier experiments carried out employing a frequency window, 0.1 Hz – 100 MHz.[34–38] More specifically, recent DR measurements in MHz-GHz frequency window have revealed ε_s ~20 – 30 for several ionic acetamide DESs. Considering ε_s ~ 70 for neat molten acetamide,[11] these values reflect substantial electrolyte-induced dielectric decrement of acetamide in these ionic DESs. This is in sharp contrast to the previous finding in Hz-MHz measurements which reported a colossal increase of the static dielectric constant ($\varepsilon_s \sim 10^6$) for ionic acetamide DESs that contained either NaSCN or CF_3COONa as an electrolyte. This mega-value of ε_s was then explained[34–36] in terms of 'charged locally ordered aggregates' formed by the host acetamide molecules and the electrolyte ions. These two conflicting DR

data sets therefore trigger a debate on the true impact of electrolyte ions on the ε_s of the host acetamide, motivating further theoretical and/or experimental investigation employing different techniques for providing a resolution to this controversial issue. This forms the basis of the present work where we have used molecular dynamics simulations coupled with classical, coarse-grained model interaction potentials to monitor the time dependent fluctuations of the collective dipole moment of these ionic DESs. Our previous simulation study[39] of DR in neat molten acetamide employing the same model interaction potential acts as a supporting work to understand, at least, qualitatively the effects of ion on the rotational, translational and ro-translational contributions to the complex dielectric relaxation spectra recorded in experiments. In this context we would like to mention that DR measurements of conducting media such as these ionic DESs in the low frequency wing is severely limited by one-over-frequency $(1/\omega)$ divergence. Consequently, estimation of ε_s becomes tricky and often associates large error because of a large conductivity contribution in this frequency regime, inducing a rise in the real part of the complex dielectric spectrum and removing the usual plateau generated by the pure dipolar response alone. There exists indeed such a possibility for the previous Hz-MHz measurements,[34–36] whereas the more recent MHz-GHz experiments might have missed a certain portion of the low frequency response because of the limited coverage of the low frequency wing. Theoretical/computational studies do not suffer from these complexities and can successfully separate the dipolar and ionic components of the total frequency dependent DR spectrum.[40–42] Although this separation involves certain approximation, it offers the necessary framework that can deal with the ongoing controversy and provide a plausible resolution.

Dielectric relaxation spectroscopy (DRS) measures the collective polarization fluctuations of a given medium in the presence of a time dependent electric field.[43–46] The coupling between the frequency dependent electric field and the solvent polarization mode is assumed to be weak and linearly dependent on the fluctuating orientational density. Addition of electrolyte in pure dipolar solvent is known to increase or decrease the ε_s of neat solvents.[43,44,47–50] Formation of ion pair and other complex ionic species in weakly dipolar solvents, for example, lithium perchlorate in ethyl acetate is known to significantly increase the ε_s of the medium.[51–54] For uni-univalent electrolytes in strongly polar solvents, on the other hand, dielectric decrement can occur via static and kinetic routes. Static dielectric decrement occurs through a partial damage of the orientational order of the dipolar solvent molecules, while the kinetic decrement

associates with the cross correlation between the dipole and ion density fluctuations[55,56] Fortunately, the underlying theoretical framework for computer simulations of the frequency dependent dielectric response of ionic media is available in the literature.[57,58] Dielectric response of aqueous solutions of uni-univalent electrolytes has been studied extensively via molecular dynamics simulations and these studies have provided important insights about the ion-induced impact on the frequency dependent dielectric response of aqueous media.[55,56,59–61] Frequency dependent dielectric spectra and conductivities of pure and aqueous solutions of ionic liquids have been investigated and ionic contributions to the total response have been separated.[40,62–67] These works have made important contributions to understand the interaction and dynamics of ionic liquids revealed by dielectric relaxation experiments,[68–70] ultrafast fluorescence measurements[71–73] and theoretical calculations.[74–79]

In the present study, temperature-dependent simulations have been performed in order to understand the effects of the ions on the DR of (CH_3CONH_2 + $LiClO_4$/ NO_3/ Br) DESs with a focus to generate a qualitatively correct description of electrolyte effects on the dielectric properties of the host acetamide which may help to remove the ongoing debate initiated by the two different sets of DR measurements. Structural aspects have been explored by calculating the Kirkwood g factor and average number of H-bonds per acetamide molecule in these DESs. Dipolar and ionic components of the temperature dependent simulated dielectric relaxation spectra of these conducting media have been separated and the contributions of rotation-translation coupling to the total DR have been estimated. As expected, the dipolar contribution has been found to dominate the total DR spectrum. Anion dependent distribution of single dipole reorientation times do not indicate the presence of any unusually long timescale in these systems, whereas the average number of H-bonds per acetamide molecule shows a clear correlation with the ε_s estimated from the MHz-GHz DR measurements and from the present simulations.

3.2 Simulation details and validation

Classical molecular dynamics simulations were performed using the GROMACS-2018.3 package[80] at four different temperatures, T(K) = 329, 336, 343, and 358. Acetamide molecules, cations and anions were taken in a ratio that mimicked the compositions employed in the MHz-GHz experiments. For each of the DESs considered, a total of 1000 particles (acetamide + cation + anion) were considered and the overall electroneutrality ensured. Composition of each

system is given in Table 3.A.1 (Appendix 3.A). OPLS (optimized potentials for liquid simulations) type model force field were used[81]. The functional forms and notations associated with different pieces of the OPLS model potential were discussed earlier[39], and also provided here.

$$V(r) = \sum_{\text{bonds}} K_r\left(r - r_{eq}\right)^2 + \sum_{\text{angles}} K_\theta\left(\theta - \theta_{eq}\right)^2 + \sum_{\text{torsions}} \left[\frac{V_1}{2}(1+\cos\phi) + \frac{V_2}{2}(1-\cos 2\phi) + \frac{V_3}{2}(1+\cos 3\phi) + \frac{V_4}{2}(1-\cos \quad 1\right. \tag{3.1}$$

$$+ \sum_i \sum_{j>i} \left\{ \frac{q_i q_j}{4\pi\epsilon_0 r_{ij}} + 4\varepsilon_{ij}\left[\left(\frac{\sigma_{ij}}{r_{ij}}\right)^{12} - \left(\frac{\sigma_{ij}}{r_{ij}}\right)^{6}\right]\right\} f_{ij}$$

where, K_r and K_θ are force constants for bond stretching and angle bending, respectively. ϕ denotes torsional angle with Fourier coefficient V. Position and charge of an atom are described by r, and q, respectively. Diameter and well depth of van der Waals interaction are denoted with σ, and ε, respectively. Geometric combinations rule has been applied to calculate Lennard-Jones parameters for two interacting atoms. The factor f_{ij} is considered as 1 except for 1-4 interactions where $f_{ij} = 0.5$.

Interaction parameters developed[82] for correctly reproducing the experimental[83] ε_s of neat molten acetamide were employed to represent the acetamide molecules. The force-field parameters for Br^-, NO_3^-, and ClO_4^- were used as those available in the relevant literature[84]. Non-bonding parameters of Li^+ were taken from another work. [85] The cationic charge was scaled as 0.8e in order to be consistent with the anionic charges. Atomic representations of acetamide, cation and anions are shown in Figure 3.A.1 (Appendix 3.A).

Initial cubic simulation boxes were constructed using the Packmol.[86] Leapfrog algorithm[87] along with a time-step of 2 fs was used for integrating the equation of motion. All bonds were kept constrained using the LINCS algorithm.[88] Non-bonded interactions were truncated at a cut-off distance of 1.1 nm. Temperature and pressure were coupled respectively to Nose-Hoover thermostat[89,90] and Parrinello-Rahman barostat [91,92] with coupling constants of 0.2 and 0.5 ps.

After energy minimization, each system was equilibrated in the NVT (10 ns) ensemble, followed by NPT equilibration for a period of another 10 ns. The equilibrated structure of the system thus obtained was further equilibrated in the NPT ensemble for another 60 ns. Subsequently, two production runs (NVT#1 and NVT#2) were performed. Among the three ionic deep eutectic systems, LiBr-DES is the most viscous one.[12] Therefore, comparatively longer simulation runs were performed for this DES. For the first NVT run (NVT#1), trajectories were saved in every 0.2 ps. This trajectory was used to calculate the rotational part of the dielectric relaxation spectra. For $LiClO_4$-DES, and $LiNO_3$-DES, these run spans were of 80 ns duration, while it was 130 ns for LiBr-DES. For each of these systems, 20 ns trajectories were saved at 0.02 ps time step (NVT#2) in order to better capture the short time dynamics. Subsequently, the validity of the force field parameters was checked by comparing the simulated densities against those from experiments.[7,93] This comparison is shown in Figure 3.A.2 (Appendix 3.A), while the numerical values are summarized in Table 3.A.2 (Appendix 3.A). Clearly, the deviation is <1% for $LiClO_4$-DES and $LiNO_3$-DES. For LiBr-DES, however, the agreement is poorer than this.

3.3 Frequency-dependent dielectric function: Connection to Experiments and Comparison

3.3.1 Necessary Equations: A Brief Discussion

Dielectric relaxation spectroscopy is an important tool to investigate collective polarization fluctuation dynamics of a wide variety of complex systems.[45,46,94–97] Moreover, data from broadband DR measurements can explain the non-Markovian character of solvation response in complex systems that contain intermolecular H-bonding and ions.[98] The intimate relationship between DR and solvation response then identifies the molecular motions that dictates the progress of a chemical reaction and unravels the associated nature of the underlying microscopic friction. [99,100]

DR experiments, however, monitor the long wavelength ($k\sigma \to 0$, k and σ being the wavenumber and particle diameter respectively) polarization fluctuations and therefore microscopic lengthscale information on dynamics involving a few to several molecules is missing. Often a wide frequency range, covering several orders of magnitude, is required to measure the full dynamics and the measured response is then assigned rather qualitatively to collective solvent rotation and translation coupled rotation.[40,101] This is because DR

experiments cannot separately measure the rotational and the translational solvent contributions and a measured relaxation time constant cannot be attributed cleanly to a particular type of molecular dynamics. This is where appropriate theoretical formalism and computations can contribute to separate the relative contributions from the total response. Fortunately, such a formalism for ionic systems is already available[41,57,58,65,102] and we discuss here the main equations.

The generalized expression for the frequency-dependent dielectric function can be written in terms of the Fourier–Laplace transform of the equilibrium total dipole moment of the system, $\boldsymbol{M}_{tot}$, as follows[41]

$$\Sigma(\omega) = \frac{1}{3\epsilon_0 V k_B T} \mathcal{L}\left[-\frac{d}{dt}\phi_{tot}(t)\right], \tag{3.2}$$

where $\phi_{tot}(t) = \langle \boldsymbol{M}_{tot}(0) \cdot \boldsymbol{M}_{tot}(t) \rangle$.

The total dipole moment of the system ($\boldsymbol{M}_{tot}(t)$) is the resultant moment of all the molecules, $\boldsymbol{M}_{tot}(t) = \sum_i \sum_\alpha q_{i,\alpha} . \boldsymbol{r}_{i,\alpha}(t)$, where, $q_{i,\alpha}$ is the charge of α-th atom of i-th molecule and $\boldsymbol{r}_{i,\alpha}$ is the position of α-th atom of i-th molecule.

Note the time dependent collective dipole moment, $\boldsymbol{M}_{tot}(t)$, can be approximated as a sum of two independently fluctuating contributions, namely, the rotational ($\boldsymbol{M}_D$) and the translational ($\boldsymbol{M}_J$) components:

$$\boldsymbol{M}_{tot}(t) = \sum_i \sum_\alpha q_{i,\alpha}(\boldsymbol{r}_{i,\alpha}(t) - \boldsymbol{r}_{i,com}(t)) + \sum_i \sum_\alpha q_{i,\alpha} . \boldsymbol{r}_{i,com}(t) \tag{3.3}$$

$$= \sum_i \sum_\alpha q_{i,\alpha}(\boldsymbol{r}_{i,\alpha}(t) - \boldsymbol{r}_{i,com}(t)) + \sum_i q_i . \boldsymbol{r}_{i,com}(t) \tag{3.4}$$

$$= \boldsymbol{M}_D(t) + \boldsymbol{M}_J(t) \tag{3.5}$$

where, $\boldsymbol{r}_{i,com}(t)$ is the position of centre-of-mass of i-th molecule and q_i is the total charge of this molecule, and $\boldsymbol{M}_D(t)$, $\boldsymbol{M}_J(t)$ represent rotational and translational components of total dipole moment, respectively.

For polar, uncharged molecules $q_i = 0$ and only $\boldsymbol{M}_D(t)$ part survives. On the other hand, only charged species have the $\boldsymbol{M}_J(t)$ part.

Now, the total correlation function can be divided into different contributions.

$$\langle \boldsymbol{M}_{tot}(0).\boldsymbol{M}_{tot}(t)\rangle = \langle \boldsymbol{M}_D(0).\boldsymbol{M}_D(t)\rangle + \langle \boldsymbol{M}_J(0).\boldsymbol{M}_J(t)\rangle + \langle \boldsymbol{M}_D(0).\boldsymbol{M}_J(t)\rangle + \langle \boldsymbol{M}_J(0).\boldsymbol{M}_D(t)\rangle$$
$$= \phi_{DD}(t) + \phi_{JJ}(t) + \phi_{DJ}(t) \quad (3.6)$$

where $\phi_{DD}(t) = \langle \boldsymbol{M}_D(0).\boldsymbol{M}_D(t)\rangle$, $\phi_{JJ}(t) = \langle \boldsymbol{M}_J(0).\boldsymbol{M}_J(t)\rangle$ and $\phi_{DJ}(t) = \langle \boldsymbol{M}_D(0).\boldsymbol{M}_J(t)\rangle + \langle \boldsymbol{M}_J(0).\boldsymbol{M}_D(t)\rangle$ represent respectively the rotational, the translational and the ro-translational contributions.

As Laplace-Fourier transform of these correlation functions form the frequency-dependent dielectric function ($\Sigma(\omega)$), we perform this operation on each of the individual correlation functions, and thus provides the individual contributions to total frequency dependent dielectric function. They are defined as follows:

(i) rotational part, $\mathcal{L}\left[-\frac{d}{dt}\phi_{DD}(t)\right] = \langle \boldsymbol{M}_D^2\rangle + i\omega\mathcal{L}[\langle \boldsymbol{M}_D(0).\boldsymbol{M}_D(t)\rangle] = \langle \boldsymbol{M}_D^2\rangle + i\omega\mathcal{L}_{DD}(\omega)$, (3.7)

(ii) translational part, $\mathcal{L}\left[-\frac{d}{dt}\phi_{JJ}(t)\right] = \frac{i}{\omega}\mathcal{L}[\langle \boldsymbol{J}(0).\boldsymbol{J}(t)\rangle] = \frac{i}{\omega}\mathcal{L}_{JJ}(\omega)$, (3.8)

(iii) ro-translational part, $\mathcal{L}\left[-\frac{d}{dt}\phi_{DJ}(t)\right] = 2\mathcal{L}[-\langle \boldsymbol{M_D}(0).\boldsymbol{J}(t)\rangle] = -2\mathcal{L}_{DJ}(\omega)$. (3.9)

In the above equations, $\mathcal{L}_{DD}(\omega) = \mathcal{L}[\langle \boldsymbol{M}_D(0).\boldsymbol{M}_D(t)\rangle]$, $\mathcal{L}_{JJ}(\omega) = \mathcal{L}[\langle \boldsymbol{J}(0).\boldsymbol{J}(t)\rangle]$ and $\mathcal{L}_{DJ}(\omega) = \mathcal{L}[\langle \boldsymbol{M_D}(0).\boldsymbol{J}(t)\rangle]$.

Notice in Eqs. (3.8) and (3.9), we have introduced a new term $\boldsymbol{J}(t)$ in place of the $\boldsymbol{M}_J(t)$. Here, $\boldsymbol{J}(t)$ is the electric current and defined as: $\boldsymbol{J}(t) = \frac{d\boldsymbol{M}_J(t)}{dt} = \sum_i q_i.\mathbf{v}_{i,com}(t)$ where $\mathbf{v}_{i,com}(t)$ is the centre-of-mass velocity of molecule *i*. It is advantageous to use total electric current $\boldsymbol{J}$, instead of $\boldsymbol{M}_J$ to avoid periodic jumps of molecules.

Finally, the frequency-dependent dielectric function ($\Sigma(\omega)$) can be expressed as,

$$\Sigma(\omega) = \frac{1}{3\epsilon_0 V k_B T}\left(\langle \boldsymbol{M}_D^2\rangle + i\omega\mathcal{L}[\langle \boldsymbol{M}_D(0).\boldsymbol{M}_D(t)\rangle] + \frac{i}{\omega}\mathcal{L}[\langle \boldsymbol{J}(0).\boldsymbol{J}(t)\rangle] - 2\mathcal{L}[\langle \boldsymbol{M_D}(0).\boldsymbol{J}(t)\rangle]\right) \quad (3.10)$$

The well-known $1/\omega$ divergence problem for conducting solutions at the low-frequency regime can be tackled in the present theoretical formalism by subtracting the zero-frequency contribution, $\mathcal{L}_{JJ}(\omega = 0)$, from the frequency dependent translational component, $\mathcal{L}_{JJ}(\omega)$.[41]

This can be done by Laplace-Fourier transforming the equation required to fit the simulated $\langle \boldsymbol{J}(0).\boldsymbol{J}(t)\rangle$. Therefore, the calculated translational contribution is modified as $\Big(\mathcal{L}_{JJ}(\omega) - \mathcal{L}_{JJ}(0)\Big)$.

The individual contributions can then be obtained from the following relations,

(i) rotational spectra, $\varepsilon_{DD}(\omega) = \frac{1}{3\epsilon_0 V k_B T}\big(\langle \boldsymbol{M}_D^2\rangle + i\omega\mathcal{L}_{DD}(\omega)\big)$, (3.11)

(ii) translational spectra, $\varepsilon_{JJ}(\omega) = \frac{1}{3\epsilon_0 V k_B T}\frac{i}{\omega}\Big(\mathcal{L}_{JJ}(\omega) - \mathcal{L}_{JJ}(0)\Big)$, (3.12)

(iii) ro-translational spectra, $\varepsilon_{DJ}(\omega) = \frac{1}{3\epsilon_0 V k_B T}\mathcal{L}_{DJ}(\omega)$. (3.13)

The conductivity-corrected generalized frequency dependent dielectric function, $\Sigma_0(\omega)$, is then expressed as follows[41]

$$\Sigma_0(\omega) = \Big(\varepsilon_{DD}(\omega) + \varepsilon_{JJ}(\omega) - 2\varepsilon_{DJ}(\omega)\Big). \quad (3.14)$$

In Eq. 3.14, the subscript (0) indicates that the static conductivity is subtracted from the original frequency-dependent dielectric function ($\Sigma(\omega)$).

$\Sigma(\omega)$ and $\Sigma_0(\omega)$ are the susceptibilities free from infinite-frequency dielectric constant (ε_∞).[40] Therefore, to calculate generalized static dielectric constant (ε_s) the ε_∞ value should be added to $\Sigma_0(\omega)$. Subsequently, the generalized static dielectric constant (ε_s) is given by[57]

$$\varepsilon_S - 1 = \lim_{\omega\to 0}\Sigma_0(\omega) \quad (3.15)$$

or,

$$\varepsilon_s = \lim_{\omega\to 0}\Big(\varepsilon_{DD}(\omega) + \varepsilon_{JJ}(\omega) - 2\varepsilon_{DJ}(\omega)\Big) + 1 \quad (3.16)$$

Note that in Eqs. 3.15 and 3.16, the dielectric constant at $\omega \to \infty$ is approximated as unity ($\varepsilon_\infty = 1$),[103] and added to the conductivity-corrected generalized frequency dependent dielectric function, $\Sigma_0(\omega)$ to estimate ε_s.

The detailed descriptions of the expressions for $\varepsilon_{DD}(\omega)$, $\varepsilon_{JJ}(\omega)$ and $\varepsilon_{DJ}(\omega)$ are provided in the Appendix A2.

3.3.2 Simulation Results: Decomposition of the DR Spectra

Figure 3.1 presents the simulated normalised decays of the pure rotational component of the collective total dipole moment autocorrelation function, $\phi_{DD}^{N}(t) = \langle \boldsymbol{M}_D(0).\boldsymbol{M}_D(t)\rangle / \langle \boldsymbol{M}_D(0).\boldsymbol{M}_D(0)\rangle$, along with their multi-exponential fits for these three ionic DESs. Notice that data at four different temperatures are shown in this figure, while the corresponding fit parameters are summarised in Table 3.A.3 (Appendix 3.A). Temperature-induced faster dynamics reflected in Figure 3.1 arises from the temperature dependence of the medium viscosity. $\phi_{DD}^{N}(t)$ tracks the collective dipole reorientation dynamics and therefore these decays represent the rotational relaxation of the acetamide molecules in these three DESs.

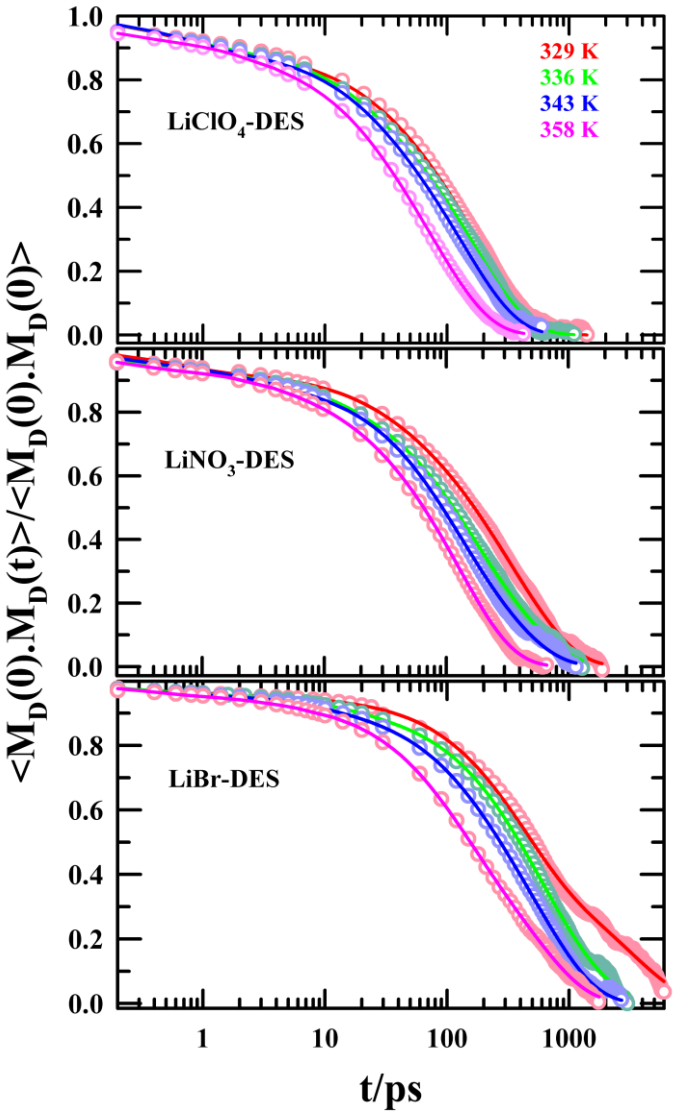

Figure 3.1: Temperature-dependent decays of the normalised collective dipole moment autocorrelation function, $\phi_{DD}^{N}(t)$, simulated for the three ionic DESs considered in the present study. Open symbols represent the simulated data while the lines going through them denote the corresponding multi-exponential fits.

Figure 3.2 displays the decay of the simulated current autocorrelation function, $\langle \boldsymbol{J}(0).\boldsymbol{J}(t)\rangle$ arising from ion translation, and relates to $\langle \boldsymbol{M}_J(0).\boldsymbol{M}_J(t)\rangle$ as follows. Because Laplace transform of the time derivative of $\langle \boldsymbol{M}_J(0).\boldsymbol{M}_J(t)\rangle$ enters into $\Sigma_0(\omega)$, we directly calculate $\boldsymbol{J}(t) = \frac{d}{dt}[\boldsymbol{M}_J(t)] = q.\frac{d}{dt}[\boldsymbol{r}(t)]$. Numerical fits through the data have also been presented in this figure, while fit functions and the associated fit parameters are provided in Table 3.A.4 (supplementary material). The oscillatory behaviour with a dip at ~50 fs and a peak at ~100 fs arises from the decay behaviour of the underlying centre-of-mass velocity autocorrelation

function (VACF).[104] A very weak temperature dependence for these decays is registered. This is because the effects of temperature on VACF decay enter indirectly through the curvature of the potential energy surface generated by the nearest neighbour particles. For harmonic potential, force constant defines the curvature which does not depend on temperature explicitly.

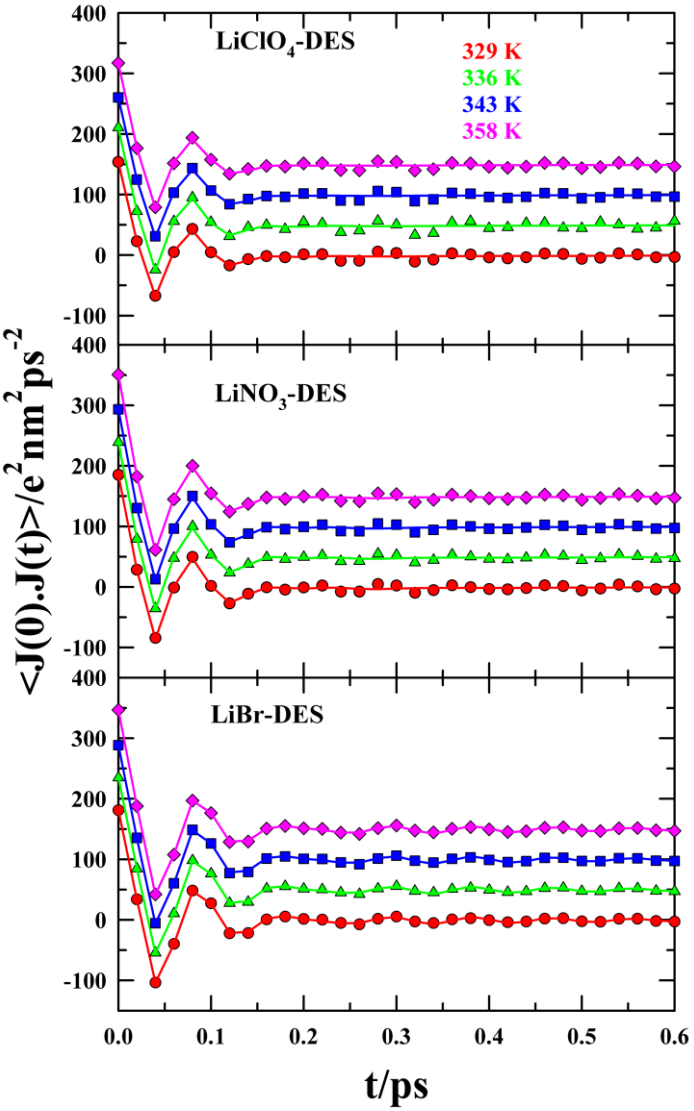

Figure 3.2: Temperature-dependent decays of the current-current autocorrelation function for ions (cations and anions) in these three DESs. Closed symbols represent simulation data and solid lines going through them denote the corresponding fits. Note that an offset of 50 unit was used for a clear presentation of the temperature dependent curves.

We next present in Figure 3.3 the simulated dipole moment-current cross correlation functions for ions in these three DESs. These correlation functions are fitted numerically and the fit

parameters are shown in Table 3.A.5 (Appendix 3.A). This cross term is important because it embodies 'translation-rotation coupling' and contributes to both the frequency dependent permittivity and the conductivity. Note the nonmonotonic behaviour of this cross-correlation function with a peak at ~100 fs. This behaviour can be understood as follows. At $t = 0$, $\frac{dr}{dt} = v = 0$, and remembering that $\boldsymbol{J}(t) = \sum_{i(ion)} q_i \mathbf{v}_i(t)$, the numerical value of the cross-correlation function becomes zero. With time, the position vector of the particle ($\boldsymbol{r}(t)$) changes as well as its direction because of its interaction with the neighbouring particles. After a certain time, the direction vector assumes an orientation that might be parallel or near parallel to the projection of the collective dipole moment vector, $\boldsymbol{M}_{\mathrm{D}}(t = 0)$. This leads to the peak value of the cross-correlation function, $\langle \boldsymbol{M}_D(t = 0) \cdot \boldsymbol{J}(t) \rangle$. Subsequently, further interaction with the neighbours randomizes their relative orientation, leading to the decay of the correlation function. The temperature effect is negligible, although the cross-correlation contribution shows anion identity dependence and is the minimum for the LiBr containing DES which is the most viscous among the three systems considered. This highlights the important role played by the medium viscosity to facilitate translation-rotation decoupling.[105]

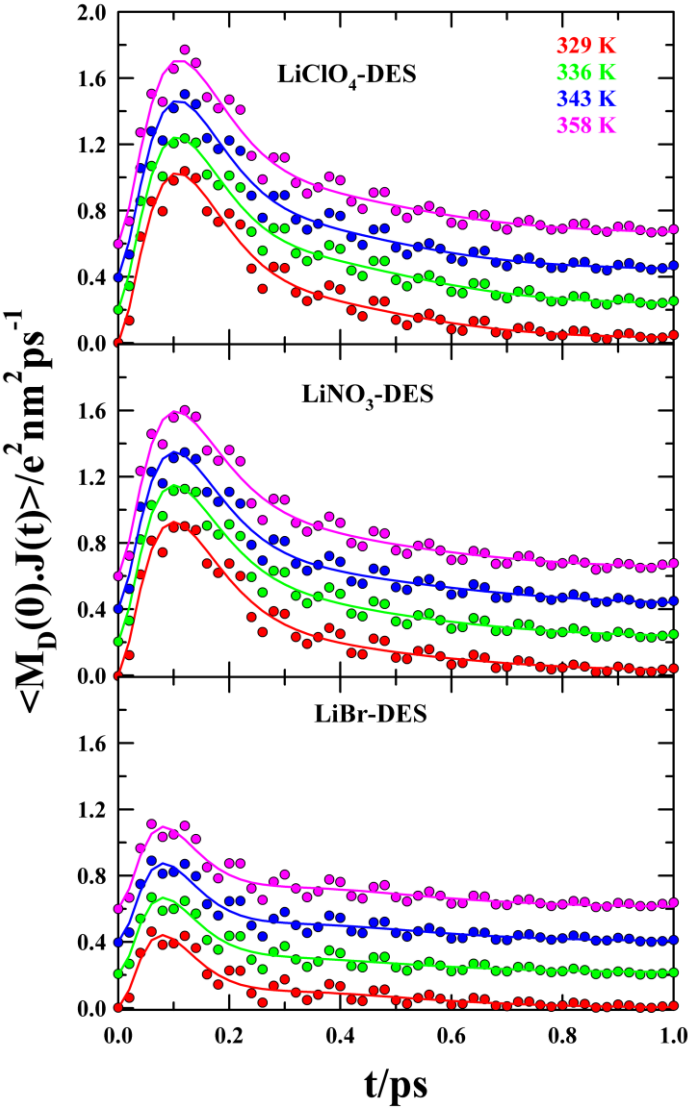

Figure 3.3: Temperature-dependent dipole moment-current cross-correlation function for the three ionic acetamide DESs studied in this work. Closed symbols represent simulation data and solid lines going through them denote corresponding fits. Note that an offset of 0.2 unit was used for a clear presentation of the temperature dependent curves.

Laplace-Fourier transform of these three correlation functions generate rotational (ε_{DD}), translational (ε_{JJ}), and ro-translational (ε_{DJ}) contributions of the total dielectric spectra ($\Sigma_0(\omega)$) described by Eq. 3.14.

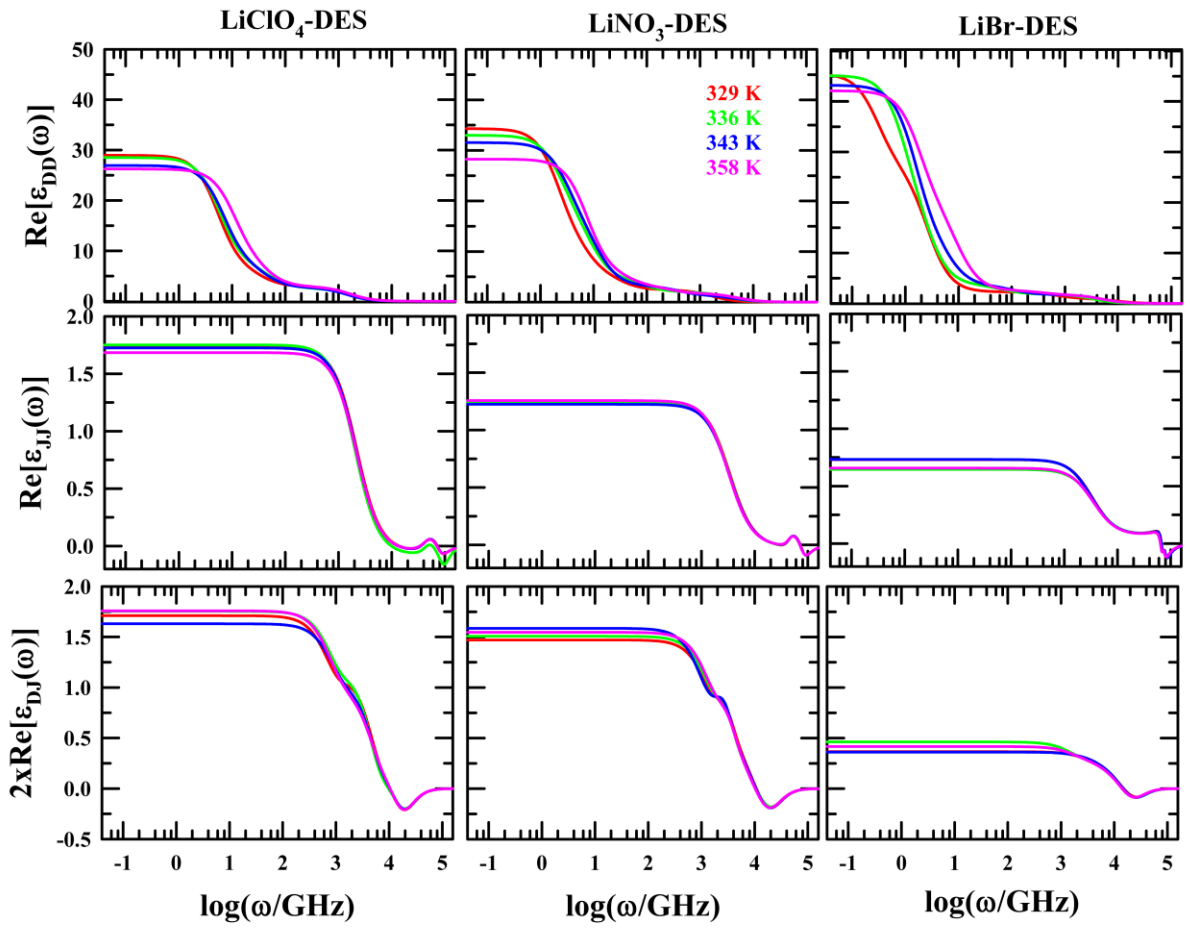

Figure 3.4: Temperature-dependent real part of the dielectric spectra of the $LiClO_4$-DES (left), $LiNO_3$-DES (middle), and LiBr-DES (right): rotational spectra (upper), translational spectra (middle), ro-translational spectra (lower). Translational and ro-translational components are quite small compared to the rotational component.

Real and imaginary components of the rotational (ε_{DD}), translational (ε_{JJ}), and ro-translational (ε_{DJ}) contributions are presented in Figure 3.4 and Figure 3.5, respectively. Numerical values of the real components of ε_{DD}, ε_{JJ}, and ε_{DJ} in the limit of zero frequency ($\omega \to 0$) are summarized in the last columns of Tables 3.A.3-3.A.5 of Appendix 3.A.

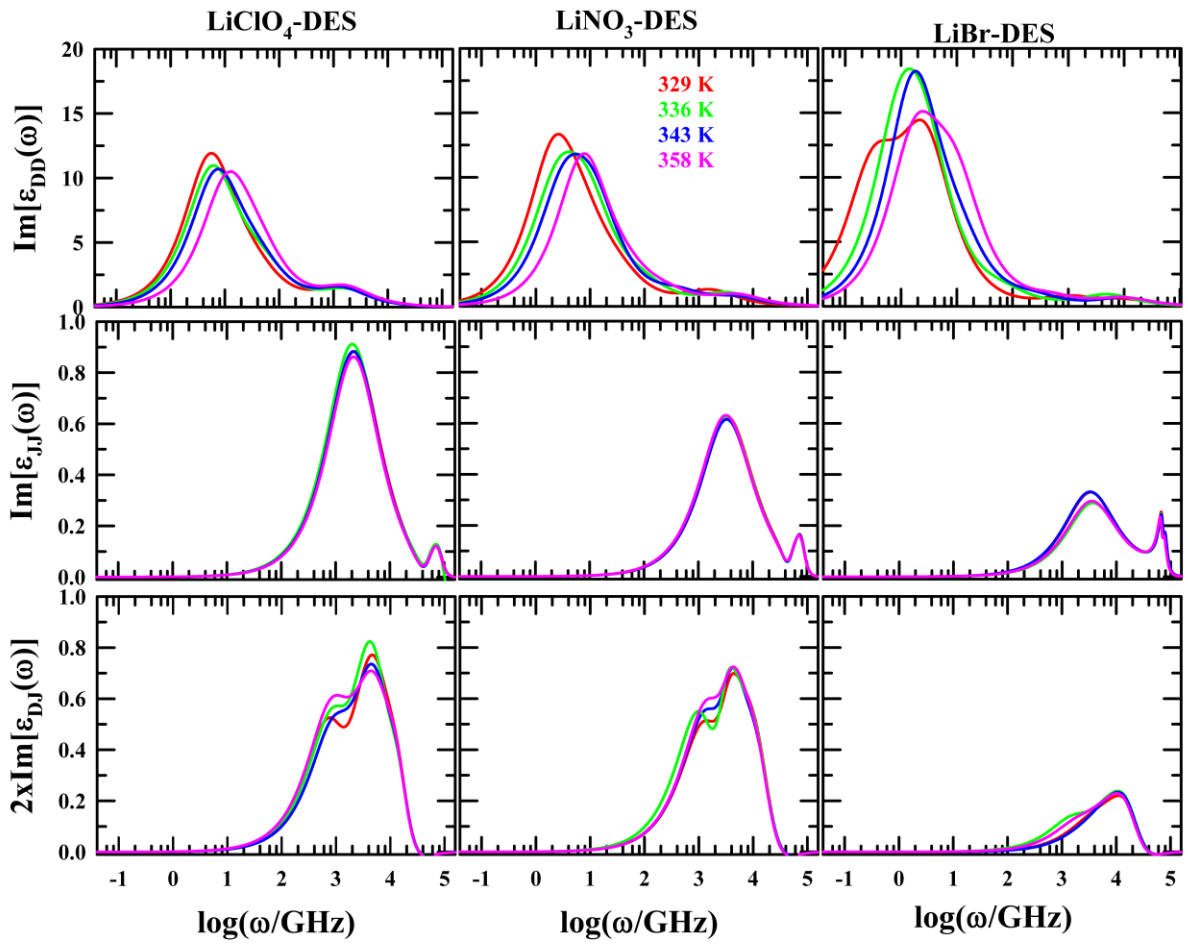

Figure 3.5: Temperature-dependent imaginary part of the dielectric spectra of the $LiClO_4$-DES (left), $LiNO_3$-DES (middle), and LiBr-DES (right): rotational spectra (upper), translational spectra (middle), ro-translational spectra (lower). Notice the rotational relaxation occurs at the lower frequency wing while the translational and the ro-translational processes occur at the higher frequencies.

It is quite evident that ε_{DD} dominates the zero frequency values in all these ionic DESs, and the ro-translation contribution (cross term), found to be small magnitude and negative, reduces the overall value. It has been previously reported that aqueous salt solutions exhibit a small yet non-zero value of the cross term.[55] Interestingly, our findings for ionic DESs show similar characteristics to those observed in the case of aqueous electrolyte solutions. In addition, these pieces reflect anion identity dependence. Subsequently, the real and the imaginary components of the frequency-dependent generalized dielectric function ($\Sigma_0(\omega)$), simulated at four different temperatures for these ionic DESs, are presented below in Figure 3.6. As observed in experiments,[11,12] multi-Debye relaxation functions were found to adequately describe the

simulated dielectric spectra. Moreover, temperature and anion identity dependencies are evident in simulations and parallel to those reported already in experimental studies.[11,12]

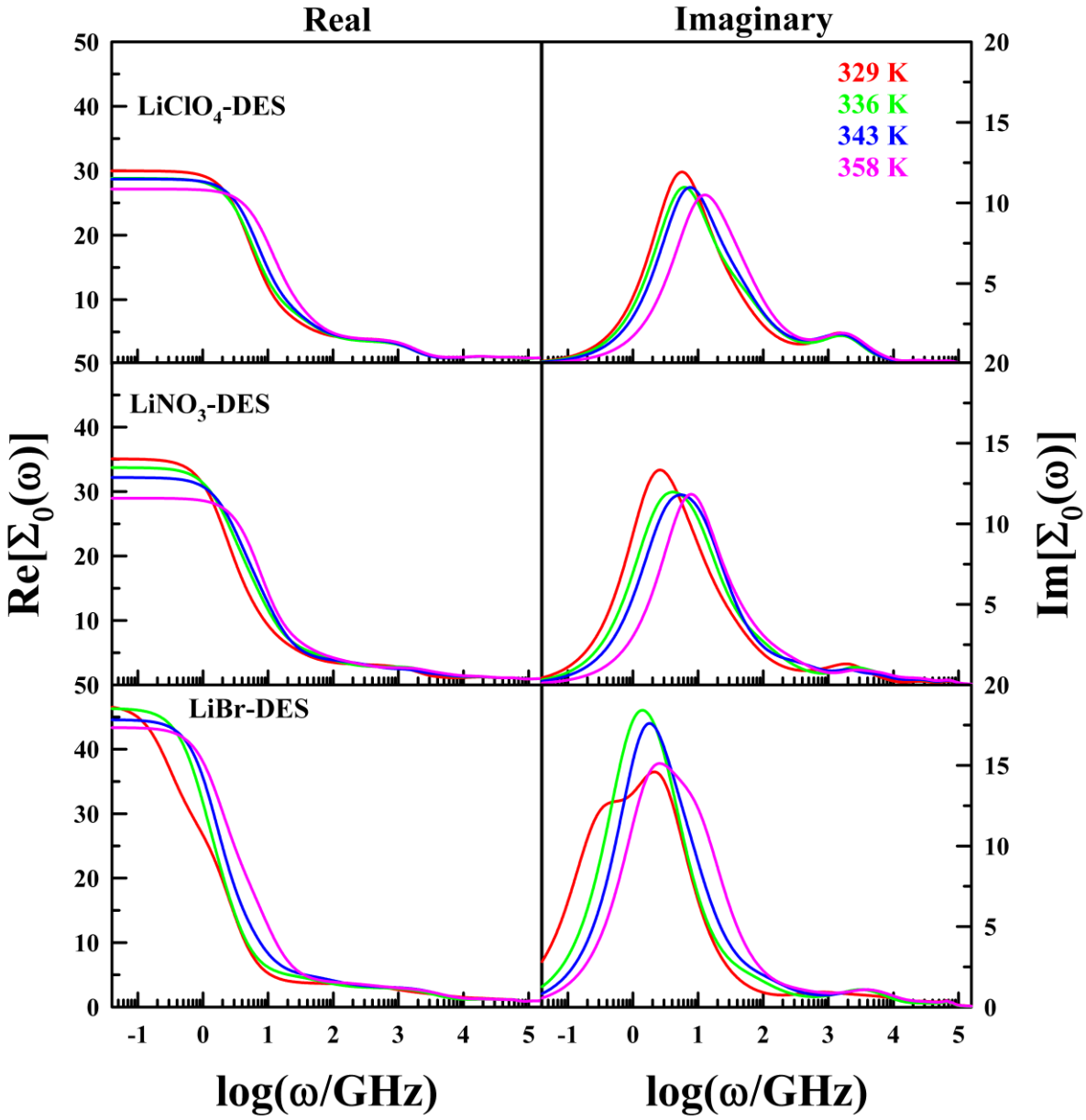

Figure 3.6: Temperature-dependent real (left panel) and imaginary (right panel) components of the generalized frequency dependent dielectric function, $\Sigma_0(\omega)$, obtained from simulations via Eq. 14 of the text. Note that the peak of the imaginary component (lower panel) shifts to higher frequency (LiBr system being somewhat irregular) with temperature, whereas the zero-frequency value of the real component (left panel) modulates with anion identity. Effects of both temperature and electrolyte are quite evident in these figures.

The temperature dependent real and imaginary components of the simulated DR Spectra shown in Figure 3.6 required four Debye (4D) relaxation functions for simultaneous fits to describe the DR processes in $LiNO_3$- and LiBr-DESs, whereas the $LiClO_4$-DES required three Debye (3D) relaxation functions. Numerical values of the temperature dependent relaxation time constants and amplitudes are summarized in Table 3.A.3 (Appendix 3.A). As we have already noticed the overwhelming dominance of the $\varepsilon_{DD}(\omega)$ over the other two contributions ($\varepsilon_{JJ}(\omega)$, and $\varepsilon_{DJ}(\omega)$) in determining $\Sigma_0(\omega)$, we consider the relaxation time constants from fits as arising from the medium dipolar response to the frequency dependent electric field. The temperature dependence of these multiple relaxation times is shown in Figure 3.7. As expected, the temperature dependence is more pronounced for the relatively slower time constants (τ_1 and τ_2) and for systems with larger viscosities.[106]

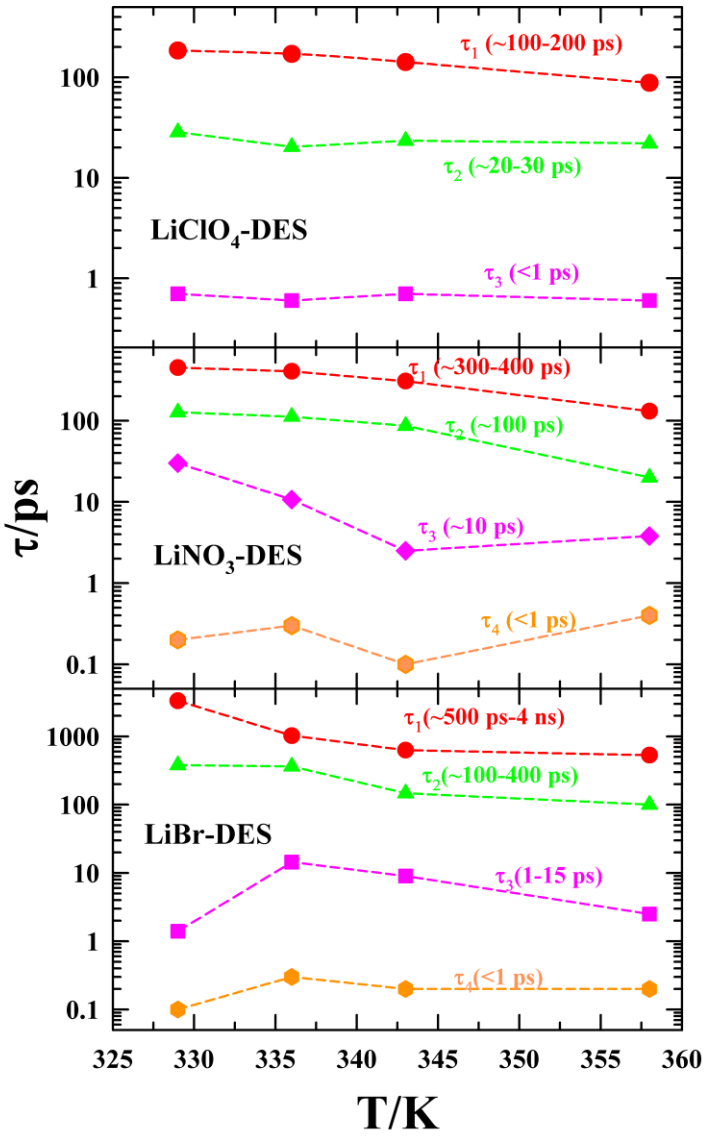

Figure 3.7: Temperature-dependent DR time constants for the three DESs studied. The dashed lines through the symbols are only guide to eyes. Viscosity (η) trend of these DESs are as follows: $\eta_{LiBr-DES} > \eta_{LiNO_3-DES} > \eta_{LiClO_4-DES}$.

Notice in Figure 3.7 the anion-dependence of the simulated DR time constants, particularly that of the relatively slower ones, τ_1 and τ_2. The slowest of the predicted DR time constants in these DESs follows the order, $\tau_{LiClO_4} < \tau_{LiNO_3} < \tau_{LiBr}$, and dictates the average DR time constant ($\langle\tau_{DR}\rangle = \sum_i a_i\tau_i$, with $\sum_i a_i = 1$) to follow the same trend. The origin and the dependencies (temperature and anion) of the experimentally measured DR time constants have already been discussed in terms of the structural hydrogen bond relaxation ($C_{HB}(t)$) and rank dependent single-particle reorientation dynamics ($C_\ell(t)$).[12] In Table 3.A.6 (Appendix 3.A) we have compared the simulated DR timescales with those from the structural hydrogen bond

relaxation ($C_{HB}(t)$) and the first rank (ℓ =1) single-particle reorientation dynamics ($C_1(t)$).[12] This comparison re-establishes the already known interconnection among the DR dynamics, the structural H-bond fluctuations and the single particle reorientational relaxation.[28]

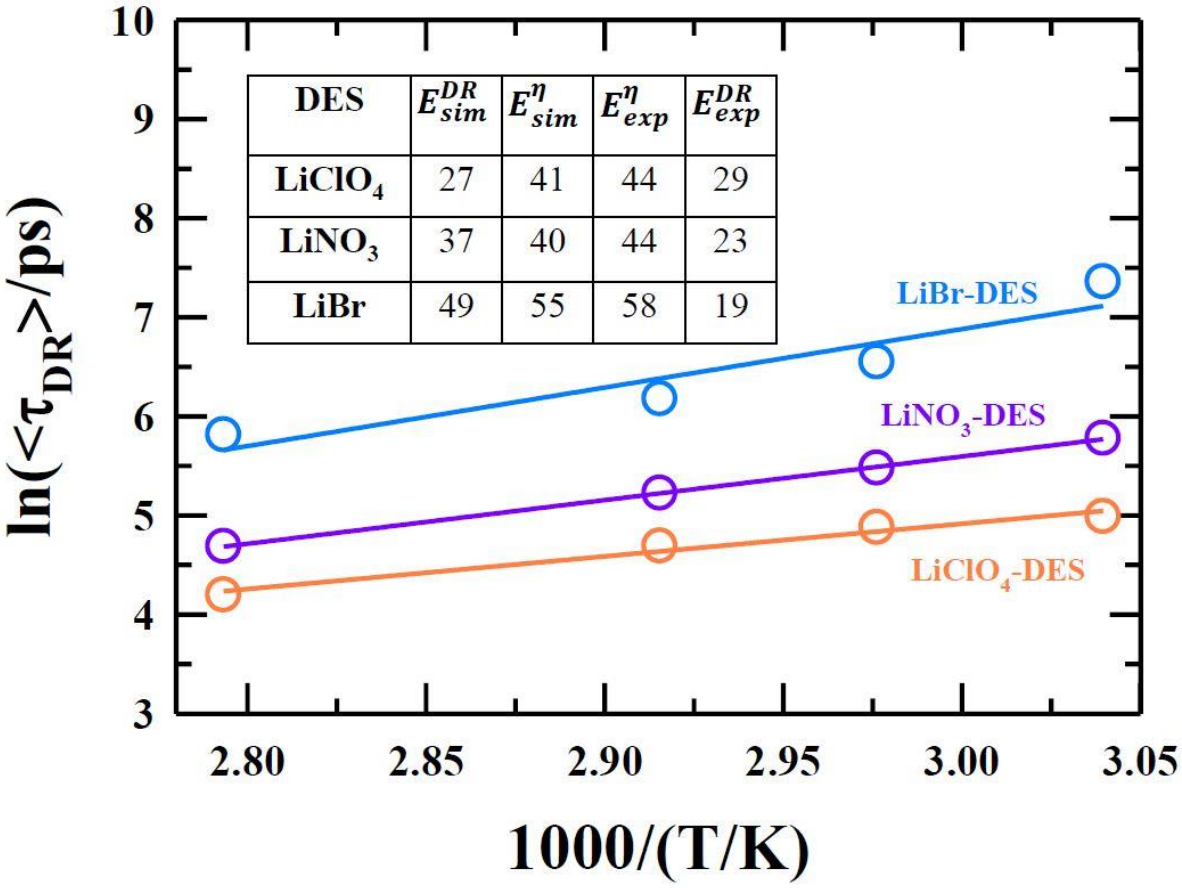

DES	E_{sim}^{DR}	E_{sim}^{η}	E_{exp}^{η}	E_{exp}^{DR}
$LiClO_4$	27	41	44	29
$LiNO_3$	37	40	44	23
LiBr	49	55	58	19

Figure 3.8: Arrhenius type plot (ln ($\langle\tau_{DR}\rangle$) vs $^1/_T$) for three ionic DESs. Estimated activation energies are compared with those obtained from other dynamical processes. The values of E_{sim}^{η} are taken from Ref. 106, and E_{exp}^{η} and E_{exp}^{DR} are from Ref. 12. Note that all values are rounded off to the nearest digit and in kJ/mol unit.

The effects of temperature on the simulated average DR times, $\langle\tau_{DR}\rangle$, is depicted in Figure 3.8. A comparison among activation energies associated with DR times and viscosities obtained from simulations and experiments are also shown in the inset. Clearly, the anion dependent DR activation energies from simulations, E_{sim}^{DR}, follow the trend of viscosity activation energies from simulations and experiments, E_{sim}^{η} and E_{exp}^{η}, respectively. Interestingly, E_{sim}^{DR} does not follow the trend found in the experimental DR activation energies, E_{exp}^{DR}, although the simulated and experimental DR activation energies agree well for the lowest viscosity system, that is,

perchlorate DES. The reason probably lies in the model interaction potential[82] employed that primarily focussed on optimizing the interaction parameters to reproduce the experimental static dielectric constant of the neat molten acetamide. This interaction potential has been found to overestimate the experimental DR times by a factor of ~2.[39] The simulated slower than experimental relaxation times fails to correctly describe the viscosity coupling of the diffusive dynamics, and as a result, the simulated DR activation energies show an anion dependence reverse of that found in measurements. An additional support to this view comes from a previous simulation study[106] which reported a much weaker decoupling between the centre-of-mass diffusion and viscosity than reported in experiments.

3.3.3 Comparison with Experiments

We now compare our simulation results with those from DR measurements[12] performed employing the frequency window, $0.2 \leq \nu/GHz \leq 50$. Note that such a narrow frequency window can reliably measure DR dynamics with timescales ranging from a couple of picoseconds to a nanosecond only and therefore, faster and slower relaxations than these timescales will remain largely undetected. The present simulations do not suffer from such limitations. However, computer simulations are often sensitive to the accuracy of the model force field employed to mimic the interactions that govern the structure and dynamics of real systems and thus inherently limited to quantitatively reproduce experimental results. Here we have used a pair-wise additive classical force field which did not consider explicit description of polarizability.[82] The explicit description of polarizability and its systematic inclusion in describing condensed phase systems, such as the present DESs where extensive inter-species H-bonding assumes a significant role, may become critically important. This is already reflected in the comparison between the simulated and the experimental DR activation energies presented in Figure 3.8. This caveat notwithstanding, we persisted with this model interaction potential because the present study focuses on qualitatively correctly predicting electrolyte effects on the static dielectric constant of acetamide hosting these ionic DESs.

Figure 3.9 compares the simulated and experimental static dielectric constants of these three DESs at two different temperatures. Clearly, the simulated dielectric constants agree well with those from the more recent MHz-GHz measurements[12] and sharply contrast the colossal increase found earlier in KHz-MHz experiments.[36–38] Also note in this figure that the agreement is better for systems with lower viscosities and follows the viscosity trend of these

DESs. Numerical values of the DR parameters tabulated in Tables 3.A.7-3.A.9 (Appendix 3.A) makes this comparison more quantitative.

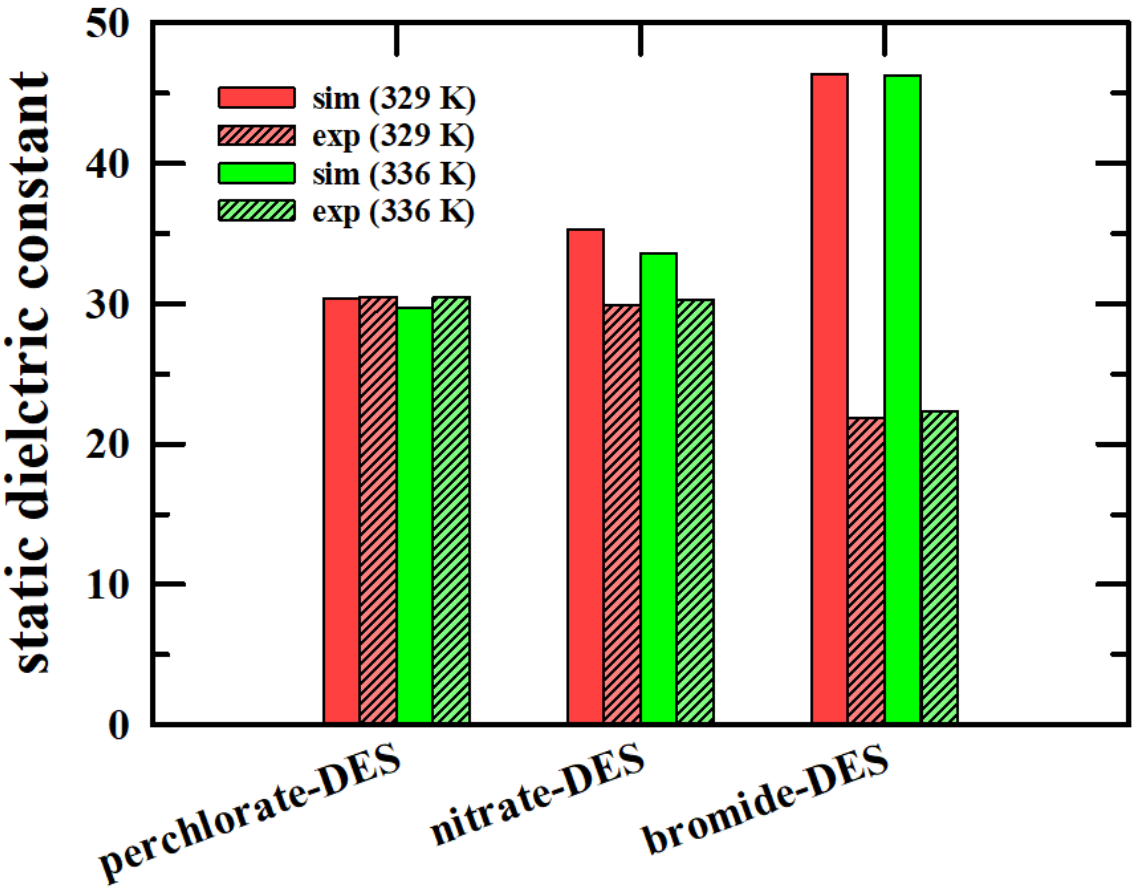

Figure 3.9: Comparison of static dielectric constant values obtained from simulation and experiment for three ionic DESs at two temperatures.

Figure 3.10 shows a comparison between the simulated and the experimental DR spectra for these three DESs at two different temperatures, 329 K and 336 K. Simulated and experimental spectra (both the real and imaginary components) are presented after appropriate normalisation as follows: $(Re[\Sigma_0(\omega)+1]-\varepsilon_\infty)/(\varepsilon_s-\varepsilon_\infty)$ and $Im[\Sigma_0(\omega)]/(\varepsilon_s-\varepsilon_\infty)$. Reflecting the limitation of the model force field parameter, simulations predict relaxations slower than those recorded in experiments. The multi-Debye or non-Debye nature of the experimental dielectric relaxation is, however, correctly predicted in the present simulations.

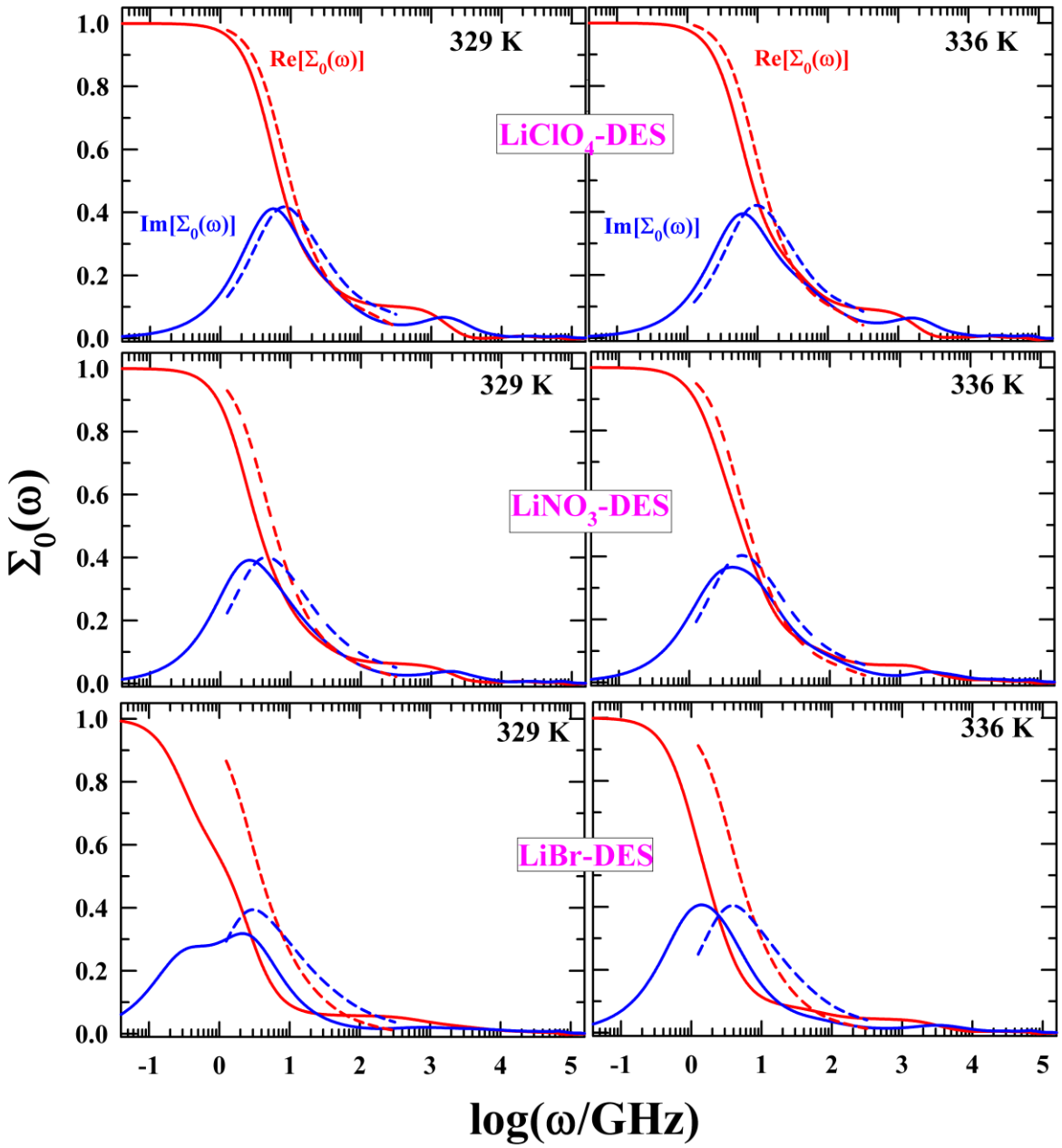

Figure 3.10: Comparison between simulated and experimental dielectric spectra $LiClO_4$-DES (upper), $LiNO_3$-DES (middle), and LiBr-DES (lower). Real and imaginary components are indicated by red and blue, respectively. Results from simulations and experiments are denoted by solid, and dashed lines, respectively. Experimental spectra are reproduced by using the fit parameters listed in Table 3.1 of Ref. 12.

The non-Debye (or multi-Debye) nature of DR can be confirmed via the Cole-Cole plot which, for a liquid with single Debye relaxation, describes a *perfect* semi-circle when the imaginary

component is shown as a function of the real component of the frequency dependent DR spectrum. Figure 3.11 presents the Cole-Cole plots by using the real and imaginary components of the simulated DR spectra for these three DESs at two different temperatures. The non-Debye feature of the simulated spectra is clearly visible and more prominent for the bromide system. Notice in this figure that the non-Debye feature is not as prominent in the measured spectra as found in the simulations, and this may be partly due to the model force field parameters and partly due to the narrow frequency window employed in the relevant experiments. The non-Debye features however, subtle or prominent, justifies the requirement of multi-Debye fit functions for describing both the simulated and experimental DR spectra of these ionic DESs.

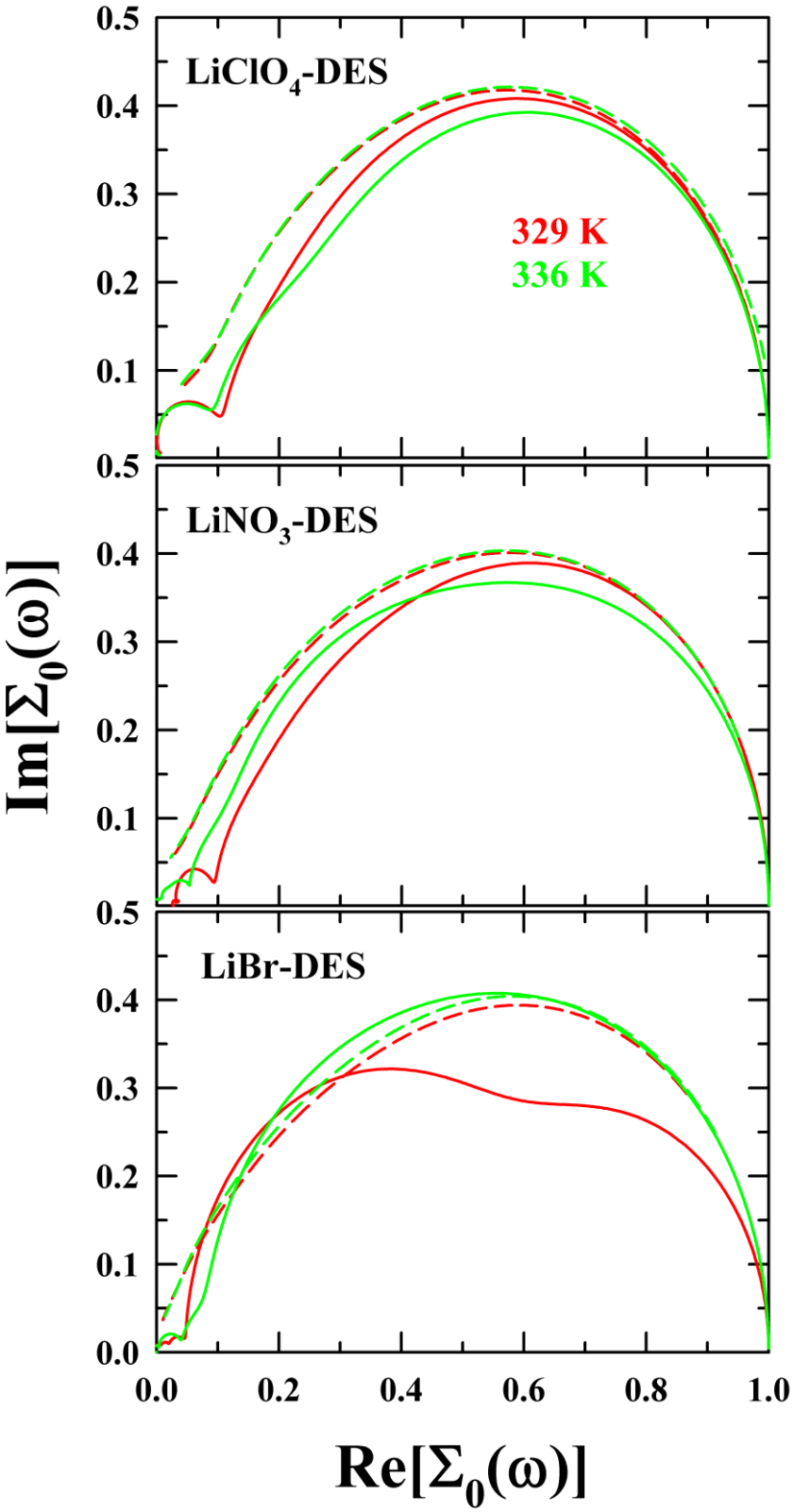

Figure 3.11: Cole-Cole plots showing the non-Debye features in the DR spectra of the three DESs studied here. Simulated and measured spectra are represented respectively by the solid and the dashed lines.

3.4 Dielectric Constant (ε_s) Decrement: Probable Reasons

Experiments carried out in recent times employing MHz-GHz frequency window have repeatedly shown substantial decrease in the value of the static dielectric constant (ε_s) of neat molten acetamide in DESs made of acetamide and uni-univalent electrolytes.[12] This electrolyte-induced decrease of ε_s or dielectric decrement is in sharp contrast to earlier reports based on KHz-MHz measurements[33,34,36–38] and thus warrants a closer scrutiny. Temperature-dependent simulated ε_s values for the three ionic acetamide DESs are shown via a bar chart in Figure 3.12 along with that for the neat molten acetamide. Clearly, ε_s values for the ionic acetamide DESs investigated are considerably lower than that of the neat molten acetamide, and shows dependence on both temperature and anion-identity. The phenomenon of the ion-induced dielectric decrement is, however, not new and has already been observed for conventional ionic solutions in both experiments[48–50,107,108] and simulations.[55,56,59–61,102,109–111] Traditionally, this has been explained considering two different scenarios. In the dynamic picture, solvent molecules in the first solvation shell are assumed to electrostatically bind with ions in solutions so comprehensively that those solvent molecules lose their orientational freedom and remain non-responsive to the frequency dependent electric field administered during DR measurements. This makes these *bound* solvent molecules to appear as *rotationally frozen* and cannot contribute to the frequency dependent dielectric function. The resultant decrease in ε_s is then termed as the kinetic dielectric decrement.[55,56]

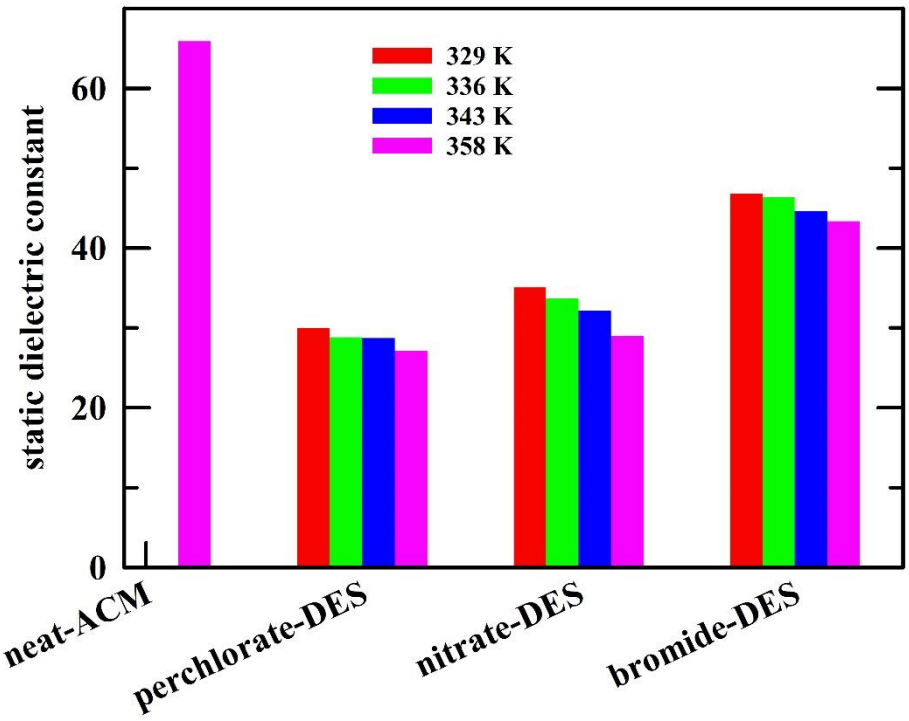

Figure 3.12: Temperature-dependent static dielectric constant for three DESs. ε_s for liquid acetamide at 358 K is also shown for comparison. Each plot is color-coded.

The other origin, being static in nature, associates with the frustrations in the static orientational correlations among the solvent dipoles. This is important for network solvents such as water where the three-dimensional H-bond network forces the molecular dipoles to orient favourably, producing a high value for the Kirkwood g factor ($g_K \approx 3.7$) in the liquid phase.[112] The Kirkwood factor (G_k) estimates the dipolar correlations and is defined as,[113]

$$G_k = \frac{\langle |\boldsymbol{M}(0)|^2 \rangle - \langle |\boldsymbol{M}(0)| \rangle^2}{N\mu^2} \quad , \tag{3.17}$$

where the numerator denotes the variance of the total dipole moment of the system, N the number of dipoles present in a given system, and μ the average value of the dipole moment.

Figure 3.13 presents the simulated G_k values for the three DESs and for the neat molten acetamide. The results are shown as a function of time in order to highlight the respective time evolutions and the fluctuations over time. A significant decrease in the value of G_k for each of

these DESs over that for the neat molten acetamide is clearly visible. This in turn reflects loss of orientational order among the molecular dipoles (acetamide molecules) in these DESs relative to that in neat molten acetamide. In addition, the extent of decrease depends on the identity of the anion. More specifically, the disruption of the static dipolar correlations is the most severe for the perchlorate ion among the three anions of the lithium salts considered. Note the simulated ε_s values shown in Figure 3.12 also follows the same trend and the connection arises because both G_k and ε_s depend upon the extent of dipolar correlations present in a given system.

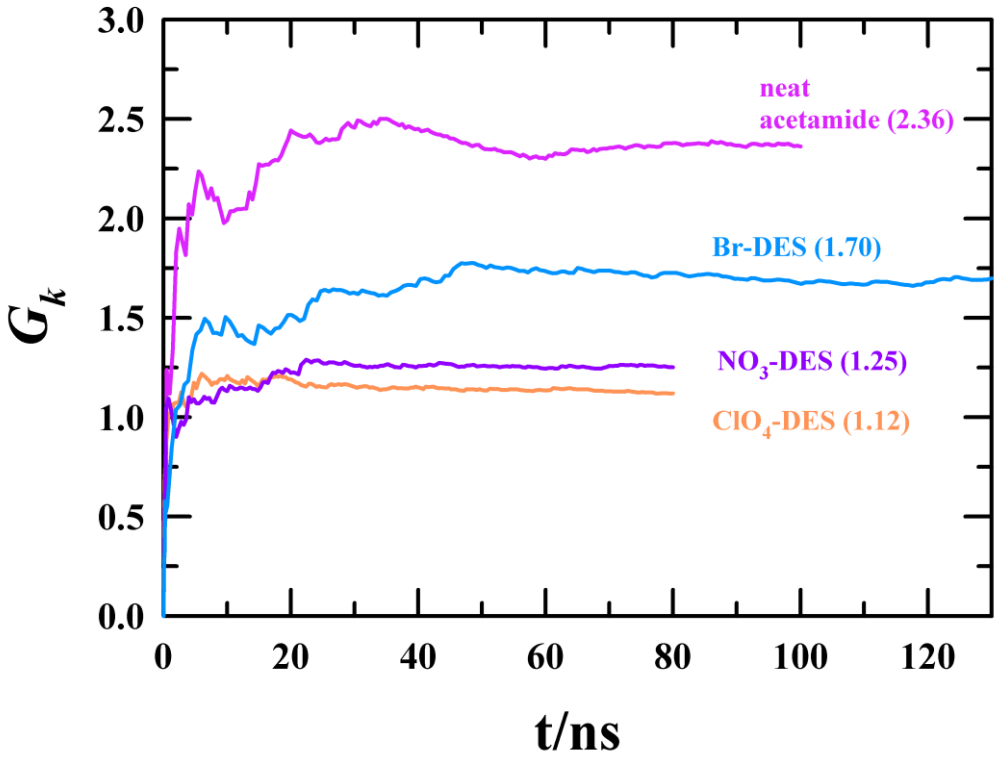

Figure 3.13: Time evolution of the Kirkwood correlation factor (G_k) during simulations for pure acetamide and the three ionic acetamide DESs at 358 K. Time averaged values for G_k are shown in parentheses.

As already mentioned, intermolecular H-bond network critically influences the relative arrangements of molecular dipoles in space (dipolar correlations) and thus loss of dipolar correlations must accompany frustrations in the intermolecular H-bond network. We have therefore examined the H-bond network of acetamide in these DESs by calculating the average

number of H-bonds per acetamide molecules in these DESs and in the neat molten acetamide. The calculation procedure is available in the literature[29,114] and briefly discussed here.

We have considered geometric condition to define a hydrogen bond between two acetamide molecules. In our calculations, donor-acceptor distance and acceptor-donor-hydrogen angle are taken into account. For one acetamide molecule, carbonyl oxygen and amide nitrogen are taken as acceptor and donor sites, respectively. Therefore, two acetamide molecules are hydrogen bonded if

(i) the distance between the acceptor and the hydrogen (r_{O-H}) is less than 0.278 nm which is the first minimum of the corresponding RDF (not shown for brevity).

(ii) the acceptor-donor-hydrogen angle is less than 30°.

Using these conditions, we have estimated the average number of hydrogen bonds per acetamide molecule, $\langle n_{HB} \rangle$, in neat molten acetamide at 358 K, and the three ionic acetamide DESs considered in this study.

Figure 3.14 shows the temperature dependent average number of H-bonds per acetamide molecule, $\langle n_{HB} \rangle$, in these three DESs. The same for the neat molten acetamide at 358 K is also shown for a qualitative comparison. Clearly, $\langle n_{HB} \rangle$ is substantially lower in these ionic DESs than that in the neat molten acetamide and exhibits an appreciable anion identity dependence. The mild temperature dependence of $\langle n_{HB} \rangle$ reflected here can be explained in terms of the relatively weaker temperature-induced randomization of the dipolar correlations. The same trend followed by the anion dependent ε_s, G_k and $\langle n_{HB} \rangle$ only highlights the fact that the dielectric decrement in the DESs is caused largely, if not solely, by the anion-induced damage of the intermolecular H-bond network among the host acetamide molecules, followed by the subsequent frustrations in the static dipolar correlations.

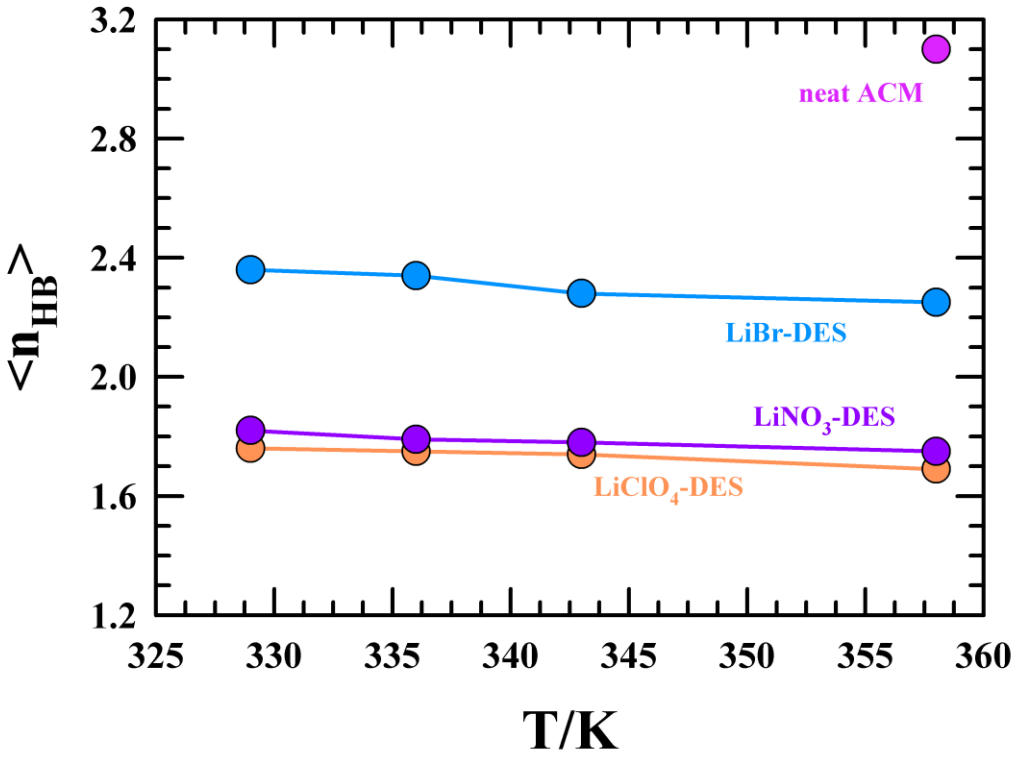

Figure 3.14: Average number of hydrogen bonds per acetamide molecule, $\langle n_{HB} \rangle$, are shown for neat molten acetamide, and three ionic DESs studied. For ionic DESs, temperature-dependence of $\langle n_{HB} \rangle$ are shown. The solid lines going through the symbols act as guides to bare eye.

Next, we examine the presence of extremely slow 'irrotationally bound' acetamide molecules in order to understand the dynamic contribution to the observed ion-induced dielectric decrement. For this, we have simulated the time averaged reorientation times ($\tau_{\boldsymbol{\mu}}$) for every single molecular dipole (acetamide molecule) present in the system by monitoring the following normalised time correlation function, $\phi_{\boldsymbol{\mu}}(t) = \frac{\langle \boldsymbol{\mu}(0).\boldsymbol{\mu}(t) \rangle}{\langle \boldsymbol{\mu}(0).\boldsymbol{\mu}(0) \rangle}$, with $\tau_{\boldsymbol{\mu}} = \int \phi_{\boldsymbol{\mu}}(t) dt$. We therefore obtained ~800 decay functions for each DES and those many individual $\tau_{\boldsymbol{\mu}}$ values.

The distributions of these individual relaxation times, $P(\tau_{\mu})$, for these three ionic DESs are presented in Figure 3.15. Interestingly, although LiBr-DES shows the most sluggish reorientation dynamics, the slowest time is limited to a few ns. This confirms the absence of 'irrotationally bound' extremely slow acetamide molecules in these model DES systems, lowering the possibility for the dynamics to contribute to the observed dielectric decrement.

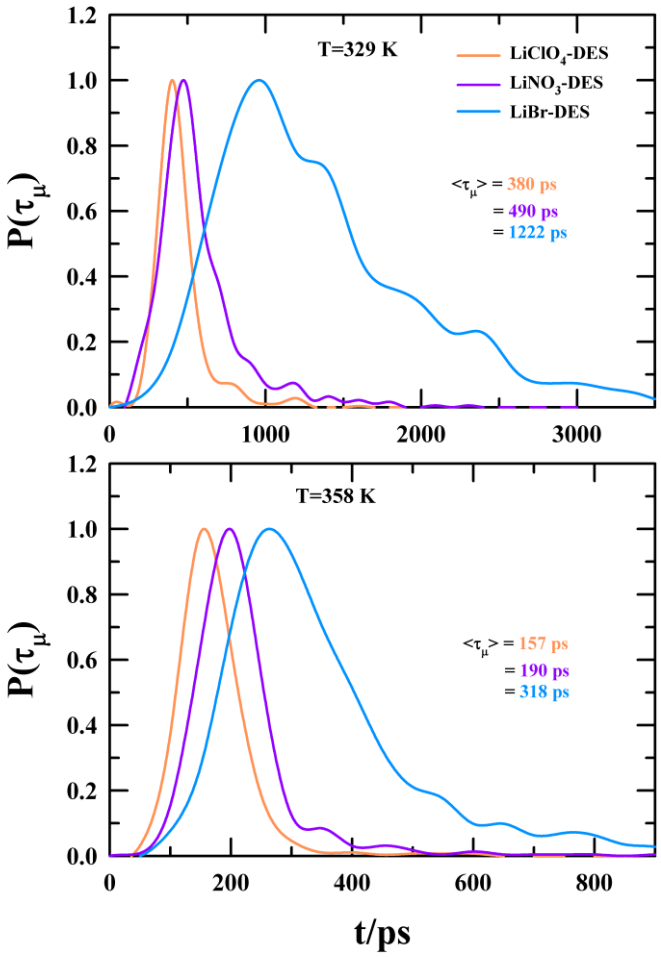

Figure 3.15: Normalised probability distributions, $P(\tau_\mu)$, of single-dipole orientation times in the three ionic DESs at 329 K (upper panel), and 358 K (lower panel).

3.5 Conclusion

To summarize, a thorough temperature dependent simulation study of dielectric relaxation in (acetamide + lithium perchlorate/ nitrate/ bromide) deep eutectics has been carried out to understand the effects of electrolyte on the dielectric behaviour of these systems. This has been done by separating out the dipole rotational, ion translational and the coupled dipole-ion ro-translational contributions that constitute the total frequency dependent dielectric function. The dipolar (rotational) contribution has been found to overwhelmingly dominate the DR spectra at all the temperatures considered, while the other two contributions are quite small. A comparison with the available experimental data indicates that the impact of the electrolyte on the static dielectric constant has been predicted successfully by the present simulations, although the simulated relaxations times have been overestimated by approximately a factor of 2. This is mainly due to the inherent nature of the force field employed to represent acetamide in this work. A novel finding of this study is the prediction of ion-induced decrement of the static dielectric constant of these DESs and its (the decrement) dependence on the identity of the anion. Further investigation suggest that this decrement is arising from the partial randomization of the dipolar correlations that accompanies substantial frustrations in the acetamide H-bonding network. Our analyses indicate that the decrement is largely static in nature because the simulated distributions of the individual dipole rotation times do not predict rotation times beyond a few nanoseconds. This is a new insight to the DR behaviour of these ionic DESs and these findings explain the recent MHz-GHz DR measurements in microscopic terms. Importantly, this simulation study provides a resolution to a long-standing debate on the actual impact of electrolytes on the static dielectric constant of acetamide in these ionic DESs.

We would like to mention that the present study could not successfully predict the experimental trend of the anion dependent DR activation energy. More precisely, these simulations have failed to predict correctly the extent of viscosity decoupling found for average DR time constants in the bromide DES. As we have already mentioned, this failure is because of the inherent limitations of the model force field parameters. Our initial study employing different force field (OPLS-AA) parameters[115] for acetamide predicted weak anion dependence of both the static dielectric constant and relaxation times (results not shown). The development of a new force field describing correctly both the experimental dielectric constant and the relaxation times for molten acetamide might be an important problem for future study.

Appendix 3.A

Table 3.A.1: Number of constituent particles in three DESs.

DES-type	$N_{acetamide}$	N_{cation}	N_{anion}
$LiClO_4$-DES	810	190	190
$LiNO_3$-DES	780	220	220
LiBr-DES	780	220	220

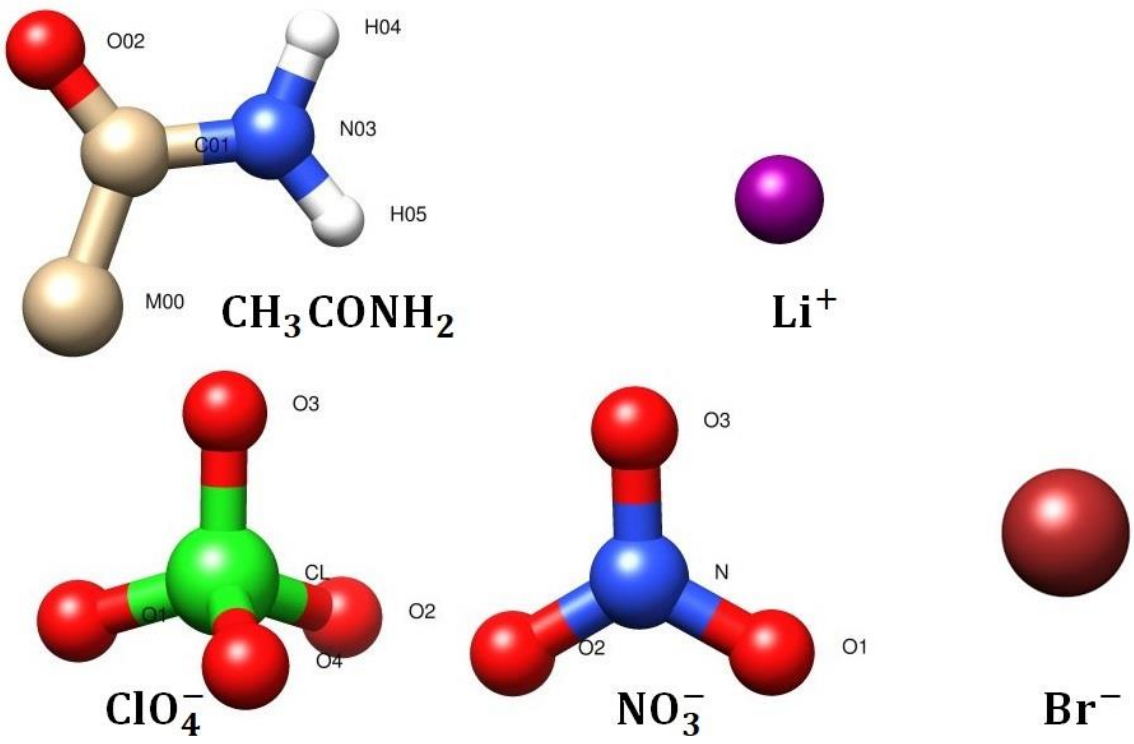

Figure 3.A.1: Molecular representation of acetamide, cation, and anions. Color codes: white (hydrogen), golden (carbon), red (oxygen), blue (nitrogen), violet (lithium), brown (bromine), green (chlorine).

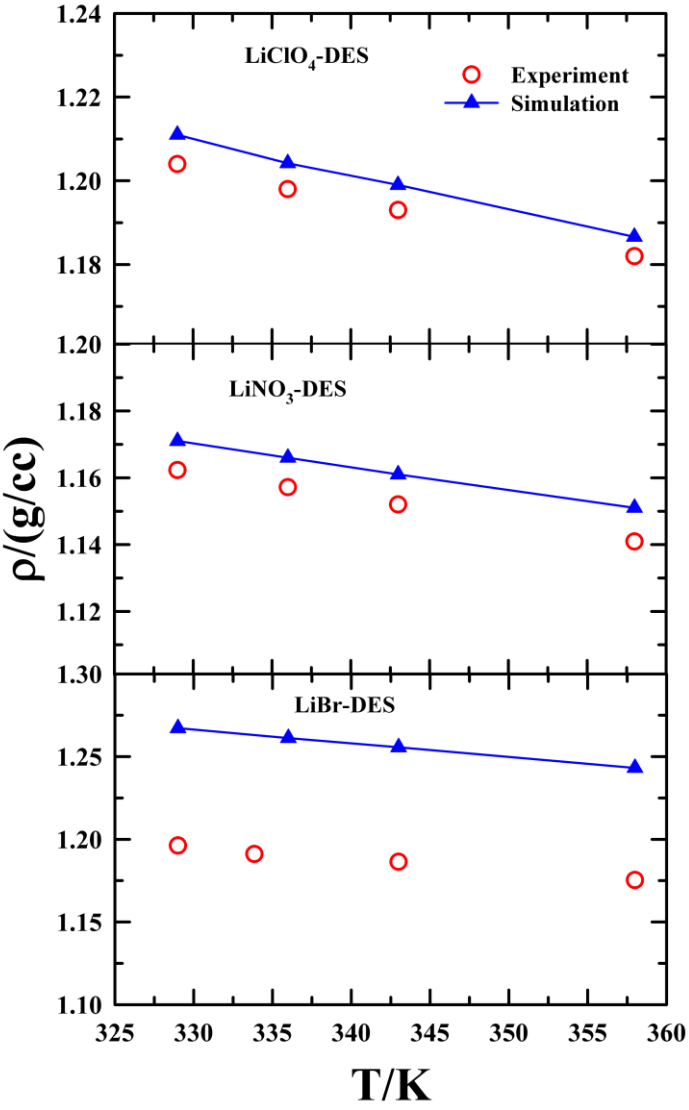

Figure 3.A.2: Temperature-dependent simulated and experimental[93,116] densities for three DESs.

Table 3.A.2: Comparison of the temperature-dependent simulated densities with those from experiments.[93,116]

T(K)	Density(g/cc)					
	CH_3CONH_2+$LiClO_4$		CH_3CONH_2+$LiNO_3$		CH_3CONH_2+LiBr	
	Expt.	Simu	Expt.	Simu	Expt.	Simu
329	1.182*	1.187	1.162*	1.171	1.196	1.267
336	1.193	1.199	1.157*	1.166	1.191	1.261
343	1.198*	1.204	1.152*	1.161	1.185*	1.255
358	1.204	1.211	1.141*	1.151	1.175*	1.243

*values are obtained from extrapolation

Table 3.A.3: Fit parameters obtained by using the fit function, $f_{DD}(t) = \sum_k A_k \exp(-t/\tau_k)$, for analytically describing the simulated $\phi_{DD}^{N}(t)$. Values are shown for the three DESs at four temperatures.

T [K]	**A_1 [D^2]**	**τ_1 [ps]**	**A_2 [D^2]**	**τ_2 [ps]**	**A_3 [D^2]**	**τ_3 [ps]**	**A_4 [D^2]**	**τ_4 [ps]**	**$\langle\tau\rangle$ [ps]**	**ε_{DD}**
$LiClO_4$-DES										
329	0.78	184.4	0.11	27.3	0.11	0.7			147	28.96
336	0.75	171	0.16	20.3	0.09	0.6			131.6	27.82
343	0.74	142	0.16	23.4	0.10	0.7			109	26.94
358	0.71	88.2	0.18	22	0.11	0.6			66.6	26.24
$LiNO_3$-DES										
329	0.66	450	0.19	127	0.08	30	0.07	0.6	323.6	34.31
336	0.48	406	0.39	112	0.07	10.7	0.06	0.3	239.3	33.00
343	0.49	307	0.41	86	0.06	2.5	0.04	0.2	185.8	31.55
358	0.81	132	0.08	20	0.05	3.8	0.06	0.2	108.7	28.28
LiBr-DES										
329	0.41	3330	0.54	380	0.03	1.4	0.03	0.1	1570.5	45.49
336	0.55	1025	0.37	362	0.04	14.4	0.04	0.3	698.3	45.16
343	0.72	628	0.20	147	0.04	9	0.04	0.2	482	43.22
358	0.56	530	0.38	100	0.02	2.5	0.04	0.2	334.8	42.13

Table 3.A.4: Fit parameters obtained by using the fit function, $f_{JJ}(t) = \sum_k A_k \cos(\omega_k . t + \delta_k) \exp(-t/\tau_k)$, for analytically describing the simulated $\langle J(0) \cdot J(t) \rangle$. Values are shown for the three DESs at four temperatures.

T [K]	A_1 [$e^2nm^2ps^{-2}$]	τ_1 [ps]	ω_1 [THz]	δ_1	A_2 [$e^2nm^2ps^{-2}$]	τ_2 [ps]	ω_2 [THz]	δ_2	A_3 [$e^2nm^2ps^{-2}$]	τ_3 [ps]	ε_{JJ}
$LiClO_4$-DES											
329	250.689	0.038	78.961	-0.317	90.62	0.048	39.73	-2.674	-3.785	0.454	1.73
336	270.904	0.037	80.250	-0.352	100.0	0.045	40.08	-2.73	-3.926	0.451	1.70
343	303.77	0.034	77.205	-0.351	126.61	0.044	42.17	-2.85	-3.782	0.468	1.73
358	317.619	0.034	76.552	-0.336	135.71	0.042	41.623	-2.818	-3.937	0.463	1.68
$LiNO_3$-DES											
329	260.332	0.042	79.356	-0.327	59.263	0.066	43.38	-2.791	-6.015	0.292	1.24
336	272.5	0.041	78.856	-0.338	64.95	0.064	44.07	-2.868	-5.873	0.300	1.24
343	272.57	0.041	79.02	-0.344	59.73	0.067	43.79	-2.882	-5.889	0.30	1.22
358	287.493	0.04	78.555	-0.357	64.29	0.065	44.05	-2.938	-5.91	0.31	1.26
LiBr-DES											
329	-211.202	0.102	75.9	3.70	141.02	0.137	71.26	-7.82	-2.848	0.30	0.73
336	-267.168	0.096	75.232	3.479	135.02	0.147	72.141	-8.35	-3.117	0.279	0.65
343	-250.75	0.094	75.54	3.48	123.04	0.148	71.828	-8.229	-2.998	0.304	0.73
358	-266.626	0.086	74.813	3.252	90.812	0.164	72.269	-8.649	-3.476	0.275	0.66

Table 3.A.5: Fit parameters obtained by using a fit function, $f_{DJ} = \sum_k A_k t^{\gamma_k - 1} \exp(-t/\tau_k)$, for the simulated $\langle M_D(0) \cdot J(t) \rangle$. Values are shown for the three DESs at four temperatures.

T[K]	A_1 [$e^2nm^2ps^{-\gamma}$]	γ_1	τ_1[ps]	A_2 [$e^2nm^2ps^{-\gamma}$]	γ_2	τ_2[ps]	A_3 [$e^2nm^2ps^{-\gamma}$]	γ_3	τ_3[ps]	$2\varepsilon_{DJ}$
$LiClO_4$-DES										
329	-4208.18	4.18	0.067	263.87	2.75	0.096	0.13	3.42	0.66	1.71
336	-4199.07	4.15	0.068	256.934	2.74	0.1	0.18	3.52	0.58	1.75
343	-4510	4.19	0.067	277.5	2.76	0.096	0.19	2.60	0.67	1.63
358	-4403.53	4.2	0.068	280.2	2.76	0.096	0.21	1.96	0.85	1.76
$LiNO_3$-DES										
329	517.931	2.913	0.049	7.664	2.574	0.17	1.506	8.81	0.21	1.47
336	517.833	2.913	0.048	8.979	2.54	0.17	2.202	8.945	0.20	1.51
343	514.66	2.908	0.05	9.496	2.70	0.17	0.898	9.56	0.22	1.59
358	514.975	2.909	0.05	10.041	2.61	0.17	2.18	7.63	0.22	1.55
LiBr-DES										
329	1150.19	3.216	0.035	358.207	5.01	0.084	0.237	2.664	0.233	0.37
336	1073.46	3.192	0.036	372.897	4.94	0.081	0.239	2.736	0.372	0.46
343	1178.53	3.22	0.036	472.73	5.12	0.084	0.144	3.512	0.278	0.36
358	1189.41	3.209	0.036	478.74	5.06	0.084	0.229	2.644	0.323	0.42

Table 3.A.6: Temperature-dependent multi-exponential fit parameters for the simulated $C_{HB}(t)$, $C_1(t)$, and DR timescales for three acetamide-based ionic DESs. $C_{HB}(t)$, and $C_1(t)$ timescales are taken from Tables S7 and **S**5 of SI of Ref. 12, respectively. DR times are from the present simulations.

DES	**T (K)**	**Relaxation function**	a_1	τ_1 (ps)	a_2	τ_2 (ps)	a_3	τ_3 (ps)	a_4	τ_4 (ps)
$LiClO_4$-DES	329	$C_{HB}(t)$	0.21	2772	0.47	268	0.19	27	0.13	0.6
		$C_1(t)$			0.58	239	0.32	38	0.10	0.9
		DR			0.78	184.4	0.11	27.3	0.11	0.7
	336	$C_{HB}(t)$	0.21	2094	0.46	210	0.20	22	0.13	0.6
		$C_1(t)$			0.60	173	0.30	28	0.10	0.8
		DR			0.75	171	0.16	20.3	0.09	0.6
LiNO3-DES	329	$C_{HB}(t)$	0.16	4195	0.47	452	0.24	53	0.13	0.7
		$C_1(t)$			0.63	281	0.28	42	0.09	0.9
		DR	0.66	450	0.19	127	0.08	30	0.07	0.6
	336	$C_{HB}(t)$	0.21	2466	0.49	254	0.18	26.7	0.12	0.6
		$C_1(t)$			0.62	208	0.28	32	0.10	0.8
		DR	0.48	406	0.39	112	0.07	10.7	0.06	0.3
LiBr-DES	329	$C_{HB}(t)$	0.22	7047	0.49	751	0.19	72	0.10	0.6
		$C_1(t)$	0.26	1304	0.53	259	0.14	22.3	0.07	0.6
		DR	0.41	3330	0.54	380	0.03	1.4	0.03	0.1
	336	$C_{HB}(t)$	0.21	4882	0.48	550	0.20	60	0.11	0.6
		$C_1(t)$	0.39	597	0.43	143	0.12	13.3	0.06	0.5
		DR	0.55	1025	0.37	362	0.04	14.4	0.04	0.3

Table 3.A.7: Comparison of the static dielectric constant and the dielectric relaxation times between the present simulation and the experiments for $LiClO_4$-DES. Experimental data are taken from Ref. 12 of the main text. Note that the dispersion ($\Delta\varepsilon_j$) values are mentioned in percentage, not in absolute values.

T/K	Method	$\Delta\boldsymbol{\varepsilon_1}$	$\boldsymbol{\tau_1}$[ps]	$\Delta\boldsymbol{\varepsilon_2}$	$\boldsymbol{\tau_2}$[ps]	$\Delta\boldsymbol{\varepsilon_3}$	$\boldsymbol{\tau_3}$[ps]	$\Delta\boldsymbol{\varepsilon_4}$	$\boldsymbol{\tau_4}$[ps]	$\langle\boldsymbol{\tau}\rangle$[ps]	$\boldsymbol{\varepsilon_s}$
329	Sim	0.78	184.4	0.11	28.5			0.11	0.7	147	29.98
	Exp	0.75	137	0.16	36	0.09	4.0			109	30.5
336	Sim	0.75	171	0.16	20.3			0.09	0.6	131.6	28.82
	Exp	0.73	117	0.17	34	0.10	4			92	30.5

Table 3.A.8: Comparison of the static dielectric constant and the dielectric relaxation times between the present simulation and the experiments for $LiNO_3$-DES. Experimental data are taken from Ref. 12. Note that the dispersion ($\Delta\varepsilon_j$) values are mentioned in percentage.

T/K	Method	$\Delta\boldsymbol{\varepsilon_1}$	$\boldsymbol{\tau_1}$[ps]	$\Delta\boldsymbol{\varepsilon_2}$	$\boldsymbol{\tau_2}$[ps]	$\Delta\boldsymbol{\varepsilon_3}$	$\boldsymbol{\tau_3}$[ps]	$\Delta\boldsymbol{\varepsilon_4}$	$\boldsymbol{\tau_4}$[ps]	$\Delta\boldsymbol{\varepsilon_4}$	$\boldsymbol{\tau_4}$[ps]	$\langle\boldsymbol{\tau}\rangle$[ps]	$\boldsymbol{\varepsilon_s}$
329	Sim	0.66	450	0.19	127	0.08	30			0.07	0.6	323.6	35.08
	Exp	0.63	275	0.24	88	0.08	23	0.05	4			196	29.9
336	Sim	0.48	406	0.39	112	0.07	10.7			0.06	0.3	239.3	33.73
	Exp	0.61	233	0.27	80	0.07	21	0.05	4			165	30.3

Table 3.A.9: Comparison of the static dielectric constant and the dielectric relaxation times between the present simulation and the experiments for LiBr-DES. Experimental data are taken from Ref. 12 of the main text. Note that the dispersion ($\Delta\varepsilon_j$) values are mentioned in percentage.

T [K]	**Method**	$\Delta\varepsilon_1$	τ_1 **[ps]**	$\Delta\varepsilon_2$	τ_2 **[ps]**	$\Delta\varepsilon_3$	τ_3 **[ps]**	$\Delta\varepsilon_4$	τ_4 **[ps]**	$\Delta\varepsilon_5$	τ_5 **[ps]**	$\Delta\varepsilon_6$	τ_6 **[ps]**	$\langle\tau\rangle$ **[ps]**	ε_s
329	Sim	0.41	3330	0.54	380					0.03	1.4	0.03	0.1	1570	46.86
	Exp			0.66	394	0.21	100	0.09	26	0.03	5			283	21.9
336	Sim	0.55	1025	0.37	362			0.04	14.4			0.04	0.3	698	46.34
	Exp			0.69	300	0.19	78	0.08	24	0.04	5			224	22.3

References

1 Q. Zhang, K. de Oliveira Vigier, S. Royer and F. Jérôme, *Chem. Soc. Rev.*, 2012, **41**, 7108-7146.

2 E. L. Smith, A. P. Abbott and K. S. Ryder, *Chem. Rev.*, 2014, **114**, 11060–11082.

3 P. Xu, G.-W. Zheng, M.-H. Zong, N. Li and W.-Y. Lou, *Bioresour. Bioprocess.*, 2017, **4**, 34.

4 R. Svigelj, N. Dossi, C. Grazioli and R. Toniolo, *Sensors*, 2021, **21**, 4263.

5 P. Atkins, J. de Paula and J. Keeler, *Atkins' physical chemistry*, Oxford University Press, 11th edn., 2017.

6 B. Guchhait, S. Daschakraborty and R. Biswas, *J. Chem. Phys.*, 2012, **136**, 174503.

7 B. Guchhait, S. Das, S. Daschakraborty and R. Biswas, *J. Chem. Phys.*, 2014, **140**, 104514.

8 B. Guchhait, H. al Rasid Gazi, H. K. Kashyap and R. Biswas, *J. Phys. Chem. B*, 2010, **114**, 5066–5081.

9 S. Dinda, A. Sil, A. Das, E. Tarif and R. Biswas, *J. Mol. Liq.*, 2022, **349**, 118126.

10 N. Subba, E. Tarif, P. Sen and R. Biswas, *J. Phys. Chem. B*, 2020, **124**, 1995–2005.

11 K. Mukherjee, A. Das, S. Choudhury, A. Barman and R. Biswas, *J. Phys. Chem. B*, 2015, **119**, 8063–8071.

12 K. Mukherjee, S. Das, J. Rajbangshi, E. Tarif, A. Barman and R. Biswas, *J. Phys. Chem. B*, 2021, **125**, 12552–12567.

13 Y. Dai, J. van Spronsen, G.-J. Witkamp, R. Verpoorte and Y. H. Choi, *J. Nat. Prod.*, 2013, **76**, 2162–2173.

14 G. García, S. Aparicio, R. Ullah and M. Atilhan, *Energy & Fuels*, 2015, **29**, 2616–2644.

15 M. Sharma, C. Mukesh, D. Mondal and K. Prasad, *RSC Adv.*, 2013, **3**, 18149.

16 S. Handy and K. Lavender, *Tetrahedron Lett.*, 2013, **54**, 4377–4379.

17 O. E. Geiculescu, D. D. Desmarteau, S. E. Creager, O. Haik, D. Hirshberg, Y. Shilina, E. Zinigrad, M. D. Levi, D. Aurbach and I. C. Halalay, *J. Power Sources*, 2016, **307**, 519–525.

18 V. Lesch, A. Heuer, B. R. Rad, M. Winter and J. Smiatek, *Phys. Chem. Chem. Phys.*, 2016, **18**, 28403–28408.

19 C. D'Agostino, R. C. Harris, A. P. Abbott, L. F. Gladden and M. D. Mantle, *Phys. Chem. Chem. Phys.*, 2011, **13**, 21383–21391.

20 A. P. Abbott, G. Capper and S. Gray, *Chem. Phys. Chem*, 2006, **7**, 803–806.

21 A. P. Abbott, J. C. Barron, K. S. Ryder and D. Wilson, *Chem. Eur. J.*, 2007, **13**, 6495–6501.

22 A. P. Abbott, D. Boothby, G. Capper, D. L. Davies and R. K. Rasheed, *J. Am. Chem. Soc.*, 2004, **126**, 9142–9147.

23 A. Das, S. Das and R. Biswas, *Chem. Phys. Lett.*, 2013, **581**, 47–51.

24 A. Das, S. Das and R. Biswas, *J. Chem. Phys.*, 2015, **142**, 034505.

25 H. A. R. Gazi, B. Guchhait, S. Daschakraborty and R. Biswas, *Chem. Phys. Lett.*, 2011, **501**, 358–363.

26 S. N. Tripathy, Z. Wojnarowska, J. Knapik, H. Shirota, R. Biswas and M. Paluch, *J. Chem. Phys.*, 2015, **142**, 184504.

27 R. Biswas, A. Das and H. Shirota, *J. Chem. Phys.*, 2014, **141**, 134506.

28 S. Das, R. Biswas and B. Mukherjee, *J. Chem. Phys.*, 2016, **145**, 084504.

29 S. Das, R. Biswas and B. Mukherjee, *J. Phys. Chem. B*, 2015, **119**, 11157–11168.

30 T. Pal and R. Biswas, *Chem. Phys. Lett.*, 2011, **517**, 180–185.

31 S. Banerjee, P. Kr. Ghorai, D. Maji and R. Biswas, *J. Phys. Chem. B*, 2022, **126**, 10146–10155.

32 D. J. Mitchell and B. W. Ninham, *J. Chem. Soc., Faraday Trans. 2*, 1981, **77**, 601.

33 G. Berchiesi, G. Vitali, P. Passamonti and R. Płowiec, *J. Chem. Soc., Faraday Trans. 2*, 1983, **79**, 1257–1263.

34 G. Berchiesi, *J. Mol. Liq.*, 1999, **83**, 271–282.

35 D. C. Prieve and R. Roman, *J. Chem. Soc., Faraday Trans. 2*, 1987, **83**, 1287.

36 G. Berchiesi, F. Farhat, M. de Angelis and S. Barocci, *J. Mol. Liq.*, 1992, **54**, 103–113.

37 A. Amico, G. Berchiesi, C. Cametti and A. Di Biasio, *J. Chem. Soc., Faraday Trans. 2*, 1987, **83**, 619–626.

38 G. Berchiesi, M. De Angelis, G. Rafaiani and G. Vitali, *J. Mol. Liq.*, 1992, **51**, 11–38.

39 D. Maji, S. Indra and R. Biswas, *J. Chem. Sci.*, 2021, **133**, 1–12.

40 C. Schröder, J. Hunger, A. Stoppa, R. Buchner and O. Steinhauser, *J. Chem. Phys.*, 2008, **129**, 184501.

41 C. Schröder and O. Steinhauser, *J. Chem. Phys.*, 2010, **132**, 244109.

42 M. Schmollngruber, D. Braun and O. Steinhauser, *J. Chem. Phys.*, 2016, **145**, 214702.

43 R. Buchner, *Pure Appl. Chem.*, 2008, **80**, 1239–1252.

44 R. Buchner and J. Barthel, *Annu. Rep. Prog. Chem., Sect. C: Phys. Chem.*, 1994, **91**, 71–106.

45 H. Weingärtner, P. Sasisanker, C. Daguenet, P. J. Dyson, I. Krossing, J. M. Slattery and T. Schubert, *J. Phys. Chem. B*, 2007, **111**, 4775–4780.

46 C. Schröder, C. Wakai, H. Weingärtner and O. Steinhauser, *J. Chem. Phys.,* 2007, **126***,* 084511.

47 R. Buchner, G. T. Hefter and P. M. May, *J. Phys. Chem. A*, 1999, **103**, 1–9.

48 R. Buchner and G. Hefter, *Phys. Chem. Chem. Phys.*, 2009, **11**, 8984.

49 T. Chen, G. Hefter and R. Buchner, *J. Phys. Chem. A*, 2003, **107**, 4025–4031.

50 W. Wachter, W. Kunz, R. Buchner and G. Hefter, *J. Phys. Chem. A*, 2005, **109**, 8675–8683.

51 D. Huppert, V. Ittah and E. M. Kosower, *Chem. Phys. Lett.*, 1989, **159**, 267–275.

52 C. F. Chapman and M. Maroncelli, *J. Phys. Chem.*, 1991, **95**, 9095–9114.

53 V. Ittah and D. Huppert, *Chem. Phys. Lett.*, 1990, **173**, 496–502.

54 E. Bart and D. Huppert, *Chem. Phys. Lett.*, 1992, **195**, 37–44.

55 A. Chandra, *J. Chem. Phys.*, 2000, **113**, 903–905.

56 S. Chowdhuri and A. Chandra, *J. Chem. Phys.*, 2001, **115**, 3732–3741.

57 J. M. Caillol, D. Levesque and J. J. Weis, *J. Chem. Phys.*, 1986, **85**, 6645–6657.

58 G. Löffler, H. Schreiber and O. Steinhauser, *J. Chem. Phys.*, 1997, **107**, 3135–3143.

59 A. Chandra, *Phys. Rev. Lett.*, 2000, **85**, 768–771.

60 A. Chandra, D. Wei and G. N. Patey, *J. Chem. Phys.*, 1993, **98**, 4959–4966.

61 A. Chandra and G. N. Patey, *J. Chem. Phys.*, 1994, **100**, 8385–8391.

62 C. Schröder, T. Rudas and O. Steinhauser, *J. Chem. Phys.*, 2006, **125**, 244506.

63 C. Schröder, T. Rudas, G. Neumayr, S. Benkner and O. Steinhauser, *J. Chem. Phys.*, 2007, **127**, 234503.

64 C. Schröder and O. Steinhauser, *J. Chem. Phys.*, 2009, **131**, 114504.

65 C. Schröder and O. Steinhauser, *J. Chem. Phys.*, 2010, **133**, 154511.

66 C. Schröder, T. Sonnleitner, R. Buchner and O. Steinhauser, *Phys. Chem. Chem. Phys.*, 2011, **13**, 12240-12248.

67 C. Schröder, M. Sega, M. Schmollngruber, E. Gailberger, D. Braun and O. Steinhauser, *J. Chem. Phys.*, 2014, **140**, 204505.

68 C. Daguenet, P. J. Dyson, I. Krossing, A. Oleinikova, J. Slattery, C. Wakai and H. Weingärtner, *J. Phys. Chem. B*, 2006, **110**, 12682–12688.

69 S. Schrödle, G. Annat, D. R. MacFarlane, M. Forsyth, R. Buchner and G. Hefter, *Chem. Commun.*, 2006, 1748–1750.

70 D. A. Turton, J. Hunger, A. Stoppa, G. Hefter, A. Thoman, M. Walther, R. Buchner and K. Wynne, *J. Am. Chem. Soc.*, 2009, **131**, 11140–11146.

71 E. W. Castner, C. J. Margulis, M. Maroncelli and J. F. Wishart, *Annu. Rev. Phys. Chem.*, 2011, **62**, 85–105.

72 H. Jin, B. O'Hare, J. Dong, S. Arzhantsev, G. A. Baker, J. F. Wishart, A. J. Benesi and M. Maroncelli, *J. Phys. Chem. B*, 2008, **112**, 81–92.

73 J. A. Ingram, R. S. Moog, N. Ito, R. Biswas and M. Maroncelli, *J. Phys. Chem. B*, 2003, **107**, 5926–5932.

74 A. Gupta, H. S. Dhattarwal and H. K. Kashyap, *J. Chem. Phys.*, 2021, **154**, 184702.

75 H. K. Kashyap, C. S. Santos, N. S. Murthy, J. J. Hettige, K. Kerr, S. Ramati, J. Gwon, M. Gohdo, S. I. Lall-Ramnarine, J. F. Wishart, C. J. Margulis and E. W. Castner, *J. Phys. Chem. B*, 2013, **117**, 15328–15337.

76 S. Indra, R. Subramanian and S. Daschakraborty, *J. Mol. Liq.*, 2021, **331**, 115608.

77 S. Indra and S. Daschakraborty, *J. Chem. Sci.*, 2018, **130**, 3.

78 S. Daschakraborty and R. Biswas, *J. Chem. Phys.*, 2014, **140**, 014504.

79 S. Daschakraborty, T. Pal and R. Biswas, *J. Chem. Phys.*, 2013, **139**, 164503.

80 M. J. Abraham, D. van der Spoel, E. Lindahl, B. Hess and the GROMACS development team, GROMACS User Manual version 2018.

81 W. L. Jorgensen, D. S. Maxwell and J. Tirado-Rives, *J. Am. Chem. Soc.*, 1996, **118**, 11225–11236.

82 J. A. Aguilar-Pineda, G. A. Méndez-Maldonado, E. Núñez-Rojas and J. Alejandre, *Mol. Phys.*, 2015, **113**, 2716–2724.

83 D. R. Lide and W. M. Haynes, Eds., *CRC Handbook of Chemistry and Physics, 2009−2010, 90th ed.*, CRC Press, Boca Raton, FL, 90th edn., 2009.

84 B. Doherty, X. Zhong, S. Gathiaka, B. Li and O. Acevedo, *J. Chem. Theory Comput.*, 2017, **13**, 6131–6135.

85 K. P. Jensen and W. L. Jorgensen, *J. Chem. Theory Comput.*, 2006, **2**, 1499–1509.

86 L. Martinez, R. Andrade, E. G. Birgin and J. M. Martínez, *J. Comput. Chem.*, 2009, **30**, 2157–2164.

87 R. W. Hockney, S. P. Goel, J. W. Eastwood, R. W. Hockney, S. P. Goel and J. W. Eastwood, *J. Co. Ph.*, 1974, **14**, 148–158.

88 B. Hess, H. Bekker, H. J. C. Berendsen and J. G. E. M. Fraaije, *J. Comput. Chem.*, 1997, **18**, 14631472.

89 S. Nosé, *Mol. Phys.*, 1984, **52**, 255–268.

90 W. G. Hoover, *Phys. Rev. A (Coll Park)*, 1985, **31**, 1695.

91 M. Parrinello and A. Rahman, *J. App. Phys.*, 1981, **52**, 7182–7190.

92 S. Nosé and M. L. Klein, *Mol. Phys.*, 1983, **50**, 1055–1076.

93 G. Kalita, K. G. Sarma and S. Mahiuddin, *J. Chem. Eng. Data*, 1999, **44**, 222–226.

94 L. C. Branco, J. N. Rosa, J. J. M. Ramos, and C. A. M. Afonso, *Chem. Eur. J.*, 2002, **8(16)**, 3671–3677.

95 W. Xu, E. I. Cooper and C. A. Angell, *J. Phys. Chem. B*, 2003, **107**, 6170–6178.

96 H. Tokuda, K. Hayamizu, K. Ishii, M. A. B. H. Susan and M. Watanabe, *J. Phys. Chem. B*, 2004, **108**, 16593–16600.

97 M. L. T. Asaki, A. Redondo, T. A. Zawodzinski and A. J. Taylor, *J. Chem. Phys.*, 2002, **116**, 10377.

98 B. Bagchi and R. Biswas, in *Advances in Chemical Physics*, (John Wiley & Sons, 1999), pp. 207–433.

99 S. Arzhantsev, H. Jin, G. A. Baker and M. Maroncelli, *J. Phys. Chem. B*, 2007, **111**, 4978–4989.

100 X. Song, *J. Chem. Phys.*, 2009, **131**, 044503.

101 J. Hunger, A. Stoppa, S. Schrödle, G. Hefter and R. Buchner, *Chem. Phys. Chem*, 2009, **10**, 723–733.

102 K. F. Rinne, S. Gekle and R. R. Netz, *J. Chem. Phys.*, 2014, **141**, 214502.

103 M. Neumann and O. Steinhauser, *Chem. Phys. Lett.*, 1984, **106**, 563–569.

104 J. P. Hansen and I. R. McDonald, *Theory of Simple Liquids*, Academic, 3rd edn., 2006.

105 M. D. Ediger, *Annu. Rev. Phys. Chem.*, 2000, **51**, 99–128.

106 S. Banerjee, P. Kr. Ghorai, S. Das, J. Rajbangshi and R. Biswas, *J. Chem. Phys.*, 2020, **153**, 234502.

107 B. U. Felderhof, *Mol. Phys.*, 1984, **51**, 801–811.

108 F. E. Harris and C. T. O'Konski, *J. Phys. Chem.*, 1957, **61**, 310–319.

109 A. Yu. Zasetsky and I. M. Svishchev, *J. Chem. Phys.*, 2001, **115**, 1448–1454.

110 J. Sala, E. Guàrdia and J. Martí, *J. Chem. Phys.*, 2010, **132**, 214505.

111 S. Seal, K. Doblhoff-Dier and J. Meyer, *J. Phys. Chem. B*, 2019, **123**, 9912–9921.

112 P. E. Smith and W. F. van Gunsteren, *J. Chem. Phys.*, 1994, **100**, 3169–3174.

113 L. Saiz, E. Guàrdia and J.-À. Padró, *J. Chem. Phys.*, 2000, **113**, 2814–2822.

114 S. Das, R. Biswas and B. Mukherjee, *J Phys Chem B*, 2015, **119**, 274–283.

115 C. Caleman, P. J. Van Maaren, M. Hong, J. S. Hub, L. T. Costa and D. van der Spoel, *J. Chem. Theory Comput.*, 2012, **8**, 61–74.

116 B. Guchhait, S. Das, S. Daschakraborty and R. Biswas, *J. Chem. Phys.*, 2014, **140**, 104514.

Chapter 4

Exploring the structural and dynamic behavior of a glucose-urea-water deep eutectic solvent via molecular dynamics simulations

4.1 Introduction

Deep Eutectic Solvents (DESs) have emerged as a fascinating class of solvents due to their unique properties and potential applications across various scientific disciplines.[1–3] These exquisite solvents are formed via eutectic formation promoted by a unique combination of hydrogen-bond acceptors (HBA) and hydrogen-bond donors (HBD), providing a stable liquid phase with tunable physicochemical properties.[4–8] The field of DES research has witnessed a significant advancement in recent years because of the increasing demand for environmentally friendly and sustainable alternatives to traditional organic solvents which are often employed as reaction media.[9–12] Among the diverse range of DESs, naturally abundant deep eutectic solvents (NADES) have garnered particular interest due to their biocompatibility and availability from renewable resources.[13,14] NADES consists of naturally occurring substances, such as sugars, amino acids, organic acids, and water.[15] These solvents are considered "green solvents" and have shown great potential for use in various applications, including green chemistry, pharmaceutical formulations, and bio-catalysis.[13,15–22] In the context of green chemistry, NADES can replace conventional organic solvents, which are often harmful to environment and human health.[23]

Understanding solvation processes in NADES is important because it is directly connected not only to the development of environmentally friendly reaction media but also for choosing the right medium for tailoring a reaction toward a desired product.[24,25] By elucidating the hydrogen bonding patterns, orientational order, and other structural characteristics, one can engineer appropriate NADES with optimized properties suitable for diverse industrial processes, such as, solvent extraction,[26–31] catalysis,[32–34] and cosmetic producions.[35] Furthermore, the dielectric properties of NADES play a crucial role in their electrical conductivity and capacitive behavior.[36] Investigating these properties allows to explore their applicability in energy storage devices[37] and electrochemical sensors[38,39]. An understanding of dielectric relaxation and solvation dynamics in NADES can therefore contribute immensely to guide more efficient designing of media for applications in sustainable technology development.

One prominent member of the NADES family is the glucose-based deep eutectic solvents.[13,14,17,40–43] As carbohydrates constitute a significant amount of biomass, renewable energy resource, they emerge as critical components of NADES.[40,44–46] Urea, on the other hand, is an organic nitrogenous compound, analogous to amino acids and known to affect protein stability.[47–51] Previously, the characteristics of the glucose-urea-water deep eutectic solvent were investigated via solute-centred steady state and time-resolved fluorescence spectroscopic measurements.[25] Additionally, molecular dynamics (MD) simulations were carried out to characterize the water molecules in this DES.[52] However, a detailed molecular-level investigation of the intra- and interspecies interactions and dynamics for this DES has not been carried out yet and thus a comprehensive understanding is still missing. This work is aimed at that direction where MD simulations have been carried out to correlate the interactions present in the system to the over-all dynamics that could be measured in experiments.

In recent years, molecular dynamics (MD) simulations have proven to be a valuable tool for investigating the structure and dynamics of complex liquid systems, including DESs.[6,53–59] MD simulations offer a detailed and atomistic-level view of molecular interactions and motion, allowing to explore the behaviour of molecules under different thermodynamic conditions. This computational approach provides valuable insights into the structural and dynamic properties of NADES in terms of species-wise contributions, which are either not easy or possible to obtain through experimental measurements alone.[60–62]

In the present work we aim to investigate the structural and dynamical behaviour of the glucose-urea-water deep eutectic solvent using extensive MD simulations at four different temperatures. Various temperature-dependent properties of the system have been analysed to understand the underlying mechanisms governing its behaviour. By performing simulations over a wide temperature range, we can elucidate how temperature influences the structural organization of the solvent, hydrogen bonding patterns, and relaxation dynamics. One of the primary objectives of this study is to investigate the formation and stability of hydrogen bonds within the NADES system. Hydrogen bonding plays a crucial role in determining the solvent's properties, including its thermal stability, viscosity, and ion solvation capacity. We will explore the persistence and lifetimes of hydrogen bonds, shedding light on the strength and cooperativity of these interactions. Another critical aspect of this work is to assess the solvent's dielectric properties as a function of temperature. The dielectric relaxation spectra, calculated from MD simulation trajectories, will provide valuable information on the collective dipole fluctuation dynamics. This analysis will enable us to investigate the relationship between

temperature and frequency dependent dielectric response, elucidating the impact of temperature on the solvent polarization and reorientation dynamics.

4.2 Simulation details

We used the GROMACS software[63] with the CHARMM-36 force field[64] for all the molecular dynamics (MD) simulations in this study. The equation of the force field used in this study is described by Eq. 4.A.1 in the supporting information. The non-bonding parameters are listed in Tables 4.A.1-4.A.3. The molecular structures of DES components are created using visual molecular dynamics (VMD) package[65] and shown in Figure 4.A.1. Initially, glucose, urea and water molecules were arranged inside a simulation box using PACKMOL.[66] Periodic boundary conditions (PBC) in all three directions (x, y, and z) were applied for all the studied systems. A timestep of 1 fs was used to solve equations of motion. The particle mesh Ewald (PME) method[67,68] was employed to account for the long-range electrostatic interactions. The temperature of the system was regulated using the V-rescale thermostat[69] with a relaxation time of 0.1 ps, while the pressure was controlled by the Parrinello-Rahman barostat[70] with a relaxation time of 1 ps. Our simulation protocol involves three steps: minimization, equilibration, and production. Firstly, the initial simulation box is energy-minimized using the steepest-descent algorithm to remove unfavourable contacts. After the energy minimization, the system underwent equilibration in the canonical ensemble (NVT) for 1 ns to reach the desired temperatures of 303 K, 318 K, 328 K, and 343 K for the four systems. Subsequently, additional equilibration was carried out in the isothermal-isobaric condition (NPT) for 10 ns. Finally, the production run was conducted for 130 ns in the NPT condition while maintaining the pressure at 1 bar. The coordinates were saved in each 0.2 ps. For the calculation of hydrogen bond lifetimes, simulation runs of 1 ns were performed, and coordinates were saved at 10 fs intervals. Structural and dynamical analyses were done by using the TRAVIS software.[71,72]

The accuracy of the force field parameters was assessed by comparing the density values obtained from simulations with the experimental measurements (Table 4.A.4 in the Appendix 4.A). The excellent agreement between the simulated and experimental values confirms the reliability and validity of the used force field parameters.

4.3 Results and discussion

4.3.1 Radial distribution function (RDF) and spatial distribution function (SDF)

The liquid structure of glucose-urea-water NADES was studied by calculating the real-space pair correlation through RDF analysis. The RDF, $g(r)$, between two species is calculated as:[73]

$$g_{A-B}(r) = \frac{\langle \rho_B(r) \rangle}{\rho_B^{ave}} = \frac{1}{N_A \rho_B^{ave}} \sum_{i \in A}^{N_A} \sum_{i \in B}^{N_B} \frac{\partial(r_{ij} - r)}{4\pi r^2}, \quad (4.1)$$

where $\langle \rho_B(r) \rangle$ indicates density of B type particles around A type at a distance r and ρ_B^{ave} is the average number density of B type particles.

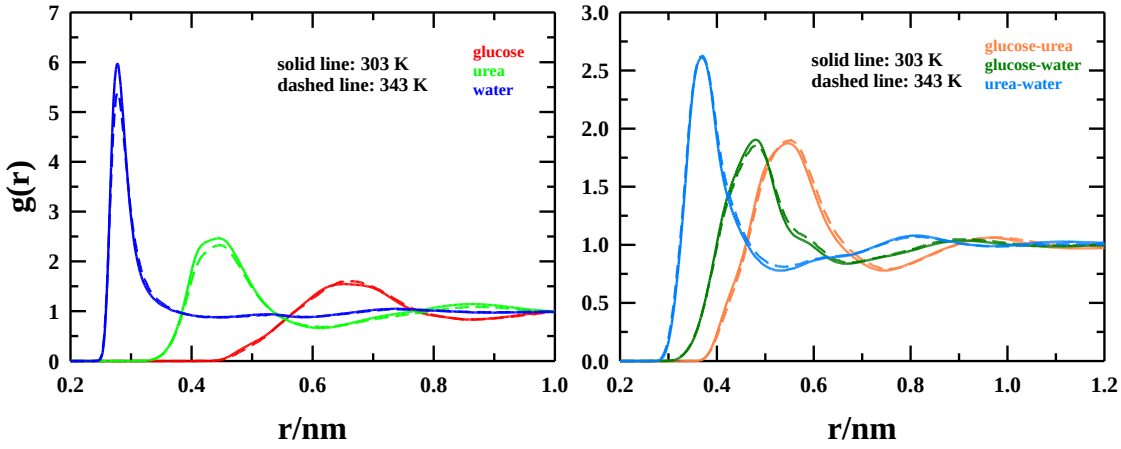

Figure 4.1: Temperature-dependent radial distribution function between centres-of-mass of molecules. The left panel shows correlation between same type of molecules and right panel shows correlations between molecules of different species.

Figure 4.1 indicates the spatial arrangement of one species with respect to itself and others. In left panel the peak of the RDF due to glucose-glucose interaction is the least intense and appears at the furthest distance. The exact opposite phenomenon can be observed in the case of water-water interaction whereas the urea-urea RDF places between them. In the right panel also, the same trend is reflected. The RDF peak positions are directly related to the size of the corresponding molecules. Here, the order of the size of the molecules is: glucose>urea>water. Therefore, it is expected that the RDFs involving glucose molecules will give peaks at the furthest distances. On the other hand, RDF peaks corresponding to interactions involving water molecules arise at the shortest distance. Therefore, the peak intensity decreases with increase of size. This can be attributed to the bulkiness of the molecules which eventually leads to less interaction among big molecules. For the glucose-urea RDF, the main peak appears at ~0.55

nm. Glucose-water RDF shows strongest probability at ~0.48 nm which is closer than glucose-glucose RDF peak (~0.67 nm). For urea-water RDF, the peak occurs at ~0.37 nm. For water-water RDF, the first peak is located at ~0.28 nm. From these observations, we may get an idea about two-dimensional relative spatial arrangements of different kinds of particles in the mixture. For example, water molecules preferentially populate the first solvation shell of glucose molecules, while urea molecules form the second layer. The peak maxima positions of water-water (~0.28 nm), urea-water (~0.37 nm) and glucose-water (~0.48 nm) suggest that the first layer around water is formed by water, followed by urea in the second layer.

Atom-atom radial distribution functions may provide additional insights into the structure of this DES. As inter-species hydrogen bond is a key to DES formation, we will discuss the probability of finding one H-bond doner site around a H bond acceptor site. We consider hydroxyl/amide hydrogen of one molecule and map the probability of finding a hydroxyl/carbonyl oxygen (acceptor) around it. The temperature-dependence has also been examined.

Figure 4.2 shows the probability of finding oxygen atoms of glucose, urea, and water around hydroxyl/amide hydrogens. In each case, the first peak is the principal peak and describes the most favourable interaction. Clearly, glucose acts as a poor acceptor. It is expected that due to their larger size, glucose molecules are being hindered to form H-bonds with their own kind. Water, being the smallest among the three species present, was expected to be preferred over a comparatively bigger molecule, urea, and this has been observed. Upon examining Figure 4.2, it is evident that the minima of hydrogen-acceptor RDFs are closely situated. While the peak minima align with the size of interacting species, the length of hydrogen bond distance corresponding to a specific donor shows minimal variation.

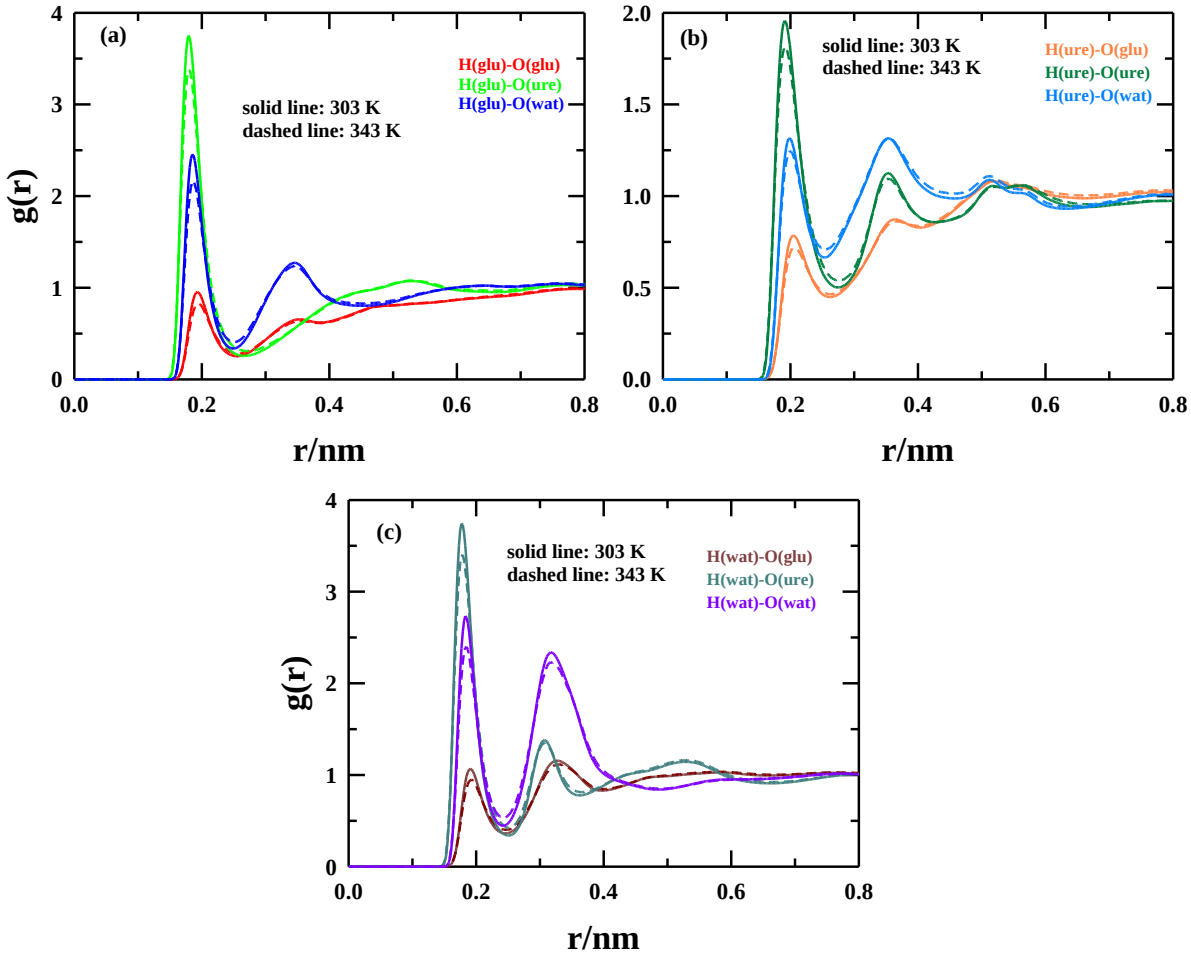

Figure 4.2: (a) Radial distribution functions (RDFs) between hydroxyl hydrogen of glucose and hydroxyl/carbonyl oxygen of glucose, urea and water. (b) . RDFs between hydroxyl hydrogen of urea and hydroxyl/carbonyl oxygen of glucose, urea and water. (c) RDFs between hydroxyl hydrogen of water and hydroxyl/carbonyl oxygen of glucose, urea and water. Each plot is colour-coded. Here, solid and dashed lines indicate results at 303 K and 343 K, respectively.

Next, we calculate the surface distribution functions (SDFs)[74,75] of glucose, urea and water to visualize the three-dimensional (3D) arrangements of center-of -mass of other species around a reference species for a better description of liquid structure. From Figure 4.3, it is evident that irrespective of the reference molecule, the first layer is formed by water molecules, followed by urea and then glucose. This ordering of arrangement is directly related to the size of the observed molecules. The formation of layers is agreed well with the peak positions reported in Figure 4.1.

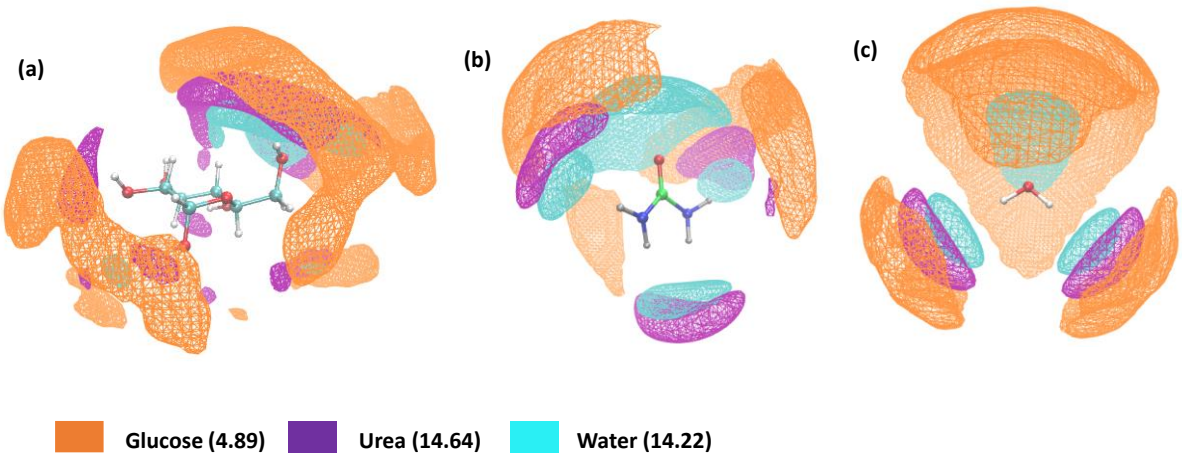

Figure 4.3: The spatial distribution function of (a) glucose, (b) urea and (c) water at 303 K. Different type of atoms is indicated with different colors: carbon → green, oxygen → red, nitrogen → blue, hydrogen → grey. Numbers in parentheses indicate corresponding isovalues in nm^{-3}.

4.3.2 Hydrogen bond topology

The system consists of glucose, urea, and water, each containing multiple atomic sites that can act as both donors and acceptors. This leads to the formation of a complex hydrogen bond (H-bond) network structure. H-bonds are defined by using geometric criteria as follows:[76,77]

(i) Distance between hydrogen (H) and acceptor (A) atoms should be less than the first minimum of the corresponding RDF.

(ii) The angle between hydrogen (H), donor (D) and acceptor (A), $\angle H - D - A$, should be less than 30°.

In this system each species can act as both donor and acceptor resulting nine different types of H-bonds. In our calculations we have considered all these different H-bonds and compare their properties. Firstly, we will discuss the number of hydrogen bonds between different interaction sites. Total number of such H-bonds are shown in Table 4.A.5 in the Appendix 4.A.

Table 4.A.5 clearly demonstrates a decrease in the number of hydrogen bonds with increasing temperature. This observation correlates to the RDF data presented earlier, which indicated a reduction in the peak heights of RDF with rising temperature. These findings suggest that molecular interactions are weakened as the solution temperature is increased. Further analysis of Table 4.A.5 reveals that, among the different species present in this system, the largest

number of H-bonds are formed between glucose and urea molecules. This can be attributed to the abundance of H-bond sites of these two species in system. Urea is the most abundant species with two donor and one acceptor sites and, one glucose molecule has five donor and six acceptor sites. Being the smallest molecule water molecules prefer to bind with larger molecules compared to itself. This fact is evident from the number of water-water H-bonds. In Figure 4.4, we present a graphical representation of the number of distinct hydrogen bonds *per* molecule of each of the species (glucose, urea, and water) present in the system. These data not only corroborate well with our previous observations but also provides a visual understanding of the variations in hydrogen bonding among the different species.

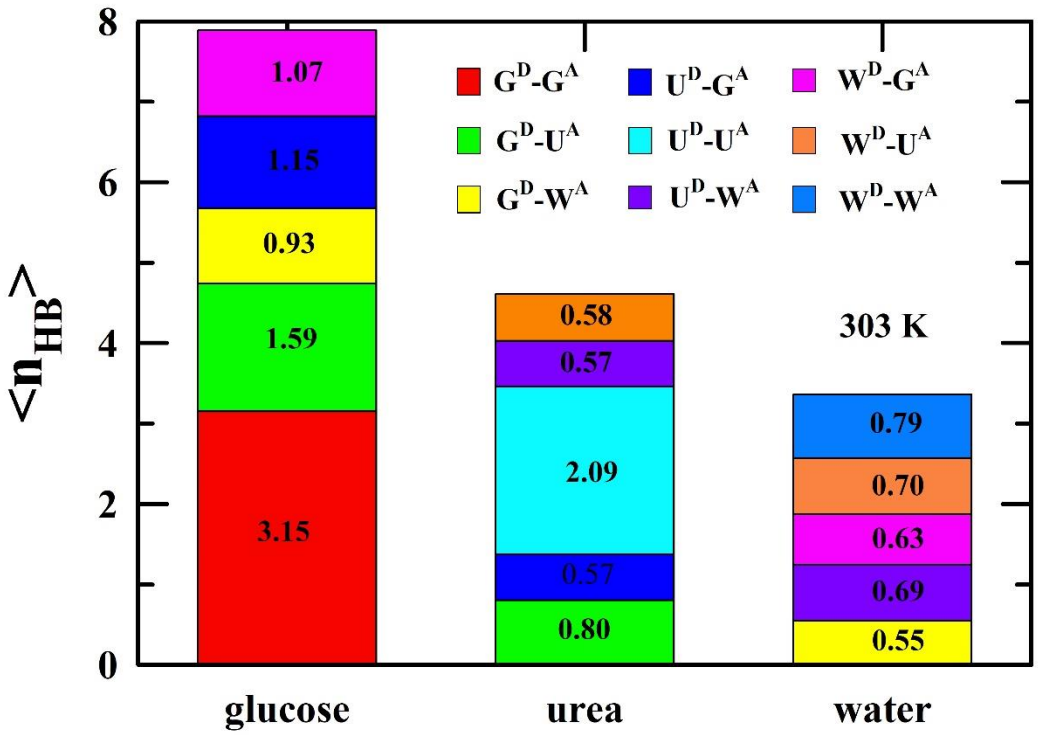

Figure 4.4: Number of different types of H-bonds per glucose, urea and molecule at 303 K. Each type of H-bond is uniquely colour-defined.

Figure 4.4 clearly illustrates that glucose molecules have the highest capacity to form hydrogen bonds, surpassing both urea and water. This observation is consistent with the number of available hydrogen bonding sites present in each species. Glucose, being a larger and more complex molecule, possesses more potential hydrogen bonding sites, enabling it to engage in a greater number of H-bonding interactions. Urea, although less abundant in H- bonding sites compared to glucose, still exhibits a substantial ability to form H-bonds, resulting in an

intermediate number of interactions. On the other hand, water, being a smaller and simpler molecule, has fewer H-bonding sites, leading to a lower count of H-bonds formed. We observe distinct patterns of intra- and interspecies interactions among glucose, urea, and water molecules within the complex H-bonding network of the system. Notably, self-interactions dominate for each molecule, indicating a strong tendency for them to form H-bonds with their own kind. Interspecies interactions between glucose and urea are more pronounced than interactions involving water. Glucose molecules exhibit a notable preference for binding with urea, while urea, in turn, shows a higher affinity for glucose over water. This preference for cross-species interactions may be attributed to the specific molecular structures and functionalities of glucose and urea, which complement each other in forming stable hydrogen bonds. Conversely, water molecules tend to interact more frequently with urea compared to glucose. This disparity in water interactions can be attributed to the differences in molecular sizes and polarities between glucose and urea. Water molecules find more favorable H-bonding partners in urea, leading to an enhanced tendency for water-urea interactions.

4.3.3 Continuous hydrogen bond relaxation functions ($S_{HB}(t)$)

In a liquid system containing molecules that can form H-bonds, the interactions between hydrogen bond donors and acceptors are dynamic and constantly changing. H-bonds can transiently form and break, influencing the overall structural and dynamical properties of the system. The continuous hydrogen bond relaxation functions ($S_{HB}(t)$) capture the temporal behaviour of these fluctuations and provide a comprehensive view of the H-bond dynamics and can be calculated as follows:[77–79]

$$S_{HB}(t) = \frac{\langle h(0)H(t)\rangle}{\langle h\rangle}, \tag{4.2}$$

where the function $h(t)$ signifies whether a specific pair of molecules is hydrogen-bonded or not at a given time. When the molecules are hydrogen-bonded, $h(t) = 1$; otherwise, it is 0. The function $H(t)$ indicates whether this pair of molecules stays hydrogen-bonded without interruption for a duration of time t. If they remain bonded, $H(t)$ is 1; otherwise, it becomes 0. The function $S_{HB}(t)$ represents the likelihood that the same pair of molecules remains hydrogen bonded for a certain duration t. As time progresses and the continuity of the hydrogen bond diminishes, $S_{HB}(t)$ approaches zero.

The average relaxation time is calculated from the relaxation functions by integrating the decay functions ($S_{HB}(t)$), $\langle \tau^{HB} \rangle = \int_0^\infty S_{HB}(t)dt$. This $\langle \tau^{HB} \rangle$ gives an estimate of the typical duration for which a H-bond persists before undergoing a significant change or breakage. A shorter average relaxation time implies faster dynamics, indicating that the H-bonds are more prone to fluctuations and reformation. On the other hand, a longer average relaxation time suggests more stable H-bonds with slower relaxation dynamics.

Figure 4.5 illustrates the average continuous hydrogen bond relaxation times at various temperatures. Different kinds of H- bonds are taken into consideration depending on their donor and acceptor species. It is evident that all types of H-bonds exhibit faster relaxation at higher temperatures, irrespective of their identity. This decrease in relaxation times is attributed to the increased thermal motion at higher temperatures. Figure 4.A.5(a) shows the lifetimes of glucose-glucose, urea-urea and water-water H-bonds. Here, urea-urea H-bond possesses the longest relaxation time, followed by glucose-glucose and water-water relaxation times. This observation suggests that urea-urea H-bonds persist for longer duration than the other intra-species H-bonds. Figure 4.A.5(b-d) represent H-bond relaxation times of various interspecies interactions. Among the studied interactions, glucose (donor)-urea (acceptor) H-bonds exhibit the longest relaxation times, followed by glucose (donor)-water (acceptor) interactions, and then urea (donor)-glucose (acceptor) H-bonds.

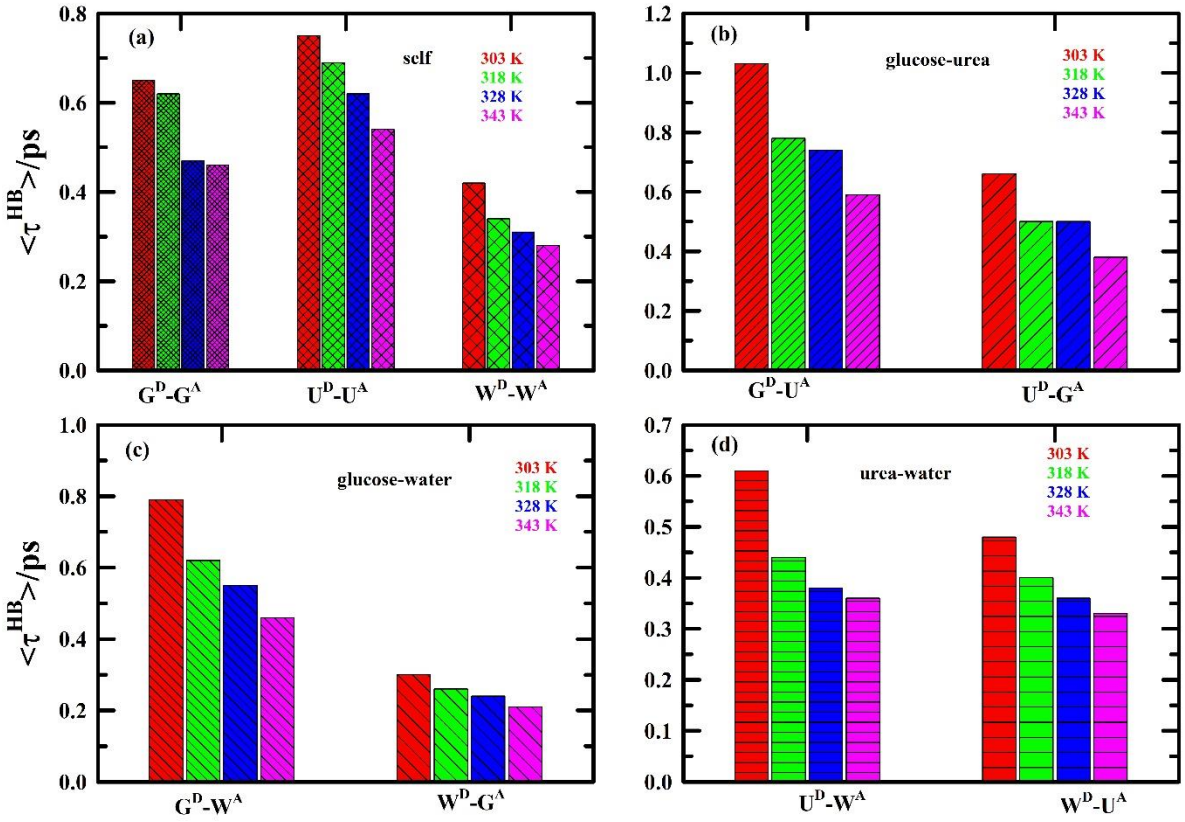

Figure 4.5: Average continuous hydrogen bond relaxation times at various temperatures, with each temperature represented by a distinct colour. Different panels display different types of hydrogen bond interactions: (a) self or intraspecies interactions, (b) glucose-urea interactions, (c) glucose-water interactions, and (d) urea-water interactions. The labels 'D' and 'A' indicate the hydrogen bond 'donor' and 'acceptor,' respectively.

Subsequently, the relaxation times decrease further for urea (donor)-water (acceptor) and water (donor)-urea (acceptor) H-bonds, with water (donor)-glucose (acceptor) H-bonds showing the shortest relaxation times. The longer relaxation times observed for glucose-donor to urea-acceptor hydrogen bonds compared to the other ones may be explained by assuming that the donor hydroxyl group of glucose and the acceptor carbonyl group of urea probably form a favourable bond geometry, thereby rendering longer persistent time. A longer relaxation time observed for glucose-donor to water-acceptor H-bond may also be explained in terms of favourable bonding geometry.

The shortest relaxation times are observed for water-donor to urea-acceptor and water-donor to glucose-acceptor H-bonds. Due to their smaller size, water molecules facilitate easier

rotation and readily form and break hydrogen bonds with neighboring acceptors. These dynamic interactions contribute to relatively faster relaxation times for these hydrogen bonds.

4.3.4 Structural hydrogen bond relaxation functions ($C_{HB}(t)$)

Another way to investigate the hydrogen bond dynamics of a system is to calculate structural hydrogen bond relaxation functions and their corresponding timescales. These timescales essentially represent the time needed for the formation and breakage of intermolecular H-bonds. These correlation functions are calculated using the following formula,[76,77,80]

$$C_{HB}(t) = \frac{\langle h(0)h(t)\rangle}{\langle h\rangle} \tag{4.3}$$

where, the function $h(t)$ signifies whether a specific pair of molecules is hydrogen-bonded or not at a given time. When the molecules are hydrogen-bonded, $h(t) = 1$; otherwise, it is 0. We have calculated $C_{HB}(t)$ at two representative temperatures (303 K and 343 K). The decay functions are shown in Figure 4.6 and corresponding fit parameters are enumerated in Table 4.A.6. Note that here we have considered only intraspecies H-bond interactions. The time correlations are calculated for H-bonds that are formed between the same type of molecules.

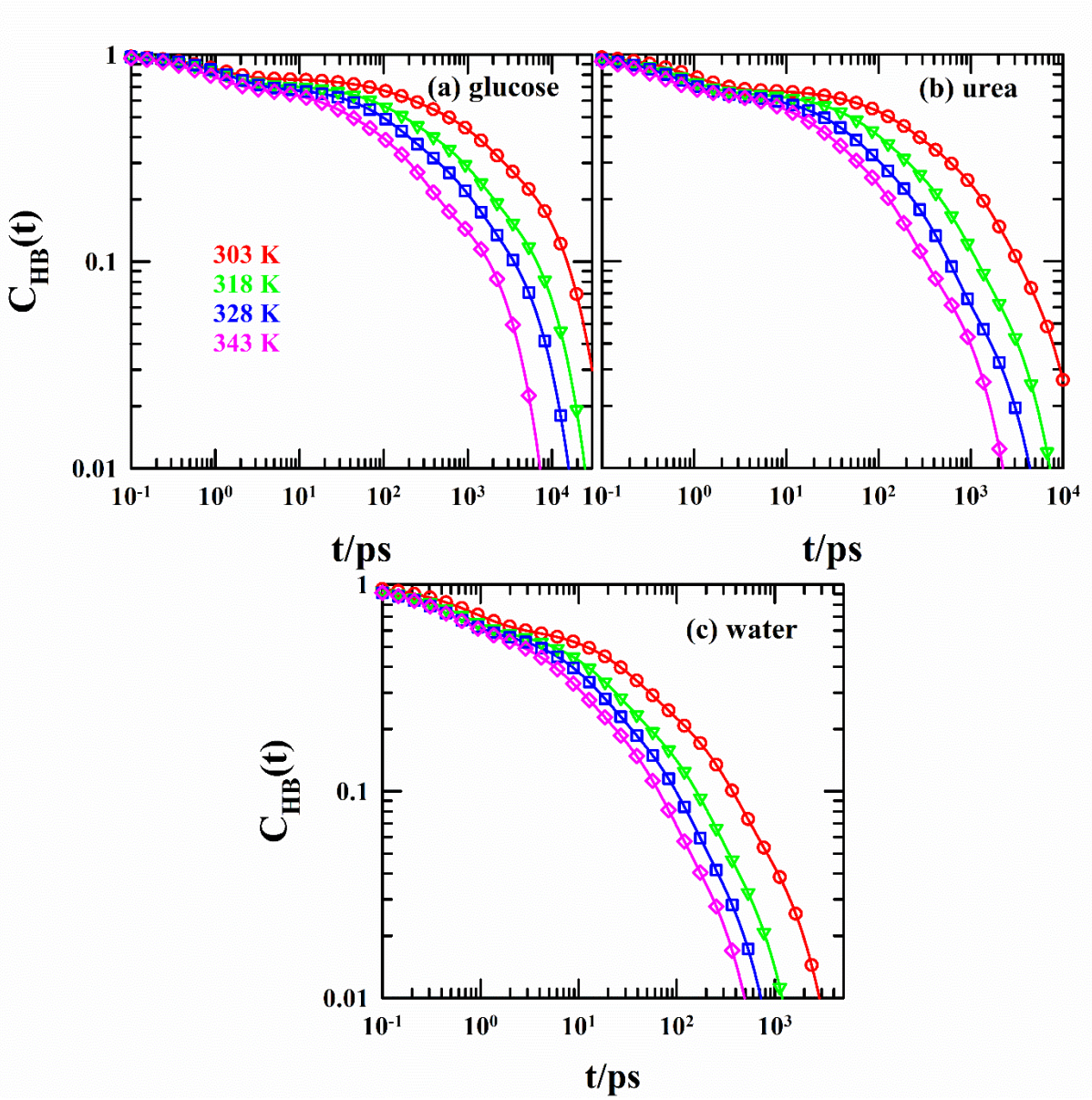

Figure 4.6: Structural decay functions of intermolecular H-bonds formed by self-interactions between glucose, urea and water molecules at 303 K (left panel), 343 K (right panel). Each type of H-bond is uniquely color-coded. The open symbols indicate calculated data points whereas the lines going through them indicate multi-exponential fits.

Table 4.A.6 illustrates notable differences in H-bond relaxation times among glucose, urea, and water. Specifically, the H-bond relaxation time of glucose is approximately 10 times slower than that of water, with urea falling in between. Interestingly, transitioning from 303 K to 343 K – the relaxation times for all species accelerate by approximately six to eight-folds. This can be explained in terms of the distinct molecular structures of glucose, urea, and water. The complex structure of glucose likely contributes to its slower H-bond relaxation, while

intermediate structure of urea aligns with its intermediate relaxation time. The monotonic decrease in relaxation times with temperature can be attributed to the heightened thermal energy at higher temperatures, facilitating more rapid molecular motion and, consequently, faster H-bond dynamics.

4.3.5 Calculation of dielectric relaxation spectra and component wise decomposition

Temperature-dependent dielectric relaxation spectra were calculated from MD simulation trajectories to gain molecular insights into the over-all or total frequency dependent dielectric spectra that are measured in experiments. The dielectric function, expressed as $\varepsilon(\omega)$ in Eq. (4.3), represents the frequency-dependent behaviour of the system. The frequency-dependent dielectric function can be expressed as,[81,82]

$$\varepsilon(\omega) - 1 = \frac{1}{3\epsilon_0 V k_B T}\{\langle \boldsymbol{M}(0)^2\rangle + i\omega\mathcal{L}[\langle \boldsymbol{M}(0).\boldsymbol{M}(t)\rangle]\} \quad (4.4)$$

Where $\boldsymbol{M}(t) = \sum_i \boldsymbol{\mu}_i(t)$ indicates the total collective dipole moment and sums over the individual molecular dipole moments. V, k_B, and T are volume of the system, the Boltzmann constant and the absolute temperature, respectively. Angular brackets represent ensemble average, and $\mathcal{L}$ denotes Fourier-Laplace transformation.

Subsequently, decomposition of the total spectra provided the individual contributions from various self- and cross-interactions. In this multi-component system, the dipole moment $\boldsymbol{M}$ was separated into distinct components for glucose, urea, and water. The cross-correlation terms between these components were calculated to account for their contributions:[83–87]

$$\langle \boldsymbol{M}(0).\boldsymbol{M}(t)\rangle = \langle \boldsymbol{M}_G(0).\boldsymbol{M}_G(t)\rangle + \langle \boldsymbol{M}_U(0).\boldsymbol{M}_U(t)\rangle + \langle \boldsymbol{M}_W(0).\boldsymbol{M}_W(t)\rangle$$
$$+2\langle \boldsymbol{M}_G(0).\boldsymbol{M}_U(t)\rangle + 2\langle \boldsymbol{M}_G(0).\boldsymbol{M}_W(t)\rangle + 2\langle \boldsymbol{M}_U(0).\boldsymbol{M}_W(t)\rangle\,, \quad (4.5)$$

where the indices *G*, *U*, *W* stand for glucose, urea and water, respectively.

In Eq. 4.5, the cross-correlation terms were assumed to be given by, $\langle \boldsymbol{M}_i(0).\boldsymbol{M}_j(t)\rangle = \frac{1}{2}\big(\langle \boldsymbol{M}_i(0).\boldsymbol{M}_j(t)\rangle + \boldsymbol{M}_j(0).\boldsymbol{M}_i(t)\big)$, where $i, j = G, U, W$.

Following this prescription, the total $\varepsilon(\omega)$ may then be expressed as a sum of individual component contributions.

$$\varepsilon(\omega) = 1 + \varepsilon_{GG}(\omega) + \varepsilon_{UU}(\omega) + \varepsilon_{WW}(\omega) + 2\varepsilon_{GU}(\omega) + 2\varepsilon_{GW}(\omega) + 2\varepsilon_{UW}(\omega) \quad (4.6)$$

where $\varepsilon_{ij}(\omega) = \frac{1}{3\epsilon_0 V k_B T}\{\langle \boldsymbol{M}_i(0)\boldsymbol{M}_j(0)\rangle + i\omega\mathcal{L}[\langle \boldsymbol{M}_i(0).\boldsymbol{M}_j(t)\rangle]\}$.

The simulated time-correlation functions were fitted with multi-exponential terms and, these fit functions were used to obtain the frequency-dependent dielectric functions:

$$\langle \boldsymbol{M}_i(0).\boldsymbol{M}_j(t)\rangle = \sum_k A_k.e^{-t/\tau_k} \quad (4.7)$$

Such fit functions along with fit parameters were then used to obtain the frequency dependent dielectric relaxation spectra and are shown in Figure 4.6.

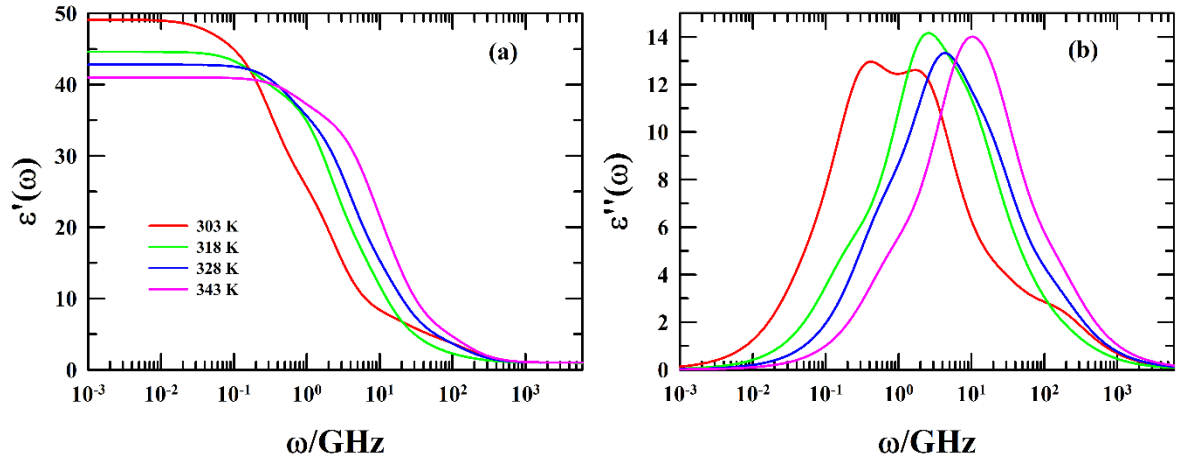

Figure 4.7: Temperature dependence of the dielectric relaxation spectra of glucose-urea-water DES: (a) frequency-dependent real component, $\varepsilon'(\omega)$ and (b) the imaginary component, $\varepsilon''(\omega)$.

In Figure 4.7(a), the real part of the dielectric spectra is presented, showing the effects of temperature on the static dielectric constant. Notice that the static dielectric constant decreases with an increase in solution temperature. This decrement in static dielectric constant can be viewed as a result of mitigation of correlations between molecular dipoles. Hydrogen bonding can strongly influence the arrangement of dipoles.[88] Therefore, in Figure 4.A.2 we show the correlation between static dielectric constant and the total number of hydrogen bonds at different temperatures. This indicates that from lower to higher temperatures both the static dielectric constant and total number of H-bonds decrease. Hence, we can infer that the H-bond network is getting disturbed by increasing temperature and eventually randomizing dipoles to cause a reduction of static dielectric constant.

In Figure 4.7(b) we investigate the temperature dependence of the imaginary components of the frequency-dependent dielectric relaxation spectra (DRS). Here, the relaxation peaks of the spectra shift towards higher frequencies upon increasing temperature, indicating faster relaxations at elevated temperatures. The timescales of different relaxation processes at various temperatures are shown in Figure 4.8. Various dielectric properties at these temperatures are summarized in Table 4.A.7.

Figure 4.7 and Table 4.A.7 indicate the presence of at least four distinct relaxation processes at each temperature. The slowest timescale (τ_1) is ~20 ns at 303 K and becomes ~1.5 ns at 343 K whereas τ_2 decreases from ~3 ns to 150 ps. The third timescale (τ_3) appears to be only exclusive to the two lowest temperatures (303 K and 318 K). At higher temperatures, this relaxation time may be getting merged to the fastest timescale (τ_4). The τ_4 timescale (~6 ps) remains almost invariant with temperature. Now we attempt to explore the possible origins of these timescales. From a previous study[25] we have calculated molecular rotation times from the Stokes-Einstein-Debye (SED) relation using measured viscosity values. The rotation times of glucose, urea, and water are shown in Table 4.A.8. It can be observed that these rotational times are many times slower than the simulated dielectric relaxation times. However, if we consider the viscosity decoupling then nonhydrodynamic movements like angular jump can facilitate such shorter DR timescales. Nevertheless, the dielectric response of such complex phenomena is essentially an overlap of many individual relaxations.

One effective approach to handle this is comparing individual spectra with the overall relaxation spectra and carefully analyze how each process contributes to different parts of the total relaxation spectra. For this purpose, we have plotted individual spectra as well as the total spectra in Figure 4.9 to comprehend the relaxation peaks in a better way. The corresponding relaxation parameters are summarized in Tables 4.A.9-4.A.12. From these Figures and Tables, it is evident that the most significant contributions arise from self-interactions between urea molecules and cross-interactions between glucose and urea molecules. These observations are supported by the relatively higher abundance of urea in the system and the presence of strong urea-glucose interactions. The manifestation of these interactions in the dielectric relaxation processes is consistent with our previous analyses.

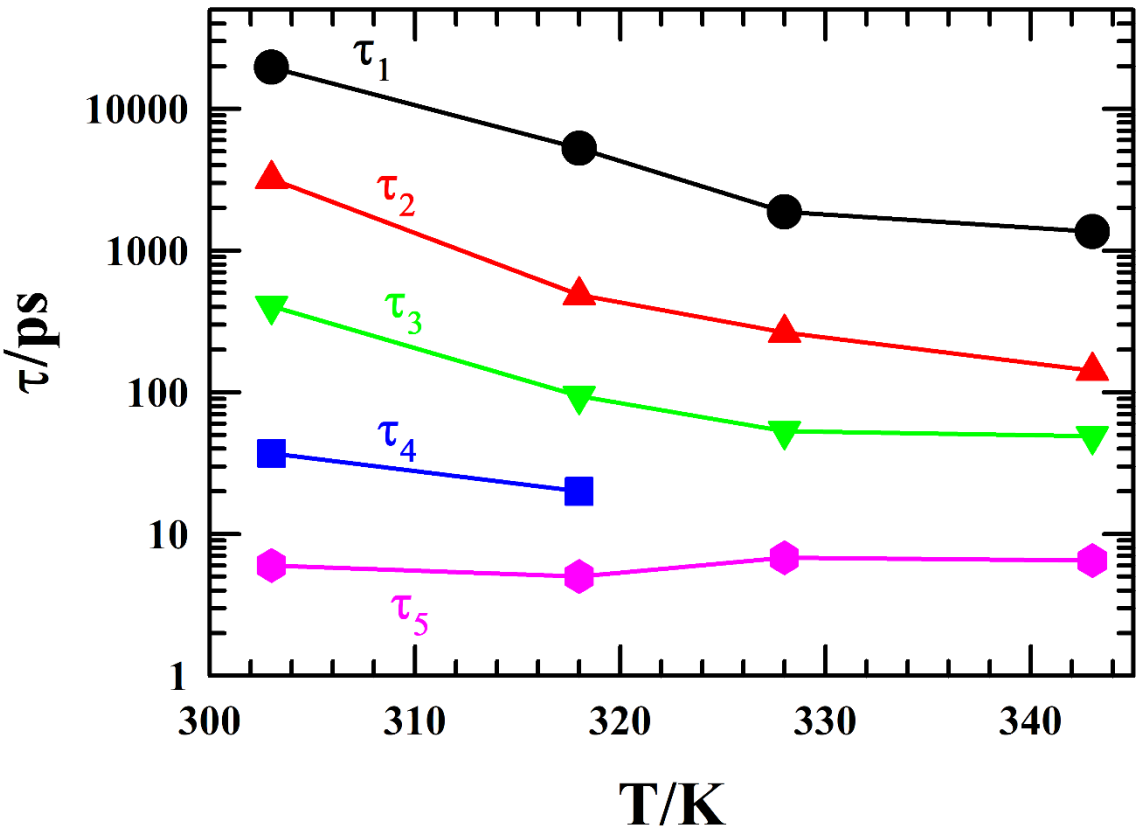

Figure 4.8: Temperature-dependent relaxation timescales observed in the NADES. The solid symbols represent the relaxation times and the lines going through them are only guides to bare eyes.

A careful analysis of Tables 4.A.9-4.A.12 reveals the relaxation times of various inter and intraspecies interactions and, we can see the resemblance of them with the relaxation times of the total DRS. For the first timescale (τ_1) if we can infer that this is nearly identical to the relaxation times of dipolar rotation of glucose molecules and, this trend is persistent with all the temperatures. Along with that other cross-interactions involving glucose (glucose-urea and glucose-water) also relax more or less in the same range. Therefore, it can be inferred that this timescale is principally the relaxation times associated with the dielectric response of glucose molecules. The second timescale (τ_2) can be qualitatively assigned to the relaxation of self- and cross-interactions of urea molecules. The third timescale (τ_3) contains the contributions of more or less all self- and cross-interactions. The self-interactions of glucose, urea, water and,

cand cross-interactions between glucose and water generate a few picosecond timescales which are similar to the fourth timescale (τ_4).

In Figure 4.9, if we examine the relaxation contributions arising from intra-species interactions (for example, glucose-glucose, urea-urea and water-water), we can see that the peaks shift from lower to higher frequency from glucose to urea to water. This suggests that glucose molecules need more time to relax compared to urea and water. This trend in relaxation times corroborates the size and the number of intra-species interaction sites of these molecules. Glucose, being the bulkiest with the largest number of interaction sites among the three different species in this DES, requires more time to orient themselves, whereas water molecules, the smallest among them, rotate most swiftly. At 303 K, there are two distinct peaks of equal amplitudes (see Figure 4.9(a)). The principal contribution to the peak at lower frequency is coming from the dipolar rotation of glucose molecules whereas the urea molecules mainly contribute to the peak at higher frequency. At other temperatures, only one principal peak is found which appears mainly around the relaxation peak of urea molecules. It is evident that no individual interaction is solely responsible for the timescales found in the total dielectric relaxation spectrum; instead, these individual spectra collectively contribute to form the overall spectrum.

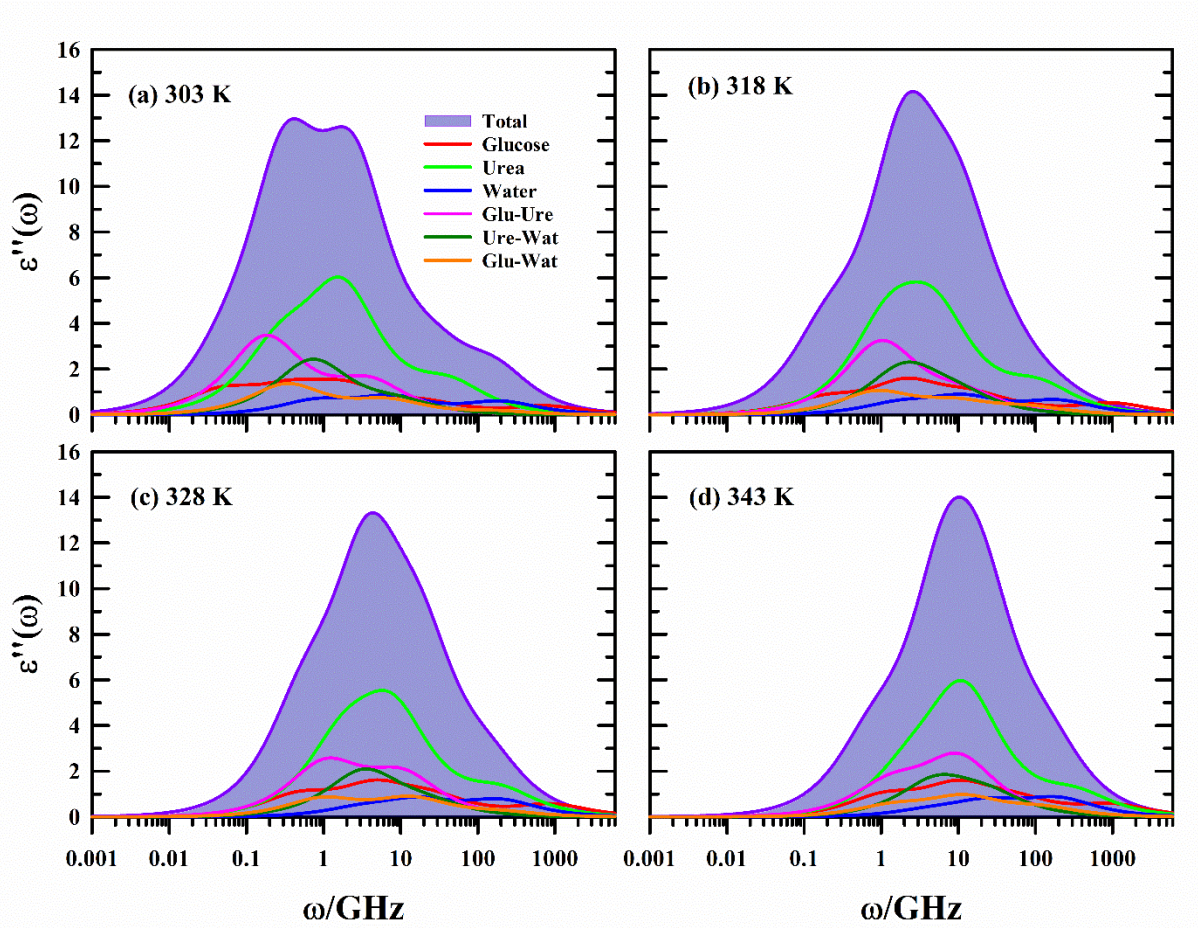

Figure 4.9: Deconvolution of dielectric loss spectrum at different temperatures. Each type of contribution is distinctly color-defined.

Dielectric relaxation times are closely related to structural hydrogen bond relaxation times. The rotation of dipolar molecules is directly influenced by the breaking and formation of H-bonds, establishing a connection to structural H-bond relaxation times.[59,89] The structural H-bond relaxation times are enumerated in Table 4.A.6 and, DR timescales of individual components can be found in Tables 4.A.9-4. A.12. A qualitative comparison of these relaxation times reveals a striking similarity between the timescales of hydrogen bond relaxation and dielectric relaxation. For glucose the slowest two H-bond relaxation times (τ_1 and τ_2) range from approximately 12 nanoseconds to 2 nanoseconds and about 1 nanosecond to 180 picoseconds, respectively. Interestingly, these timescales closely resemble the corresponding dielectric relaxation times (approximately 20 nanoseconds to 1 nanosecond and about 3 nanoseconds to 100 picoseconds). Furthermore, the other two timescales (τ_3 and τ_4) also align closely with dielectric relaxation times. This pattern of correlation between structural hydrogen bond relaxation times and dielectric relaxation times holds for urea and water as well. The strong

agreement observed between hydrogen bond relaxation times and dielectric relaxation times validates the interpretation of dielectric relaxation timescales as representing the continuous rearrangement of the hydrogen bond network within the system.

Therefore, the comprehensive analysis of the DR spectrum leads to a definitive conclusion that the observed overall timescales cannot be solely attributed to any individual relaxation process within the system. Instead, these timescales arise as a collective outcome of multiple relaxation processes that intricately interact and combine to form the resultant spectrum. The intricate interplay of molecular interactions and dynamics contributes to the complexity of the DR spectrum, where the individual relaxation processes of various species collaboratively contribute to the observed relaxation behavior.

4.4 Conclusion

In summary, this study investigated a glucose-based naturally abundant deep eutectic solvent (NADES) using classical molecular dynamics simulations. Valuable insights were gained towards the understanding of structural and dynamic aspects of this complex system. The investigation of real-space pair correlations, as shown in the RDFs, provided a vivid picture of the molecular interactions within the NADES. Notably, the RDFs highlighted that the extent of molecular interactions was linked to the sizes of the interacting species. This was evident in the diverse interaction lengths for different species pairs, where water-water interactions manifested over shorter distances, while glucose-glucose interactions extended to longer distances. This finding was reinforced through the three-dimensional spatial arrangements of the species, quantified by the SDFs. The correlation between these distributions and RDFs emphasized the significance of size in dictating the nature of interactions. Further insight was obtained through an exploration of hydrogen bonding analysis, a fundamental aspect of molecular interactions. The temperature-induced changes in RDFs between hydrogen bonding sites unveiled a subtle decrease in these interactions as temperature increased. Interestingly, the preference for self-interactions within species was evident, with glucose demonstrating the highest propensity for forming hydrogen bonds, while water exhibited the lowest. The dynamic nature of hydrogen bonds was revealed through the computation of hydrogen bond lifetimes. The lifespan of these bonds is a crucial parameter to quantify the strength of H-bond interactions. These relaxation times exhibited a consistent trend of decreasing with increasing temperature. Hydrogen bonds, primarily involving urea-urea, glucose-urea, and glucose-

glucose interactions were found to be remarkably persistent compared to others. These stable bonds contributed to the overall stability of the NADES structure. The dielectric relaxation (DR) spectra provided valuable insights into the temporal aspects of the NADES behavior. The multiple Debye relaxation processes that underlie the spectra unveiled a complex interplay of molecular motions within the system. Notably, the relaxation timescales exhibited a consistent decrease as the temperature rose. This observation was indicative of the heightened molecular mobility induced by thermal energy. The origin of the relaxation timescales was unveiled through a thorough comparison of individual spectra with the total relaxation spectrum. This analysis highlighted that the relaxation processes were not simply attributed to the contributions of individual species, but rather resulted from a synergy of diverse relaxation phenomena. The broader relaxation spectrum was a harmonious blend of various relaxation processes. Through different temperatures, the DR timescales bear strong signatures of structural H-bond relaxation phenomena indicating the connection between these two processes. Note that the selection of an appropriate force field is a pivotal aspect of this study. Given that glucose and urea do not naturally exist in a liquid state at the studied temperature, the choice of force field was a nuanced decision. This underscored the intricate nature of simulation-based investigations and the importance of ensuring the chosen models accurately represent the real-world system.

Finally, we provided a comprehensive exploration of the structural and dynamical aspects of glucose-based NADES using molecular dynamics simulations. These findings shed light on the temperature-dependent behaviors, revealing size-dependent interactions, hydrogen bonding propensities, and complex relaxation dynamics. This molecular-level insight can be useful in studying the inherent interaction and dynamics of such systems.

Appendix 4.A

$$E = \sum_{bonds} k_b\,(b - b_0)^2 + \sum_{angles} k_\theta(\theta - \theta_0)^2 + \sum_{\substack{improper \\ dihedrals}} k_\varphi(\varphi - \varphi_0)^2 + \sum_{dihedrals} \sum_{n=1}^{6} k_{\emptyset,n}\,(1 + \cos(n\emptyset - \delta_n) + \sum_{\substack{nonbonded \\ pair\ i,j}} \sqrt{\varepsilon_i \varepsilon_j}\left[\left(\frac{(\sigma_i+\sigma_j)}{2R_{ij}}\right)^{12} - 2\left(\frac{(\sigma_i+\sigma_j)}{2R_{ij}}\right)^{6}\right] + \sum_{\substack{nonbonded \\ pair\ i,j}} \frac{q_i q_j}{4\pi D R_{ij}} \quad (4.A.1)$$

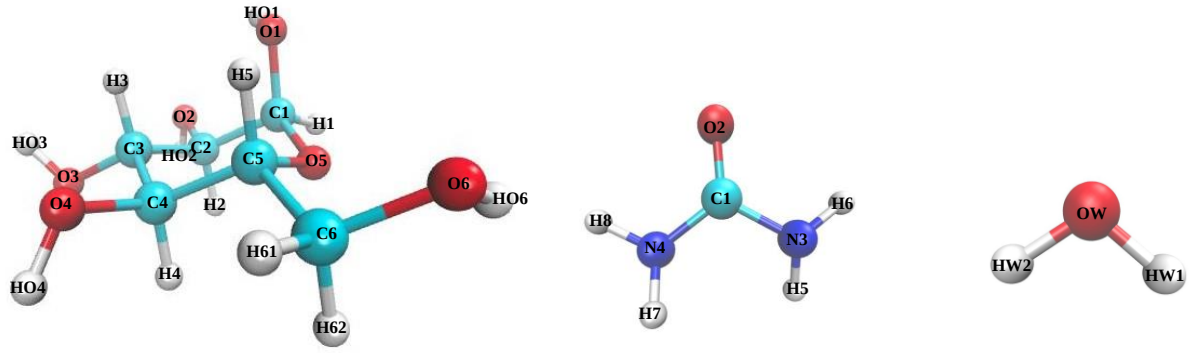

(a) glucose **(b) urea** **(c) water**

Figure 4.A.1: Representation of molecular structures of (a) glucose, (b) urea and (c) water. Atom names are shown as they are used in simulations. Different type of atoms is indicated with different colors: carbon → cyan, oxygen → red, nitrogen → blue, hydrogen → white.

Table 4.A.1: Non-bonding parameters of atoms in glucose.

Atom	q **(e)**	σ **(nm)**	ε **(kJ/mol)**
C1	0.34	0.3564	0.13389
H1	0.09	0.2388	0.18828
O1	-0.65	0.3145	0.80375
HO1	0.42	0.0400	0.19246
C5	0.11	0.3564	0.13389
H5	0.09	0.2388	0.18828
O5	-0.4	0.2940	0.41840
C2	0.14	0.3564	0.13389
H2	0.09	0.2388	0.18828
O2	-0.65	0.3145	0.80375
HO2	0.42	0.0400	0.19246
C3	0.14	0.3564	0.13389
H3	0.09	0.2388	0.18828
O3	-0.65	0.3145	0.80375
HO3	0.42	0.0400	0.19246
C4	0.14	0.3564	0.13389
H4	0.09	0.2388	0.18828
O4	-0.65	0.3145	0.80375
HO4	0.42	0.0400	0.19246
C6	0.05	0.3581	0.23430
H61	0.09	0.2388	0.14644
H62	0.09	0.2388	0.14644
O6	-0.65	0.3145	0.80375
HO6	0.42	0.0400	0.19246

Table 4.A.2: Non-bonding parameters of atoms in urea.

Atom	q (e)	σ (nm)	ε (kJ/mol)
C1	0.597	0.3564	0.29288
O2	-0.579	0.3029	0.50208
N3	-0.689	0.3296	0.83680
N4	-0.689	0.3296	0.83680
H5	0.34	0.0400	0.19246
H6	0.34	0.0400	0.19246
H7	0.34	0.0400	0.19246
H8	0.34	0.0400	0.19246

Table 4.A.3: Non-bonding parameters of atoms in water.

Atom	q (e)	σ (nm)	ε (kJ/mol)
OW	-0.834	0.3151	0.63639
HW1	0.417	0.0400	0.19246
HW2	0.417	0.0400	0.19246

Table 4.A.4: Comparison of temperature-dependent density (simulation vs experiment).

T (K)	Density (g/cm^3)		% deviation
	simulation	experiment	
303	1.379	1.380	0.07
318	1.368	1.370	0.14
323	1.361	1.363	0.15
343	1.348	1.353	0.37

Table 4.A.5: Number of inter- and intraspecies H-bonds at various temperatures.

Interaction	**Type of H-bond**	**No. of hydrogen bonds**			
		303 K	**318 K**	**328 K**	**343 K**
Glucose-glucose	O(G)-H(G)---O(G)	104.01	98.49	98.17	93.42
Glucose-urea	O(G)-H(G)---O(U)	105.00	102.30	102.63	100.14
	N(U)-H(U)---O(G)	172.41	168.58	166.45	158.47
Glucose-water	O(G)-H(G)---O(W)	61.20	61.00	59.46	57.74
	O(W)-H(W)---O(G)	70.38	69.08	67.41	66.24
Urea-urea	N(U)-H(U)---O(U)	138.92	136.90	135.08	132.46
Urea-water	N(U)-H(U)---O(W)	76.22	73.05	74.17	71.20
	O(W)-H(W)---O(U)	77.89	66.31	65.94	62.89
Water-water	O(W)-H(W)---O(W)	43.78	42.62	41.62	40.01
Total		849.81	818.33	810.93	782.57

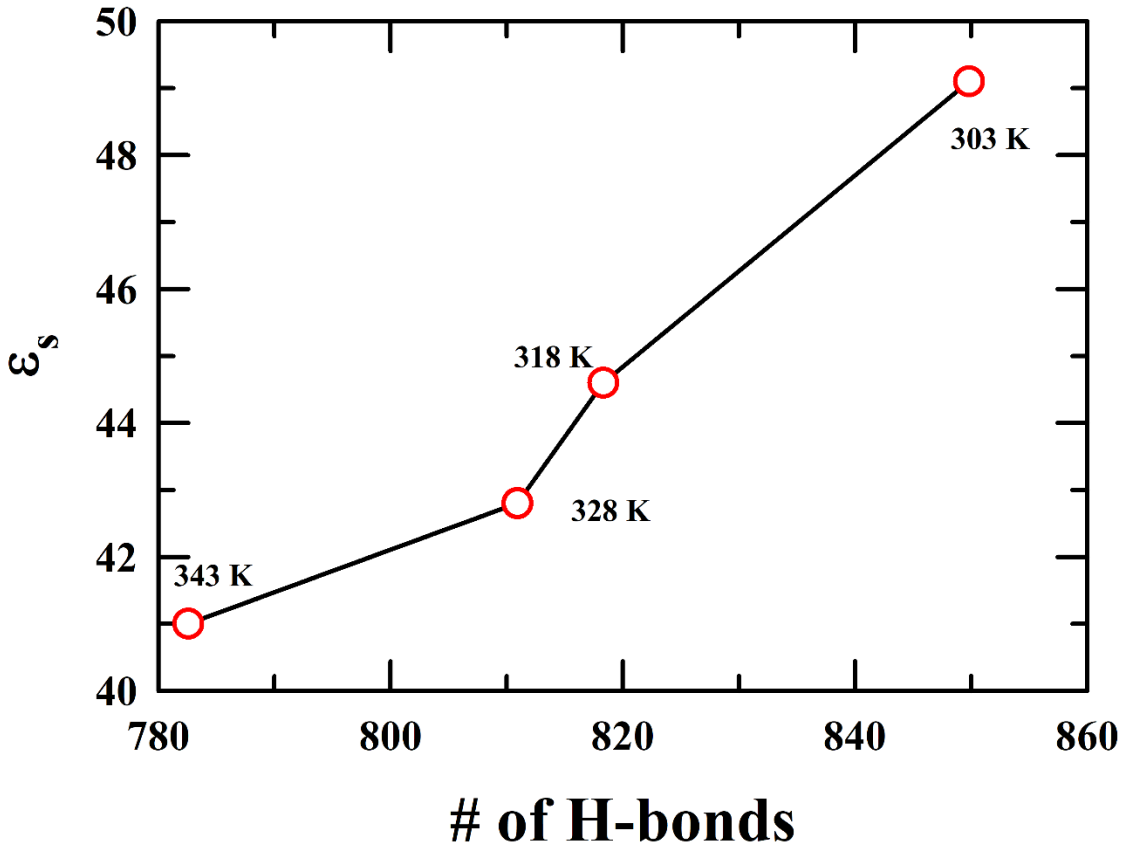

Figure 4.A.2: Dependence of the static dielectric constant (ε_s) on the total number of H-bonds present in the system.

Table 4.A.6: Multi-exponential fit parameters ($\sum_k a_k exp(-t/\tau_k)$) to the structural hydrogen bond autocorrelation function ($C_{HB}(t)$).

glucose-glucose									
T/K	a_1	τ_1 (ps)	a_2	τ_2 (ps)	a_3	τ_3 (ps)	a_4	τ_4 (ps)	$open-angle\langle\tau\rangle$ (ps)
303	0.34	12322	0.29	1140	0.14	141	0.23	1	4540
318	0.23	7870	0.28	817	0.21	119	0.27	1.2	2085
328	0.19	5370	0.24	671	0.27	103	0.30	1.3	1210
343	0.21	2373	0.33	180	0.16	27	0.30	0.8	562
urea-urea									
303	0.16	5574	0.28	993	0.24	142	0.32	0.9	1204
318	0.12	2916	0.28	442	0.26	72	0.34	0.7	493
328	0.09	1994	0.28	271	0.28	42	0.35	0.6	267
343	0.12	900	0.31	110	0.24	18	0.33	0.4	147
water-water									
303	0.09	1297	0.23	189	0.31	26	0.37	0.7	168
318	0.08	574	0.21	95	0.33	14	0.38	0.5	71
328	0.08	348	0.21	59	0.33	10	0.38	0.4	44
343	0.08	237	0.23	37	0.32	6	0.37	0.4	30

Table 4.A.7: Temperature-dependent dielectric relaxation parameters obtained from Figure 1*.

T (K)	ε_s	$\Delta\varepsilon_1$	τ_1 (ps)	$\Delta\varepsilon_2$	τ_2 (ps)	$\Delta\varepsilon_3$	τ_3 (ps)	$\Delta\varepsilon_4$	τ_4 (ps)	$\Delta\varepsilon_5$	τ_5 (ps)	$\langle\tau\rangle$ (ps)
303	49.1	2.89	19623	19.72	3197	18.76	406	3.37	37	3.37	6	2650
318	44.6	5.67	5260	21.8	486	13.1	94	2.2	20	0.87	5	956
328	42.8	7.52	1875	20.04	264	10.87	53			3.34	6.8	478
343	41.0	5.20	1359	17.59	142	12.8	49			4.4	6.5	256

*Fit parameters are according to the eqn. $\varepsilon(\omega) = \varepsilon_\infty + \sum_k \frac{\Delta\varepsilon_k}{1+i\omega\tau_k}$ where $\varepsilon_\infty = 1$ and $\varepsilon_s = \varepsilon_\infty + \sum_k \Delta\varepsilon_k$

Table 4.A.8: Hydrodynamic molecular rotation times for water, urea and glucose at different temperatures calculated using the SED relation with stick boundary condition, $\tau_r = 3\eta V/k_B T$. The van der Waals volumes of water, urea and glucose used here are calculated from a previous work.[90] Viscosity values are taken from Ref. 25.

T/K	τ_r^{glu} (ns)	τ_r^{ure} (ns)	τ_r^{wat} (ns)
318	63.12	21.04	6.62
328	27.38	9.13	2.87
343	9.86	3.28	1.04

Table 4.A.9: Dielectric relaxation parameters of total spectrum as well as individual spectra at 303 K.

Component	$\varepsilon_s - 1$	$\Delta\varepsilon_1$	τ_1 (ps)	$\Delta\varepsilon_2$	τ_2 (ps)	$\Delta\varepsilon_3$	τ_3 (ps)	$\Delta\varepsilon_4$	τ_4 (ps)	$\Delta\varepsilon_5$	τ_5 (ps)
Total	48.1	2.89	19623	19.72	3197	18.76	406	3.37	37	3.37	6
glucose	7.41	1.93	20773	1.78	2678	2.07	507	0.89	46	0.74	1.3
urea	17.78			4.98	3779	10.31	570	2.49	23		
water	3.66			1.13	1280	1.43	129			1.10	5
glucose-urea	9.47			6.72	5667	2.75	252				
urea-water	5.69			4.72	1389	0.97	104				
glucose-water	4.09			2.62	3002	1.19	145			0.29	6

Table 4.A.10: Dielectric relaxation parameters of total spectrum as well as individual spectra at 318 K.

Component	$\varepsilon_s - 1$	$\Delta\varepsilon_1$	τ_1 (ps)	$\Delta\varepsilon_2$	τ_2 (ps)	$\Delta\varepsilon_3$	τ_3 (ps)	$\Delta\varepsilon_4$	τ_4 (ps)	$\Delta\varepsilon_5$	τ_5 (ps)
Total	43.6	5.67	5260	21.8	486	13.1	94	2.2	20	0.87	5
glucose	6.45	1.29	5351	2.58	475	1.35	67	0.26	16	0.97	1
urea	16.83	6.90	814	7.57	199					2.36	9
water	3.57	0.86	607			1.43	87			1.28	5
glucose-urea	7.82	6.26	1002			1.56	82				
urea-water	5.36			4.07	486	1.29	100				
glucose-water	3.52	1.94	1166			0.98	107			0.59	12

Table 4.A.11: Dielectric relaxation parameters of total spectrum as well as individual spectra at 328 K.

Component	$\varepsilon_s - 1$	$\Delta\varepsilon_1$	τ_1 (ps)	$\Delta\varepsilon_2$	τ_2 (ps)	$\Delta\varepsilon_3$	τ_3 (ps)	$\Delta\varepsilon_4$	τ_4 (ps)
Total	41.8	7.52	1875	20.04	264	10.87	53	3.34	6.8
glucose	6.56	1.70	2174	2.43	214	1.38	37	1.05	1.1
urea	15.85	5.55	564	8.24	126			2.06	5
water	3.27	0.62	341			1.31	61	1.34	5
glucose-urea	7.82	4.46	960			3.36	93		
urea-water	4.81			3.94	299	0.86	43		
glucose-water	3.45	1.52	1060			1.55	72	0.38	5

Table 4.A.12: Dielectric relaxation parameters of total spectrum as well as individual spectra at 343 K.

Component	$\varepsilon_s - 1$	$\Delta\varepsilon_1$	τ_1 (ps)	$\Delta\varepsilon_2$	τ_2 (ps)	$\Delta\varepsilon_3$	τ_3 (ps)	$\Delta\varepsilon_4$	τ_4 (ps)	$\Delta\varepsilon_5$	τ_5 (ps)
Total	40.0	5.20	1359	17.59	142	12.8	49			4.4	6.5
glucose	6.24	1.62	948	2.5	97			1.12	16	1.0	1
urea	15.38	2.77	451	10.77	86					1.84	3
water	3.08	0.43	246			1.17	45			1.48	5
glucose-urea	7.48	2.54	790	4.94	97						
urea-water	4.58			3.02	191	1.56	40				
glucose-water	3.20	0.86	729	1.63	85					0.70	8

References

1 A. P. Abbott, D. Boothby, G. Capper, D. L. Davies and R. K. Rasheed, *J. Am. Chem. Soc.*, 2004, **126**, 9142–9147.

2 M. Francisco, A. van den Bruinhorst and M. C. Kroon, *Angew. Chem. Int. Ed.*, 2013, **52**, 3074–3085.

3 D. V. Wagle, H. Zhao and G. A. Baker, *Acc. Chem. Res.*, 2014, **47**, 2299–2308.

4 Q. Zhang, K. De Oliveira Vigier, S. Royer and F. Jérôme, *Chem. Soc. Rev.*, 2012, **41**, 7108–7146.

5 B. Guchhait, S. Daschakraborty and R. Biswas, *J. Chem. Phys.*, 2012, **136**, 174503.

6 B. Guchhait, S. Das, S. Daschakraborty and R. Biswas, *J. Chem. Phys.*, 2014, **140**, 104514.

7 H. A. R. Gazi, B. Guchhait, S. Daschakraborty and R. Biswas, *Chem. Phys. Lett.*, 2011, **501**, 358–363.

8 B. Guchhait, H. A. R. Gazi, H. K. Kashyap and R. Biswas, *J. Phys. Chem. B*, 2010, **114**, 5066–5081.

9 E. L. Smith, A. P. Abbott and K. S. Ryder, *Chem. Rev.*, 2014, **114**, 11060–11082.

10 N. Winterton, *Clean Technol. Environ. Policy*, 2021, **23**, 2499–2522.

11 J. H. Clark and S. J. Tavener, *Org. Process Res. Dev.*, 2007, **11**, 149–155.

12 J. M. DeSimone, *Science (1979)*, 2002, **297**, 799–803.

13 Y. Dai, J. van Spronsen, G.-J. Witkamp, R. Verpoorte and Y. H. Choi, *Anal. Chim. Acta*, 2013, **766**, 61–68.

14 A. Paiva, R. Craveiro, I. Aroso, M. Martins, R. L. Reis and A. R. C. Duarte, *ACS Sustain. Chem. Eng.*, 2014, **2**, 1063–1071.

15 Y. Liu, J. B. Friesen, J. B. McAlpine, D. C. Lankin, S.-N. Chen and G. F. Pauli, *J. Nat. Prod.*, 2018, **81**, 679–690.

16 C. G. González, N. R. Mustafa, E. G. Wilson, R. Verpoorte and Y. H. Choi, *Flavour Fragr. J.*, 2018, **33**, 91–96.

17 M. Faggian, S. Sut, B. Perissutti, V. Baldan, I. Grabnar and S. Dall'Acqua, *Molecules*, 2016, **21**, 1531.

18 Y.-L. Chen, X. Zhang, T.-T. You and F. Xu, *Cellulose*, 2019, **26**, 205–213.

19 Y. H. Choi, J. van Spronsen, Y. Dai, M. Verberne, F. Hollmann, I. W. C. E. Arends, G.-J. Witkamp and R. Verpoorte, *Plant Physiol.*, 2011, **156**, 1701–1705.

20 W.-C. Huang, D. Zhao, N. Guo, C. Xue and X. Mao, *J. Agric. Food Chem.*, 2018, **66**, 11897–11901.

21 S. Gore, S. Baskaran and B. Koenig, *Green Chemistry*, 2011, **13**, 1009.

22 M. Espino, M. de los Ángeles Fernández, F. J. V. Gomez and M. F. Silva, *TrAC, Trends Anal. Chem.*, 2016, **76**, 126–136.

23 Z. Yang, in *Deep Eutectic Solvents*, Wiley, 2019, pp. 43–60.

24 E. Tarif, J. Mondal and R. Biswas, *J. Mol. Liq.*, 2020, **303**, 112451.

25 E. Tarif, J. Mondal and R. Biswas, *J. Phys. Chem. B*, 2019, **123**, 9378–9387.

26 A. Maimulyanti, I. Nurhidayati, B. Mellisani, F. Amelia Rachmawati Putri, F. Puspita and A. Restu Prihadi, *Arab. J. Chem.*, 2023, **16**, 104634.

27 A. N. Shikov, V. M. Kosman, E. V. Flissyuk, I. E. Smekhova, A. Elameen and O. N. Pozharitskaya, *Molecules*, 2020, **25**, 1826.

28 P. Velásquez, D. Bustos, G. Montenegro and A. Giordano, *Molecules*, 2021, **26**, 984.

29 G.-Y. Yang, J.-N. Song, Y.-Q. Chang, L. Wang, Y.-G. Zheng, D. Zhang and L. Guo, *Molecules*, 2021, **26**, 2079.

30 E. D. Obluchinskaya, O. N. Pozharitskaya, L. V. Zakharova, A. V. Daurtseva, E. V. Flisyuk and A. N. Shikov, *Molecules*, 2021, **26**, 4198.

31 M. Panić, V. Gunjević, K. Radošević, M. Cvjetko Bubalo, K. K. Ganić and I. R. Redovniković, *Molecules*, 2021, **26**, 4722.

32 M.-A. Karadendrou, I. Kostopoulou, V. Kakokefalou, A. Tzani and A. Detsi, *Catalysts*, 2022, **12**, 249.

33 M. Zuo, Q. Niu, Y. Zhu, S. Li, W. Jia, Z. Zhou, X. Zeng and L. Lin, *Ind. Crops Prod.*, 2023, **192**, 115953.

34 Y. Zhou, Y.-J. Wu, L. Wang, J. Han, J.-C. Wu, C.-M. Li and Y. Wang, *Int. J. Biol. Macromol.*, 2021, **190**, 206–213.

35 C. Benoit, C. Virginie and V. Boris, *BotRv*, 2021, **97**, 309–332.

36 A. Gómez, A. Biswas, C. Tadini, R. Furtado, C. Alves and H. Cheng, *J. Braz. Chem. Soc.*, 2019, **30(4)**, 717-726.

37 S. Azmi, M. F. Koudahi and E. Frackowiak, *Energy Environ. Sci.*, 2022, **15**, 1156–1171.

38 C. M. Teglia, F. A. Gutierrez and H. C. Goicoechea, *Talanta*, 2022, **242**, 123290.

39 S. M. Azcarate, R. Elia Dazat, J. M. Camiña, M. F. Silva and F. J. V. Gomez, *Food Control*, 2022, **140**, 109144.

40 G. Imperato, E. Eibler, J. Niedermaier and B. König, *Chem. Commun.*, 2005, 1170–1172.

41 A. Hayyan, F. S. Mjalli, I. M. AlNashef, Y. M. Al-Wahaibi, T. Al-Wahaibi and M. A. Hashim, *J. Mol. Liq.*, 2013, **178**, 137–141.

42 C. Florindo, M. M. Oliveira, L. C. Branco and I. M. Marrucho, *J. Mol. Liq.*, 2017, **247**, 441–447.

43 V. Fischer and W. Kunz, *Mol. Phys.*, 2014, **112**, 1241–1245.

44 C. Ruß and B. König, *Green Chemistry*, 2012, **14**, 2969.

45 K. B. Möllers, D. Cannella, H. Jørgensen and N.-U. Frigaard, *Biotechnol. Biofuels*, 2014, **7**, 64.

46 G. Markou, I. Angelidaki and D. Georgakakis, *Appl. Microbiol. Biotechnol.*, 2012, **96**, 631–645.

47 L. Hua, R. Zhou, D. Thirumalai and B. J. Berne, *PNAS*, 2008, **105**, 16928–16933.

48 A. Das and C. Mukhopadhyay, *J. Phys. Chem. B*, 2009, **113**, 12816–12824.

49 D. Bandyopadhyay, S. Mohan, S. K. Ghosh and N. Choudhury, *J. Phys. Chem. B*, 2014, **118**, 11757–11768.

50 L. B. Sagle, Y. Zhang, V. A. Litosh, X. Chen, Y. Cho and P. S. Cremer, *J. Am. Chem. Soc.*, 2009, **131**, 9304–9310.

51 B. J. Bennion and V. Daggett, *PNAS*, 2003, **100**, 5142–5147.

52 A. Baksi, J. Rajbangshi and R. Biswas, *Physical Chemistry Chemical Physics*, 2021, **23**, 12191–12203.

53 S. Das, R. Biswas and B. Mukherjee, *J. Phys. Chem. B*, 2015, **119**, 274–283.

54 S. Das, R. Biswas and B. Mukherjee, *J. Chem. Phys.*, 2016, **145**, 84504.

55 S. Das, R. Biswas and B. Mukherjee, *J. Phys. Chem. B*, 2015, **119**, 11157–11168.

56 A. Das, S. Das and R. Biswas, *J. Chem. Phys.*, 2015, **142**, 034505.

57 A. Das, S. Das and R. Biswas, *Chem. Phys. Lett.*, 2013, **581**, 47–51.

58 S. Banerjee, P. Kr. Ghorai, S. Das, J. Rajbangshi and R. Biswas, *J. Chem. Phys.*, 2020, **153**, 234502.

59 K. Mukherjee, S. Das, J. Rajbangshi, E. Tarif, A. Barman and R. Biswas, *J. Phys. Chem. B*, 2021, **125**, 12552–12567.

60 A. Kovács, E. C. Neyts, I. Cornet, M. Wijnants and P. Billen, *ChemSusChem*, 2020, **13**, 3789–3804.

61 I. Baruah and G. Borgohain, *J. Mol. Graph. Model.*, 2023, **125**, 108582.

62 J. Yao, L. Xiao, C. Li, B. Wang, Y. Chen, X. Yan and Z. Cui, *J. Mol. Liq.*, 2022, **363**, 119768.

63 M. J. Abraham, D. van der Spoel, E. Lindahl, B. Hess and and the GROMACS development team, GROMACS User Manual version 2018.

64 J. Lee, X. Cheng, J. M. Swails, M. S. Yeom, P. K. Eastman, J. A. Lemkul, S. Wei, J. Buckner, J. C. Jeong, Y. Qi, S. Jo, V. S. Pande, D. A. Case, C. L. Brooks, A. D.

MacKerell, J. B. Klauda and W. Im, *J. Chem. Theory Comput.*, 2016, **12**, 405–413.

65 W. Humphrey, A. Dalke and K. Schulten, *J. Mol. Graph.*, 1996, **14**, 33–38.

66 L. Martínez, R. Andrade, E. G. Birgin and J. M. Martínez, *J. Comput. Chem.*, 2009, **30**, 2157–2164.

67 A. Toukmaji, C. Sagui, J. Board and T. Darden, *J. Chem. Phys.*, 2000, **113**, 10913–10927.

68 U. Essmann, L. Perera, M. L. Berkowitz, T. Darden, H. Lee and L. G. Pedersen, *J. Chem. Phys.*, 1995, **103**, 8577–8593.

69 G. Bussi, D. Donadio and M. Parrinello, *J. Chem. Phys.*, 2007, **126**, 14101.

70 M. Parrinello and A. Rahman, *J. Appl. Phys.*, 1981, **52**, 7182–7190.

71 M. Brehm, M. Thomas, S. Gehrke and B. Kirchner, *J. Chem. Phys.*, 2020, **152**, 164105.

72 M. Brehm and B. Kirchner, *J. Chem. Inf. Model.*, 2011, **51**, 2007–2023.

73 D. A. McQuarrie, *Statistical Mechanics*, Harper Collins, New York, 1976.

74 S. Kaur and H. K. Kashyap, *J. of Chem. Sci.* 2017, **129**, 103–116.

75 I. M. Svishchev and P. G. Kusalik, *J Chem Phys*, 1993, **99**, 3049–3058.

76 A. Luzar and D. Chandler, *Nature*, 1996, **379**, 55–57.

77 A. Chandra, *Phys. Rev. Lett.*, 2000, **85**, 768–771.

78 S. Balasubramanian, S. Pal and B. Bagchi, *Phys. Rev. Lett.*, 2002, **89**, 115505.

79 A. Luzar, *Faraday Discuss.*, 1996, **103**, 29.

80 A. Luzar and D. Chandler, *Nature*, 1996, **379**, 55–57.

81 M. Neumann, *J. Chem. Phys.*, 1986, **85**, 1567–1580.

82 M. Neumann and O. Steinhauser, *Chem. Phys. Lett.*, 1984, **106**, 563–569.

83 S. Boresch, M. Willensdorfer and O. Steinhauser, *J. Chem. Phys.*, 2004, **120**, 3333–3347.

84 S. Boresch, P. Höchtl and O. Steinhauser, *J. Phys. Chem. B*, 2000, **104**, 8743–8752.

85 R. K. Murarka and T. Head-Gordon, *J. Phys. Chem. B*, 2008, **112**, 179–186.

86 K. Fuchs and U. Kaatze, *J. Phys. Chem. B*, 2001, **105**, 2036–2042.

87 M. T. Sonoda, M. Dolores Elola and M. S. Skaf, *J. Phys.: Cond. Matt.*, 2016, **28**, 414018.

88 D. Maji and R. Biswas, *J. Chem. Phys.*, 2023, **158**, 174503.

89 K. Mukherjee, S. Das, E. Tarif, A. Barman and R. Biswas, *J. Chem. Phys.*, 2018, **149**, 124501.

Chapter 5

Enhanced solubility of paracetamol in (ChCl + polyol) deep eutectics: A novel interplay between non-polar and H-bond interactions

5.1 Introduction

The oral administration of therapeutic agents stands as the most convenient and straightforward method of delivering drugs, especially for chronic therapies.[1] Liquid formulations play a pivotal role in oral pharmacotherapy, particularly for patients facing challenges in swallowing solid dosage forms like tablets or capsules. This is especially pertinent for specific patient types such as children or the elderly persons, and situations demanding dosing flexibility. Liquid form also assumes special importance for certain administration routes such as nasal, otic or ophthalmic, ensuring efficient delivery of active ingredients. Moreover, injectable drug products are predominantly formulated in liquid form, chosen for its convenience and flexibility in comparison to other parenteral dosage forms. The simplicity of liquid formulations finds its epitome in aqueous solutions. However, a significant challenge arises as many active pharmaceutical ingredients (APIs) exhibit inadequate solubility in water, rendering the creation of practical solutions challenging.[2,3] Furthermore, numerous APIs are prone to decomposition through various pathways, compromising stability in aqueous solutions.[4] A case in point is the hydrolysis of ester-containing pharmaceuticals like aspirin during prolonged storage in water.[5]

While organic solvents present a potential solution to solubilize certain drugs and mitigate water-mediated decomposition, their usage is often impractical and undesirable in pharmaceutical settings. The drawbacks include concerns principally related to toxicity and regulatory issues. Additionally, the use of organic solvents is hindered by unpleasant odors or tastes, further discouraging their application in pharmaceutical formulations. This necessitates exploration into alternative approaches that ensure both solubility and stability of APIs without compromising safety and practicality in pharmaceutical formulations.

Researchers have delved into the potential of various ILs to serve as pharmaceutical solvents, addressing the dissolution challenges posed by poorly soluble APIs. Additionally, ILs have

undergone scrutiny for their suitability as carriers in drug delivery applications.[6,7] Notably, ILs have been harnessed as vehicles for crafting stable microemulsions, facilitating the dissolution and transdermal delivery of APIs with low solubility.[8,9] In specific investigations, imidazolium-based ILs emerged as promising candidates for drug reservoirs, offering controlled release capabilities.[10] However, despite their promising applications, the "greenness" of ILs confronts challenges, primarily stemming from concerns about their poor biodegradability, limited biocompatibility, and questions regarding long-term sustainability.[11] As the pharmaceutical industry grapples with these considerations, the quest for ILs that strike a harmonious balance between effectiveness and environmental responsibility continues, necessitating ongoing exploration and refinement in this evolving field.

Deep eutectic solvents (DESs) belong to a special group of solvents created by blending different compounds in right proportions, resulting in a unique mixture with a melting point significantly lower than each component on its own.[12] This innovative class of solvents, often promoted as a promising alternative to traditional ionic liquids (ILs), successfully tackles various limitations associated with ILs. Natural DESs, specifically those composed of components derived from natural sources, emerge as exceptionally appealing solvents for pharmaceutical uses. They have some exceptional qualities such as biodegradability, low toxicity, easy preparation.[11,12] They are also capable of dissolving a wide array of compounds, encompassing those challenging to dissolve in water, such as benzoic acid, griseofulvin, danazol, itraconazole, AMG517, rutin, cinnamic acid, and taxol.[13,14] Moreover, these solvents exhibit the ability to dissolve larger molecules like DNA, starch, chitin, and proteins.[15,16] The notable versatility of natural DESs positions them as a noteworthy solution for pharmaceutical applications, holding the potential to address challenges posed by both small, water-insoluble compounds and larger macromolecules. An exciting facet of this study is the development of DESs that incorporate an API as one of their components, signaling a novel avenue in solvent design for pharmaceutical purposes.[17–20] Consequently, while some preliminary investigations have explored the application of DESs in drug-related contexts, a significant void still persists.[21–23] Specifically, there remains a dearth of comprehensive insights into the utilization of deep eutectic solvents for the solubilization of APIs. Both experimental and molecular-level mechanisms in this domain lack the depth of understanding needed to propel this promising field forward.

Categorization of drugs, or APIs, can be approached through various considerations, including chemical class, mechanism of action, mode of action, and therapeutic class, among other

criteria. The classification based on therapeutic use emerges as particularly valuable, providing a useful means through which the pathology targeted by the drug is highlighted. This approach facilitates the grouping of APIs based on their ultimate medical purposes. Non-steroidal anti-inflammatory drugs (NSAIDs) stand out as the most prominent and extensively utilized medications, offering a remarkable spectrum of properties. Their effects encompass alleviating fever, joint pain, headache, and rheumatism. Beyond their exceptional analgesic, anti-pyretic, and anti-inflammatory attributes, NSAIDs play a critical role in the primary and secondary prevention of cardiovascular diseases.[24] Despite these merits, NSAIDs encounter a challenge as they tend to be either insoluble or poorly soluble in water. For instance, aspirin, a widely used NSAID, exhibits limited solubility in water (0.33 g in 100 mL).[25] Similarly, naproxen and ibuprofen are nearly insoluble in water, adding a layer of complexity to their pharmaceutical formulations.[25]

The unique compositional versatility of DESs allows for the design of solvents with specific properties that cater to the solubilization needs of diverse drug compounds. Understanding the interplay between DES components and drug molecules enables the rational design of solvents tailored to the physicochemical characteristics of the drugs in question. This knowledge is pivotal for creating efficient drug delivery systems that enhance bioavailability and therapeutic outcomes. Molecular dynamics (MD) simulation is capable of providing insights about these molecular level interactions. A few theoretical studies, complemented by computational works, have already been performed to explore molecular-level properties of several drugs in different DESs.[26–28]

Paracetamol is a well-known pain reliever (analgesic) and fever reducer (anti-pyretic) drug. It is utilized to temporarily alleviate mild to moderate pain and fever. The solubility of paracetamol in water is ~20 mg/mL but increases to ~15 fold when dissolved in choline chloride (ChCl)-based DESs (~287 mg/mL in ChCl-ethylene glycol (EG) DES and ~324 mg/mL in ChCl-propylene glycol (PG) DES).[25] In this comprehensive study, we conducted MD simulations to predict the solubility behavior of the NSAID, paracetamol (PCM), in two distinct ChCl-based DESs. The hydrogen bond donors (HBD) in these DESs are EG and PG, respectively. Notably, these two diols bear close similarity, differing only by the presence of an extra methyl group in PG. Our primary objective is to understand the interaction contributions that are responsible for the above-mentioned solubility differences by carrying out concentration dependent computational investigation. Additionally, we have investigated how the presence of an extra methyl group contributes to PCM solubility in PG.

5.2 Simulation details

MD simulations were performed in GROMACS[29] software using CHARMM force field model[30] potentials. Different DES + PCM mixtures were considered with varying numbers of PCM molecules. The details about these systems can be found in Table 5.A.1. The atomic representations of the constituent molecules can be found in Figure 5.A.1. For each DES, six different systems were simulated varying the concentration from ~0.9 to ~2 mol L^{-1}. Required numbers of molecules were arranged in cubic boxes using the PACKMOL software.[31] Subsequently, each box was subjected to energy minimization employing the steepest descent algorithm.[32] After energy minimization, systems were equilibrated in isothermal-isobaric condition (NPT) for 30-40 ns at 298 K and 1 bar. After the density of the systems reached convergence, production runs in isothermal-isochoric condition (NVT) for 100 ns were performed at 298 K. The pressure and temperature of the systems were maintained by the velocity-rescaling[33] thermostat and Berendsen barostat[34] with time constants 0.1 ps and 2 ps, respectively. Coulombic interactions were treated using the particle mesh Ewald (PME) method[35] while van der Waals interactions were modeled via Lennard-Jones potential. For both the non-bonding interactions, the cut-off distances were the same and set to 1.2 nm. The leap - frog algorithm[36] was used to solve the equations of motion. Trajectory analyses were performed using GROMACS,[29] VMD,[37] and TRAVIS[38,39] programs.

For interaction energy calculations, the simulated trajectories were subjected to 'gmx rerun' module as described in the GROMACS manual.[40]

5.3 Results and discussion

In this work, we gradually add paracetamol in two ChCl-based DESs (ChCl + EG and ChCl + PG). First, we will check the fidelity of our force-field model by comparing the simulated densities of pure DESs with experimental ones. Such comparison can be found in Table 5.A.1 and the deviation is less than 1% which affirms the viability of used potential models. The addition of PCM to (ChCl + EG) DES and (ChCl + PG) DES causes a change in volumetric properties. From Table 5.A.1, it is clear that the addition of PCM increases the density of mixtures for both DESs. The DES molecules are expected to change their spatial arrangement to accommodate incoming PCM molecules. Hence, the volume of the solutions should

gradually change. This change can be calculated by using the percentage volume expansion, $\%V_{\text{exp}}$, as defined earlier,[28,41]

$$\%V_{\text{exp}} = \frac{V_{\text{DES+PCM}}(T,P,X) - V_{\text{DES}}(T,P_0)}{V_{\text{DES}}(T,P_0)} \quad (5.1)$$

where, $V_{\text{DES+PCM}}(T,P,X)$ denotes the volume of DES + PCM solutions at a given temperature (T), pressure (P) and mole fraction of solute (X); $V_{\text{DES}}(T,P_0)$ indicates the volume of neat DES at the same temperature and 1 bar pressure.

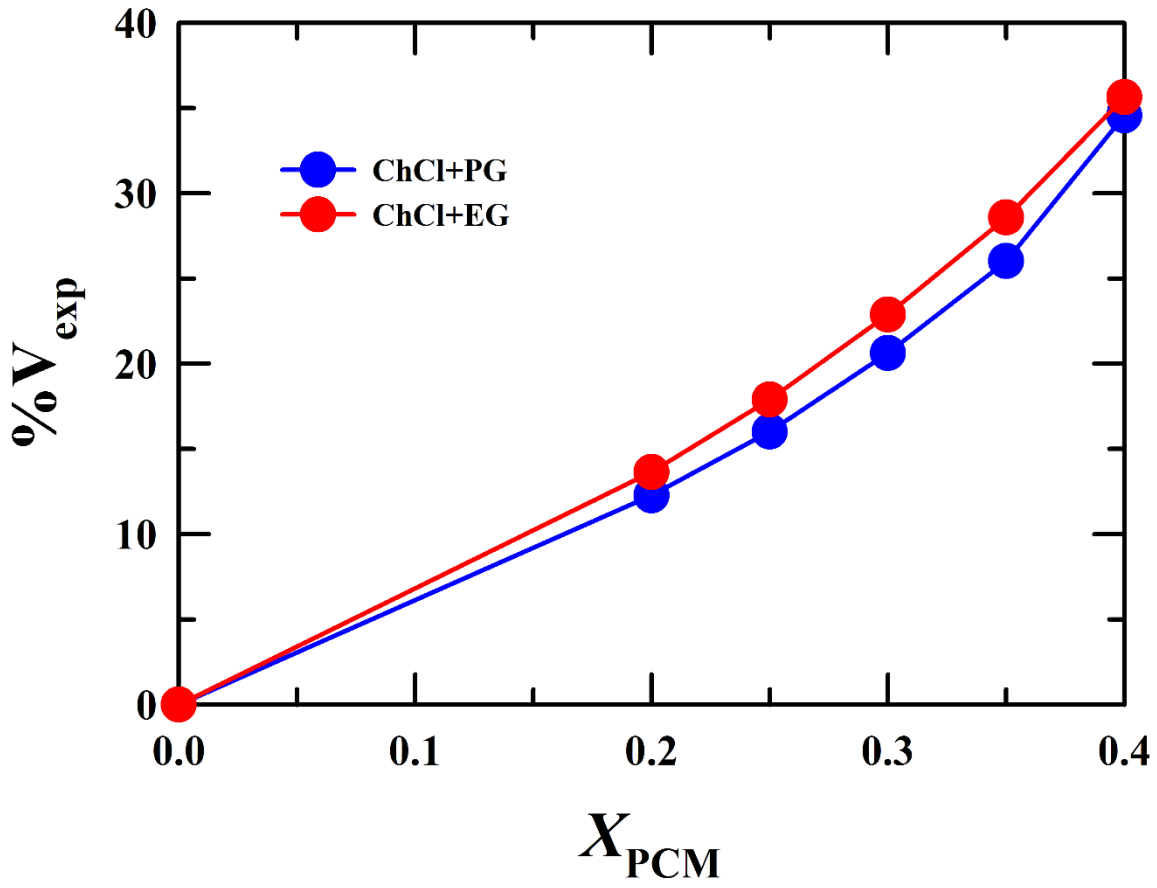

Figure 5.1: Percentage volume expansion, $\%V_{\text{exp}}$, for the reported ChCl-DES (EG/PG) + paracetamol solutions from MD simulation at 298 K and 1 bar.

Figure 5.1 shows the calculated expansivity of both the DESs upon the addition of PCM. Remarkably, even in highly concentrated solutions, the expansivity remains at a moderate level, approximately around 35%. This is interesting because it means these DESs can take in PCM without causing substantial disruption to their intrinsic structure. This, in turn, provides

additional confirmation regarding the effectiveness of these DESs in solubilizing PCM while keeping their structure intact.

5.3.1 Liquid structure of DESs and solubility of paracetamol

To closely introspect this observation, we have calculated center-of-mass radial distribution functions (RDFs) of constituent molecules in neat DESs as well as their solutions.

The center of mass radial distribution was computed to analyze interactions within and between the components (cation, anion, and HBD) of ChCl-based DESs — ChCl + EG and ChCl + PG (see Figures 5.A.2 and 5.A.3 in Appendix 5. A). The introduction of paracetamol, induced a non-monotonic alteration in peak heights, while peak positions remained invariant. This trend is visible across six distinct RDFs for each DES, encompassing both the neat DESs and solutions enriched with paracetamol. This intriguing observation implies that the spatial configuration of the DES components undergoes minimal changes with the addition of paracetamol. The non-monotonic shifts in peak heights suggest a subtle influence on the distribution of cations, anions, and HBDs within the DESs upon paracetamol incorporation. Nevertheless, the constancy in peak positions depicts the preservation of the fundamental structural framework. This is consistent with the previous volume expansivity analyses.

Next, we delve into the interactions between PCM and the DES molecules. Initial scrutiny focuses on how PCM molecules interact within (ChCl + EG) DES, as depicted in Figure 5.2. Consistent with prior observations, the configuration of surrounding molecules remains structurally unaltered. The gradual introduction of PCM induces changes in the population around the reference molecule without disrupting the inherent solvation structure. Figure 5.2 shows a peak for PCM-$[Ch]^+$ at ~0.73 nm preceded by a minor hump. For PCM-$[Cl]^-$ two sharp peaks are observed at ~0.45 nm and 0.6 nm where the first one is minor. The interaction of PCM and EG displays a peak maximum of around 0.52 nm. The PCM-PCM peaks also appear at around this distance. Crucially, this analysis provides insights into the solubility of paracetamol within (ChCl + EG) DES. Notably, the arrangement of other molecules around PCM exhibits no structural variations. The solubility is discerned by examining the first solvation shell around a PCM molecule, where the key indicators are (i) the maximum number of cations, anions, and HBD molecules, and (ii) the minimum number of PCM molecules present. This approach allows us to gauge the solubility of paracetamol based on the composition of its immediate solvation environment.

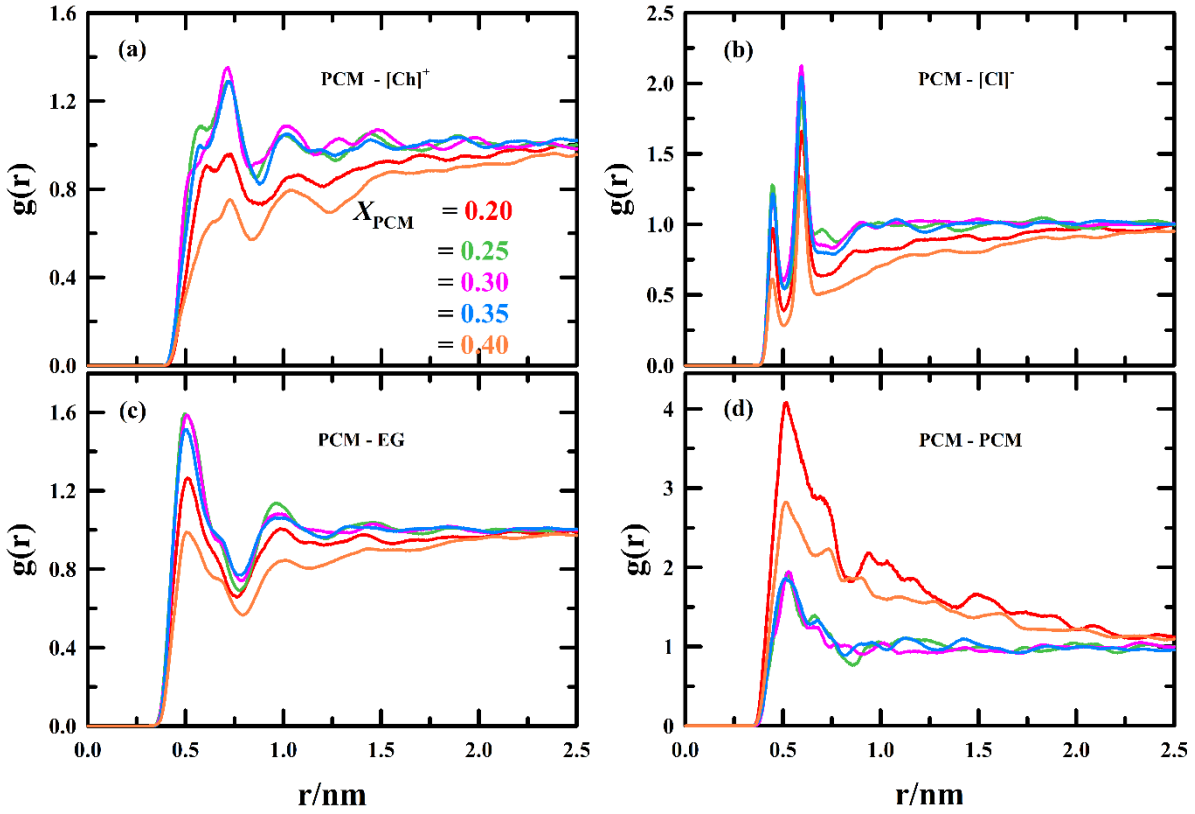

Figure 5.2: Center-of-mass (COM) radial distribution functions, g(r), for the reported (ChCl + EG) DES + paracetamol solutions from MD simulation at 298 K and 1 bar. The RDFs are calculated keeping PCM as a reference molecule. Each concentration is uniquely color-coded.

Subsequently, we conducted a more detailed analysis by calculating the coordination number (CN), representing the number of surrounding molecules in the first solvation shell of PCM. The CNs were computed across various solutions featuring different mole fractions of PCM, and illustrated in Figure 5.3. A non-monotonic change across all species is observed. Specifically, for $[Ch]^+$, $[Cl]^-$, and EG, the CN peaks in the solution at X_{PCM}=0.25. Notably, at this concentration, the solvation shell contains the smallest number of PCM molecules. This observation suggests a maximum interaction between PCM and DES molecules. Simultaneously, the aggregation among PCM molecules is the least. This particular solution stands out as the one where PCM exhibits the highest solubility. Interestingly, this computed solubility of PCM in (ChCl + EG) DES, 215 mg/mL, is lower by ~25% than the experimental solubility [25] (287 mg/mL).

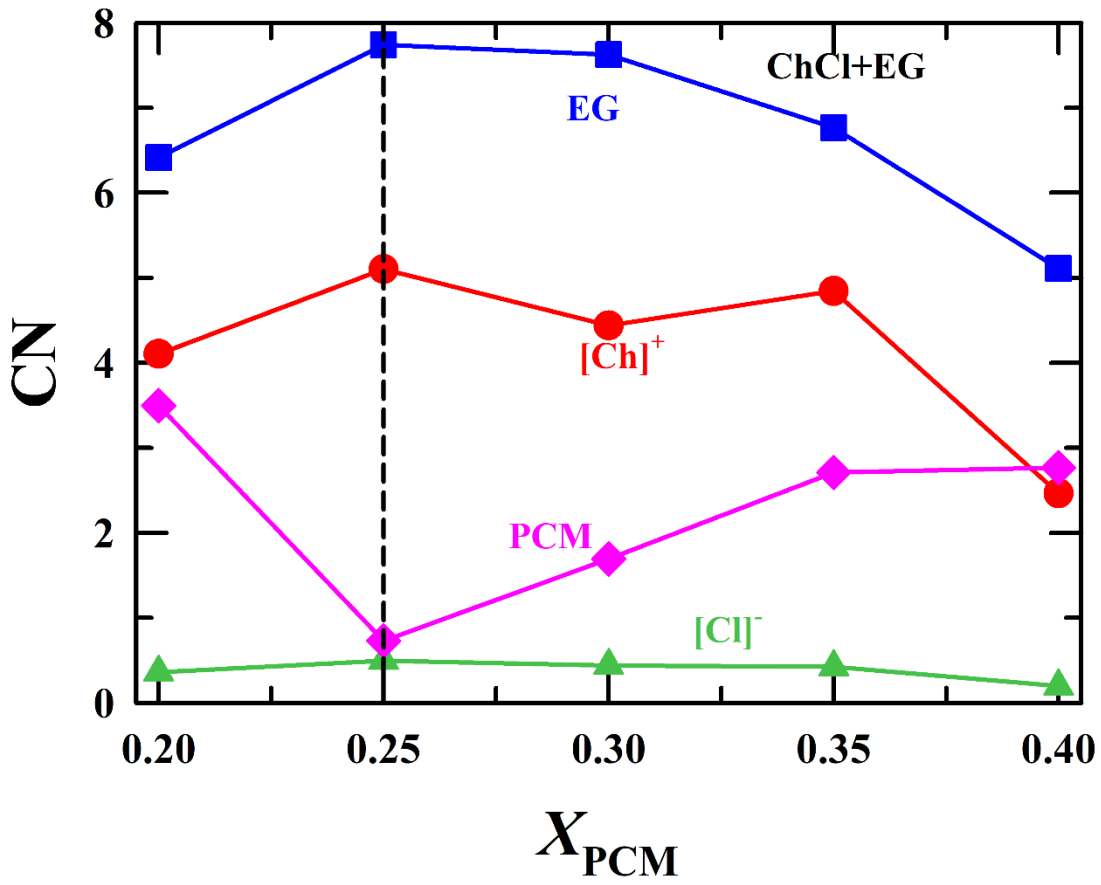

Figure 5.3: Coordination numbers (CN) calculated from Figure 5.2, for the reported (ChCl + EG) DES + paracetamol solutions from MD simulation at 298 K and 1 bar. The vertical dashed line indicates the maximum solubility.

Using a similar approach, we computed RDFs with PCM as the reference molecule in (ChCl + PG) DES across different concentrations. The microstructural configuration of various species around PCM is depicted in Figure 5.4. Analogous to the observations in (ChCl + EG) DES, the introduction of PCM brings about changes in peak heights, maintaining the overall solvation structures almost intact. A notable peak for PCM-$[Ch]^+$ is evident at approximately 0.74 nm, accompanied by a minor hump. This hump is most pronounced at the lowest concentration and gradually diminishes with increasing concentration. For PCM-$[Cl]^-$, two distinct peaks appear at around 0.45 nm and 0.6 nm, with the former being smaller. The interaction of PCM with PG exhibits a peak maximum at approximately 0.55 nm. Peaks for PCM-PCM interactions also manifest at around this distance.

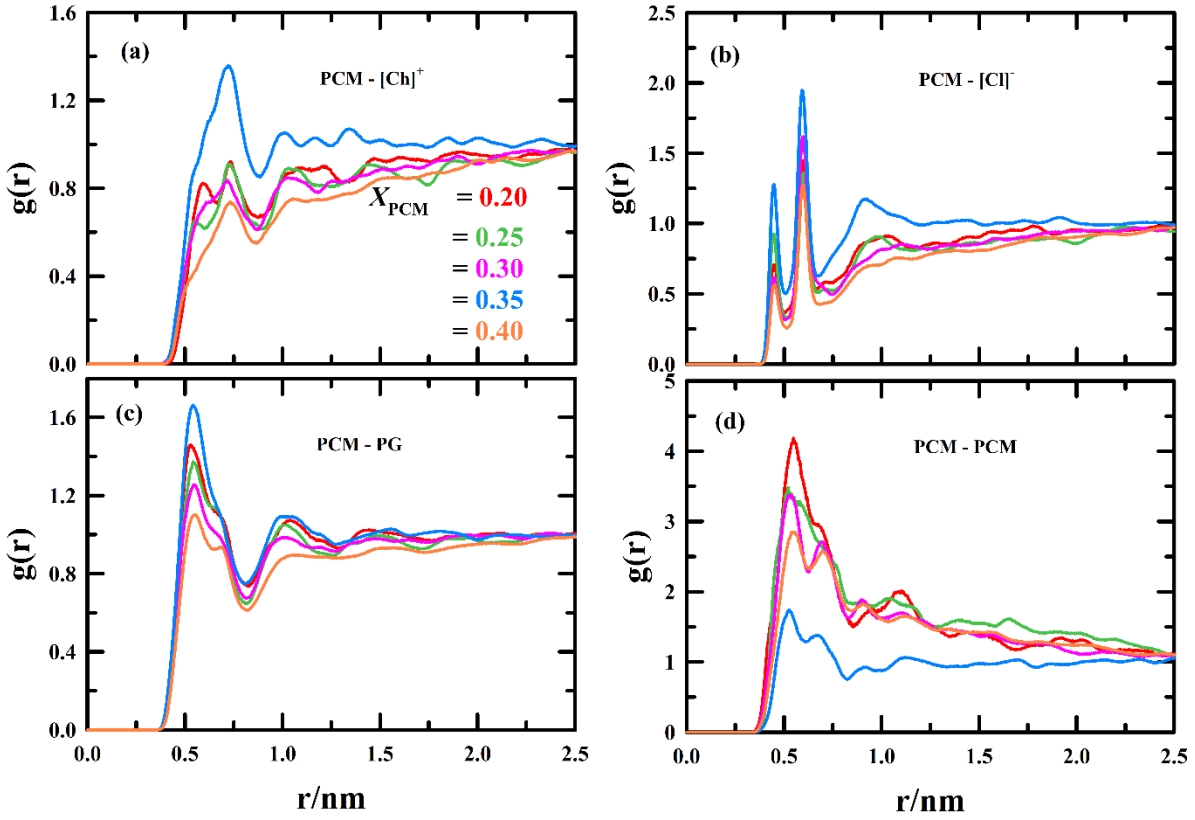

Figure 5.4: Center-of-mass (COM) radial distribution functions, g(r), for the reported (ChCl + PG) DES + paracetamol solutions from MD simulation at 298 K and 1 bar. The RDFs are calculated keeping PCM as a reference molecule. Each concentration is uniquely color-coded.

Similar to our approach in (ChCl + EG) DES, we determined the coordination numbers around PCM in (ChCl + PG) DES, and the results are illustrated in Figure 5.5. Notably, as the concentration varies, the CNs exhibit a non-monotonic evolution. At X_{PCM}=0.35, solvent particles ($[Ch]^+$, $[Cl]^-$, and PG) surround the solute molecule (PCM) to the maximum extent. Concurrently, at the same concentration, PCM-PCM interactions reach a minimum. This specific concentration (X_{PCM}=0.35) can be regarded as the point of highest solubility. In this solution, the solubility of PCM is calculated to be 303 mg/mL. Interestingly, this computed solubility is relatively much closer to the experimental solubility of PCM (324 mg/mL) and underpredicted only by ~6.5%.

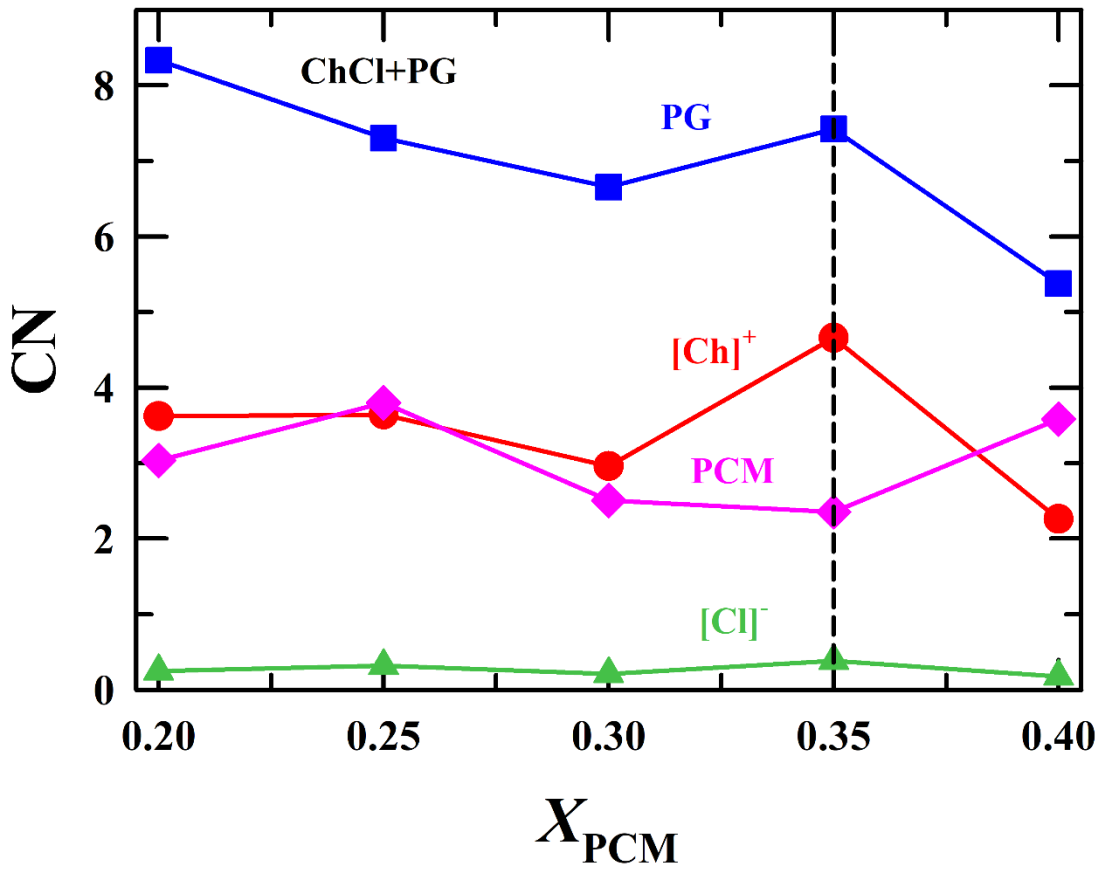

Figure 5.5: Coordination numbers (CN) calculated from Figure 5.4, for the reported (ChCl + PG) DES + paracetamol solutions from MD simulation at 298 K and 1 bar. The vertical dashed line indicates the maximum solubility.

5.3.2 Interaction energy

Now that we have determined the solubility of PCM in (ChCl + EG) and (ChCl +PG) DESs, our focus shifts to understand the strength of intermolecular interactions within these solutions. The key parameter in our analysis is the interaction energy, denoted as E_{int}. This energy comprises both van der Waals (Lennard-Jones) and electrostatic (Coulombic) energies. A negative E_{int} signifies attractive interactions, while a positive value indicates repulsive interactions. In both DESs, counting of interactions between the solute (PCM) and solvent (DES) produces a negative value for the interaction energy, implying the dominance of attractive interaction. Conversely, interactions between PCM molecules produce a positive value for the interaction energy, indicating an overall repulsion among them. Figure 5.6 shows the calculated interaction energies (E_{int}) for both the DESs. Examination of solute-solvent

interactions at different concentrations reveals that E_{int} reaches a minimum, suggesting maximum interactions, at a specific composition. On the contrary, solute-solute interaction energy demonstrates a maximum, indicating dominance of the overall repulsion, at the same concentration. These extrema are as follows: X_{PCM}=0.25 for (ChCl + EG) DES and X_{PCM}=0.35 for (ChCl + PG) DES. This observation can be rationalized by considering the presence of molecules in the solvation shells. The greater the number of molecules in these solvation shells, the lower the E_{int} (more negative). This observation correlates well with the results presented in Figures 5.3 and 5.5. In summary, the negative solute-solvent interaction energies represent the dominance of attractive interaction facilitating the solubility of guest in the host, while the positive solute-solute interaction energies reflect repulsion among PCM molecules, negating the self-aggregation.

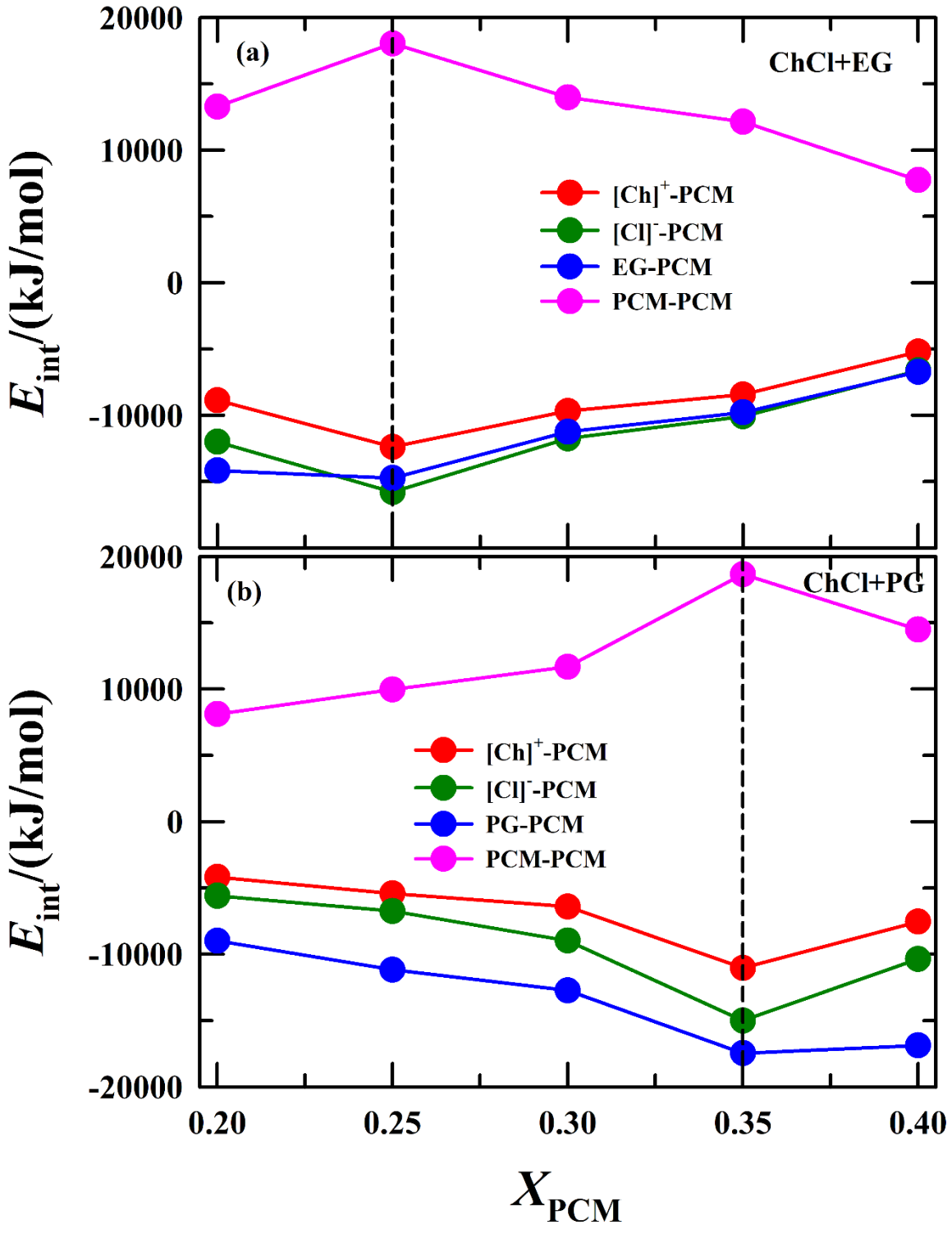

Figure 5.6: Intermolecular interaction energy, E_{int} (sum of Lennard-Jones and Coulombic contributions, $E_{int}=E_{LJ}+E_{Coul}$), for the reported ChCl-DES (EG/PG) + paracetamol solutions from MD simulation at 298 K and 1 bar. Each solution is uniquely color-coded. The dashed lines indicate the maximum interaction between solute and solvent molecules.

5.3.3 Hydrogen bond interactions

We have so far identified a specific concentration where PCM-DES interaction is the maximum and PCM-PCM interaction is the minimum in both DESs, representing the solubility limit. Our next focus is on understanding the role of H-bond interactions in the solubilization of PCM in DESs. Considering quite a few potential hydrogen-bonding (H-bonding) sites within the constituent molecules, we first discuss about the formation of hydrogen bonds (H-bonds) with PCM. This is important because it may provide a critical understanding on why PCM dissolves well in these DESs. We have calculated RDFs to explore potential hydrogen bonding sites between paracetamol (PCM) and $[Ch]^+$ in (ChCl + EG) DES and, the results are shown in Figures 5.A.4- 5.A.7. In Figure 5.A.4(a), the RDFs between O7($[Ch]^+$) and O1(PCM) reveal a small but distinct and sharp first peak. Moving on to Figure 5.A.4(b), the O7($[Ch]^+$)-O2(PCM) RDFs exhibit a relatively stronger and sharp first peak. Figure 5.A.4(c) demonstrates O7($[Ch]^+$)-N3(PCM) interactions, displaying an intense first peak. These observations suggest the existence of potential hydrogen bonding interactions between $[Ch]^+$ and PCM within the DES. The distinct peaks indicate a specific spatial arrangement, hinting at the formation of hydrogen bonds. In Figure 5.A.5, we can see how $[Cl]^-$ interacts with PCM in (ChCl + EG) DES. Figures 5.A.5(a) and 5.A.5(b) specifically show interactions with O1(PCM) and N3(PCM). In both cases, there are sharp and strong peaks at the beginning. These peaks suggest a robust interaction between $[Cl]^-$ and PCM, indicating the possible formation of hydrogen bonds. In Figure 5.A.6, we get a closer look at how EG interacts with PCM in (ChCl + EG) DES. Figure 5.A.6(a) displays the interactions between the hydroxyl oxygens of EG (O1, O9) and PCM (O1). Figure 5.A.6(b) shifts the focus to interactions between the carbonyl oxygen of PCM (O2) and the hydroxyl oxygens of EG (O1, O9). Figure 5.A.6(c) demonstrates RDFs between the amide nitrogen of PCM (N3) and the hydroxyl oxygens of EG (O1, O9). In each case, a strong, sharp peak signals a potent interaction. These findings strongly suggest the formation of hydrogen bonds between EG and PCM in the DES. In our exploration of the solubilization mechanism, understanding not only solvent-solute interactions but also solute-solute interactions is critically important. Examining RDFs between potential H-bond sites of PCM molecules, as depicted in Figure 5.A.7, provides valuable insights. Figure 5.A.7(a) illustrates O1(PCM)-N3(PCM) RDFs with a small first peak observed only at specific concentrations, suggesting a limited possibility of H-bond formation through these sites. Similar interactions are seen in O1(PCM)-O1(PCM) RDFs (Figure 5.A.7(c)), further supporting the exclusion of these sites in H-bond formation. N3(PCM)-N3(PCM) RDFs

(Figure 5.A.7(e)) show no distinct peak, eliminating the likelihood of H-bond formation involving these sites. On the contrary, Figure 5.A.7(b) portraying RDFs between O2(PCM)-N3(PCM) and Figure 5.A.7(d) depicting RDFs between O1(PCM)-O2(PCM) interactions exhibit sharp, strong principal peaks, indicating a robust potential for hydrogen bond formation.

In addition to RDFs, the corresponding running coordination numbers (CNs) are depicted within the plots. Upon careful examination, it becomes apparent that coordination numbers change as the concentration increases. Interestingly, the solution with a 0.25 mole fraction of PCM exhibits the highest CN, regardless of the specific atoms involved in the interaction. This pattern mirrors the results obtained from the analysis of center-of-mass radial distribution functions (COM-COM RDFs).

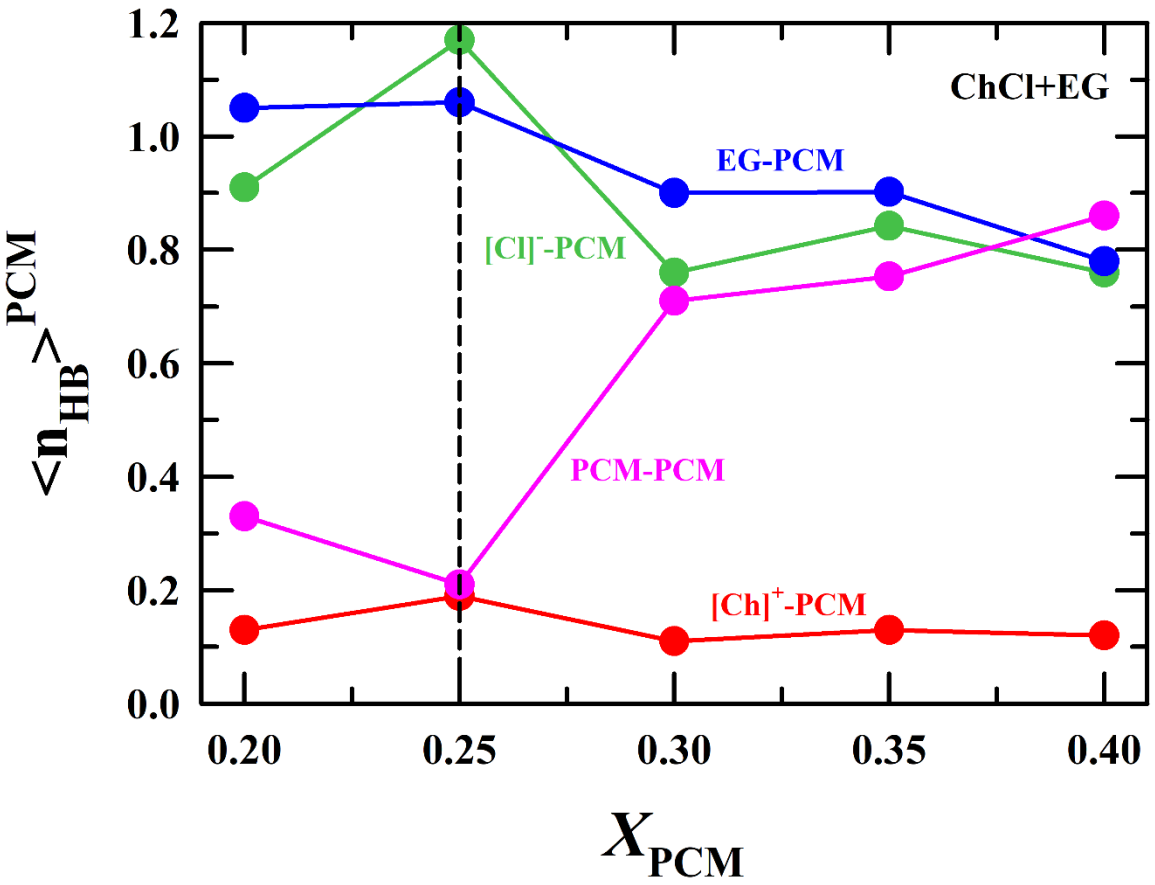

Figure 5.7: Number of intermolecular H-bonds per paracetamol molecule ($\langle n_{HB} \rangle^{PCM}$) for the reported (ChCl + EG) DES + paracetamol solutions from MD simulation at 298 K and 1 bar. The dashed line indicates the maximum solvent-solvent and minimum solute-solute interactions.

In our investigation, we have calculated the number of hydrogen bonds per PCM molecule ($\langle n_{HB} \rangle^{PCM}$) in (ChCl + EG) DES, presented in Figure 5.7. To identify H-bonds, we applied the following geometric criteria:[42,43]

(i) The distance between the donor (D) and acceptor (A) should be less than a cut-off distance, determined as the minimum of the corresponding RDF.

(ii) The angle between hydrogen (H), donor (D), and acceptor (A) atoms ($\angle H - D - A$) should be less than 30◦.

In Figure 5.7, we can see that the $\langle n_{HB} \rangle^{PCM}$ undergoes non-monotonic changes with concentration. At lower concentrations, the maximum number of H-bonds forms with $[Cl]^-$ and EG. However, at higher concentrations, PCM-PCM H-bonds notably increase. An intriguing inflection point emerges at X_{PCM}=0.25, where the maximum number of solute-solvent and the minimum number of solute-solute H-bonds occur. Remarkably, this specific solution aligns with our earlier discussions, identifying it as the point of highest solubility.

Next, we perform a similar analysis for PCM in (ChCl + PG) DES. The RDFs involving possible H-bond sites of PCM in (ChCl + PG) DES are shown in Figures 5.A.8- 5.A.11. In Figure 5.A.8(a), the RDFs between O7($[Ch]^+$) and O1(PCM) show a small but clear and sharp first peak. Moving to Figure 5.A.8(b), the O7($[Ch]^+$)-O2(PCM) RDFs reveal a relatively stronger and sharp first peak. Figure 5.A.8(c) illustrates O7($[Ch]^+$)-N3(PCM) interactions, displaying a robust and sharp first peak. These observations strongly suggest the presence of potential hydrogen bonding interactions between $[Ch]^+$ and PCM in the DES. In Figure 5.A.9, we examine how $[Cl]^-$ interacts with PCM in (ChCl + PG) DES. Specifically, Figures 5.A.9(a) and 5.A.9(b) show interactions with N3(PCM) and O1(PCM), respectively. In both cases, there are sharp and strong peaks at the beginning, suggesting a robust interaction between $[Cl]^-$ and PCM and indicating possible hydrogen bond formation. Moving on to Figure 5.A.10, we focus on how PG interacts with PCM in (ChCl + PG) DES. Figure 5.A.10(a) displays interactions between the hydroxyl oxygens of PG (O4, O5) and PCM (O1). Figure 5.A.10(b) shifts the focus to interactions between the carbonyl oxygen of PCM (O2) and the hydroxyl oxygens of PG (O4, O5). Figure 5.A.10(c) demonstrates RDFs between the amide nitrogen of PCM (N3) and the hydroxyl oxygens of PG (O4, O5). In each case, a strong, sharp peak signals a potent interaction, strongly suggesting the formation of hydrogen bonds between PG and PCM in the DES. Examining RDFs between potential H-bond sites of PCM molecules, as depicted in Figure 5.A.11, provides valuable insights. Figure 5.A.11(a) illustrates O1(PCM)-N3(PCM) RDFs with a small first peak observed only at specific concentrations, suggesting a limited possibility of H-bond formation through these sites. Similar interactions are seen in O1(PCM)-O1(PCM) RDFs (Figure 5.A.11(c)), further supporting the exclusion of these sites in H-bond formation. N3(PCM)-N3(PCM) RDFs (Figure 5.A.11(e)) show no distinct peak, eliminating the likelihood of H-bond formation involving these sites. On the contrary, Figure 5.A.11(b) portraying RDFs between O2(PCM)-N3(PCM) and Figure 5.A.11(d) depicting RDFs between O1(PCM)-O2(PCM) interactions exhibit sharp, strong principal peaks, indicating a robust potential for hydrogen bond formation. One thing to note here is that the H-bond site-site RDFs

for (ChCl + EG) and (ChCl + PG) behaves more or less similar indicating presence of same type H-bonds in both DESs. Similar to (ChCl + EG), the coordination number analysis in (ChCl + PG) DES reveals the maximum coordination number at X_{PCM}=0.35 which perfectly aligns with our previous observations.

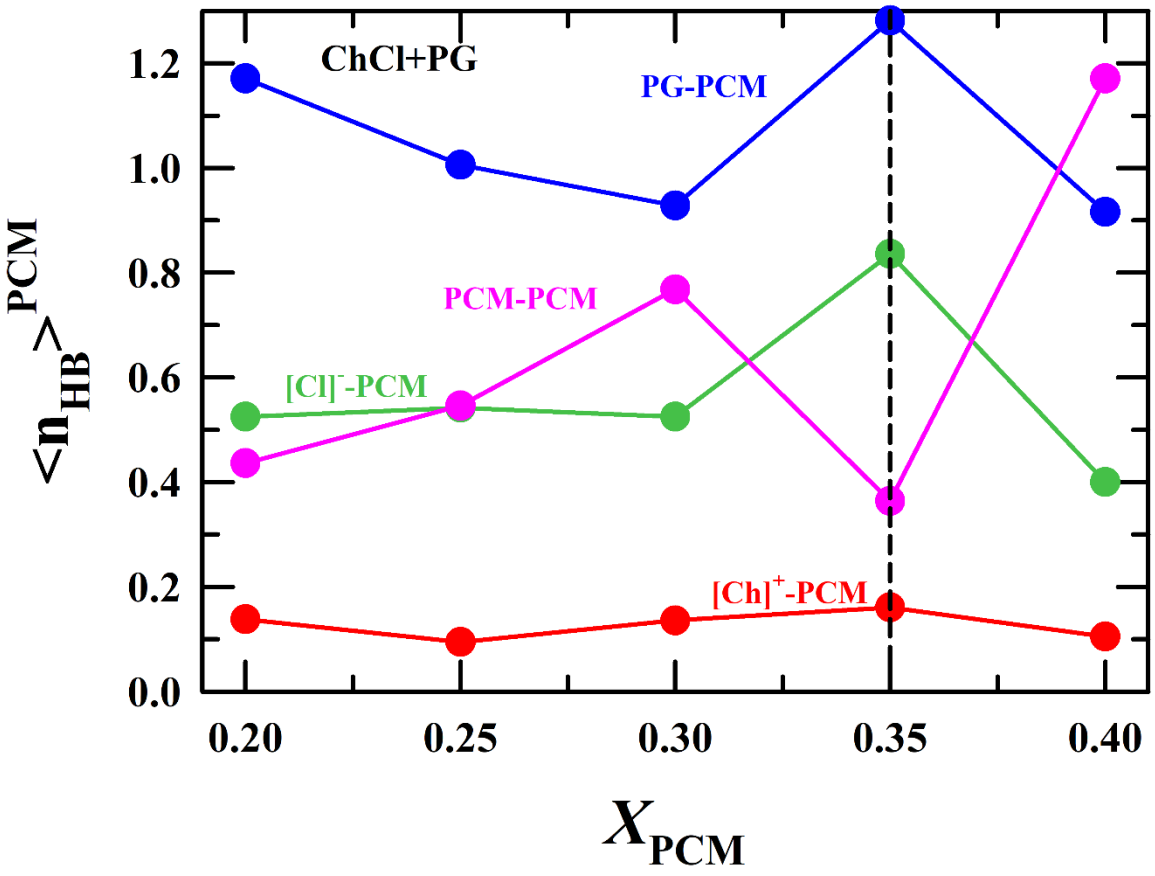

Figure 5.8: Number of intermolecular H-bonds per paracetamol molecule ($\langle n_{HB} \rangle^{PCM}$) for the reported (ChCl + PG) DES + paracetamol solutions from MD simulation at 298 K and 1 bar. The dashed line indicates the maximum solvent-solvent and minimum solute-solute interactions.

Using the geometric criteria, we have calculated the number of intermolecular H-bonds per paracetamol molecule ($\langle n_{HB} \rangle^{PCM}$) in (ChCl + PG) DES, as shown in Figure 5.8. Like (ChCl + EG), here also a non-monotonic change with concentration is observed. The inflection point is found at X_{PCM}=0.35. Note that, this particular solution corresponds with our earlier discussions, pinpointing it as the maximum solubility point.

Therefore, this comprehensive analysis illustrates the fundamental role of hydrogen bonding in dictating the solubility of PCM within these DESs. The interplay between solvent-solute and solute-solute interactions, primarily governed by hydrogen bonding, intricately regulates the solubilization process. This correlates with the broader understanding that hydrogen bonds, with their distinctive spatial arrangements and strengths, act as molecular bridges crucial for the efficient dissolution of PCM in these DESs. This finding may play a pivotal role in designing solvents for drug solubilization.

5.3.4 Non-polar interactions

In addition to hydrogen bonding, non-polar interactions emerge as pivotal factors influencing drug solubility in DESs. The substantial increase in paracetamol solubility, approximately 15 times higher in DESs [(287 mg/mL in (ChCl + EG) and 324 mg/mL in (ChCl + PG)] compared to water (20 mg/mL), indicates the potential role of non-polar interactions, especially considering the large non-polar group present in PCM molecules. Interestingly, (ChCl + PG) exhibits superior efficiency in solubilizing PCM compared to (ChCl + EG). The only difference between these DESs is in their hydrogen bond donor (HBD) molecules. PG has an extra methyl group compared to EG. We are exploring how they interact with non-polar groups. Figure 5.9 illustrates these interactions between PCM and EG/PG, with first-shell coordination numbers providing insights into the population of HBD molecules around PCM. The RDF shapes suggest similar interaction patterns for both EG and PG, but the coordination number analysis reveals differences in population. Notably, the coordination numbers peak at concentrations identified in previous analyses, indicating that non-polar interactions, akin to hydrogen bonding, follow a similar trend in solubilizing PCM. A comparison between EG and PG shows a higher population of PG around PCM, affirming that the non-polar interactions of PG are stronger, leading to enhanced PCM solubility in (ChCl + PG) DES.

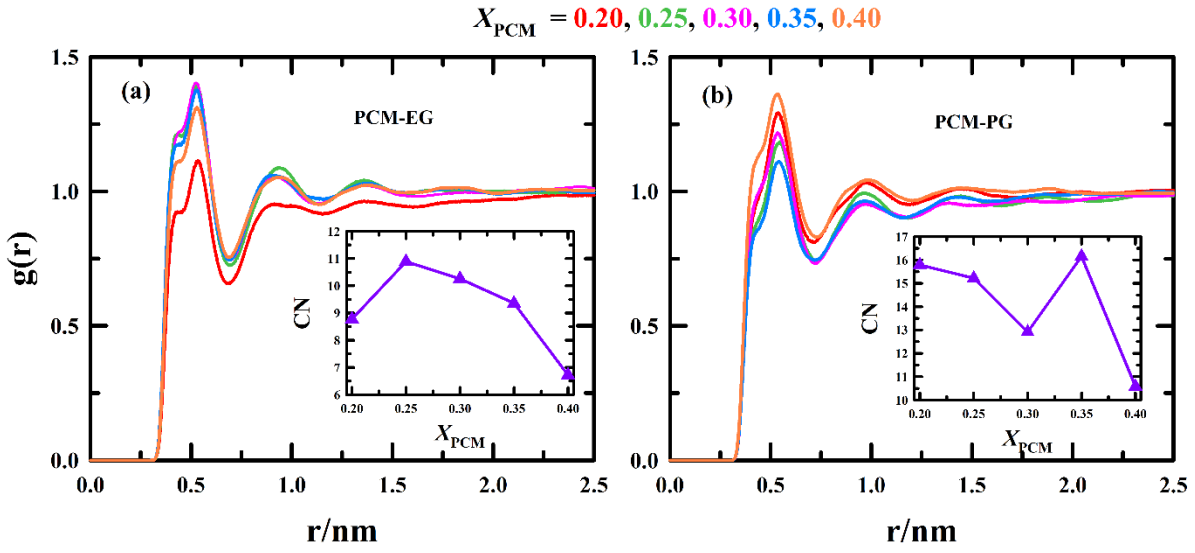

Figure 5.9: Site-site RDFs, g(r), for the reported ChCl-DES (EG/PG) + paracetamol solutions from MD simulation at 298 K and 1 bar. Results show interactions between non-polar groups of paracetamol and EG/PG. Coordination numbers (CN) are shown in the inset of each graph.

Along with PCM-HBD interactions, PCM-PCM interactions are also vital in determining the solubility of PCM. The RDFs corresponding to interactions between PCM molecules are displayed in Figure 5.10.

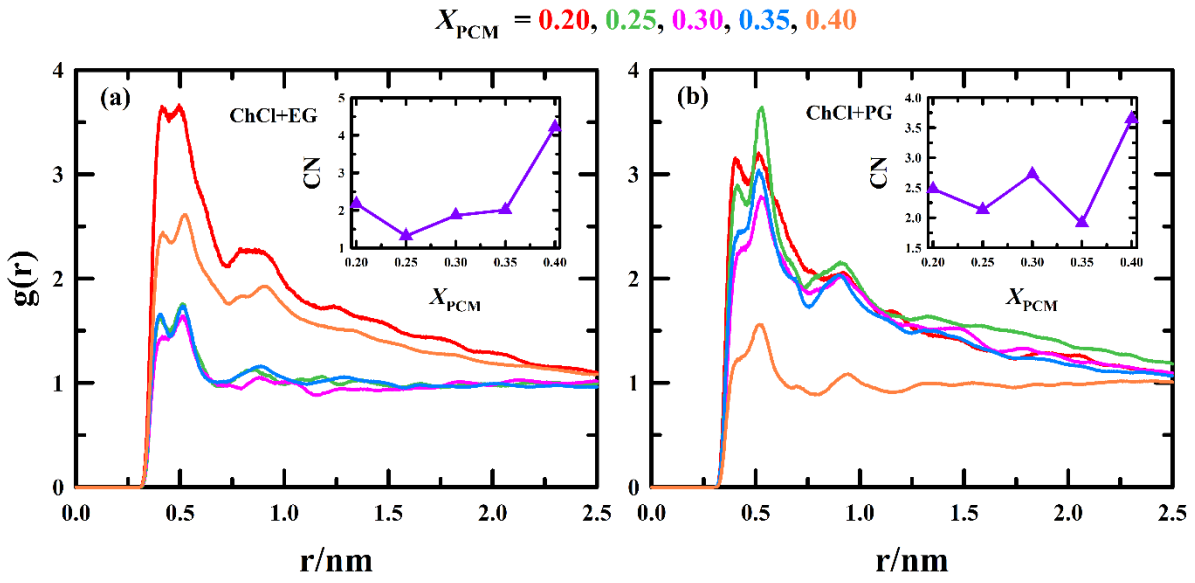

Figure 5.10 Site-site RDFs, g(r), for the reported ChCl-DES (EG/PG) + paracetamol solutions from MD simulation at 298 K and 1 bar. Results show interactions between non-polar groups of paracetamol molecules. Coordination numbers (CN) are shown in the inset of each graph.

In both cases, we observe broad peaks with a preceding hump, suggesting similar PCM-PCM interactions in both DESs. It is important to note that these non-polar interactions influence the aggregation of PCM molecules to some extent. Examining the coordination numbers (CNs), we notice that the minimum population occurs at concentrations defined for the highest solubility. This observation confirms that, in addition to H-bonding, non-polar interactions play a crucial role in determining solubility.

5.4 Conclusions

In summary, we investigated the behavior of paracetamol (PCM) in (ChCl + EG) and (ChCl + PG) deep eutectic solvents (DESs) to unravel the microscopic reasons that govern the solubilization of PCM in these media. Concentration-dependent molecular dynamics simulations were carried out, and coordination numbers and H-bond metrics were monitored. Estimation of the solubility of PCM and subsequent comparison with experiments was a key focal point, considering that both solvent-solute and solute-solute structural aspects in these media were governed by non-polar and H-bond interactions. Interestingly, the predicted solubility of PCM in (ChCl + EG) DES was found to be 215 mg/mL, while the same in (ChCl +PG) DES was 305 mg/mL. These computed solubilities not only numerically correlate well with those reported in experiments (287 mg/mL and 324 mg/mL, respectively), but also reproduce the experimental trend with the change in the polyol identity. This finding suggests that non-polar interaction plays a critical role in dictating the dissolution behavior of organic compounds in associating solvents, highlighting an important aspect related to pharmaceutical research. This, in conjunction with H-bond interactions, is pivotal for designing carrier solvents for drug dissolution and transport for therapeutic purposes. Importantly, these interactions depend on solute (here PCM) concentration, producing the solubility limit. This insight is vital for understanding drug dissolution in liquid media. We found that additional non-polar interaction is a key reason for (ChCl + PG) DES to become a better solvent for paracetamol than the EG counterpart, showing how a subtle balance between non-polar and H-bond interactions can critically influence drug dissolution. This may offer a roadmap for designing novel solvents tailored for effective drug solvation.

Appendix 5.A

Table 5.A.1: Number of constituting molecules, mole fraction of paracetamol, molar concentration and density for different simulated DES systems. Here, $N\rightarrow$ number of molecules, $X\rightarrow$ mole fraction, $C\rightarrow$ concentration in molarity, $\rho\rightarrow$ density. Experimental densities[44] are shown in parentheses.

(ChCl + EG) DES						
$N_{[Ch]+}$	$N_{[Cl]-}$	N_{HBD}	N_{PCM}	X_{PCM}	C/ M	ρ/ (g cm^{-3})
512	512	1024	0	0.00	0.0	1.1109 (1.117)
512	512	1024	128	0.20	0.9279	1.1202
512	512	1024	170	0.25	1.1879	1.1228
512	512	1024	219	0.30	1.4682	1.1259
512	512	1024	276	0.35	1.7685	1.1294
512	512	1024	341	0.40	2.0710	1.1334
(ChCl + PG) DES						
512	512	1024	0	0.00	0.0	1.0866 (1.0810)
512	512	1024	128	0.20	0.8304	1.0956
512	512	1024	170	0.25	1.0672	1.0990
512	512	1024	219	0.30	1.3224	1.1045
512	512	1024	276	0.35	1.5952	1.1068
512	512	1024	341	0.40	1.8454	1.1079

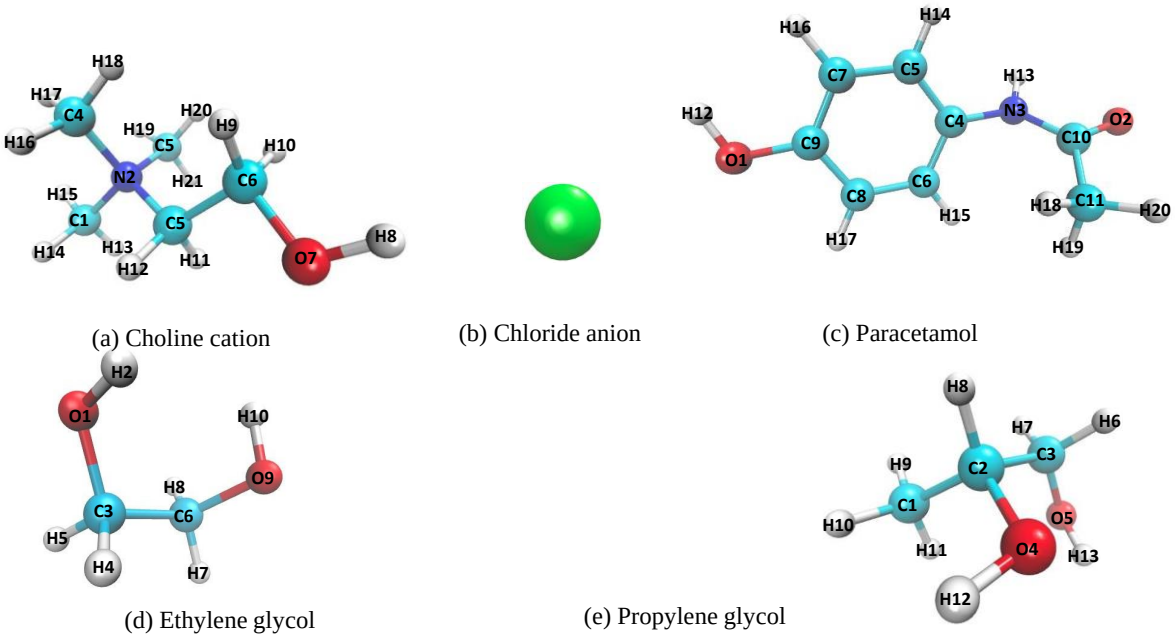

Figure 5.A.1: Atomic representations of (a) choline cation, (b) chloride anion, (c) paracetamol, (d) ethylene glycol, and (e) propylene glycol molecules.

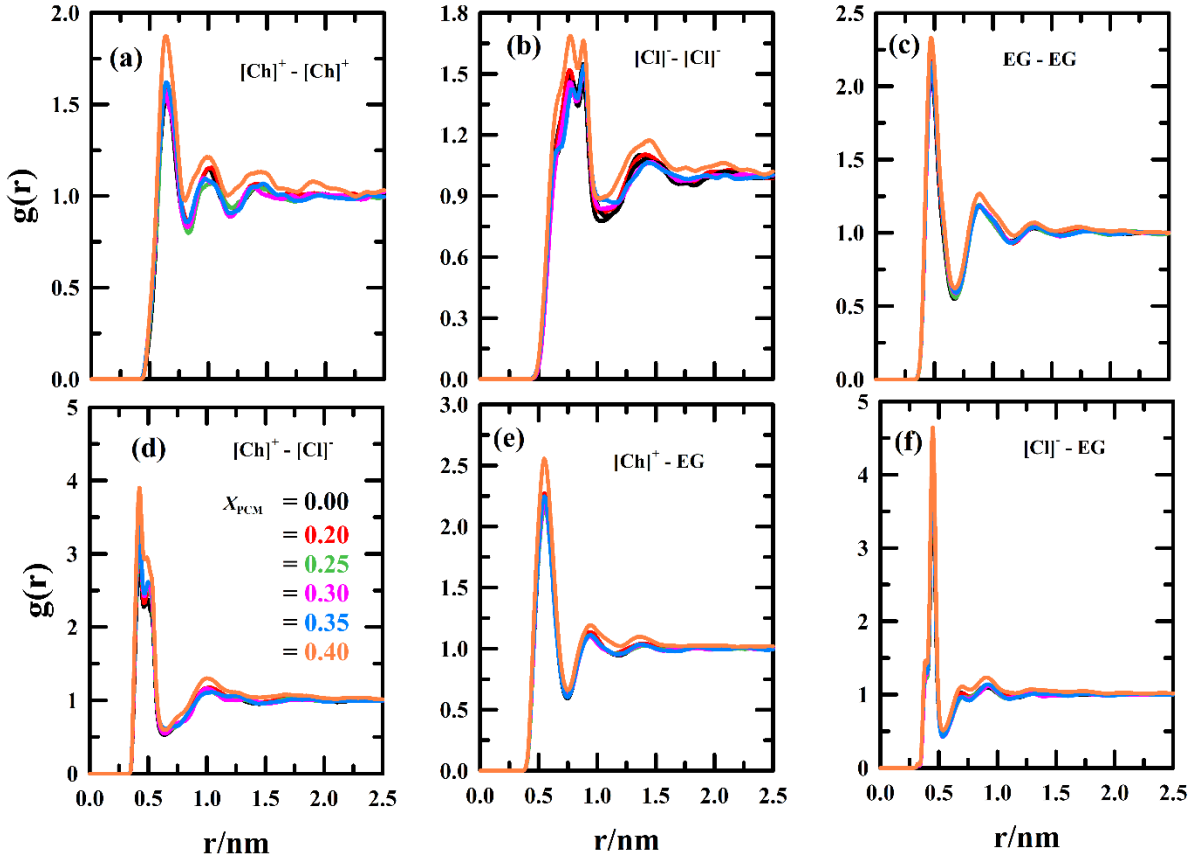

Figure 5.A.2: Center-of-mass (COM) radial distribution functions, g(r), for the reported (ChCl + EG) DES + paracetamol solutions from MD simulation at 298 K and 1 bar. Each concentration is uniquely color-coded.

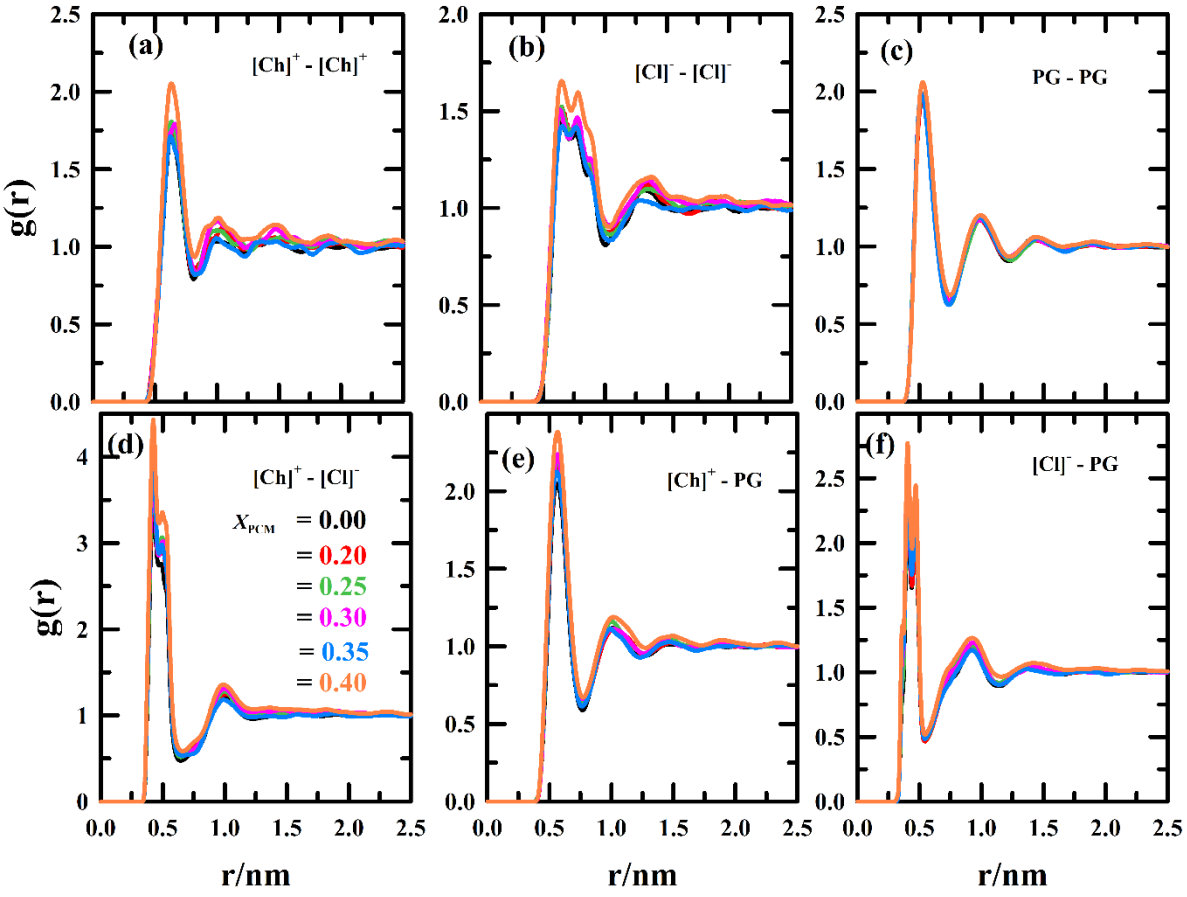

Figure 5.A.3: Center-of-mass (COM) radial distribution functions, g(r), for the reported (ChCl + PG) DES + paracetamol solutions from MD simulation at 298 K and 1 bar. Each concentration is uniquely color-coded.

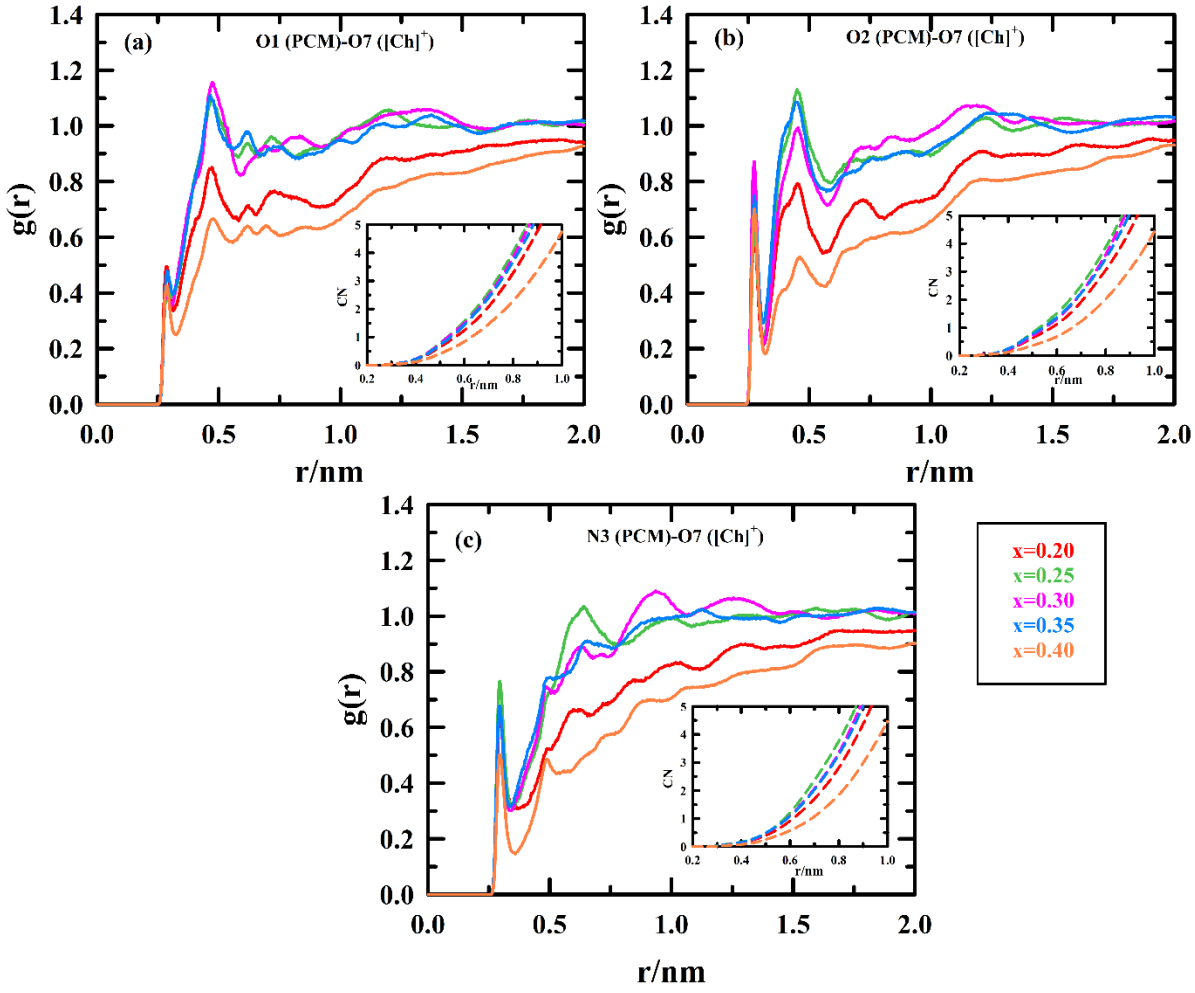

Figure 5.A.4: Site-site RDFs, g(r), for the reported (ChCl + EG) DES + paracetamol solutions from MD simulation at 298 K and 1 bar. Results show interactions between $[Ch]^+$ and PCM. Running coordination numbers (CN) are shown in the inset of each graph.

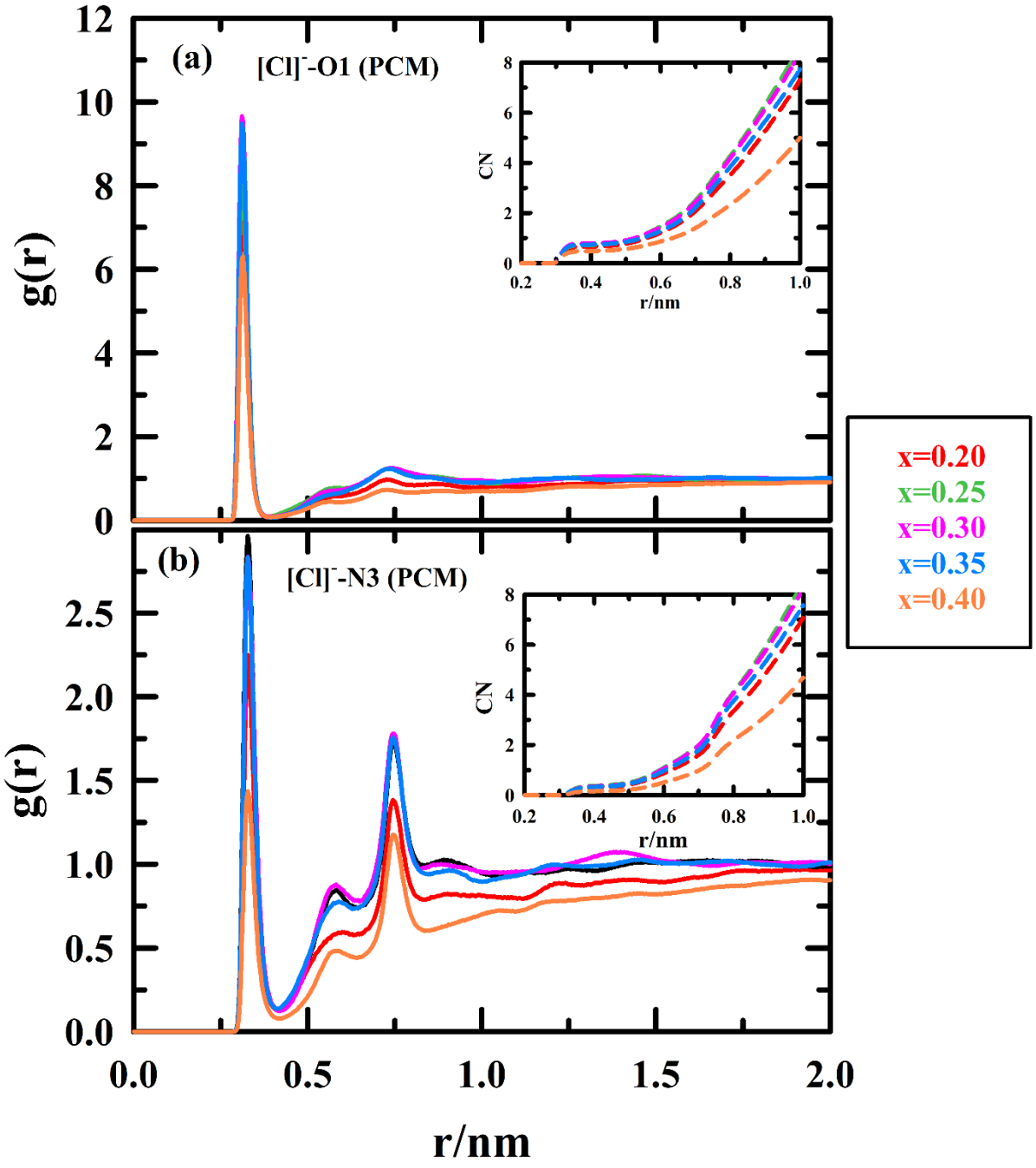

Figure 5.A.5: Site-site RDFs, g(r), for the reported (ChCl + EG) DES + paracetamol solutions from MD simulation at 298 K and 1 bar. Results show interactions between $[Cl]^-$ and PCM. Running coordination numbers (CN) are shown in the inset of each graph.

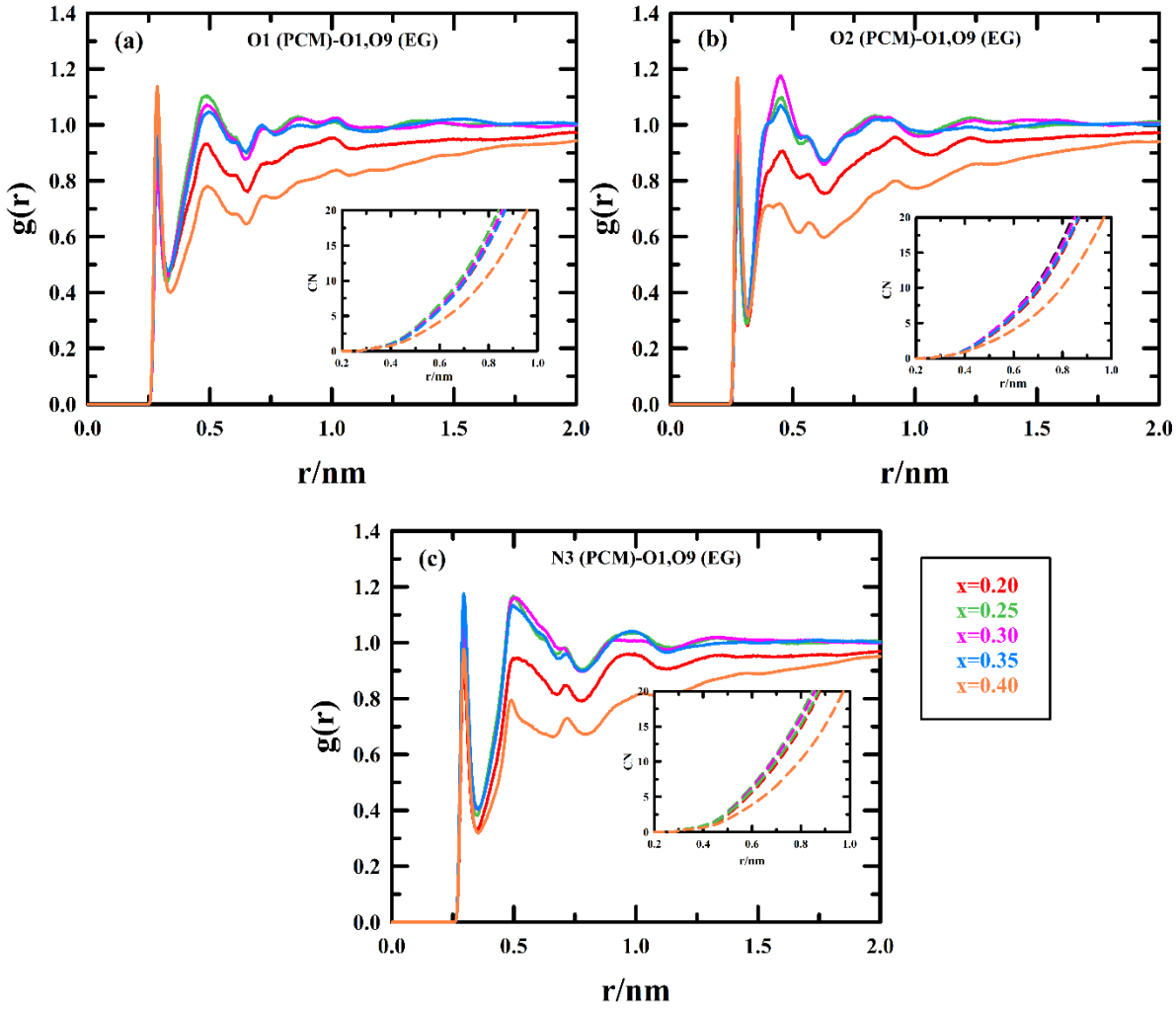

Figure 5.A.6: Site-site RDFs, g(r), for the reported (ChCl + EG) DES + paracetamol solutions from MD simulation at 298 K and 1 bar. Results show interactions between EG and PCM. Running coordination numbers (CN) are shown in the inset of each graph.

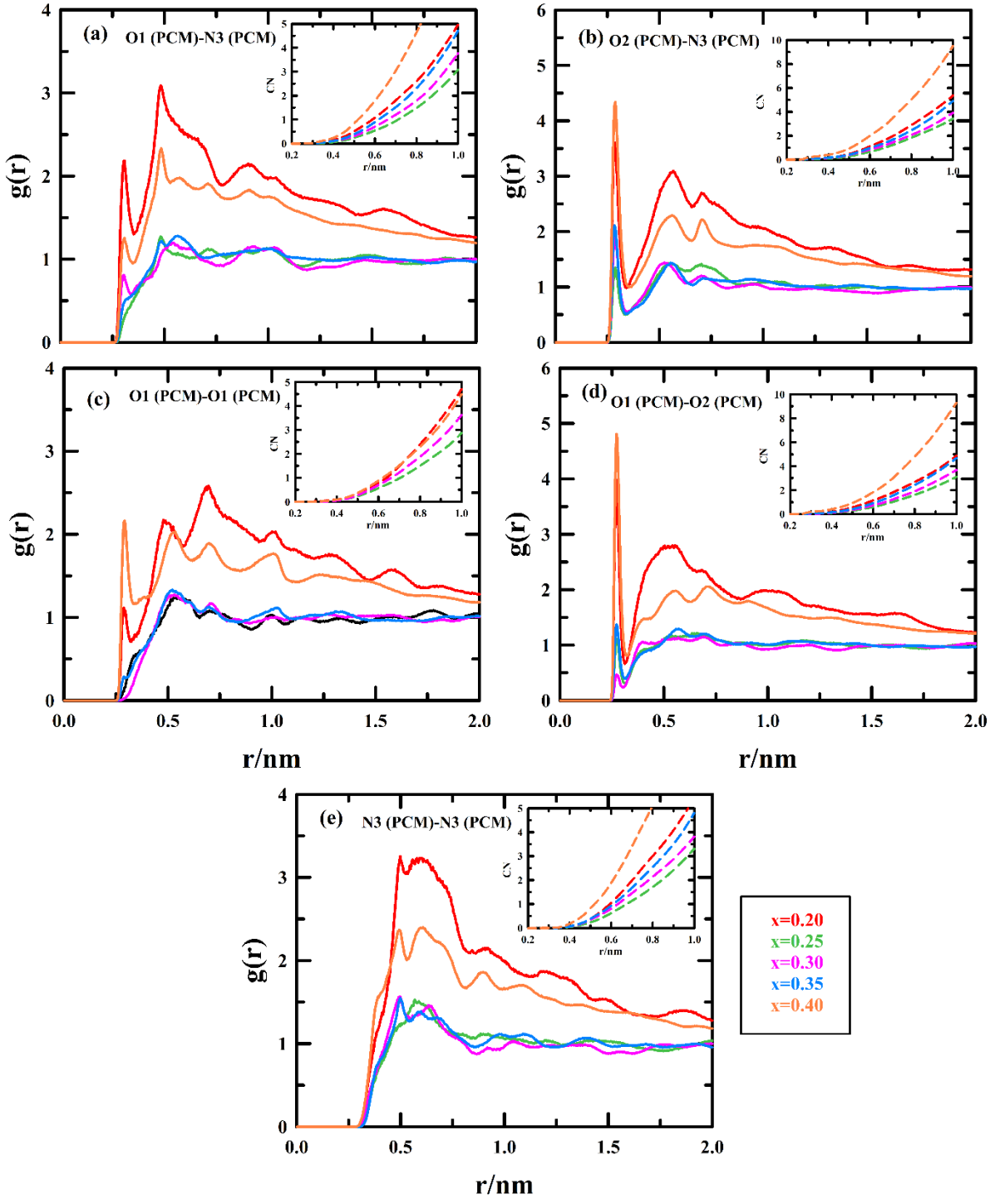

Figure 5.A.7: Site-site RDFs, g(r), for the reported (ChCl + EG) DES + paracetamol solutions from MD simulation at 298 K and 1 bar. Results show interactions between PCM molecules. Running coordination numbers (CN) are shown in the inset of each graph.

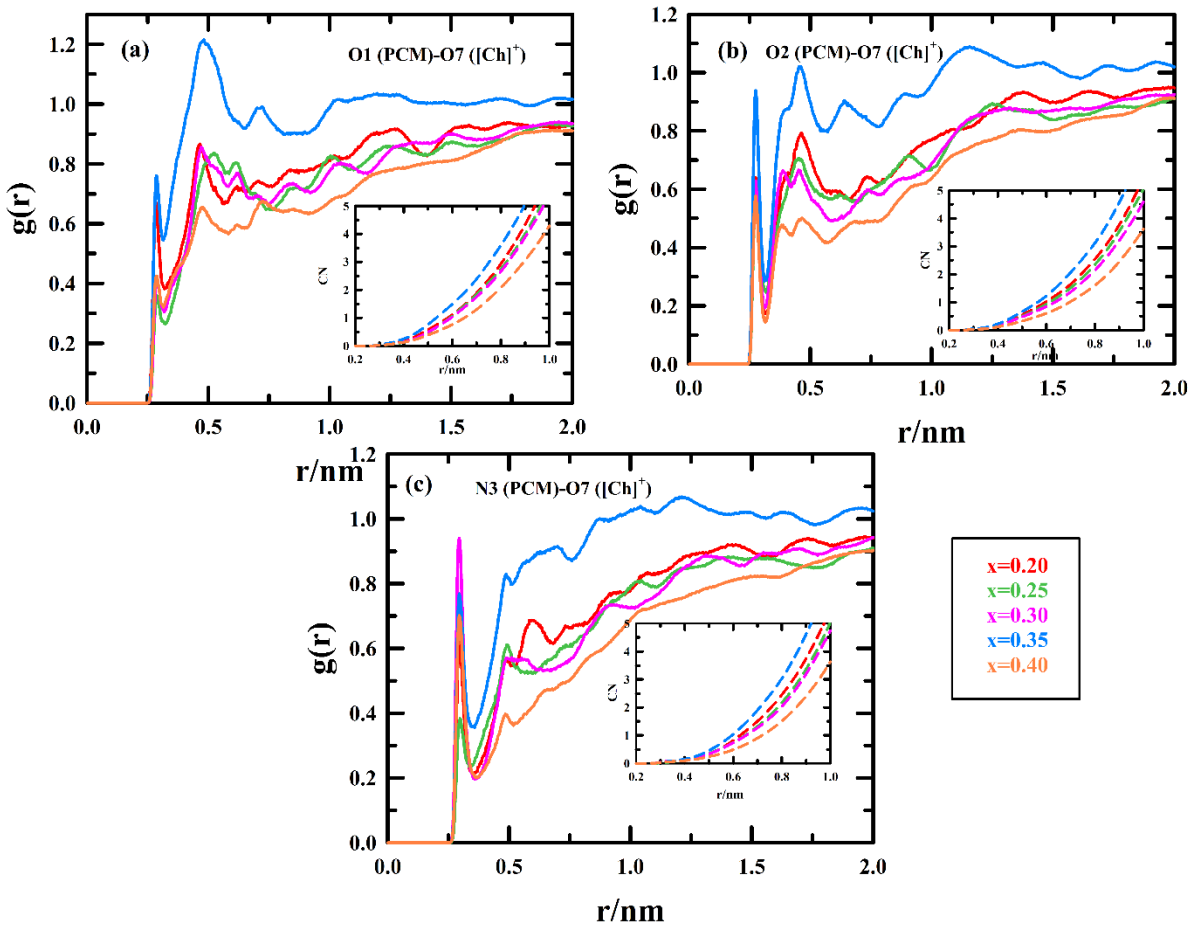

Figure 5.A.8: Site-site RDFs, g(r), for the reported (ChCl + PG) DES + paracetamol solutions from MD simulation at 298 K and 1 bar. Results show interactions between $[Ch]^+$ and PCM. Running coordination numbers (CN) are shown in the inset of each graph.

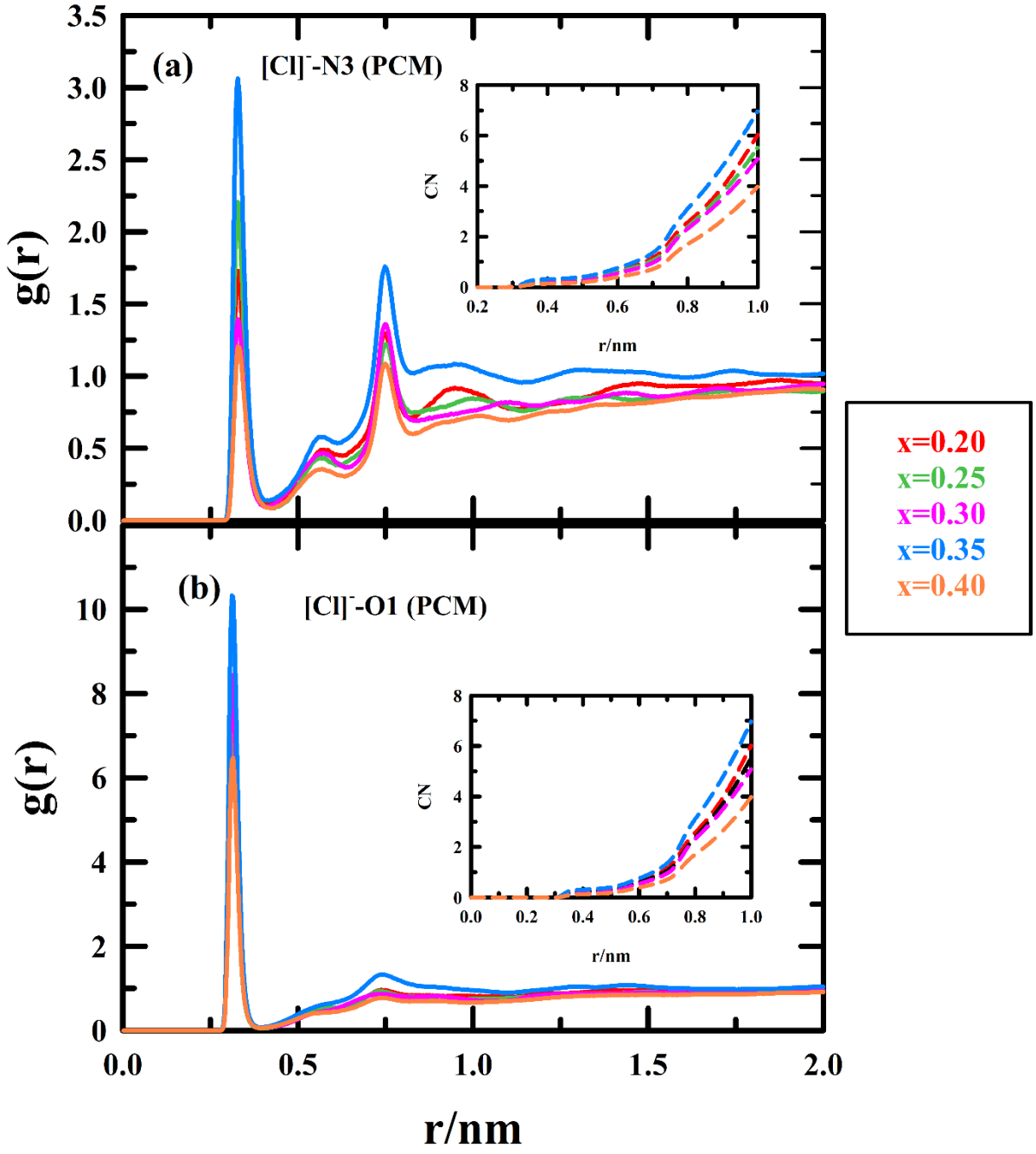

Figure 5.A.9: Site-site RDFs, g(r), for the reported (ChCl + PG) DES + paracetamol solutions from MD simulation at 298 K and 1 bar. Results show interactions between $[Cl]^-$ and PCM. Running coordination numbers (CN) are shown in the inset of each graph.

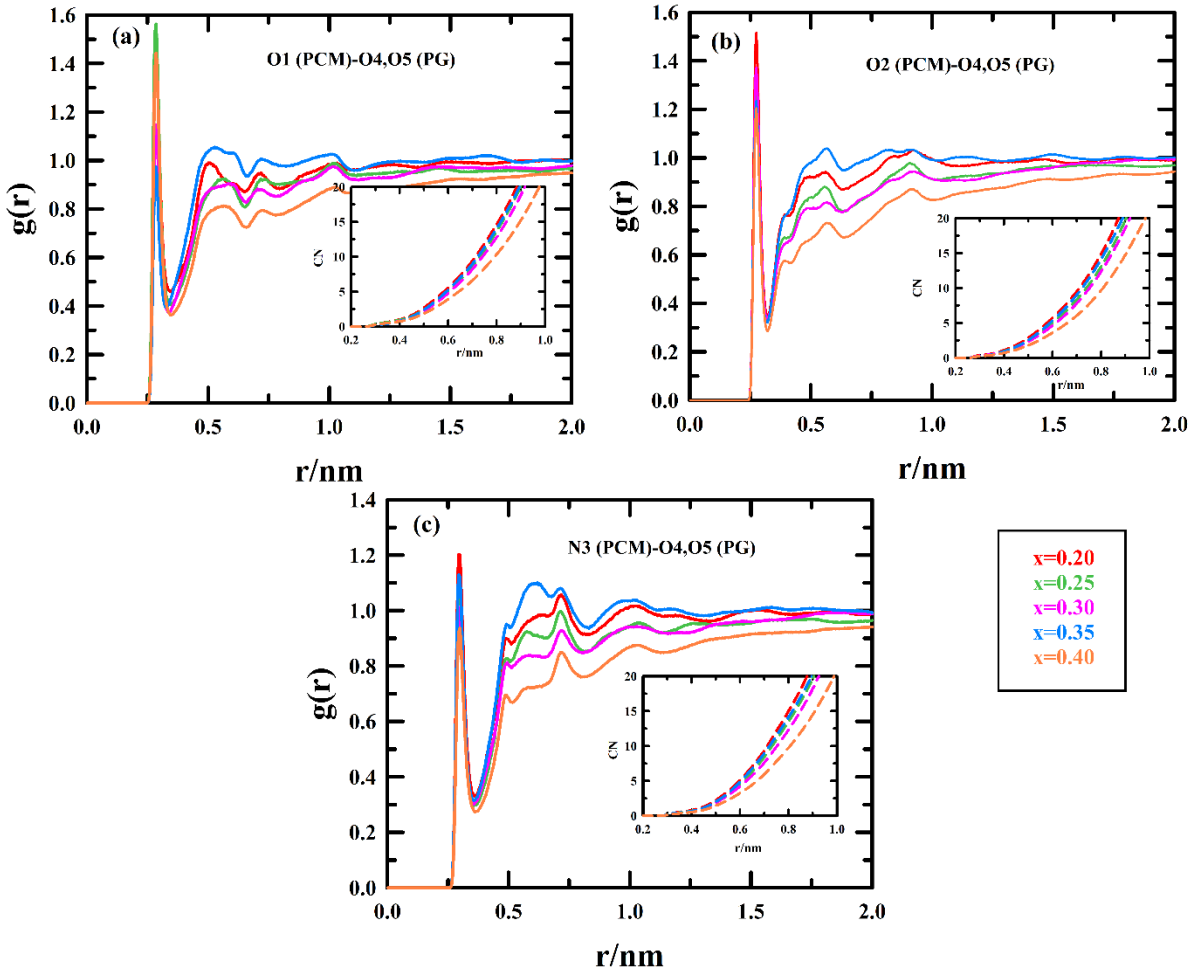

Figure 5.A.10: Site-site RDFs, g(r), for the reported (ChCl + PG) DES + paracetamol solutions from MD simulation at 298 K and 1 bar. Results show interactions between PG and PCM. Running coordination numbers (CN) are shown in the inset of each graph.

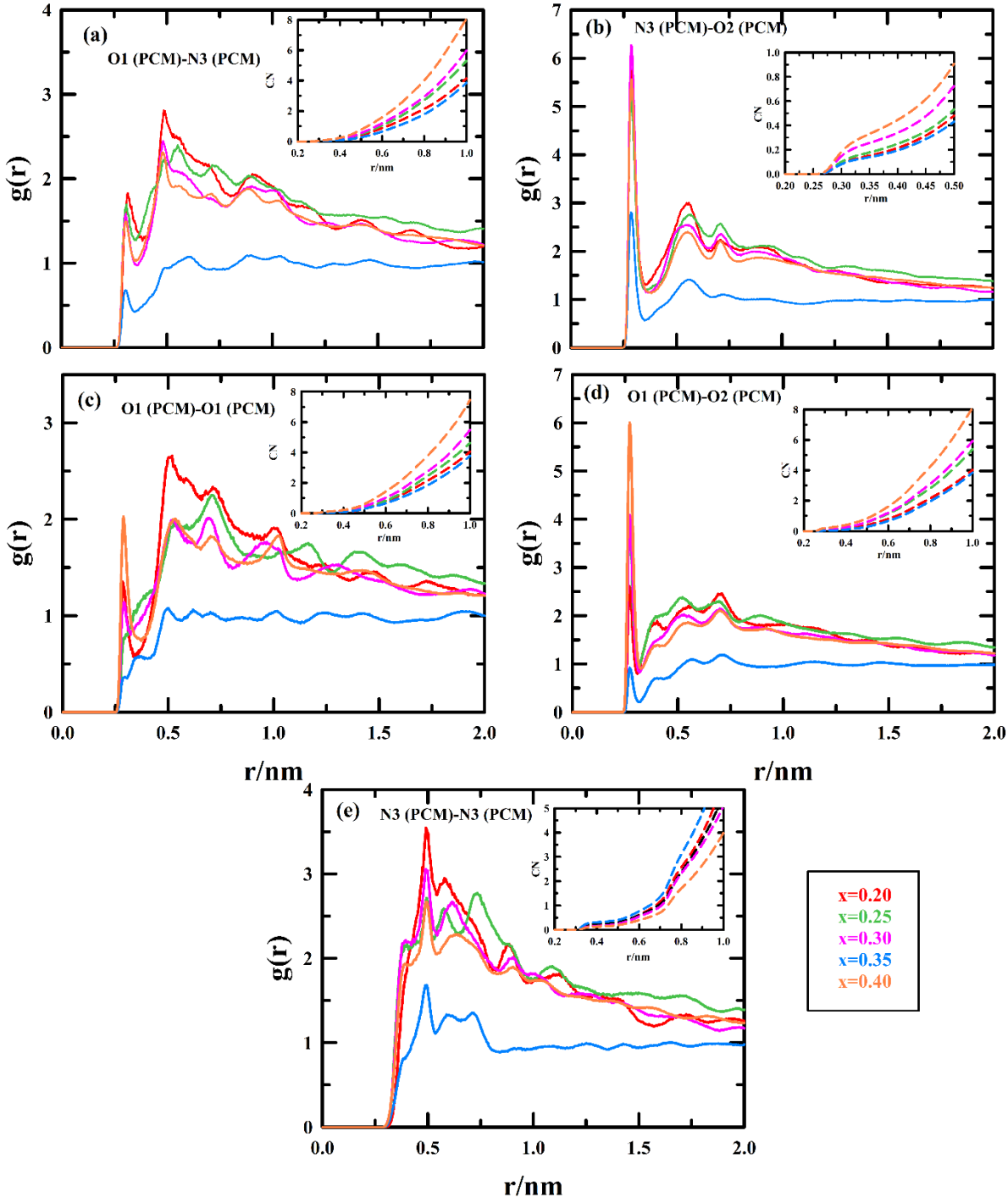

Figure 5.A.11: Site-site RDFs, g(r), for the reported (ChCl + PG) DES + paracetamol solutions from MD simulation at 298 K and 1 bar. Results show interactions between PCM molecules. Running coordination numbers (CN) are shown in the inset of each graph.

References

1 M. F. Francis, M. Cristea and F. M. Winnik, *Pure Appl. Chem.*, 2004, **76**, 1321–1335.

2 V. Saharan, V. Kukkar, M. Kataria, M. Gera and P. Choudhury, *Int. J. Health Res.*, 2009, **2**, 107–124.

3 V. Saharan, V. Kukka, M. Kataria, M. Gera and P. Choudhury, *Int. J. Health Res.*, 2009, **2**, 207–223.

4 M. Blessy, R. D. Patel, P. N. Prajapati and Y. K. Agrawal, *J. Pharm. Anal.*, 2014, **4**, 159–165.

5 M. Ferrit, C. del Valle and F. Martínez, *J. Mol. Liq.*, 2008, **142**, 64–71.

6 H. Mizuuchi, V. Jaitely, S. Murdan and A. T. Florence, *Eur. J. Pharm. Sci.*, 2008, **33**, 326–331.

7 K. B. Smith, R. H. Bridson and G. A. Leeke, *J. Chem. Eng. Data*, 2011, **56**, 2039–2043.

8 M. Moniruzzaman, N. Kamiya and M. Goto, *J. Colloid Interface Sci.*, 2010, **352**, 136–142.

9 M. Moniruzzaman, M. Tamura, Y. Tahara, N. Kamiya and M. Goto, *Int. J. Pharm.*, 2010, **400**, 243–250.

10 V. Jaitely, A. Karatas and A. T. Florence, *Int. J. Pharm.*, 2008, **354**, 168–173.

11 A. Paiva, R. Craveiro, I. Aroso, M. Martins, R. L. Reis and A. R. C. Duarte, *ACS Sustain. Chem. Eng.*, 2014, **2**, 1063–1071.

12 Q. Zhang, K. De Oliveira Vigier, S. Royer and F. Jérôme, *Chem. Soc. Rev.*, 2012, **41**, 7108–7146.

13 H. G. Morrison, C. C. Sun and S. Neervannan, *Int. J. Pharm.*, 2009, **378**, 136–139.

14 Y. Dai, J. van Spronsen, G.-J. Witkamp, R. Verpoorte and Y. H. Choi, *Anal. Chim. Acta.*, 2013, **766**, 61–68.

15 I. Mamajanov, A. E. Engelhart, H. D. Bean and N. V. Hud, *Angew. Chem., Int. Ed. Engl.*, 2010, **49**, 6310–6314.

16 M. Sharma, C. Mukesh, D. Mondal and K. Prasad, *RSC Adv.*, 2013, **3**, 18149–18155.

17 M. C. Serrano, M. C. Gutiérrez, R. Jiménez, M. L. Ferrer and F. del Monte, *Chem. Commun.*, 2012, **48**, 579–581.

18 R. J. Sánchez-Leija, J. A. Pojman, G. Luna-Bárcenas and J. D. Mota-Morales, *J. Mater. Chem. B*, 2014, **2**, 7495–7501.

19 I. M. Aroso, J. C. Silva, F. Mano, A. S. D. Ferreira, M. Dionísio, I. Sá-Nogueira, S. Barreiros, R. L. Reis, A. Paiva and A. R. C. Duarte, *Eur. J. Pharm. Biopharm.*, 2016, **98**, 57–66.

20 J. D. Mota-Morales, M. C. Gutiérrez, M. L. Ferrer, I. C. Sanchez, E. A. Elizalde-Peña, J. A. Pojman, F. Del Monte and G. Luna-Bárcenas, *J. Polym. Sci. A Polym. Chem.*, 2013, **51**, 1767–1773.

21 Z. Li and P. I. Lee, *Int. J. Pharm.*, 2016, **505**, 283–288.

22 K. Sekiguchi and N. Obi, *Chem. Pharm. Bull. (Tokyo)*, 1961, **9**, 866–872.

23 S. Jin, J. Jang, S. Lee and I. W. Kim, *Pharmaceutics*, 2020, **12**, 1098.

24 A. Y. Gasparyan, T. Watson and G. Y. H. Lip, *J. Am. Coll. Cardiol.*, 2008, **51**, 1829–1843.

25 C. Lu, J. Cao, N. Wang and E. Su, *Medchemcomm*, 2016, **7**, 955–959.

26 A. Gutiérrez, M. Atilhan and S. Aparicio, *J. Chem. Eng. Data*, 2020, **65**, 4669–4683.

27 A. Gutiérrez, M. Atilhan and S. Aparicio, *Phys. Chem. Chem. Phys.*, 2018, **20**, 27464–27473.

28 A. Gutiérrez, M. Atilhan and S. Aparicio, *J. Phys. Chem. B*, 2020, **124**, 1794–1805.

29 M. J. Abraham, D. Van Der Spoel, E. Lindahl and B. Hess, *GROMACS user manual version*.

30 J. Lee, X. Cheng, J. M. Swails, M. S. Yeom, P. K. Eastman, J. A. Lemkul, S. Wei, J. Buckner, J. C. Jeong, Y. Qi, S. Jo, V. S. Pande, D. A. Case, C. L. Brooks, A. D. MacKerell, J. B. Klauda and W. Im, *J. Chem. Theory Comput.*, 2016, **12**, 405–413.

31 L. Martínez, R. Andrade, E. G. Birgin and J. M. Martínez, *J. Comput. Chem.*, 2009, **30**, 2157–2164.

32 E. J. Haug, J. S. Arora and K. Matsui, *J. Optim. Theory Appl.*, 1976, **19**, 401–424.

33 G. Bussi, D. Donadio and M. Parrinello, *J. Chem. Phys.*, 2007, **126**, 14101.

34 H. J. C. Berendsen, J. P. M. Postma, W. F. van Gunsteren, A. DiNola and J. R. Haak, *J. Chem. Phys.*, 1984, **81**, 3684–3690.

35 U. Essmann, L. Perera, M. L. Berkowitz, T. Darden, H. Lee and L. G. Pedersen, *J. Chem. Phys.*, 1995, **103**, 8577–8593.

36 R. W. Hockney, S. P. Goel and J. W. Eastwood, *J. Comput. Phys.*, 1974, **14**, 148–158.

37 W. Humphrey, A. Dalke and K. Schulten, *J. Mol. Graph.*, 1996, **14**, 33–38.

38 M. Brehm, M. Thomas, S. Gehrke and B. Kirchner, *J. Chem. Phys.*, 2020, **152**, 164105.

39 M. Brehm and B. Kirchner, *J. Chem. Inf. Model*, 2011, **51**, 2007–2023.

40 M. J. Abraham, D. van der Spoel, E. Lindahl, B. Hess and and the GROMACS development team, GROMACS User Manual version 2018, http://www.gromacs.org.

41 P. M. Gallagher, M. P. Coffey, V. J. Krukonis and N. Klasutis, in *Supercritical Fluid Science and Technology*, eds. K. P. Johnson and J. M. L. Penninger, American Chemical Society, Washington D.C., 1989, pp. 334–354.

42 A. Luzar and D. Chandler, *Nature*, 1996, **379**, 55–57.

43 A. Luzar and D. Chandler, *Phys. Rev. Lett.*, 1996, **76**, 928–931.

44 E. S. C. Ferreira, I. V. Voroshylova, C. M. Pereira and M. N. D. S. Cordeiro, *J. Phys. Chem. B*, 2016, **120**, 10124–10137.

Chapter 6

Can the structural and dynamical behaviors of ChCl:EG mixtures provide insight into deep eutectic formation?

6.1 Introduction

Deep eutectic solvents (DESs) are a relatively new class of environmentally friendly solvents.[1] They offer an appealing alternative to ionic liquids and traditional organic solvents due to their eco-friendly nature, cost-effectiveness, and unique properties.[2–4] They hold enormous potential across a wide range of applications, including metal processing, gas absorption, chemical synthesis, and biotransformation.[5–14]

DESs are multi-component mixtures which melt at a much lower temperature than the melting points of individual components.[1] Depending on their components, DESs are classified into different types.[5,15] As the prefix 'deep' suggests, the depression in freezing point (ΔT_f) of a DES must be significantly greater than the ideal eutectic mixture.[16] However, the definition of DES is neither universal nor straightforward. The best way to characterize a mixture as DES is to assess the corresponding solid-liquid phase diagram.[17] In many cases the lack of fusion enthalpy data hinders the possibility of calculation of phase diagram.[16] Although several experimental[18–21] and theoretical[22–26] studies reveal the importance of hydrogen bond (H-bond) network in lowering the melting point, the mere presence of the same does not guarantee the formation of DES.[27]

A DES is often defined by ΔT_f as well as a fixed molar ratio between the components, such as, choline chloride (ChCl) and urea form DES at 1:2 mole ratio.[28,29] Hence, the question arises that how rigid or significant this ratio is? What happens when the composition is slightly changed in either way of the fixed composition? This is one of our motivations for this study.

One of the most celebrated and studied DESs, reline remains liquid at ~285 K whereas the melting temperatures of ChCl and urea are ~575 K and ~406 K, respectively.[29] However, recent studies report a substantially higher melting point for samples with low water content.[30,31] Many DESs proposed in the literature do not meet the criteria of either eutectic or pronounced

ΔT_f or both.[16] For ethaline (ChCl: ethylene glycol (EG) = 1:2) which is believed to be a DES with melting point of ~208 K, recent observations cast doubt on it.[32–34] The eutectic composition is reported as at 1:4.85 molar ratio of ChCl: EG.[32] The melting point of this mixture is ~244 K, which is only ~16 K lower than the melting point of pure EG. Therefore, it has been decided that ethaline (ChCl:2EG mixture) cannot be considered to be a DES as neither the composition nor the extent of freezing-point depression support this. Another study reports the eutectic composition at the mole fraction of ChCl (X_{ChCl}) lies between 0.01 to 0.02.[33] Here, the melting temperature is ~245 K. Therefore, it is clear that the mixture of ChCl and EG is not a 'deep' eutectic one, rather simply eutectic and the eutectic composition is unanimously not defined yet.

Both simulation[35] and experimental[32,33] studies have been performed to elucidate the composition effects on possible eutectic formation. The simulation study is limited to only two compositions (X_{ChCl} = 0.333, 0.5).[35] They primarily focused on the changes in structural properties. The experimental study measured the conductivity and followed dielectric relaxation for several mixtures with X_{ChCl} varying from 0.0056 to 0.3333.[34] In this study, they did not detect any 'magic composition' and described the mixtures as simple binary mixtures.[34]

In this context, it is crucial to study the inherent structure and dynamics of ChCl:EG mixtures for a rather large range of composition. It is one of the systems of immense interest due to wide application window, such as, metal processing,[36–39] drug solubility[40] etc. Experimental studies performed so far aimed at quantifying physicochemical properties[41,42] and exploring potential applications,[43,44] while computational investigations delved into uncovering the inherent interactions and their influences on molecular-level solution structures.[45–48] Here, our focus is to perform simulation studies for a wide range of compositions, carefully observe the various structural and dynamical changes across the mixtures and, detect any possible anomalous behavior at a particular composition which might indicate formation of a DES.

In this study, we calculated several composition dependent structural and dynamic properties of the mixture, such as, densities, radial distribution functions (RDFs), coordination numbers (CNs), average number of hydrogen bonds per molecules or moieties, dielectric relaxation parameters, structural hydrogen bond relaxation functions, and viscosity coefficients (or simply viscosities). Our results indicate that the structural and dynamic properties of the mixture vary significantly with composition. We have also observed that the number of hydrogen bonds and the structural hydrogen bond relaxation time decrease with increasing ChCl concentration.

Additionally, viscosity and density of the mixtures show expected changes with the composition.

6.2 Computational details

Five mixtures of ChCl and EG with different concentrations, along with pure EG have been studied via classical molecular dynamics (MD) simulation method in GROMACS-2018.3 package.[49] Molecules were inserted into simulation boxes using PACKMOL.[50] Details of systems can be found in Table 6.A.1. The force field parameters were generalized Amber force field (GAFF)-type and taken from literature.[51] First, each box was energy minimized by steepest descent algorithm.[52] Then each system was subjected to equilibration in NVT condition for 10 ns. The systems were further equilibrated in NPT condition for 20 ns. The temperature and pressure were controlled by using Nosé-Hoover thermostat[53] and Parrinello-Rahman barostat,[54] respectively. The corresponding time-constants were 0.1 ps and 0.5 ps, respectively. The simulations were carried out at 298.15 K and 1 bar. The equilibrated structures are further subjected to production runs in NPT conditions for 100 ns. The trajectory files were saved at every 0.5 ps to calculate density, self-diffusion constants and structural properties. Separate runs, each spanning 100 ns in NVT condition, were performed to calculate dynamic properties where trajectories are saved at every 0.1 ps. Another five separate NVT runs for each composition were performed to calculate viscosity. In these runs the energy files were stored in a frequency of 5 fs. The bonds involving H were kept constraint using the LINCS algorithm. The long-range electrostatic interactions were modelled with PPME method. A short-range cut-off distance of 1.2 nm was set for both van der Waals and coulombic interactions. The equations of motion were integrated using leap-frog algorithm with a time step of 1 fs.

All the trajectory analyses and calculations were done using GROMACS, TRAVIS[55,56] and in-house codes.

6.3 Results and discussion

6.3.1 Thermophysical properties and force field validation

We have calculated density, viscosity and self-diffusion coefficients for each composition. These properties are important because they provide valuable insights into the behavior and

characteristics of the deep eutectic solvent mixtures. Moreover, these properties are often used as good measures to check the fidelity of force field parameters.

6.3.1.1 Density

Density offers information about how closely packed the molecules are within the solvent, which can have implications for its overall structure and stability. We have calculated the density values and shown in Table 6.A.2 along with experimental results.[57] The simulation and measured values are in close agreement and validates the efficacy of the used force field model.

6.3.1.2 Viscosity

Viscosity measures the resistance of the solvent to flow. We have used Green-Kubo relation to calculate the viscosity for both pure EG and ChCl/EG mixtures.

The viscosity is calculated from the integration of pressure tensor autocorrelation functions at long time.[58]

$$\eta = \frac{V}{6k_BT}\sum_{\alpha\leq\beta}\int_0^\infty \langle \bar{P}_{\alpha\beta}(t).\bar{P}_{\alpha\beta}(0)\rangle\, dt \qquad (6.1)$$

where V, k_B, T are system volume, Boltzmann constant and temperature, respectively. $\bar{P}_{\alpha\beta}$ indicates a modified pressure tensor. Six different types of pressure tensor elements are considered to improve the statistics: $\bar{P}_{xy} = P_{xy}$, $\bar{P}_{yz} = P_{yz}$, $\bar{P}_{xz} = P_{zx}$, $\bar{P}_{xx} = 0.5(P_{xx} - P_{yy})$, $\bar{P}_{yy} = 0.5(P_{yy} - P_{zz})$, $\bar{P}_{zz} = 0.5(P_{xx} - P_{zz})$. The calculated shear viscosities are shown in Figure 6.1 with experimental values.[51] Time-dependent shear viscosity values are displayed in Figure 6.A.1.

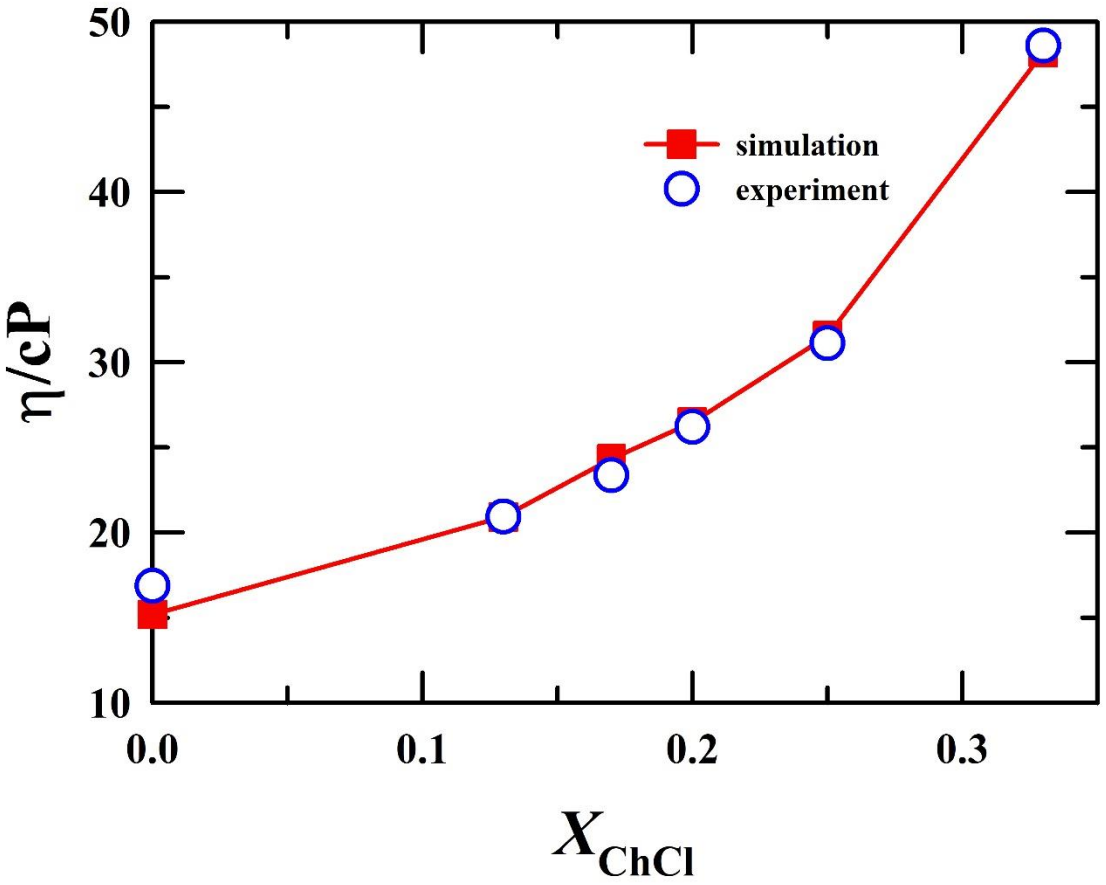

Figure 6.1: Concentration-dependent simulated and experimental[51] shear viscosity values at 298 K. The solid line through simulated data points is only a guide to bare eyes.

Figure 6.1 clearly illustrates a remarkable agreement between simulations and experiments. This striking agreement reinforces our confidence in the accuracy and effectiveness of the force field parameters we employed in our study. Another aspect to note that as the quantity of choline chloride (ChCl) within the solution increases, there is a discernible and noteworthy rise in the viscosity of the mixture.

6.3.1.3 Self-diffusion coefficient

The self-diffusion coefficients were determined by analyzing the mean-square displacements (MSDs) of the center of mass of each species through molecular dynamics simulations, employing the Einstein relation.[59]

$$D = \frac{1}{6}\lim_{t\to\infty}\frac{\mathrm{d}}{\mathrm{dt}}\frac{1}{N}\sum_{i=1}^{N}\langle|\mathbf{r}_i(t)-\mathbf{r}_i(0)|^2\rangle \qquad (6.2)$$

Here, $\mathbf{r}_i(t)$ represents the position of the center of mass of species i at time t, and N denotes the total number of individual species in the system. We have calculated the self-diffusion coefficients of these components by analyzing the MSD plots in the limit of long-time.

The diffusive regime of the MSD plots was determined by calculating the $\beta(t)$ parameter which is defined as:[60]

$$\beta(t) = \frac{\mathrm{d}\log\langle|\mathbf{r}_i(t)-\mathbf{r}_i(0)|^2\rangle}{\mathrm{d}\log t} \tag{6.3}$$

At $\beta \sim 1$, the system is in diffusive regime and it is suitable to calculate self-diffusion coefficient at that region.

The simulated MSDs along with their corresponding $\beta(t)$ values as a function of time for various ChCl/EG mixtures are shown in Figure 6.2. As the concentration rises, the movement of all species, regardless of their type, slows down. This decrease in translational dynamics can be attributed to the higher viscosity of the solutions at higher concentrations. Comparing the MSD values, we find that within the duration of our simulations, ethylene glycol (EG) covers the most distance, while $[Ch]^+$ travels the least.

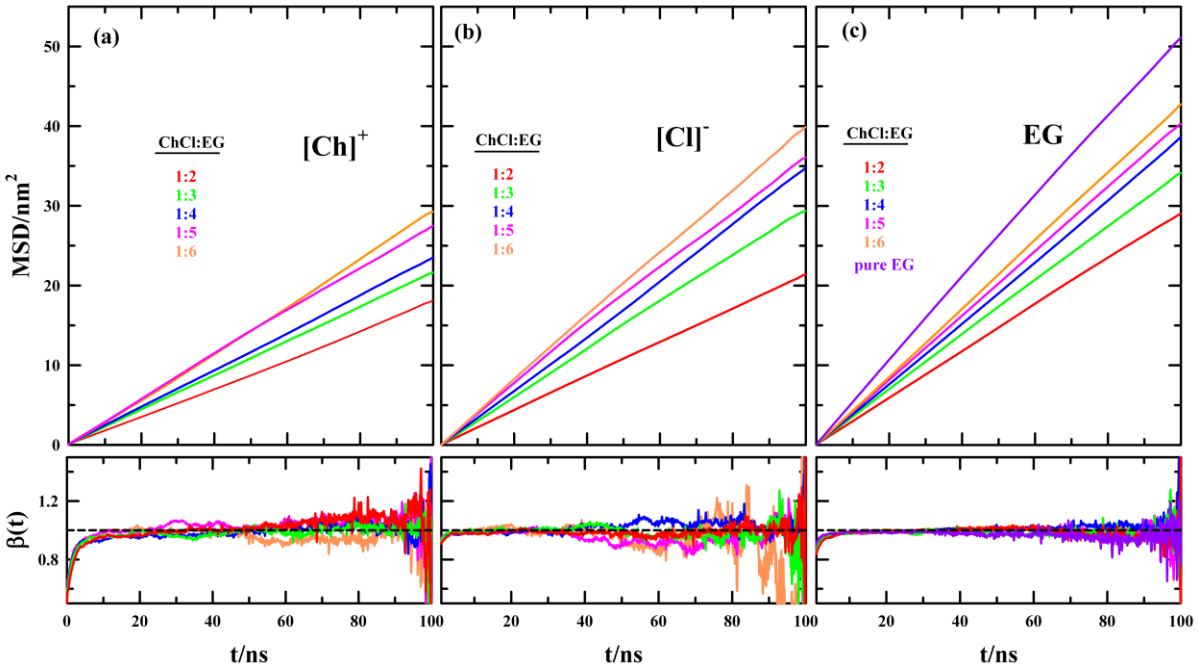

Figure 6.2: MSD and $\beta(t)$ plots for (a) $[Ch]^+$, (b) $[Cl]^-$ and (c) EG at various concentrations. Each composition is uniquely color-coded.

The self-diffusion coefficient values for components of ChCl/EG mixtures are calculated from MSD and shown in Table 6.1.

Table 6.1: The calculated self-diffusion coefficient values of components of ChCl/EG mixtures at 298 K. The experimental[61] values are shown in parentheses.

ChCl:EG	**D (/10^{-11} m^2/s)**		
	$[Ch]^+$	**$[Cl]^-$**	**EG**
1:2	2.93 (2.62)	3.59	4.91 (4.77)
1:3	3.59	5.07	5.68
1:4	4.01	5.61	6.41
1:5	4.79	6.44	6.74
1:6	4.93	6.80	7.17
Pure EG			8.80 (8.34)

Consistent with our observations in the MSD analysis, the diffusion coefficient values follow a similar trend of mobility. An interesting point worth noting is that our simulation model tends to slightly overestimate the diffusion coefficients, both for the ChCl:2EG mixture and pure EG (comparison to experimental[61] values is possible for only this two compositions). However, the deviation in the diffusion coefficients is within a reasonable margin of error, typically lying below 10%. The close agreement between the experimental and simulated diffusion coefficients highlights the overall effectiveness of our model potential. At a particular solution, the diffusion coefficients follow the trend: $D_{[Ch]^+}<D_{[Cl]^-}<D_{EG}$. This difference in mobility can be explained in terms of their charge and size. The $[Ch]^+$ cations are relatively large and carry a positive charge. Their larger size can lead to slower diffusion as they experience greater frictional resistance while moving through the solution. Additionally, the positive charge can interact with negatively charged species (such as chloride ions) in the solution, further affecting their mobility. On the other hand, $[Cl]^-$ ions are smaller than choline cations and carry a negative charge. While their smaller size allows for more rapid movement through the solution, their negative charge can lead to interactions with positively charged species, such as choline cations, which can slightly hinder their diffusion. Although EG molecules are larger than chloride ions, they lack a net charge. Their larger size contributes to some hindrance in

diffusion, but the absence of a charge means they do not strongly interact with other charged species. As a result, EG molecules exhibit relatively higher diffusion coefficients compared to ions.

6.3.2 Liquid structure

6.3.2.1 Radial distribution function (RDF)

We have calculated center of mass (COM) RDFs to gain insight into how molecules are organized around each other at the microstructural level. Figure 6.3 shows the RDFs of center of mass of cation and anion whereas Figure 6.4 illustrates the arrangement of other species around EG.

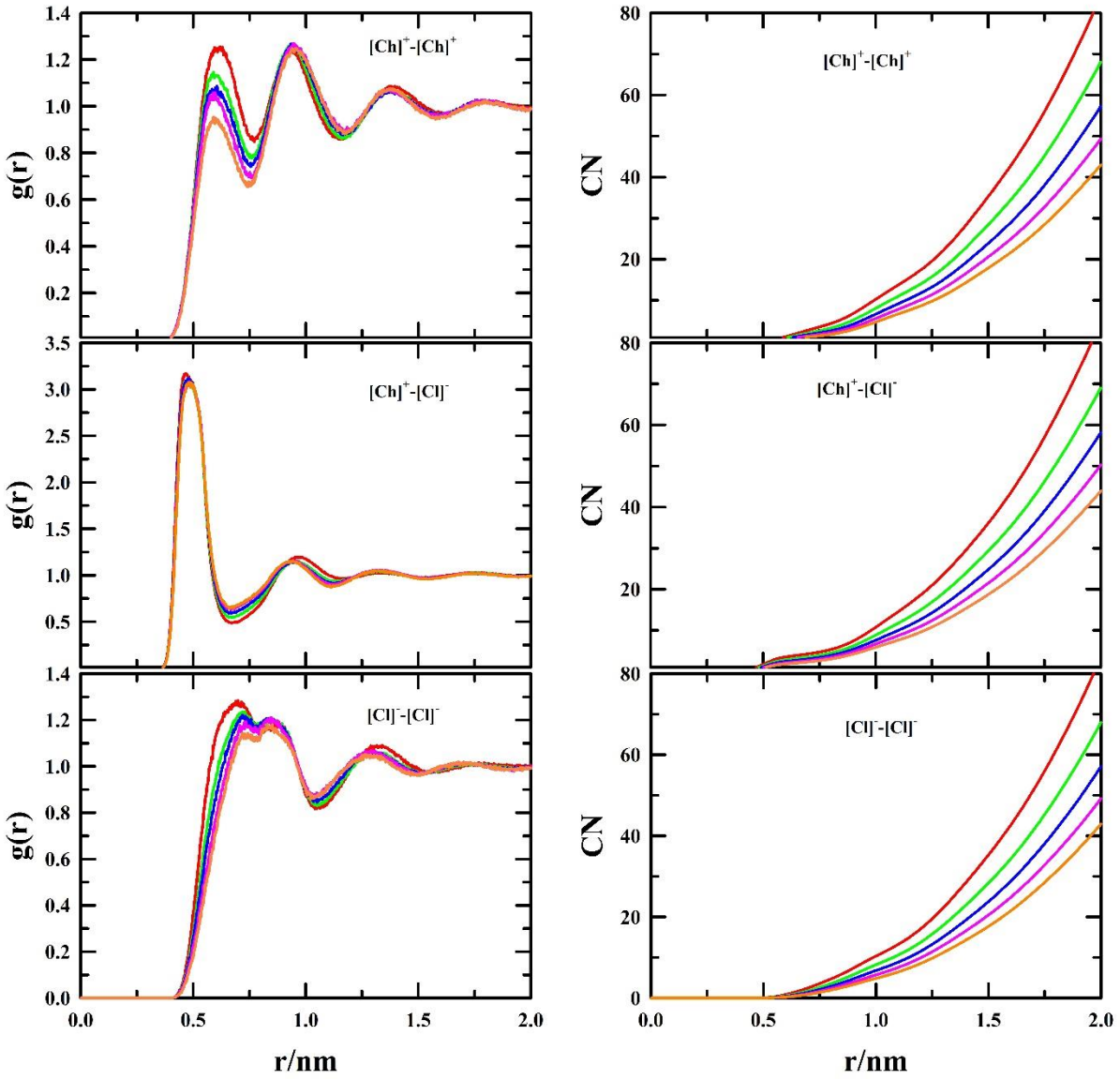

Figure 6.3: Center of mass radial distribution functions (RDFs) and coordination numbers (CNs) are presented for both oppositely charged ions and like ions in all five systems (ChCl:2EG - red, ChCl:3EG - green, ChCl:4EG - blue, ChCl:5EG - pink, ChCl:6EG - orange). Notably, the CNs for $[Ch]^+$-$[Cl]^-$ interaction are similar to those for $[Cl]^-$-$[Ch]^+$.

An inspection of these figure reveals that the peak positions remain nearly constant at all concentrations. However, the coordination numbers (CNs) either increase or decrease monotonically. This change in the number of observed molecules or ions in the solvation shells around a reference molecule or ion can be attributed to the increasing concentration of ions in the solution as ChCl is incrementally introduced. The stability of peak positions suggests that there is no sudden alteration in the structural arrangement of mixtures.

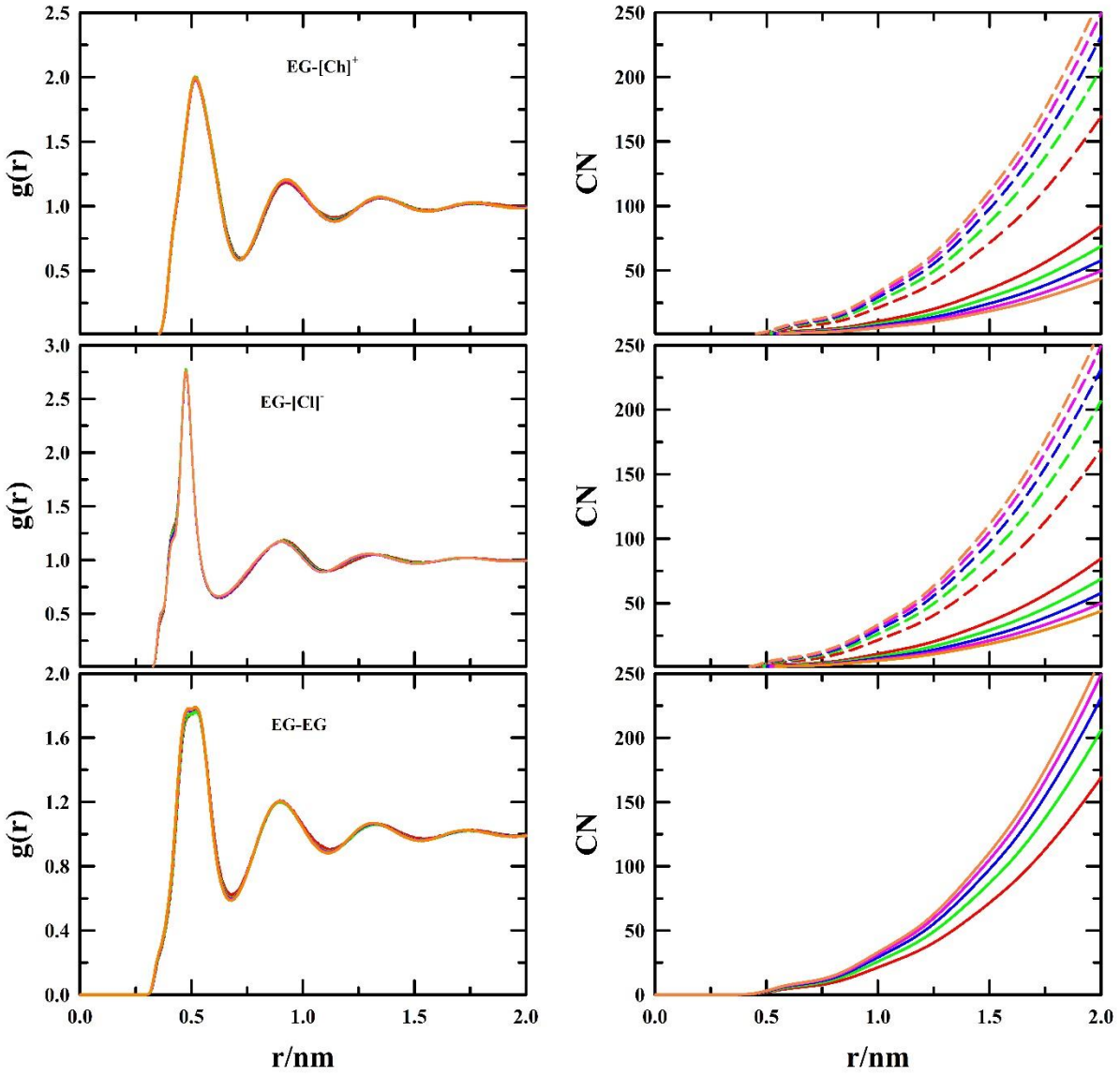

Figure 6.4: Center of mass Radial Distribution Functions (RDFs) and Coordination Numbers (CNs) are presented for interactions involving EG as the reference molecule in all five systems (ChCl:2EG - red, ChCl:3EG - green, ChCl:4EG - blue, ChCl:5EG - pink, ChCl:6EG - orange). In the coordination number plots of EG-$[Ch]^+$ and EG-$[Cl]^-$ interactions the solid lines indicate number of ions around EG and, the dashed lines indicate number of EG around ions.

The two strongest interactions are appeared to be involving $[Cl]^-$ anion with $[Ch]^+$ cation and EG. The cation-anion interaction involves the electrostatic as well as hydrogen bonding (H-bonding) interactions whereas EG interacts only through H-bonding. For the $[Ch]^+$-$[Ch]^+$ RDF the main peak appears at ~0.61 nm. Notably, as the ChCl content increases, the peak becomes more pronounced, with its height steadily rising. Additionally, there is a subtle, gradual shift in the peak position towards slightly longer distances. This observation can be explained by the

intensified interactions between $[Ch]^+$ ions as the concentration of the solution increases. Conversely, the cation-anion RDF exhibits an intense primary peak at ~0.47 nm bearing the signature of a strong $[Ch]^+$-$[Cl]^-$ interaction. A distinct peak at ~0.5 nm is observed for $[Ch]^+$-EG interactions in all concentrations. This peak reveals a preferred distance at which EG molecules are situated concerning cations. These findings indicate that the primary layer surrounding the cation consists mainly of anions, followed by EG, with the cation residing in the outermost layer. The anion-anion RDFs present a unique pattern with a bifurcated peak structure. The primary peak, located at approximately 0.7 nm, is followed by a secondary peak at around 0.84 nm. This dual-peak pattern suggests that anions exhibit two preferred distances from each other. This complexity hints at a multifaceted structural organization among anions, likely influenced by various factors within the solution. In contrast, the RDF between EG molecules showed a single peak with a maximum at about 0.5 nm. This peak highlights the characteristic distance at which EG molecules tend to be positioned around other EG molecules. This implies a specific arrangement or clustering behavior of EG molecules, contributing to the overall solution structure. Lastly, when examining the RDF between anions and EG, the peak appeared at less than 0.5 nm. This proximity suggests a close association between anions and EG molecules, possibly indicating a strong interaction between these species. We will discuss more about the liquid structure in the following two sections.

6.3.2.2 Spatial distribution function (SDF)

We used spatial distribution functions (SDFs) to visualize how molecules are arranged in three-dimensional space. In our analysis, we selected one choline cation as a reference point, and then we displayed the distribution of the center of mass (COM) of other species (cation, anion, and EG) around it. Figure 6.5 shows concentration-dependent SDFs, with the $[Ch]^+$ cation as the reference. In Figures 6.5(a)-(e), the concentration of the solution gradually decreases. As indicated by the RDF analysis, the $[Cl]^-$ anions are closest to $[Ch]^+$, followed by EG. With dilution, the concentration of $[Ch]^+$ (orange) decreases while that of EG (violet) increases.

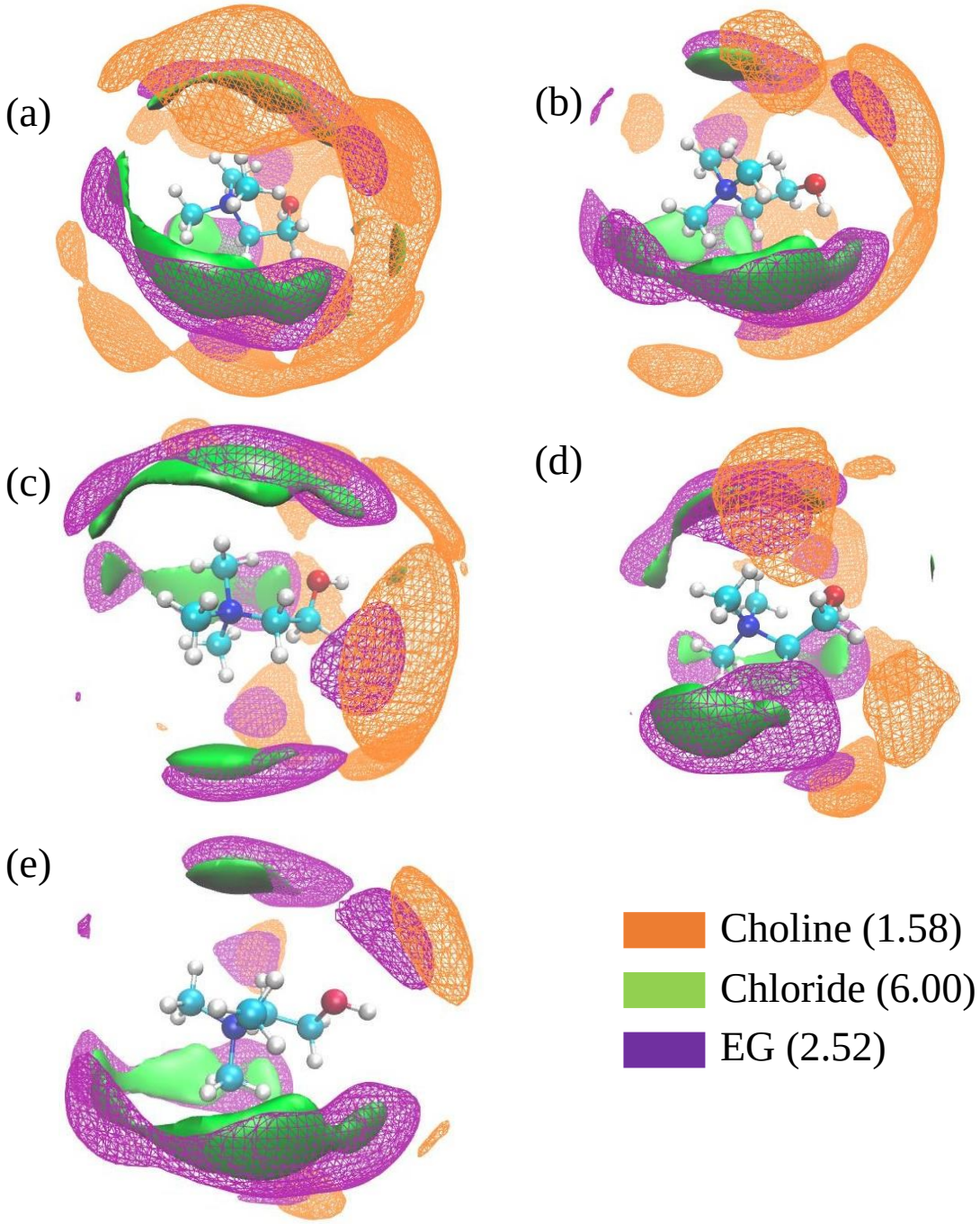

Figure 6.5: Three-dimensional spatial distribution function (SDF) of center of mass of $[Ch]^+$ cation (orange color), $[Cl]^-$ anion (green color), EG (violet color) about a central choline cation for (a) ChCl:2EG, (b) ChCl:3EG, (c) ChCl:4EG, (d) ChCl:5EG, (e) ChCl:6EG at 298.15 K. Corresponding isodensity values (in nm^{-3}) are given inside parenthesis.

6.3.2.3 Contact structure

In our earlier analyses, we explored the interactions among the species through their center of mass (COM) interactions. This is useful in case of studying the overall structures. In this section

we will discuss about the site-specific atomic interactions. As H-bonding play a pivotal role in determining the structure and dynamics of such systems, our focus will be to investigate possible H-bonding interactions. Figure 6.6 represents the possible H-bond interactions through RDF. For $[Ch]^+$-$[Ch]^+$ interaction, a sharp principal peak suggests strong correlation between hydroxyl oxygens of $[Ch]^+$ cation. However, with dilution, this correlation diminishes.

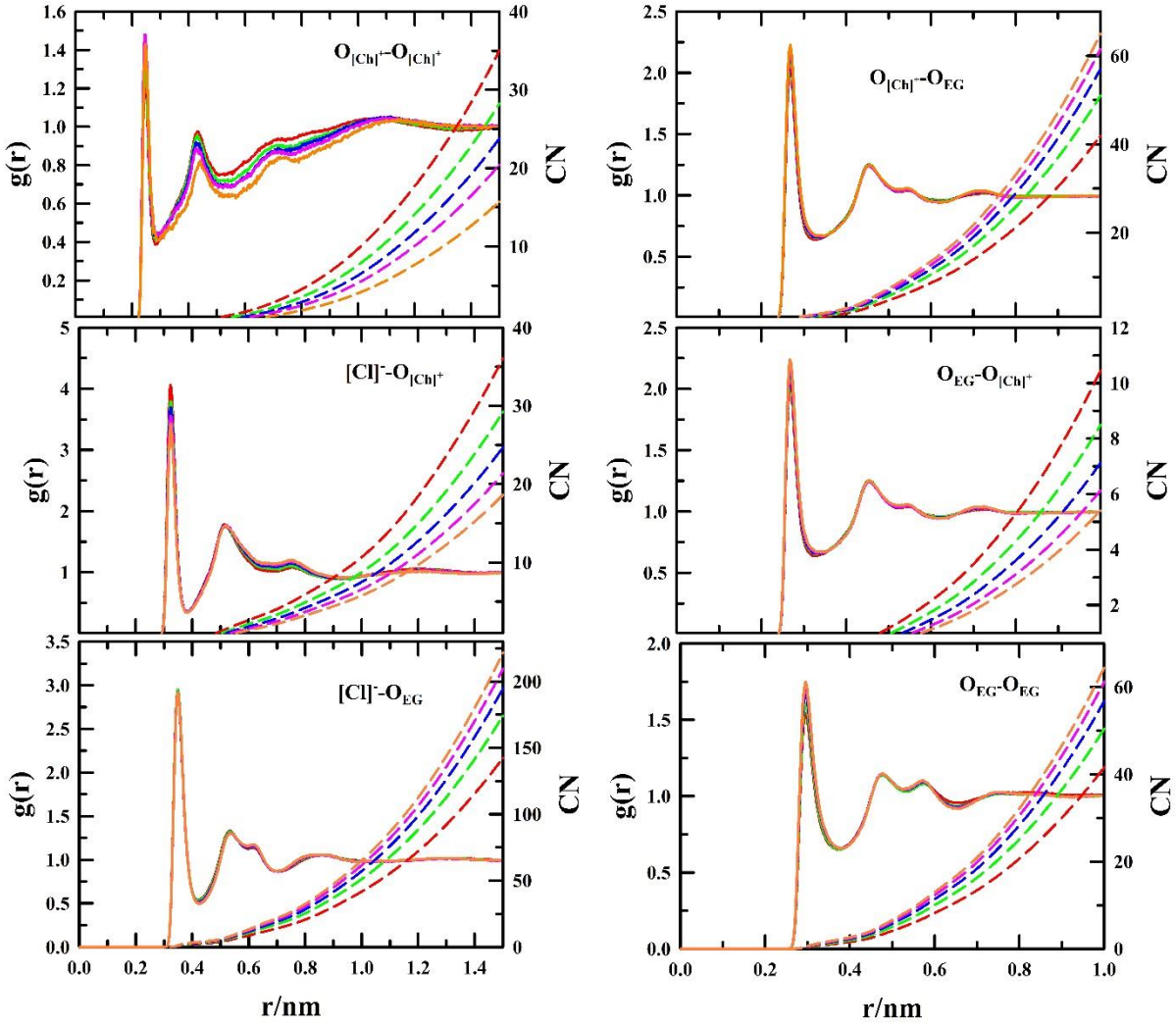

Figure 6.6: Radial distribution functions are shown for different atom-pairs. The right axes indicate the coordination number corresponding to respective RDFs. Each system is defined by unique color-codes as: ChCl:2EG - red, ChCl:3EG - green, ChCl:4EG - blue, ChCl:5EG - pink, ChCl:6EG – orange.

$[Cl]^-$ anion acts as an acceptor and shows strong interactions with hydroxyl oxygens of both $[Ch]^+$ and EG. Moreover, hydroxyl oxygen of EG depicts strong interactions to form possible hydrogen bonds with $[Ch]^+$ as well as with itself. The increment or decrement in CNs involving

these interactions are monotonic and can be explained in terms of dilution effect. Remarkably, throughout our comprehensive structural analyses of these mixtures, no anomalous changes have been detected.

6.3.2.4 Number of hydrogen bonds

Our structural analysis suggests presence of strong H-bonding interactions among these species. To get an idea about the extent of interaction, we have calculated number of H-bonds per $[Ch]^+$ cation, $[Cl]^-$ anion and EG. All possible donor-acceptor combinations have been considered for hydrogen bond calculation. The cut-off distance is taken as the minimum of the corresponding RDF. The angle criterion is the angle connecting donor-hydrogen and donor-acceptor vectors is maximum 30°. The number of H-bonds are shown in Figure 6.7.

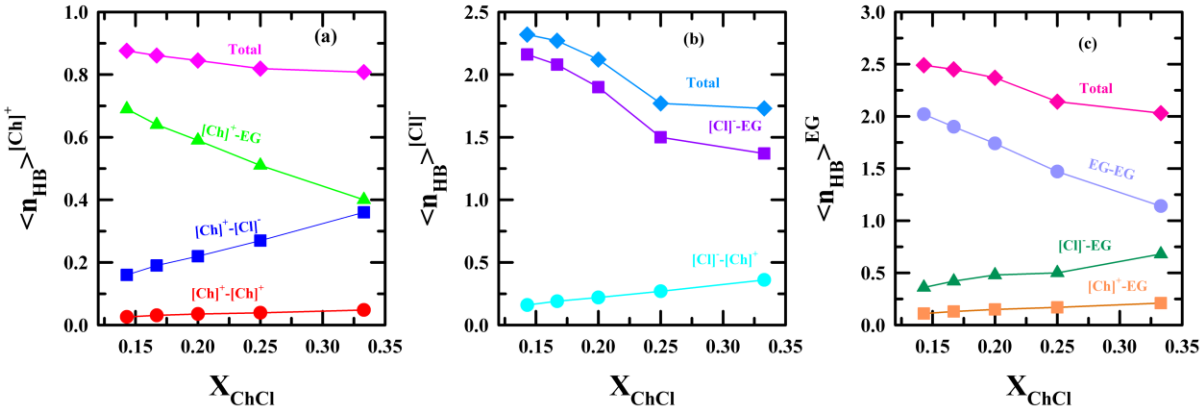

Figure 6.7: Number of H-bonds per (a) $[Ch]^+$ cation, (b) $[Cl]^-$ anion and (c) EG for ChCl/EG mixtures with varying ChCl concentration.

Figure 6.7 demonstrates the variation of number of H-bond per species with ChCl concentration. For $[Ch]^+$, maximum number of H-bonds are formed with $[Cl]^-$. The negative charge of $Cl]^-$ makes it a strong acceptor species to form H-bond with hydroxyl hydrogens. The number $[Ch]^+$-$[Cl]^-$ H-bonds increases gradually with addition of ChCl. This can be attributed to the increasing number of ions in the solutions manifests the stronger cation-anion interactions. On the other hand, $[Ch]^+$-EG H-bond diminishes as cation is getting preferably bound to anion rather than EG. The $[Ch]^+$-$[Ch]^+$ H-bond interaction exists in small extent and nominally increase with rising ChCl concentration. The $[Cl]^-$ acts as a potent acceptor towards both $[Ch]^+$ and EG to form ~1.5-2.5 H-bonds per anion. At a given concentration, both $[Ch]^+$ and $[Cl]^-$ can form H-bonds in greater extent with EG than with $[Cl]^-$ and $[Ch]^+$, respectively. This can be explained in terms of greater abundance of EG in the solution than counter ions.

Moreover, the presence of two hydroxyl groups in a EG molecule enhances its possibility to form H-bonds to a great extent. For the same reason, EG molecules are prone to bind with themselves and number of EG-EG H-bonds decreases with rising concentration indicating the effect of ions on the EG-EG network structure. A monotonic increase in number of H-bonds per EG molecule with cations and anions depicts the addition of ions incrementally favors the H-bonds between EG and ions.

$[Ch]^+$ cation and EG can act as both donor and acceptor in formation of H-bonds. Therefore, an in-depth analysis to find their donating and accepting probability would be helpful to assess their H-bonding nature. Table 6.2 provides such a detailed analysis of number of H-bonds per donor-acceptor pairs.

Table 6.2: Breakdown of number of H-bonds per species into different donor-acceptor interactions

species	**Donor site**	**Acceptor site**	**Number of H-bonds**				
			ChCl:6EG	**ChCl:5EG**	**ChCl:4EG**	**ChCl:3EG**	**ChCl:2EG**
$[Ch]^+$	$HO_{[Ch]+}$	$O_{[Ch]+}$	0.026	0.031	0.035	0.04	0.048
	$HO_{[Ch]+}$	$[Cl]^-$	0.16	0.19	0.22	0.27	0.38
	$HO_{[Ch]+}$	O_{EG}	0.51	0.48	0.44	0.39	0.31
	HO_{EG}	$O_{[Ch]+}$	0.18	0.16	0.15	0.12	0.094
$[Cl]^-$	$HO_{[Ch]+}$	$[Cl]^-$	0.16	0.19	0.22	0.27	0.38
	HO_{EG}	$[Cl]^-$	2.16	2.10	1.92	1.50	1.37
EG	$HO_{[Ch]+}$	O_{EG}	0.085	0.096	0.11	0.13	0.16
	HO_{EG}	$O_{[Ch]+}$	0.03	0.033	0.038	0.04	0.047
	HO_{EG}	$[Cl]^-$	0.36	0.42	0.48	0.50	0.68
	HO_{EG}	O_{EG}	2.02	1.90	1.74	1.47	1.16

Table 6.2 gives us valuable insights into how different species engage in H-bonding. Notably, the $[Ch]^+$ cation does not form H-bonds as efficiently and tends to be more of an acceptor in these interactions. On the other hand, the $[Cl]^-$ anion excels at accepting H-bonds, showing a strong preference for bonding with EG over $[Ch]^+$. Interestingly, EG plays a versatile role,

serving as both donor and acceptor in H-bond interactions, highlighting its dual role in facilitating these bonding interactions within the solution.

6.3.3 Ion complex analysis

In concentrated electrolyte solutions, ions tend to form complexes, which can be classified into contact ion pairs (CIPs), solvent separated ion pairs (SSIPs) or aggregates (AGGs) based on their degree of association.[62] The study of such ion complexes in concentrated electrolyte solutions is crucial for understanding the structure and dynamics of the solution. These complexes directly impact the characteristics of the solution. Understanding the prevalence and behavior of these complexes helps elucidate the complex interplay between ions and solvent molecules, shedding light on the inherent structure and dynamics of such solutions. In our analysis, we consider $[Ch]^+$ cations as central ions and examine the presence of counter ions, $[Cl]^-$, to determine potential ion complexes. We define a spherical solvation shell around each $[Ch]^+$ cation, with its radius set at the first minimum of the cation-anion radial distribution function (RDF). If only one $[Cl]^-$ ion is found within this shell, we classify these two ions as a contact ion pair (CIP). When there are multiple $[Cl]^-$ ions within the solvation shell, we identify it as an aggregate (AGG). If no $[Cl]^-$ ion is located within this shell, we label it as a solvent separated ion Pair (SSIP).

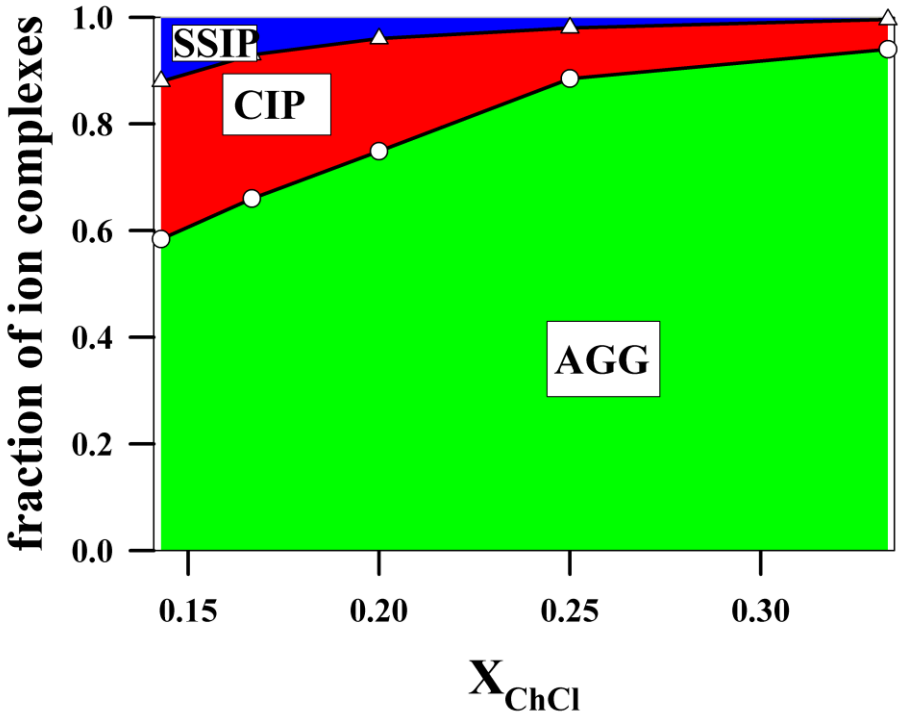

Figure 6.8: The fraction of different ion complexes formed by $[Ch]^+$ cation at ChCl/EG solutions of various concentrations. Each type of complexes is indicated with different colors

In Figure 6.8, we observe how the concentration affects the formation of various ion complexes. It is evident that a significant portion of $[Ch]^+$ cations tend to form aggregates, highlighting robust cation-anion interactions. As the concentration of ions increases, the fraction of aggregates also rises. This may be attributed to the fact that at higher concentrations, there are more ions available to participate in these complex formations. On the other hand, CIPs are still significant but become less common with increasing ion concentration. This might be because as more ions enter the mix, some of them are drawn into the aggregate formations rather than staying in close pairs. SSIPs are quite rare and become even scarcer as ChCl concentration increases. This suggests that the majority of ions prefer to associate with one another rather than staying isolated within the solvent. Overall, these findings reveal important information regarding ion-association in the solutions.

6.3.4 Dynamical properties

In this section we will discuss the concentration-dependent dynamics of ChCl/EG mixtures. It is necessary to explore the dynamical aspects to gain a comprehensive idea about the characteristic of such systems. From diffusion analysis we have seen that the translational

dynamics of $[Ch]^+$ cation, $[Cl]^-$ anion and EG are getting slower with incremental addition of ChCl. Now, we will focus on the hydrogen bond (H-bond) dynamics and dielectric relaxation spectra to elucidate the orientational dynamics happening in the solutions.

6.3.4.1 Structural hydrogen bond relaxation functions ($C_{\mathrm{HB}}(t)$)

Structural hydrogen bond relaxation functions ($C_{\mathrm{HB}}(t)$) were calculated using the following equation:[63,64]

$$C_{HB(t)} = \langle h(0)h(t)\rangle / \langle h(0)^2\rangle \tag{6.4}$$

where $h(t)$ indicates the presence or absence of hydrogen bond at a particular time between a pair of molecules: $h(t) = 1$ if there is a hydrogen bond and $h(t) = 0$ otherwise. This type of decay function allows the braking and making of hydrogen bonds between initial and final time limits. We have calculated correlation functions for both intraspecies and interspecies interactions. Figure 6.9 shows these correlation functions and the corresponding multi-exponential fit parameters are summarized in Table 6.A.3. Note that $[Ch]^+$-$[Ch]^+$ interactions are not considered here as there are minimal number of hydrogen bonds between them.

For any type of interaction, the decay of correlation functions gets faster with dilution elucidating the faster dynamics. The slowest two relaxation processes involve $[Cl]^-$ as acceptor. The H-bond relaxation between $[Ch]^+$ and EG is faster when EG act as donor. This relaxation becomes slower when EG is acceptor and $[Ch]^+$ is donor. The EG-EG H-bond relaxations are the fastest one. As ChCl is added to EG, the timescales are getting gradually slower. This incremental characteristic of timescales linearly follows the concentration dependence. Like our previous analyses, H-bond relaxation times also do not indicate the presence of any kind of anomalous composition.

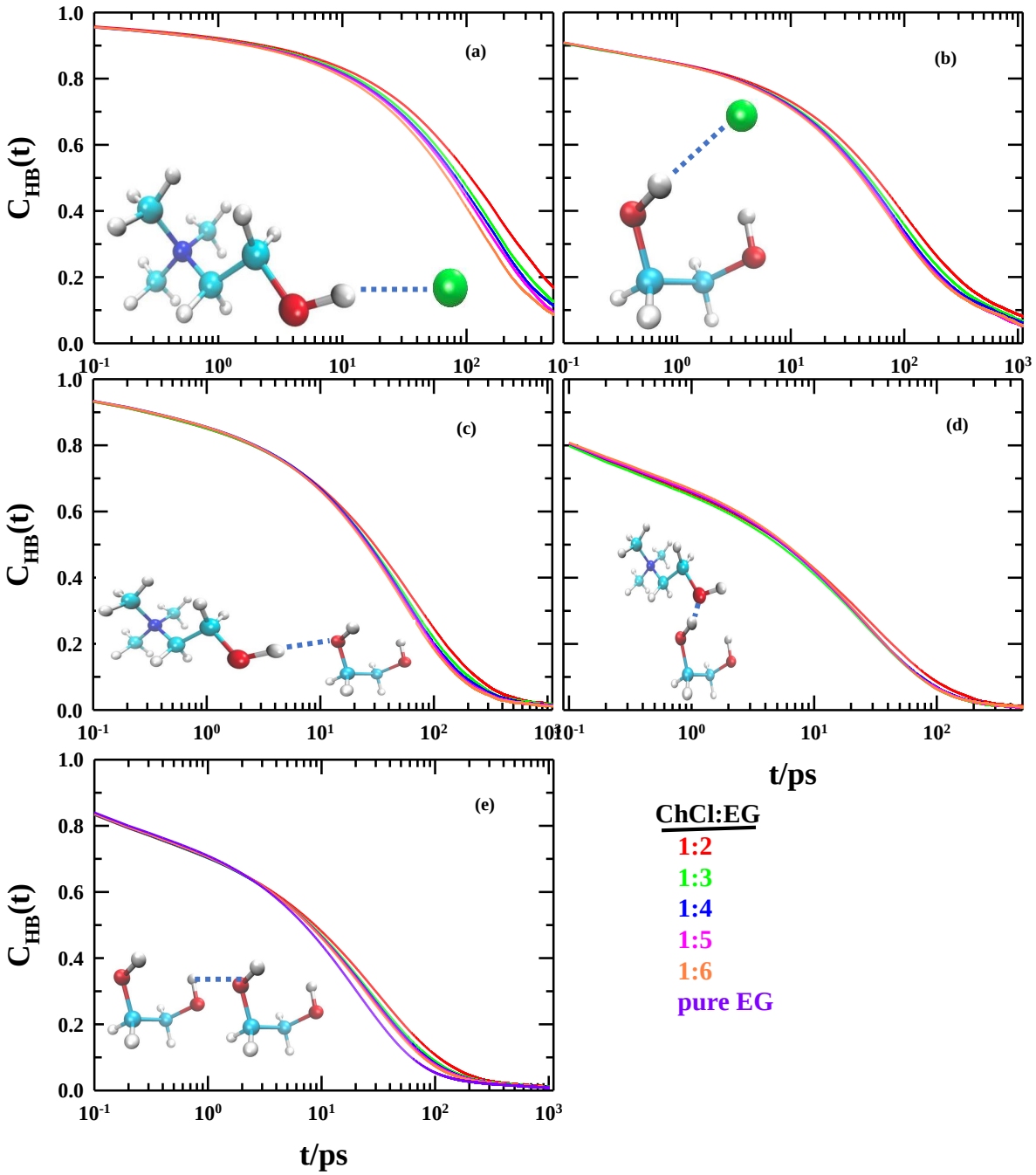

Figure 6.9: Concentration-dependent structural H-bond relaxation functions ($C_{\mathrm{HB}}(t)$) for intermolecular H-bonding interactions for different pairs: (a) $[Cl]^-$-----$HO_{[Ch]+}$, (b) $[Cl]^-$-----HO_{EG}, (c) O_{EG}-----$HO_{[Ch]+}$, (d) $O_{[Ch]+}$----HO_{EG}, (e) O_{EG}-----HO_{EG}. Each composition is uniquely color coded.

6.3.4.2 Dielectric relaxation dynamics

In addition to studying the hydrogen bonding behavior of the DES systems described earlier, we have also calculated the dielectric relaxation spectra (DRS) for these systems using MD simulation trajectories. This provides valuable insight into the dynamic behavior of the systems and their ability to support charge transfer. In order to compare the DRS of the DES systems with those of pure EG, we have also calculated the DRS for pure EG. The results of these calculations will be discussed in the following section.

First, we will briefly discuss about the analysis protocol to calculate dielectric relaxation spectra (DRS) from MD simulation trajectory.

The frequency-dependent dielectric function can be written as,[65–74]

$$\Sigma(\omega) = \frac{1}{3\epsilon_0 V k_B T}\mathcal{L}\left[-\frac{d}{dt}\langle \boldsymbol{M}_{tot}(0).\boldsymbol{M}_{tot}(t)\rangle\right] \quad (6.5)$$

The total dipole moment of the system ($\boldsymbol{M}_{tot}(t)$) is the resultant moment of all the molecules.

$$\boldsymbol{M}_{tot}(t) = \sum_i \sum_\alpha q_{i,\alpha}.\boldsymbol{r}_{i,\alpha}(t) \quad (6.6)$$

where, $q_{i,\alpha}$ is the charge of α-th atom of i-th molecule and $\boldsymbol{r}_{i,\alpha}$ is the position of α-th atom of i-th molecule.

Therefore,

$$\boldsymbol{M}_{tot}(t) = \sum_i \sum_\alpha q_{i,\alpha}(\boldsymbol{r}_{i,\alpha}(t) - \boldsymbol{r}_{i,com}(t)) + \sum_i \sum_\alpha q_{i,\alpha}.\boldsymbol{r}_{i,com}(t) \quad (6.7)$$

$$= \sum_i \sum_\alpha q_{i,\alpha}(\boldsymbol{r}_{i,\alpha}(t) - \boldsymbol{r}_{i,com}(t)) + \sum_i q_i.\boldsymbol{r}_{i,com}(t) \quad (6.8)$$

$$= \boldsymbol{M}_D(t) + \boldsymbol{M}_J(t) \quad (6.9)$$

where, $\boldsymbol{r}_{i,com}(t)$ is the position of center-of-mass of i-th molecule and q_i is the total charge of this molecule, and $\boldsymbol{M}_D(t)$, $\boldsymbol{M}_J(t)$ represent rotational and translational components of total dipole moment, respectively.

For polar, uncharged molecules $q_i = 0$ and only $\boldsymbol{M}_D(t)$ part survives. On the other hand, only charged species have the $\boldsymbol{M}_J(t)$ part.

Now, the total correlation function can be divided into different contributions.

$$\langle \boldsymbol{M}_{tot}(0).\boldsymbol{M}_{tot}(t)\rangle = \langle \boldsymbol{M}_D(0).\boldsymbol{M}_D(t)\rangle + \langle \boldsymbol{M}_J(0).\boldsymbol{M}_J(t)\rangle + \langle \boldsymbol{M}_D(0).\boldsymbol{M}_J(t)\rangle + \langle \boldsymbol{M}_J(0).\boldsymbol{M}_D(t)\rangle$$
$$= \phi_{DD}(t) + \phi_{JJ}(t) + \phi_{DJ}(t) \quad (6.10)$$

Theoretically, $\langle \boldsymbol{M}_D(0).\boldsymbol{M}_J(t)\rangle$ and $\langle \boldsymbol{M}_J(0).\boldsymbol{M}_D(t)\rangle$ are equal and $\phi_{DJ}(t)$ can be written as $\phi_{DJ}(t) = 2\langle \boldsymbol{M}_D(0).\boldsymbol{M}_J(t)\rangle$.

As Laplace-Fourier transform of these correlation functions form the frequency-dependent dielectric function ($\Sigma(\omega)$), we perform this operation on each of the individual correlation functions.

$$\mathcal{L}\left[-\frac{d}{dt}\phi_{DD}(t)\right] = \langle \boldsymbol{M}_D^2\rangle + i\omega\mathcal{L}[\langle \boldsymbol{M}_D(0).\boldsymbol{M}_D(t)\rangle] = \langle \boldsymbol{M}_D^2\rangle + i\omega\mathcal{L}_{DD}(\omega) \tag{6.11}$$

$$\mathcal{L}\left[-\frac{d}{dt}\phi_{JJ}(t)\right] = \frac{i}{\omega}\mathcal{L}[\langle \boldsymbol{J}(0).\boldsymbol{J}(t)\rangle] = \frac{i}{\omega}\mathcal{L}_{JJ}(\omega) \tag{6.12}$$

$$\mathcal{L}\left[-\frac{d}{dt}\phi_{DJ}(t)\right] = 2\mathcal{L}[-\langle \boldsymbol{M_D}(0).\boldsymbol{J}(t)\rangle] = -2\mathcal{L}_{DJ}(\omega) \tag{6.13}$$

where, $\mathcal{L}_{DD}(\omega) = \mathcal{L}[\langle \boldsymbol{M}_D(0).\boldsymbol{M}_D(t)\rangle]$, $\mathcal{L}_{JJ}(\omega) = \mathcal{L}[\langle \boldsymbol{J}(0).\boldsymbol{J}(t)\rangle]$ and $\mathcal{L}_{DJ}(\omega) = \mathcal{L}[\langle \boldsymbol{M_D}(0).\boldsymbol{J}(t)\rangle]$.

Notice in Eq. 6.12 and Eq. 6.13, we have introduced a new term $\boldsymbol{J}(t)$ in place of the $\boldsymbol{M}_J(t)$. Here, $\boldsymbol{J}(t)$ is the electric current and defined as: $\boldsymbol{J}(t) = \frac{d\boldsymbol{M}_J(t)}{dt} = \sum_i q_i.\mathbf{v}_{i,com}(t)$ where $\mathbf{v}_{i,com}(t)$ is the centre-of-mass velocity of molecule *i*. It is advantageous to use total electric current $\boldsymbol{J}$, instead of $\boldsymbol{M}_J$ to avoid periodic jumps of molecules.

Finally, the frequency-dependent dielectric function ($\Sigma(\omega)$) can be expressed as,[65]

$$\Sigma(\omega) = \frac{1}{3\epsilon_0 V k_B T}\left(\langle \boldsymbol{M}_D^2\rangle + i\omega\mathcal{L}[\langle \boldsymbol{M}_D(0).\boldsymbol{M}_D(t)\rangle] + \frac{i}{\omega}\mathcal{L}[\langle \boldsymbol{J}(0).\boldsymbol{J}(t)\rangle] - 2\mathcal{L}[\langle \boldsymbol{M_D}(0).\boldsymbol{J}(t)\rangle]\right) \tag{6.14}$$

To overcome the $1/\omega$ divergence in the low-frequency regime, we subtract the zero-frequency contribution of $\mathcal{L}_{JJ}(\omega)$ and $\mathcal{L}_{JJ}(\omega)$ becomes $(\mathcal{L}_{JJ}(\omega) - \mathcal{L}_{JJ}(0))$.

Now this corrected frequency-dependent dielectric function ($\Sigma_0(\omega)$) can be expressed as,

$$\Sigma_0(\omega) = \left(\varepsilon_{DD}(\omega) + \varepsilon_{JJ}(\omega) - 2\varepsilon_{DJ}(\omega)\right) \tag{6.15}$$

with

$$\varepsilon_{DD}(\omega) = \frac{1}{3\epsilon_0 V k_B T}\left(\langle \boldsymbol{M}_D^2 \rangle + i\omega \mathcal{L}_{DD}(\omega)\right), \tag{6.16}$$

$$\varepsilon_{JJ}(\omega) = \frac{1}{3\epsilon_0 V k_B T}\frac{i}{\omega}\Big(\mathcal{L}_{JJ}(\omega) - \mathcal{L}_{JJ}(0)\Big), \tag{6.17}$$

$$\varepsilon_{DJ}(\omega) = \frac{1}{3\epsilon_0 V k_B T}\mathcal{L}_{DJ}(\omega). \tag{6.19}$$

The formalism and equations are as per shown by Schröder et al.[65] The detailed derivation of Eq.6.16 to Eq.6.19 can be found there.

In this formalism the non-polarizable force field parameters are considered. Hence, the dielectric constant at $\omega \to 0$ is approximated as unity ($\varepsilon_\infty = 1$).

Therefore, the overall dielectric spectrum containing all the dynamic contributions as well as ε_∞ can be written as,

$$\varepsilon(\omega) = \varepsilon'(\omega) - i\varepsilon''(\omega) = \Sigma_0(\omega) + 1 \tag{6.20}$$

where, $\varepsilon'(\omega)$ and $\varepsilon''(\omega)$ are the frequency-dependent real and imaginary parts, respectively, and the generalized static dielectric constant, $\varepsilon_s = \lim_{\omega \to 0} \varepsilon(\omega)$.

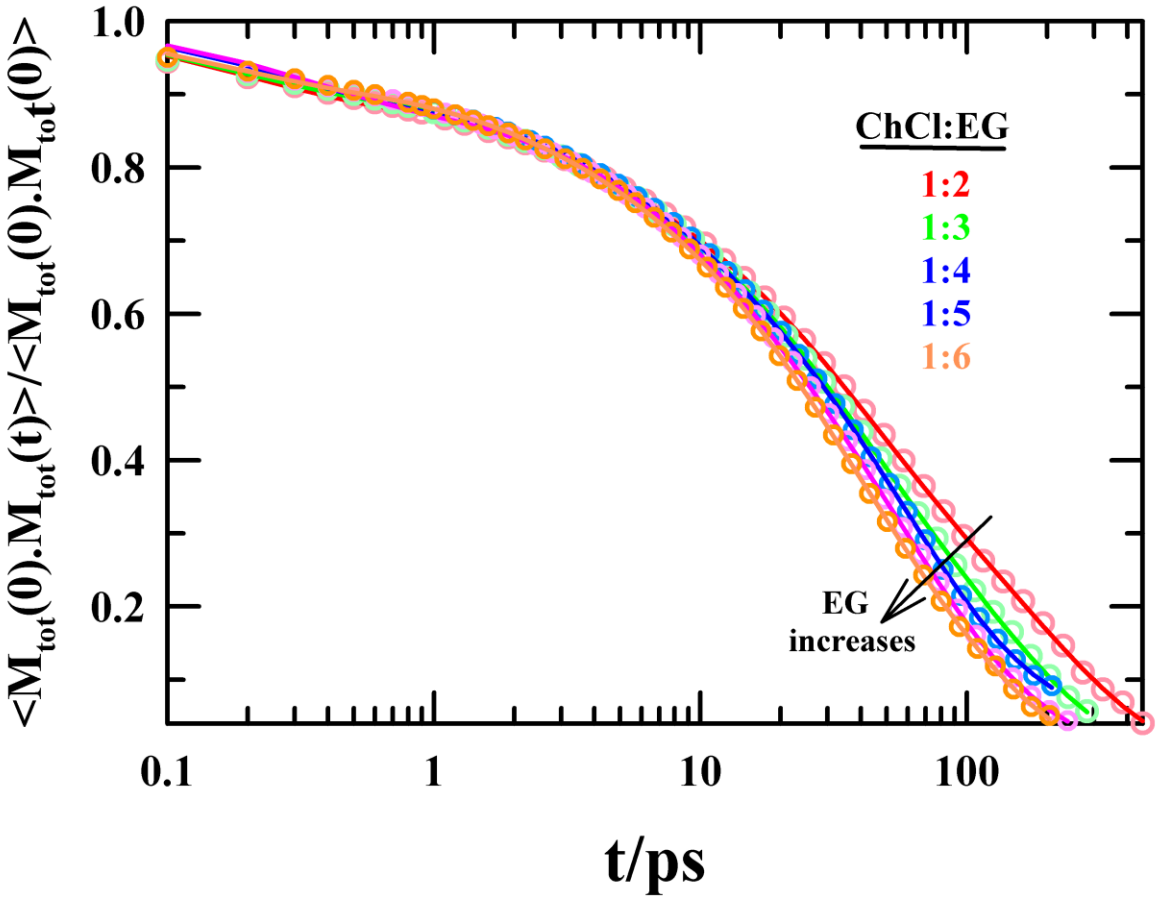

Figure 6.9: Composition-dependent total dipole-moment autocorrelation functions are shown for ChCl/EG mixtures. The open symbols represent the simulated data and solid lines going through them denote multi-exponential fits.

Figure 6.9 displays composition-dependent collective dipole moment autocorrelation function at 298.15 K. The corresponding multiexponential fit parameters are summarized in Table 6.A.4.

Our analysis of the concentration-dependent total dipole-moment autocorrelation function revealed the presence of four well-separated timescales required to accurately describe the correlation functions. We observed that the timescales decreased with dilution of the system. These findings indicate that the relaxation behavior of the system is influenced by its composition, with changes in the concentration of the constituent components leading to alterations in the dynamic properties of the system.

Next, we look into the current-current correlation functions of these systems. The autocorrelation functions are presented in Figure 6.10 and corresponding fit parameters are summarized in Table 6.A.5.

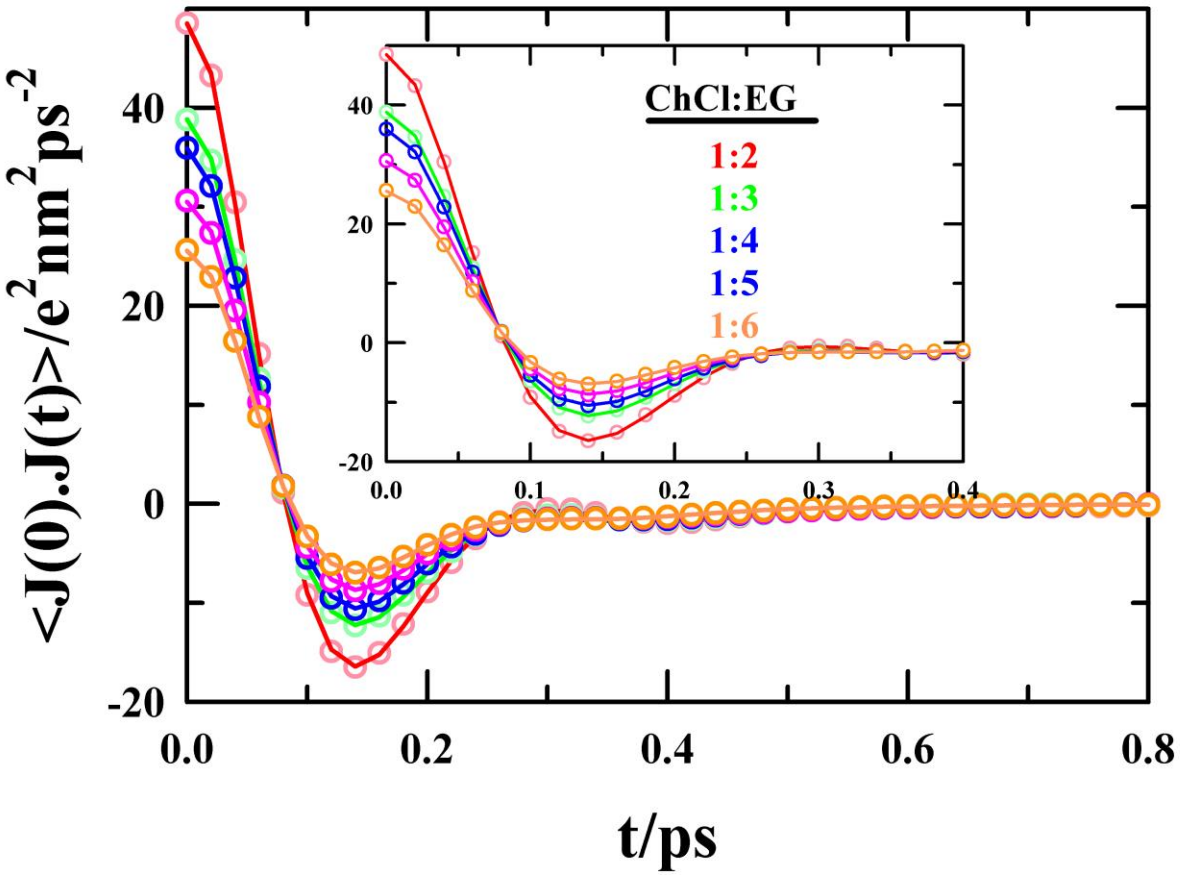

Figure. 6.10: Composition-dependent total current-current autocorrelation function. The open symbols represent the simulated data and solid lines going through them denote fits lines. Fast relaxations for first 0.4 ps are shown in the inset.

Figure 6.10 illustrates the fast-decaying nature of current-current autocorrelation functions. All the functions roughly decays to zero within 0.4 ps. The correlation is maximum at zero-time lag and show a dip at ~0.4 nm. The extent of correlation is maximum for ChCl:2EG mixture (most concentrated solution) and gradually decrease with dilution. Interestingly, the depth of the minimum at ~0.15 ps gradually decreases with dilution of the solutions. These observations indicate that extent of both correlation and anti-correlation mitigates with dilution due to presence of lesser number ions.

We also looked at another crucial correlation function called the dipole-current correlation function. This function helps us to understand how molecular/ionic dipoles and electric currents in the solution interact. However, because these two relaxation processes happen at quite different timescales, the correlations between them are generally quite weak or small. Such

correlation functions are represented in Figure 6.11 and corresponding fit parameters are shown in Table 6.A.6.

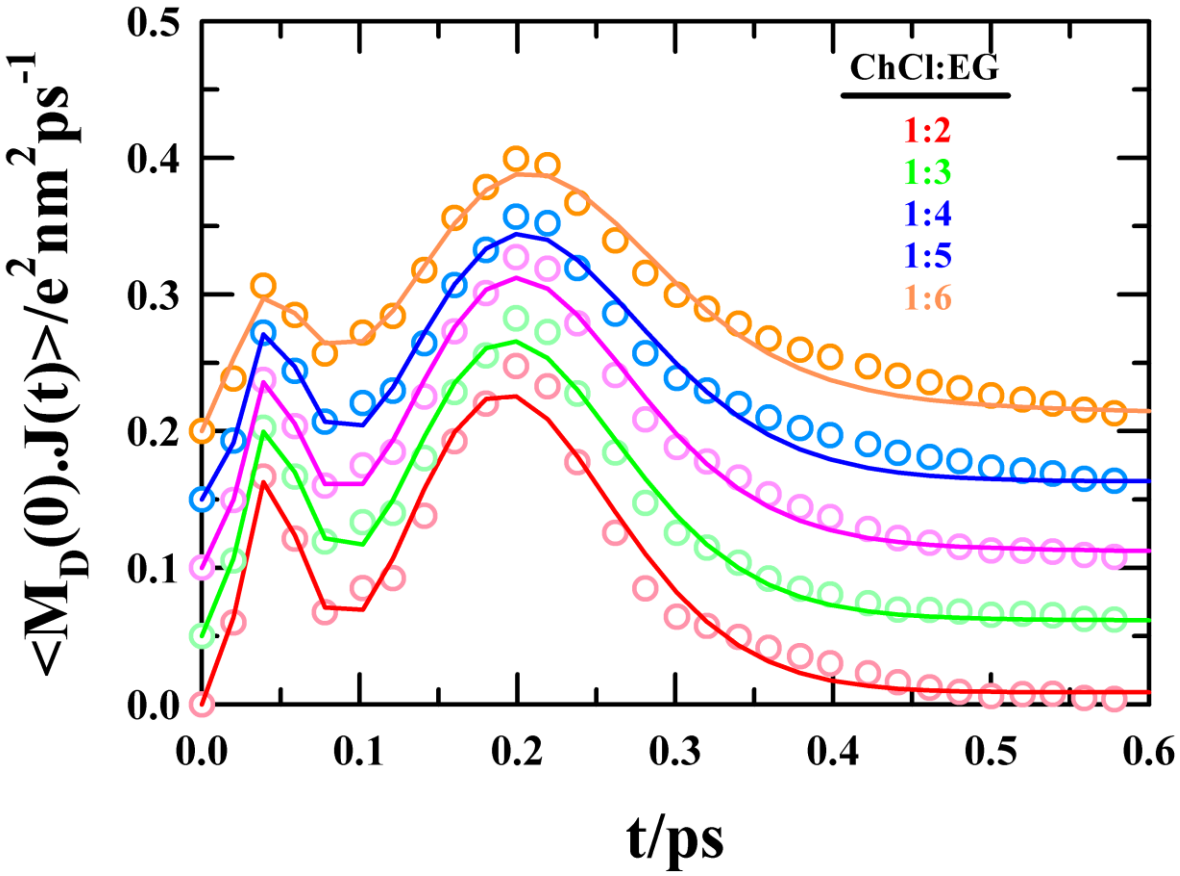

Figure. 6.11: Composition-dependent total current-current autocorrelation function. The open symbols represent the simulated data and solid lines going through them denote fits lines. An offset of 0.05 is used in y-axis for clear representation.

The dipole-current cross-correlation functions reveal some interesting features. They exhibit two distinct peaks: one sharp peak around 0.05 ps and a broader peak at approximately 0.2 ps. Initially, at zero-time lag, there is no correlation between the dipole moment and current. As time progresses, we see the emergence of correlation, resulting in the sharp peak around 0.05 ps. This peak indicates that there is a strong connection between changes in the dipole moment and adjustments in the current distribution, happening quite rapidly. However, as we move beyond 0.1 ps, this initial correlation starts to fade, and another peak appears at around 0.2 ps. This broader peak suggests a more complex dynamic where changes in the dipole moment and current are still related, but with a bit of delay between them. As we wait longer, past approximately 0.4 ps, this correlation diminishes entirely, returning to zero.

Following the method discussed above we have calculated dielectric relaxation spectra for these ChCl/EG solution. The rotational, translational and ro-translational dielectric spectra are shown in Figure 6.12.

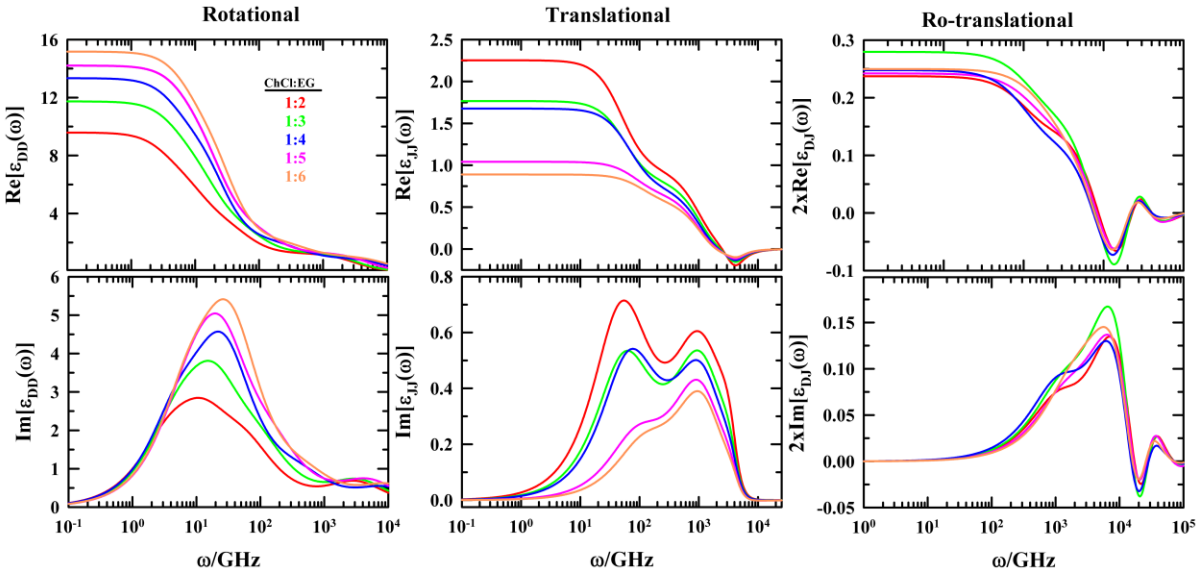

Figure 6.12: Concentration-dependent real (upper panel) and imaginary (lower panel) parts of dielectric spectra of the ChCl/EG mixtures: rotational spectra (left), translational spectra (middle), ro-translational spectra (right). Translational and ro-translational components are quite small compared to the rotational component.

It is clear that rotational processes play the primary role in the overall dielectric spectra, while translational processes make smaller but notable contributions. In contrast, ro-translational spectra have only minimal effects. Within the rotational spectra, the magnitude consistently increases with dilution, reflecting the influence of higher dielectric constant of EG. The timescales also get monotonously faster with dilution. Simultaneously, timescales become progressively faster as the solution becomes more dilute. These rotational spectra represent a complex interplay of contributions stemming from $[Ch]^+$, EG, and their interactions, as illustrated in Figure 6.A.2. Notably, EG contributes the most, followed by $[Ch]^+$, while their cross-interactions have a minor impact. This can be partly attributed to the dipole moments, with EG having a slightly higher value (3.1 D) than $[Ch]^+$ (2.79 D) in our model. Additionally, EG has a slightly higher Kirkwood g factor than $[Ch]^+$, (1.35 vs 1.08 at ChCl:2EG composition), and there are more EG than $[Ch]^+$ in any given solution. As solutions become more dilute, the contribution from $[Ch]^+$ decreases, and that of EG increases. Since these changes are in opposite directions, the variation in cross-interactions does not follow a consistent trend. Regardless of the species involved, the peaks in the dielectric loss spectrum

shift towards higher frequencies in diluted solutions, indicating faster dynamics. The dielectric dispersion and relaxation timescales for different self- and cross-interactions are shown in Tables 6.A.7-6.A.9. Therefore, we did not find any sudden changes in the rotational dielectric spectra across the compositions we studied, indicating absence of any anomalous composition.

The rotational dynamics of the overall dielectric spectra are summarized in Table 6.A.2. The slowest timescale (τ_1) ranges from ~130-300 ps, showing an amplitude of roughly 30%. This timescale likely arises from the individual timescales of $[Ch]^+$ and EG, which can be found in Tables 6.A.5 and 6.A.6, respectively. Upon comparison, it becomes clear that this 130-300 ps timescale falls between the rotational timescales of $[Ch]^+$ and EG. Consequently, it represents the combined rotational motion of both $[Ch]^+$ and EG, appearing as an intermediate timescale. The τ_2 timescale spans approximately 30-80 ps in the overall spectra. The corresponding timescales for $[Ch]^+$ and EG vary between ~50-90 ps and 15-30 ps, respectively. Therefore, this τ_2 timescale is also influenced by both $[Ch]^+$ and EG dynamics. Similarly, the other two timescales result from a combination of dielectric relaxations in $[Ch]^+$ and EG molecules. The consistent decrease in relaxation times with increasing dilution reflects the impact of reduced viscosity and the prevalence of faster-relaxing EG molecules. One interesting fact to note here that, the $C_{HB}(t)$ timescales between $[Ch]^+$-EG and EG-EG interactions are very similar to that of DR timescales. This elucidates the effect of structural H-bond formation process on the dielectric relaxation of constituent molecules. Notably, the relaxation timescales of $[Ch]^+$ cations are the slowest, followed by those of EG and their cross-interactions. This difference can be attributed to the larger size of $[Ch]^+$ cations, which reorient more slowly compared to the smaller EG molecules. Additionally, the interactions between $[Ch]^+$ and EG are relatively dynamic and short-lived. It is worth noting that the relaxation timescales of the overall rotational dielectric spectra fall within the range of relaxation times for both $[Ch]^+$ and EG. This suggests that the resulting spectra carry the signatures of timescales associated with all these interactions.

Next, we will discuss how the concentration of ions affects the translational dynamics in the solutions. Figure 6.12 displays the translational part of the dielectric spectra. It can be observed that when there are more ions in the solutions, the translational spectra become larger. The plateau region at low-frequency limit of real components accounts for the contribution of translational processes towards the static dielectric constant. In the imaginary part of the spectra, we can see two clear relaxation peaks. However, when the solutions become more

diluted, these peaks become smaller. The lower-frequency peak diminishes quite rapidly as the dilution progresses.

The coupling between rotational and translational dynamics (ro-translation spectra), as depicted in Figure 6.12, contribute minimally to the overall spectra compared to their individual rotational and translational counterparts. Interestingly, these spectra exhibit a non-monotonic pattern, unlike the rotational and translational spectra. This behavior can be explained by the contrasting changes observed in rotational and translational spectra. Rotational spectra decrease with increasing ChCl concentration, while translational spectra increase. As a result, their coupling interaction does not follow a linear relationship with the concentration of ChCl, leading to this non-monotonic trend.

The real and the imaginary components of the frequency-dependent generalized dielectric function ($\varepsilon(\omega)$), simulated at various concentrations for these ChCl/EG mixtures, are presented below in Figure 6.13.

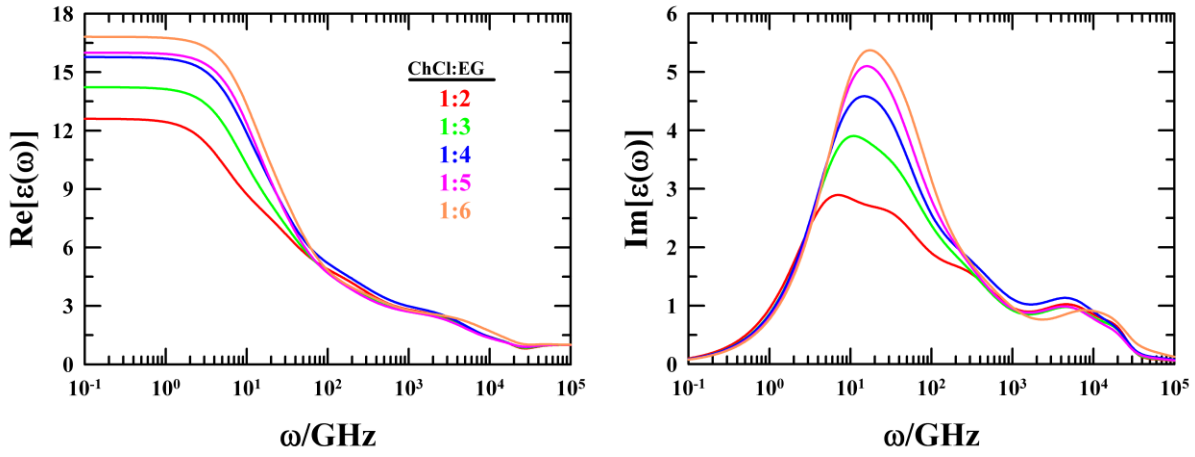

Figure 6.13: Concentration-dependent real (left panel) and imaginary (right panel) components of the generalized frequency dependent dielectric function, $\varepsilon(\omega)$, obtained from simulations via Eq. 6.20 of the text.

Note that the peak of the imaginary component shifts to lower frequency with addition of ChCl, whereas the zero-frequency value of the real component modulates with ChCl concentration. Effect of concentration is quite evident in these figures. Moreover, the addition of ChCl affects the DRS linearly indicating no anomalous dynamics across the studied compositions.

The contributions of various species-specific dynamics to the overall dielectric relaxation spectra are summarized in Table 6.3. When ChCl is added to EG, there is a decrease in the

static dielectric constant primarily due to the reduction in the contribution of EG. In all compositions, the rotational dynamics make the most significant contribution, while the ro-translational part has a minimal impact. In solutions ranging from ChCl:EG = 1:6 to 1:2, the contribution of translational part increases from ~6% to ~20% because of the additional ions. Even in the most concentrated solution, rotational dynamics dominate with a substantial contribution of around 83%. Among the rotational components, EG plays a crucial role due to its high abundance. Although the contribution of EG decreases from ~84% to ~57% when transitioning from ChCl:EG = 1:6 to 1:2, it still surpasses the rotational contribution of $[Ch]^+$, which hovers at ~19%. The interaction between $[Ch]^+$ and EG accounts for only about 5-7% of the total contribution, indicating different timescales for the dynamics of $[Ch]^+$ and EG. Consequently, it is reasonable to conclude that rotational dynamics predominantly govern the overall dynamics of these mixtures.

Table 6.3: Contributions of different mode of dynamics as well as different species to overall dielectric spectra

ChCl:EG	$\boldsymbol{\varepsilon_s - 1}$	**Rotational**				**Translational**	**Ro-translational**
		Choline	**EG**	**Cross**	**Total**		
1:2	11.60	2.21 (19.0%)	6.57 (56.6%)	0.80 (6.9%)	9.59 (82.7%)	2.25 (19.4%)	-0.24 (-2.1%)
1:3	13.22	1.76 (13.3%)	9.07 (68.6%)	0.90 (6.8%)	11.74 (88.8%)	1.76 (13.3%)	-0.28 (-2.1%)
1:4	14.78	1.45 (9.8%)	10.91 (73.8%)	0.98 (6.6%)	13.34 (90.2%)	1.68 (11.4%)	-0.24 (-1.6%)
1:5	14.99	1.33 (8.9%)	12.01 (80.1%)	0.86 (5.7%)	14.20 (94.7%)	1.04 (6.9%)	-0.25 (-1.7%)
1:6	15.81	1.06 (6.7%)	13.29 (84.1%)	0.82 (5.2%)	15.17 (96.0%)	0.89 (5.6%)	-0.25 (-1.6%)
Pure EG	29.11		29.11 (100%)		29.11 (100%)		

*$\varepsilon_s = \Sigma_0(\omega = 0) + 1$

6.4 Conclusion

In conclusion, our simulation studies on ChCl/EG mixtures across various compositions have provided valuable insights into the structural and dynamic behavior of these systems. Our primary objective was to detect anomalous behavior, particularly indicative of possible deep eutectic solvent (DES) formation, by carefully observing changes at different compositions. We specifically investigated molar ratios of 1:2, 1:3, 1:4, 1:5, and 1:6.

Analyzing a multitude of structural and dynamic properties, including RDF, CN, hydrogen bonds, dielectric relaxation parameters, and viscosity, revealed a composition-dependent variation in the mixture properties. Notably, the number of hydrogen bonds decreased and structural hydrogen bond relaxation time increased with increasing composition, while viscosity and density exhibited an increment. The detailed analysis of individual properties provided further insights. Viscosity showed a consistent increase from the 1:6 mixture to the 1:2 mixture, indicating a concentration-dependent influence. Self-diffusion coefficients reflected that Ch^+ ions exhibited slower diffusion compared to EG, and diffusion coefficients decreased with increasing mixture concentration. The examination of hydrogen bond formations unveiled distinct patterns, with $[Ch]^+$-$[Cl]^-$ interactions increasing gradually with ChCl addition, reflecting stronger cation-anion associations. Meanwhile, $[Ch]^+$-EG hydrogen bonds diminished, emphasizing the preference of $[Ch]^+$ for anion binding over EG. Analysis of ion complexes highlighted the prevalence of aggregates, suggesting robust cation-anion interactions that intensified with higher concentrations. Dynamical properties, including structural hydrogen bond correlation and dielectric relaxation dynamics, were investigated. While H-bond relaxation times showed faster dynamics with dilution, dielectric spectra displayed changes in timescales and interaction strengths. Notably, rotational dynamics were found to govern overall dynamics, with EG playing a crucial role. The translational dynamics, captured in real and imaginary parts of dielectric spectra, reflected the intricate interplay between ions and EG. Interestingly, ro-translation spectra exhibited a non-monotonic pattern, deviating from the linear trends observed in rotational and translational spectra.

In summary, our comprehensive study sheds light on the intricate interplay of structural and dynamic properties in ChCl:EG mixtures. The concentration-dependent variations observed provide a nuanced understanding of these systems, paving the way for future investigations into the behavior of deep eutectic solvents in similar contexts.

Appendix 6.A

Table 6.A.1: Number of choline ($[Ch]^+$), chloride ($[Cl]^-$) and ethylene glycol (EG) molecules in each mixture.

ChCl: EG	$\mathbf{N_{Ch^+}}$	$\mathbf{N_{Cl^-}}$	$\mathbf{N_{EG}}$	$\boldsymbol{X_{ChCl}}$	$\boldsymbol{c}$**/M**
1:2	250	250	500	0.333	4.193
1:3	200	200	600	0.250	3.411
1:4	175	175	700	0.200	2.869
1:5	150	150	750	0.167	2.473
1:6	125	125	750	0.143	2.172
Pure EG	0	0	1000	0	

Table 6.A.2: Density comparison between simulation and experiment.

ChCl: EG	**Density (g/cm^3)**		
	Sim	Exp	% Deviation
1:2	1.11391	1.11646	0.23
1:3	1.11172	1.11500	0.29
1:4	1.1138	1.11474	0.08
1:5	1.1103	1.11344	0.28
1:6	1.10744	1.11364	0.56
Pure EG	1.10574	1.10985	0.37

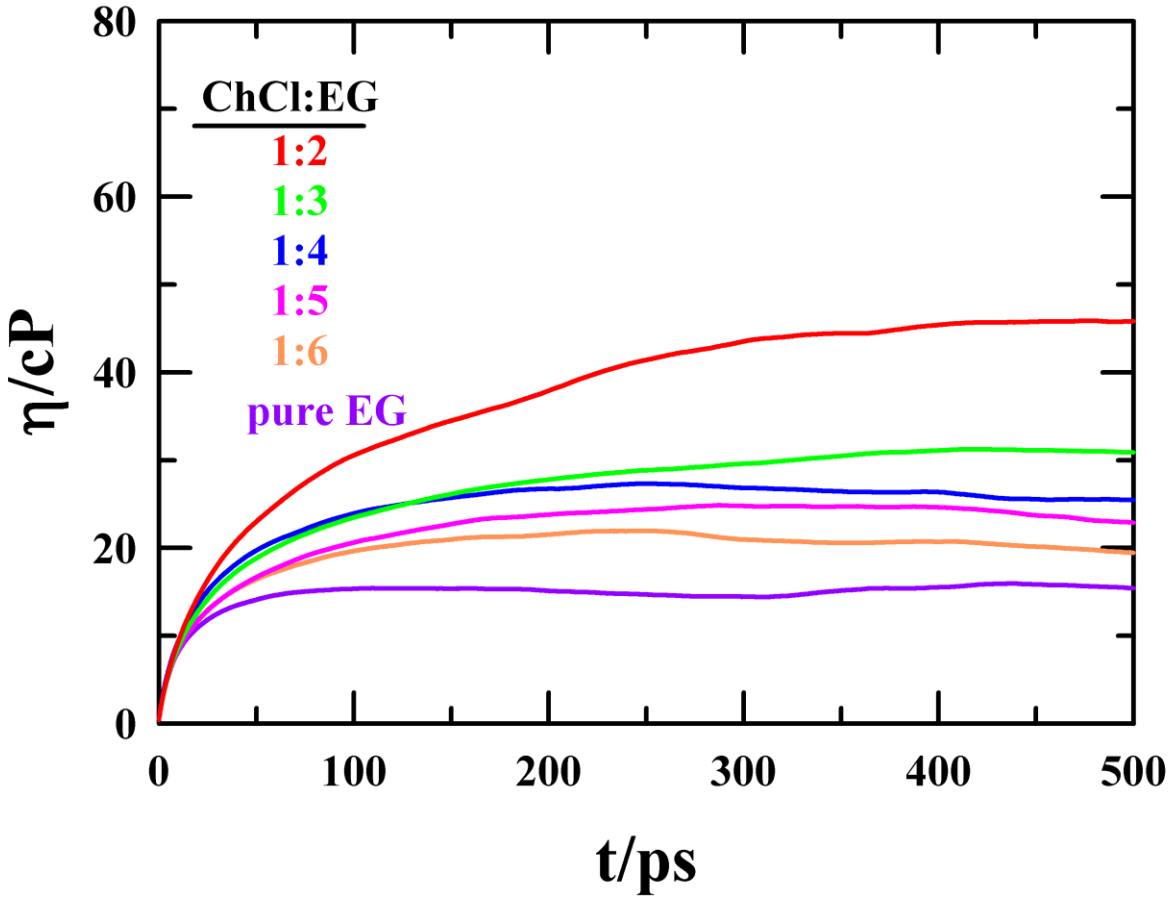

Figure 6.A.1: Time evolution of simulated shear viscosity for ChCl/EG mixtures at different compositions as well as for pure EG at 298 K. Each system is uniquely color-coded.

Table 6.A.3: Multiexponential parameters ($f_{DD}(t) = \sum_k A_k e^{-t/\tau_k}$) to fit structural hydrogen bond relaxation functions.

ChCl:EG	A_1	τ_1 (ps)	A_2	τ_2 (ps)	A_3	τ_3 (ps)	A_4	τ_4 (ps)	A_5	τ_5 (ps)	$\langle\tau\rangle$ (ps)
$[Cl]^-$-----$HO_{[Ch]+}$											
1:2	0.15	1665	0.56	215	0.16	48	0.06	6	0.07	0.16	378
1:3	0.13	1397	0.47	198	0.25	81	0.08	11	0.07	0.24	296
1:4	0.15	900	0.56	157	0.13	58	0.08	10	0.08	0.25	231
1:5	0.11	974	0.58	167	0.17	46	0.06	6	0.08	0.17	212
1:6	0.16	707	0.66	112	0.08	15	0.04	2	0.06	0.10	188
$[Cl]^-$-----HO_{EG}											
1:2	0.15	1851	0.34	183	0.28	58	0.09	7	0.14	0.13	357
1:3	0.16	1313	0.33	149	0.29	52	0.09	7	0.13	0.13	275
1:4	0.16	1109	0.31	126	0.29	55	0.09	7	0.15	0.14	233
1:5	0.17	938	0.40	108	0.22	39	0.08	5	0.13	0.12	213
1:6	0.17	934	0.48	91	0.15	26	0.07	3	0.12	0.10	206
O_{EG}-----$HO_{[Ch]+}$											
1:2			0.25	238	0.46	58	0.15	9	0.14	0.31	88
1:3			0.26	194	0.48	47	0.13	6	0.13	0.23	74
1:4			0.25	187	0.52	44	0.11	5	0.12	0.20	70
1:5			0.25	170	0.51	45	0.12	6	0.12	0.21	66
1:6			0.25	162	0.52	42	0.11	5	0.12	0.19	63
$O_{[Ch]+}$----HO_{EG}											
1:2			0.09	190	0.39	38	0.20	6	0.32	0.1	33
1:3			0.09	155	0.42	31	0.18	4	0.31	0.1	27.7
1:4			0.10	156	0.42	30	0.18	4	0.30	0.1	29
1:5			0.10	149	0.43	30	0.18	4	0.29	0.1	28.5
1:6			0.10	152	0.46	28	0.17	3	0.27	0.1	28.1
O_{EG}-----HO_{EG}											
1:2			0.22	124	0.38	27	0.16	4	0.24	0.1	38
1:3			0.22	103	0.40	24	0.14	3	0.24	0.1	33
1:4			0.20	101	0.41	24	0.15	3	0.24	0.1	30
1:5			0.20	98	0.42	23	0.14	3	0.24	0.1	30
1:6			0.20	93	0.42	22	0.15	3	0.23	0.1	28
Pure EG			0.18	78	0.47	19	0.13	3	0.22	0.1	23

Table 6.A.4: Multiexponential fit parameters ($f_{DD}(t) = \sum_k A_k e^{-t/\tau_k}$) to fit simulated data presented in Figure 6.9.

ChCl:EG	A_1	τ_1 (ps)	A_2	τ_2 (ps)	A_3	τ_3 (ps)	A_4	τ_4 (ps)	$\langle\tau\rangle$ (ps)
1:2	0.28	281	0.35	79	0.24	16	0.13	0.32	110
1:3	0.28	200	0.44	54	0.17	10	0.11	0.29	81
1:4	0.28	194	0.56	38	0.09	2.4	0.07	0.11	76
1:5	0.26	138	0.52	42	0.13	6	0.09	0.20	58
1:6	0.30	130	0.56	30	0.07	1.9	0.07	0.10	56

Table 6.A.5: Fit parameters for current-current autocorrelation functions obtained by using a fit function ($f_{JJ}(t) = \sum_k A_k \cos(\omega_k . t + \delta_k) \exp(-t/\tau_k)$). Values are shown for ChCl/EG solutions at various concentrations.

ChCl:EG	A_1	τ_1	ω_1	δ_1	A_2	τ_2	ω_2	δ_2	A_3	τ_3
1:2	64.5073	0.0862	22.1315	-0.520	56.202	0.127	1.2400	1.7032	-0.0555	3.166
1:3	47.9857	0.0827	22.729	-0.599	57.464	0.119	1.8284	1.5837	-0.0498	2.836
1:4	42.3108	0.0790	23.2527	-0.657	62.308	0.115	1.9671	1.5313	-0.0766	2.338
1:5	36.4771	0.0767	23.2789	-0.700	54.445	0.12	1.7944	1.535	-0.0514	1.822
1:6	26.117	0.0759	24.6962	-0.798	56.201	0.109	2.4153	1.439	-0.0662	1.431

Table 6.A.6: Fit parameters for dipole-current cross-correlation functions obtained by using a fit function ($f_{DJ} = \sum_k A_k t^{\gamma_k - 1} \exp(-t/\tau_k)$). Values are shown for ChCl/EG solutions at various concentrations.

System	A_1	τ_1	γ_1	A_2	τ_2	γ_2	A_3	τ_3	γ_3
1:2	4.732e9	0.021	9.954	1.949e7	0.009	5.448	0.038	0.64	2.004
1:3	3.462e9	0.022	9.927	2.133e7	0.009	5.517	0.039	0.66	1.6
1:4	2.848e9	0.022	9.959	6.514e8	0.008	6.375	0.033	0.70	1.241
1:5	5.277e9	0.024	9.389	8.339e7	0.008	5.905	0.044	0.70	1.703
1:6	6.571e8	0.024	9.622	6.602e7	0.009	6.029	0.046	0.54	1.067

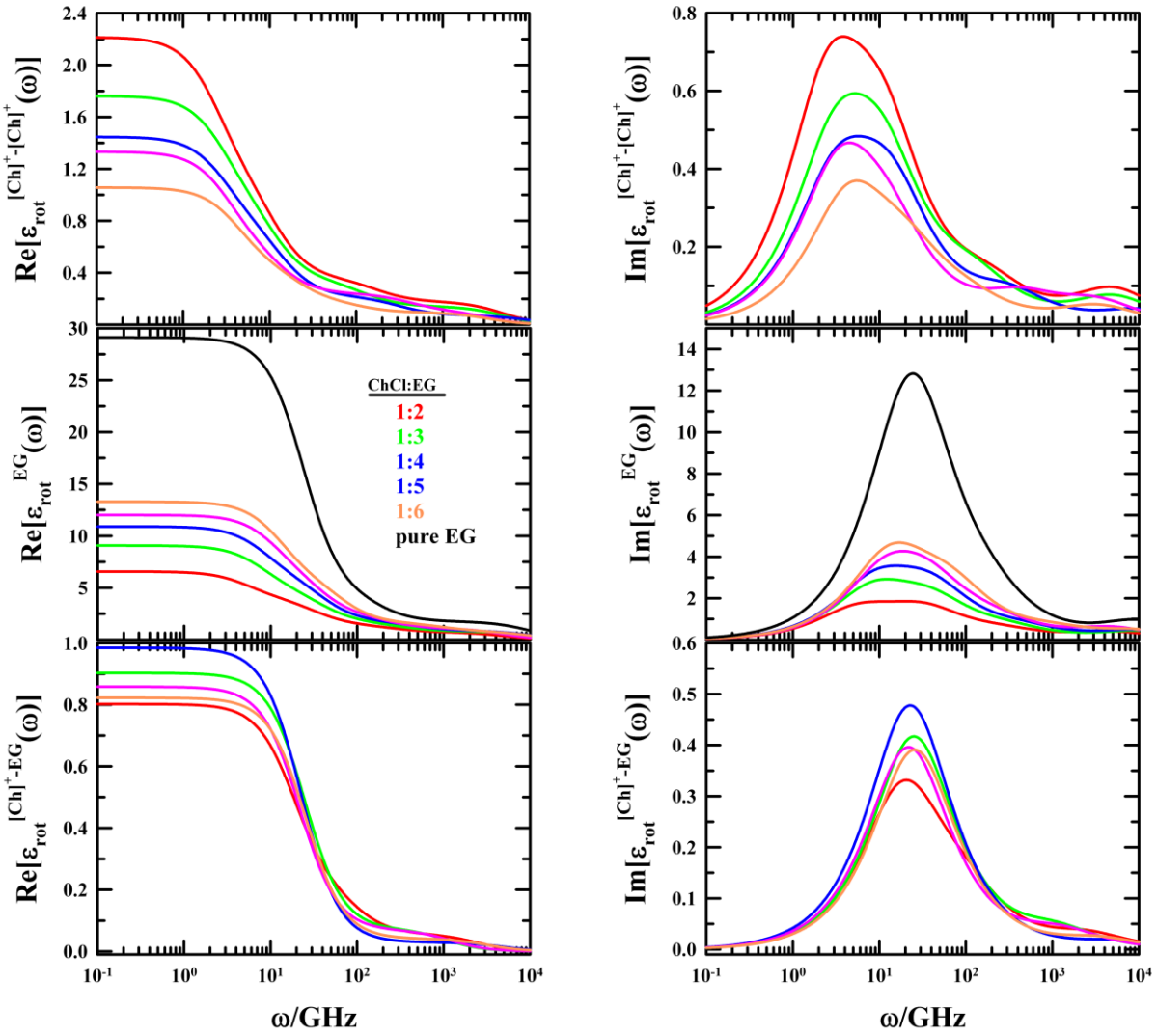

Figure 6.A.2: Contributions of $[Ch]^+$ cation, EG and their cross interactions to the total rotational dielectric spectra for various ChCl/EG mixtures.

Table 6.A.7: Dispersion coefficients ($\Delta\varepsilon_i$) and relaxation times (τ_i) of rotational dielectric spectra of $[Ch]^+$ at various ChCl/EG solutions.

ChCl:EG	$\Delta\boldsymbol{\varepsilon_1}$	$\boldsymbol{\tau_1}$ **(ps)**	$\Delta\boldsymbol{\varepsilon_2}$	$\boldsymbol{\tau_2}$ **(ps)**	$\Delta\boldsymbol{\varepsilon_3}$	$\boldsymbol{\tau_3}$ **(ps)**	$\Delta\boldsymbol{\varepsilon_4}$	$\boldsymbol{\tau_4}$ **(ps)**	$\boldsymbol{\varepsilon_{rot}^{[Ch]+}}$
1:2	1.08	389	0.75	87	0.18	5.7	0.20	0.2	2.21
1:3	0.77	334	0.65	90	0.19	8	0.14	0.2	1.76
1:4	0.65	321	0.58	74	0.15	3.2	0.07	0.1	1.45
1:5	0.72	293	0.37	80	0.13	2.4	0.11	0.3	1.33
1:6	0.61	224	0.27	48	0.08	9.3	0.10	0.2	1.06

Table 6.A.8: Dispersion coefficients ($\Delta\varepsilon_i$) and relaxation times (τ_i) of rotational dielectric spectra of EG at various ChCl/EG solutions.

ChCl:EG	$\Delta\boldsymbol{\varepsilon_1}$	$\boldsymbol{\tau_1}$ **(ps)**	$\Delta\boldsymbol{\varepsilon_2}$	$\boldsymbol{\tau_2}$ **(ps)**	$\Delta\boldsymbol{\varepsilon_3}$	$\boldsymbol{\tau_3}$ **(ps)**	$\Delta\boldsymbol{\varepsilon_4}$	$\boldsymbol{\tau_4}$ **(ps)**	$\boldsymbol{\varepsilon_{rot}^{EG}}$
1:2	2.63	181	2.56	30	0.66	3.7	0.72	0.2	6.57
1:3	4.35	120	3.08	25	0.82	3.2	0.82	0.1	9.07
1:4	4.91	114	4.25	25	0.87	2.2	0.87	0.1	10.91
1:5	5.52	86	4.20	27	1.20	4.4	1.08	0.2	12.01
1:6	7.58	75	4.12	15	0.80	1	0.80	0.1	13.29
Pure EG	25.03	42			2.33	5.4	1.75	0.1	29.11

Table 6.A.9: Dispersion coefficients ($\Delta\varepsilon_i$) and relaxation times (τ_i) of rotational dielectric spectra of $[Ch]^+$-EG cross-interactions at various ChCl/EG solutions.

ChCl:EG	$\Delta\boldsymbol{\varepsilon_1}$	$\boldsymbol{\tau_1}$ **(ps)**	$\Delta\boldsymbol{\varepsilon_2}$	$\boldsymbol{\tau_2}$ **(ps)**	$\Delta\boldsymbol{\varepsilon_3}$	$\Delta\boldsymbol{\varepsilon_1}$	$\boldsymbol{\varepsilon_{rot}^{[Ch]+-EG}}$
1:2	0.61	53	0.14	10.2	0.06	0.4	0.80
1:3	0.83	40			0.07	0.9	0.90
1:4	0.95	44			0.03	0.2	0.98
1:5	0.79	46			0.07	0.8	0.86
1:6	0.78	39			0.04	0.3	0.82

References

1 E. L. Smith, A. P. Abbott and K. S. Ryder, *Chem. Rev.*, 2014, **114**, 11060–11082.

2 Z. Yang, in *Deep Eutectic Solvents*, Wiley, 2019, pp. 43–60.

3 G. García, S. Aparicio, R. Ullah and M. Atilhan, *Energ. Fuel.*, 2015, **29**, 2616–2644.

4 R. Svigelj, N. Dossi, C. Grazioli and R. Toniolo, *Sensors*, 2021, **21**, 4263.

5 Q. Zhang, K. De Oliveira Vigier, S. Royer and F. Jérôme, *Chem. Soc. Rev.*, 2012, **41**, 7108–7146.

6 P. Xu, G.-W. Zheng, M.-H. Zong, N. Li and W.-Y. Lou, *Bioresour. Bioprocess*, 2017, **4**, 34.

7 S. Handy and K. Lavender, *Tetrahedron Lett.*, 2013, **54**, 4377–4379.

8 M. Sharma, C. Mukesh, D. Mondal and K. Prasad, *RSC Adv.*, 2013, **3**, 18149.

9 D. V. Wagle, H. Zhao and G. A. Baker, *Acc. Chem. Res.*, 2014, **47**, 2299–2308.

10 Y.-L. Chen, X. Zhang, T.-T. You and F. Xu, *Cellulose*, 2019, **26**, 205–213.

11 A. E. Ünlü, A. Arıkaya and S. Takaç, *Green Process. Synth.*, 2019, **8**, 355–372.

12 C. Florindo, M. M. Oliveira, L. C. Branco and I. M. Marrucho, *J. Mol. Liq.*, 2017, **247**, 441–447.

13 J. S. Lee, *Nanotechnol. Rev.*, 2017, **6**, 271–278.

14 F. G. Calvo-Flores and C. Mingorance-Sánchez, *ChemistryOpen*, 2021, **10**, 815–829.

15 D. O. Abranches, M. A. R. Martins, L. P. Silva, N. Schaeffer, S. P. Pinho and J. A. P. Coutinho, *Chem. Commun.*, 2019, **55**, 10253–10256.

16 M. A. R. Martins, S. P. Pinho and J. A. P. Coutinho, *J. Sol. Chem.*, 2019, **48**, 962–982.

17 I. N. Levine, *Physical Chemistry (6th ed.)*, 2009, McGraw-Hill.

18 A. H. Turner and J. D. Holbrey, *Phys. Chem. Chem. Phys.*, 2019, **21**, 21782–21789.

19 R. Stefanovic, M. Ludwig, G. B. Webber, R. Atkin and A. J. Page, *Phys. Chem. Chem. Phys.*, 2017, **19**, 3297–3306.

20 O. S. Hammond, D. T. Bowron and K. J. Edler, *Green Chemistry*, 2016, **18**, 2736–2744.

21 Y. Zhang, D. Poe, L. Heroux, H. Squire, B. W. Doherty, Z. Long, M. Dadmun, B. Gurkan, M. E. Tuckerman and E. J. Maginn, *J. Phys. Chem B*, 2020, **124**, 5251–5264.

22 E. O. Fetisov, D. B. Harwood, I.-F. W. Kuo, S. E. E. Warrag, M. C. Kroon, C. J. Peters and J. I. Siepmann, *J. Phys. Chem. B*, 2018, **122**, 1245–1254.

23 S. Zahn, *Phys. Chem. Chem. Phys.*, 2017, **19**, 4041–4047.

24 G. García, M. Atilhan and S. Aparicio, *Chem. Phys. Lett.*, 2015, **634**, 151–155.

25 S. Kaur, S. Sharma and H. K. Kashyap, *J. Chem. Phys.*, 2017, **147**, 194507.

26 P. Kumari, Shobhna, S. Kaur and H. K. Kashyap, *ACS Omega*, 2018, **3**, 15246–15255.

27 D. O. Abranches, R. O. Martins, L. P. Silva, M. A. R. Martins, S. P. Pinho and J. A. P. Coutinho, *J. Phys. Chem. B*, 2020, **124**, 4174–4184.

28 A. Yadav and S. Pandey, *J. Chem. Eng. Data*, 2014, **59**, 2221–2229.

29 A. P. Abbott, G. Capper, D. L. Davies, R. K. Rasheed and V. Tambyrajah, *Chem. Commun.*, 2003, 70–71.

30 M. Gilmore, M. Swadzba-Kwasny and J. D. Holbrey, *J. Chem. Eng. Data*, 2019, **64**, 5248–5255.

31 V. Agieienko and R. Buchner, *J. Chem. Eng. Data*, 2019, **64**, 4763–4774.

32 V. Agieienko and R. Buchner, *Phys. Chem. Chem. Phys.*, 2022, **24**, 5265–5268.

33 H. J. Hayler and S. Perkin, *Chem. Commun.* 2022, **58**, 12728–12731.

34 V. Agieienko, V. Neklyudov and R. Buchner, *J. Phys. Chem. Lett.*, 2022, **13**, 10805–10809.

35 V. Alizadeh, F. Malberg, A. A. H. Pádua and B. Kirchner, *J. Phys. Chem. B*, 2020, **124**, 7433–7443.

36 M. K. Tran, M.-T. F. Rodrigues, K. Kato, G. Babu and P. M. Ajayan, *Nat. Energy*, 2019, **4**, 339–345.

37 A. P. Abbott, G. Capper, K. J. McKenzie and K. S. Ryder, *J. Electroanal. Chem.*, 2007, **599**, 288–294.

38 G. R. T. Jenkin, A. Z. M. Al-Bassam, R. C. Harris, A. P. Abbott, D. J. Smith, D. A. Holwell, R. J. Chapman and C. J. Stanley, *Miner Eng.*, 2016, **87**, 18–24.

39 J. D. Gamarra, K. Marcoen, A. Hubin and T. Hauffman, *Electrochim. Acta.*, 2019, **312**, 303–312.

40 H. Shekaari, M. T. Zafarani-Moattar, A. Shayanfar and M. Mokhtarpour, *J. Mol. Liq.*, 2018, **249**, 1222–1235.

41 A. R. Harifi-Mood and R. Buchner, *J. Mol. Liq.*, 2017, **225**, 689–695.

42 A. Yadav, J. R. Kar, M. Verma, S. Naqvi and S. Pandey, *Thermochim. Acta*, 2015, **600**, 95–101.

43 O. S. Hammond, H. Li, C. Westermann, A. Y. M. Al-Murshedi, F. Endres, A. P. Abbott, G. G. Warr, K. J. Edler and R. Atkin, *Nanoscale Horiz.*, 2019, **4**, 158–168.

44 N. Fanjul-Mosteirín, C. Concellón and V. del Amo, *Org. Lett.*, 2016, **18**, 4266–4269.

45 S. L. Perkins, P. Painter and C. M. Colina, *J. Chem. Eng. Data*, 2014, **59**, 3652–3662.

46 E. S. C. Ferreira, I. V. Voroshylova, C. M. Pereira and M. N. D. S. Cordeiro, *J. Phys. Chem. B*, 2016, **120**, 10124–10137.

47 S. Kaur, A. Gupta and H. K. Kashyap, *J. Phys. Chem. B*, 2020, **124**, 2230–2237.

48 S. Kaur, A. Malik and H. K. Kashyap, *J. Phys. Chem. B*, 2019, **123**, 8291–8299.

49 M. J. Abraham, D. van der Spoel, E. Lindahl, B. Hess and and the GROMACS development team, GROMACS User Manual version 2018.

50 L. Martínez, R. Andrade, E. G. Birgin and J. M. Martínez, *J. Compu.t Chem*, 2009, **30**, 2157–2164.

51 Y. Zhang, H. Squire, B. Gurkan and E. J. Maginn, *J. Chem. Eng. Data*, 2022, **67**, 1864–1871.

52 E. J. Haug, J. S. Arora and K. Matsui, *J. Optim. Theory Appl.*, 1976, **19**, 401–424.

53 S. Nosé, *J. Chem. Phys.*, 1984, **81**, 511–519.

54 M. Parrinello and A. Rahman, *J. Appl. Phys.*, 1981, **52**, 7182–7190.

55 M. Brehm, M. Thomas, S. Gehrke and B. Kirchner, *J. Chem. Phys.*, 2020, **152**, 164105.

56 M. Brehm and B. Kirchner, *J. Chem. Inf. Model.*, 2011, **51**, 2007–2023.

57 N. F. Gajardo-Parra, V. P. Cotroneo-Figueroa, P. Aravena, V. Vesovic and R. I. Canales, *J. Chem. Eng. Data*, 2020, **65**, 5581–5592.

58 Y. Zhang, A. Otani and E. J. Maginn, *J. Chem. Theory Comput.*, 2015, **11**, 3537–3546.

59 A. Einstein, *Ann. Phys.*, 1905, **322**, 549–560.

60 M. G. Del Pópolo and G. A. Voth, *J. Phys. Chem. B*, 2004, **108**, 1744–1752.

61 C. D'Agostino, R. C. Harris, A. P. Abbott, L. F. Gladden and M. D. Mantle, *Phys. Chem. Chem. Phys.*, 2011, **13**, 21383.

62 M. Mynam, S. Kumari, B. Ravikumar and B. Rai, *J. Chem. Phys.*, 2021, **154**, 214503.

63 A. Luzar, *Faraday Discuss.*, 1996, **103**, 29.

64 A. Chandra, *Phys. Rev. Lett.*, 2000, **85**, 768–771.

65 C. Schröder and O. Steinhauser, *J. Chem. Phys.*, 2010, **132**, 244109.

66 J. M. Caillol, D. Levesque and J. J. Weis, *J. Chem. Phys.*, 1986, **85**, 6645–6657.

67 G. Löffler, H. Schreiber and O. Steinhauser, *J. Chem. Phys.*, 1997, **107**, 3135–3143.

68 C. Schröder, M. Haberler and O. Steinhauser, *J. Chem. Phys.*, 2008, **128**, 134501.

69 C. Schröder, T. Rudas and O. Steinhauser, *J. Chem. Phys.*, 2006, **125**, 244506.

70 T. Rudas, C. Schröder, S. Boresch and O. Steinhauser, *J. Chem. Phys.*, 2006, **124**, 234908.

71 C. Schröder, C. Wakai, H. Weingärtner and O. Steinhauser, *J. Chem. Phys.*, 2007, **126**, 084511.

72 C. Schröder, J. Hunger, A. Stoppa, R. Buchner and O. Steinhauser, *J. Chem. Phys.*, 2008, **129**, 184501.

73 C. Schröder, T. Rudas, G. Neumayr, S. Benkner and O. Steinhauser, *J. Chem. Phys.*, 2007, **127**, 234503.

74 C. Schröder, M. Sega, M. Schmollngruber, E. Gailberger, D. Braun and O. Steinhauser, *J. Chem. Phys.*, 2014, **140**, 204505.

Chapter 7

Structure and dynamics of a glucose-based cryoprotectant mixture: A computer simulation study

7.1 Introduction

Enduring in harsh environmental conditions like extreme low temperature and humidity requires special designing and adaptation of living cells [1–6]. To prevent cell damage, plants and animals in such conditions synthesize antifreeze chemicals, like sugars [7–9] and polyols [10,11]. These compounds help to keep the function of cells intact. This process is known as cryopreservation and these compounds are known as cryoprotectants [12–17]. The main function of cryoprotectants is to protect cells from icing of water [9,10]. Cryoprotectants are usually poly-hydroxy alcohols or sugars and can form strong hydrogen bond (H-bond) networks. In this process it replaces biological water molecules from cell and get bound itself to biomolecules [18,19]. In other words, it may break the tetrahedral network of water and prevent from being frozen to ice [20]. Cryoprotectants or cryoprotective agents (CPA) breaks the H-bond network of water outside cell which is known as 'extracellular fluid' and eventually inhibit crystallization of water [21]. Cryoprotectants also function inside a cell via preferential hydration of biomolecules and are known as intracellular CPA [22–24].

Glucose is a common cryoprotectant which is readily used in cryopreservation of biological moieties [25–27]. It has six sites for efficient H-bonding, and also easily available in nature. Ethylene glycol (EG) is a dihydroxy alcohol, and has been effectively used in various fields of cryogenic preservation [28–31]. Binary, or ternary mixtures of cryoprotectants may show better efficiency in cryopreservation than one single CPA. Several examples in this regard are glucose/glycerol [32], trehalose/glycerol [33], trehalose/ethylene glycol [34], glucose/ethylene glycol [35], sucrose/ethylene glycol [36] and ethylene glycol/dimethyl sulfoxide [37].

Among these mixtures we have taken the glucose/ethylene glycol system for investigation. One component of the mixture, glucose, is a nonpermeable CPA, that is, it cannot go beyond cell membrane and act as extracellular CPA [7,9]. EG, on the other hand, can diffuse through the cell membrane and, functions in both intra- and extracellular regions [36]. Therefore, their

mixture can work in both sides of a cell membrane. The efficiency and activity of this mixture can be regulated by varying CPA concentrations. Potential usage of glucose/ethylene glycol mixtures have been reported by a few earlier studies [35,38–40]. These works were focused on the CPA-biomolecule interactions. However, the inherent interspecies, and intraspecies interactions and dynamics of glucose/EG system were not explored. In the study reported here, we have followed the intra- and inter-species interactions present in the glucose/EG system by probing the solution structural aspects, and then monitored relaxation properties that were governed by these complex interactions. In this study, we explore the structure, and dynamics of this binary mixture using molecular dynamics (MD) simulations. Extensive analyses are done to attain comprehensive idea about the effect of concentration on the structure, and dynamics of the binary mixtures. MD simulations have been performed at 298.15 K with five different systems containing 0, 10, 20, 30, and 40 wt% of glucose. Experiments were carried out at 298±1 K to measure density and viscosity of these systems.

7.2 Methods and materials

7.2.1 Computational details

7.2.1.1 Methods and relevant equations

Molecular dynamics simulation results presented here were obtained from simulations performed by using GROMACS-2018.3 package [41] and classical coarse-grained interaction potentials. Four glucose solutions in ethylene glycol with varying glucose concentrations were considered along with one neat ethylene glycol system. The weight percentages of glucose in solutions were taken as 10, 20, 30, 40. Details of the simulation boxes are provided in Table 7.A.1 of Appendix 7.A. Glucose and EG molecules were arranged in cubic simulation boxes using PACKMOL software [42]. After energy minimization, systems were first equilibrated in NVT ensemble for 5 ns. Next, equilibrations of 20 ns were carried out employing NPT ensemble. Temperature and pressure were maintained as 298.15 K and 1 bar using Nose-Hoover thermostat [43,44] and Parrinello-Rahman barostat [45,46], respectively. For each system, a production run of 200 ns was performed and trajectories saved for analysis. Generalized Amber Force Field (GAFF) parameters [47,48] were used to model the bonded and non-bonded interactions between molecules. Functional form of the model potential is as follows:

$$E = E_{bonds} + E_{angles} + E_{dihedrals} + E_{non-bonded}$$
$$= \sum_{bonds} K_r(r - r_{eq})^2 + \sum_{angles} K_\theta\left(\theta - \theta_{eq}\right)^2 + \sum_{dihedrals} K_\phi(1 + \cos(n\phi - \phi_s))$$
$$+ \sum_{i=1}^{N-1}\sum_{j>i}^{N}\left\{4\epsilon_{ij}\left[\left(\frac{\sigma_{ij}}{r_{ij}}\right)^{12} - \left(\frac{\sigma_{ij}}{r_{ij}}\right)^{6}\right] + \frac{q_i q_j}{4\pi\epsilon_0 r_{ij}}\right\} \quad (7.1)$$

In Eq. 7.1, K_r and K_θ are force constants for bond stretching and angle bending, respectively. ϕ denotes torsional angle with Fourier coefficient K_ϕ, multiplicity n and phase angle ϕ_s. Position and charge of an atom are described by r, and q, respectively. The van der Waals parameters are described by σ and ε.Note that the non-bonded and electrostatic interactions were represented by the Lennard-Jones (LJ) potential and the Coulomb equation, respectively. The short-range cut-off distance was fixed at 1 nm and the Particle Mesh Ewald (PME) method was used for the Coulomb-type interactions. Leapfrog algorithm with a time step of 1 fs was used to solve equations of motion. Linear Constraint Solver (LINCS) [49] algorithm was used to constrain the bonds involving hydrogens.

Spatial correlations were followed via calculating the radial distribution functions (RDFs), $g_{A-B}(r)$:

$$g_{A-B}(r) = \frac{\langle\rho_B(r)\rangle}{\rho_B^{ave}} = \frac{1}{N_A\rho_B^{ave}}\sum_{i\in A}^{N_A}\sum_{i\in B}^{N_B}\frac{\partial(r_{ij}-r)}{4\pi r^2}, \quad (7.2)$$

where $\langle\rho_B(r)\rangle$ indicates density of B type particles around A type at a distance r and ρ_B^{ave} is the average number density of B type particles.

From the simulated RDF, the static structure factor ($S(q)$) was obtained by using the following formula:[50–52]

$$S(q) = \frac{\rho\sum_i^N\sum_j^N x_i x_j f_i(q) f_j(q)\int_0^{L/2} 4\pi r^2[g(r)-1]\frac{\sin qr}{qr}\omega(r)dr}{\left[\sum_i^N x_i f_i(q)\right]\left[\sum_j^N x_j f_j(q)\right]} \quad (7.3)$$

In Eq. 7.3, ρ is the total number density, x and f are mole fraction and X-ray atomic form factor, respectively [53]. L, and V are the length and volume of the simulation box, respectively. Lorch-window function ($\omega(r) = \sin(2\pi r/L)/(2\pi r/L)$) [54,55] was used to reduce initial noise. This function could be directly compared to experimentally measured X-ray scattering function.

From equilibrium simulation trajectory, shear viscosity (η) was calculated by using the Green-Kubo relation [56].

$$\eta = \frac{V}{k_B T}\int_0^\infty dt\langle P_{\alpha\beta}(0)P_{\alpha\beta}(t)\rangle \quad (7.4)$$

In the above equation, V, k_B, and T are box volume, Boltzmann constant, and temperature, respectively. $P_{\alpha\beta}$ denotes cross-diagonal elements of pressure tensor.

The translational dynamics of different species was characterized by calculating the mean square displacements (MSDs) from the simulated trajectories. The self-diffusion coefficients were obtained from the Einstein relation [57]

$$\mathrm{D} = \frac{1}{6}\lim_{t\to\infty}\frac{d}{dt}\langle|\boldsymbol{r}_i(t) - \boldsymbol{r}_i(0)|^2\rangle \quad (7.5)$$

where D, and r_i denote self-diffusion coefficient, and position of center-of-mass (COM) of ith molecule, respectively. The angular bracket denotes ensemble average over all molecules. The self-diffusion coefficients were calculated from the diffusive regime of the respective MSDs, where the diffusive regime was defined by $\beta(t)$ =1 where

$$\beta(t) = \frac{dlog\langle|\boldsymbol{r}_i(t)-\boldsymbol{r}_i(0)|^2\rangle}{dlog(t)}. \quad (7.6)$$

Structural H-bond autocorrelation function, ($C_{HB}(t)$), was calculated by using the formula [58,59]

$$C_{HB}(t) = \langle h(0)h(t)\rangle/\langle h(0)^2\rangle \quad (7.7)$$

where *h(t)* is a variable which denote presence or absence of H-bonds between to moieties. If one particular H-bond exists at t=0 and at time t then $h(t)$=1 otherwise $h(t)$=0. However, breaking of the H-bond in the meantime is not considered here. The commonly used geometric criteria was used to define a H-bond.

(i) $r_{\mathrm{DA}} \leq r_{\mathrm{DA}}^c$,

(ii) $r_{\mathrm{HA}} \leq r_{\mathrm{HA}}^c$,

(iii) $\angle\mathrm{HDA} \leq 30^\circ$ (intermolecular), and $\angle\mathrm{HDA} \leq 60^\circ$ (intramolecular).

where H, D, A denote to hydrogen, donor, and acceptor, respectively. The cutoff distance (r^c) is set as the first minimum of the corresponding RDFs.

Reorientational dynamics of molecules were investigated by analyzing the decay of the reorientational time correlation functions ($C_1(t)$)[60]:

$$C_1(t) = \langle P_1|\boldsymbol{u}(0).\boldsymbol{u}(t)|\rangle / \langle P_1|\boldsymbol{u}(0).\boldsymbol{u}(0)|\rangle \quad (7.8)$$

In eq. (8) $\boldsymbol{u}$ denotes the backbone vector of a molecule and P_1 the first-order Legendre polynomial. We will discuss the detailed methods later.

Molecular representations were generated in UCSF Chimera, [61] and TRAVIS [62,63]. All analyses were performed using in-house codes, and TRAVIS [62–66].

7.2.1.2 Validation of the model interaction potential

In this work, structural and dynamical aspects of EG-glucose cryoprotective agent (CPA) were investigated. Starting from pure EG, glucose was gradually added to EG to form binary mixture solutions with glucose weight percentages (0%, 10%, 20%, 30%, and 40%). The atomic representations of EG, and glucose are shown in Figure 7.A.1 of Appendix 7.A. First, we will discuss a few structural and dynamical properties of neat EG, and compare our results with the available data.

Several studies have reported the presence of dominant *gauche* isomer (~80%) in liquid ethylene glycol compared to *trans* isomer (20%) [67–70]. We have calculated dihedral angle (-OCCO-) distribution of liquid EG and defined *gauche* and *trans* isomers following a method described elsewhere [48]. The probability of finding *gauche* and *trans* isomers in our model EG are as ~78%, and ~22%, respectively (see Figure 7.A.2 of Appendix 7.A). Our simulated results are therefore agreeing well with existing experimental and simulation data [48,67–71].

Next, the computed static structure factor ($S(q)$) of liquid EG are compared with experimental results. A good qualitative agreement between simulations and experiments therefore proves the efficacy of the force field model employed here. In Figure 7.A.3, a principal peak around q = 15.4 nm^{-1} (r = 0.41 nm) followed by a small hump at ~ q = 26.6 nm^{-1} (r = 0.24nm) can be noticed. In Figure 7.A.4 of Appendix 7.A, different atom-atom RDFs of liquid EG are presented. The C-C and C-O correlations arise at ~ 0.4 nm which is the distance where principal peak of $S(q)$ was observed. Hence, the major contributions to the principal peak are arising from C-C and C-O correlations. The small peak at ~0.24nm is mainly due to O-O interactions which can be visible from Figure 7.A.4(b).

Density, viscosity, and self-diffusion coefficients were calculated and compared with experimental data [72–74] in Table 7.A.2. Density and diffusion coefficient values deviated less than 2% from the corresponding experimental data whereas the deviation for viscosity was

relatively more (< 20%). Considering the complexity of these systems and the approximations involved in representing the interactions, this deviation between experiments and simulations may be acceptable for developing a semi-quantitative description of these cryoprotectants.

7.2.2 Experimental method

D (+) Glucose (≥99.5) and ethylene glycol (≥99%) were purchased from Sigma Aldrich and used for preparation of sample without purification. The multi-component cryoprotectant mixtures were prepared by dissolving of ethylene glycol and glucose with magnetic stirring cum hot plate at high temperature for 2-3 hrs. The detailed procedure to preparation of the four experimental glucose / ethylene glycol mixtures (10, 20, 30 and 40 wt% of glucose in ethylene glycol) ware as follows: for 10 wt% glucose, requisite amount of glucose and ethylene glycol were weighed in glass container and a Teflon coated magnetic bar was entered into this glass container before making it airtight. The airtight glass container was heated on a magnetic stirrer hot plate at 343 K for 2-3 hrs at 600 rpm in an oil bath. Using the above-mentioned strategies, a colourless transparent solution is obtained without any solute crystal appearance. In the same way, 20, 30 and 40 wt% glucose solution were prepared by raising solution temperature to 348 K, 353 K, and 363 K, respectively for 3 hrs. The prepared solutions were cooled to room temperature before performing density and viscosity measurements. Density (ρ) and viscosity coefficient (η) of experimental mixtures were measured at 298 K by using an automated temperature-controlled density cum sound velocity analyser (Anton Parr, model DSA 5000) and micro viscometer (AMVn, Anton Paar), respectively [75,76]. The temperature fluctuation during all measurements was limited within ±1 K.

7.3 Results and discussion

7.3.1 Radial distribution functions (RDFs)

Atom-atom, and COM-COM (center-of-mass: COM) RDFs were calculated to explore microscopic structures of the investigated systems. As both glucose and EG can form extensive H-bonds, first we checked the RDFs involving oxygen, and hydroxyl hydrogen atoms. Intermolecular RDFs between oxygen, and hydroxyl hydrogen atoms of EG are presented in Figure 7.1.

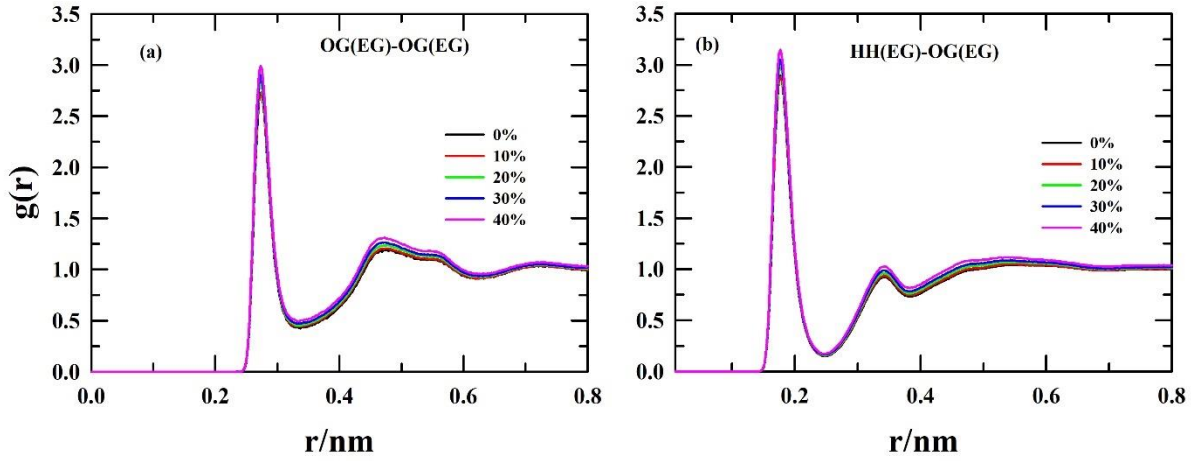

Figure 7.1: Intermolecular radial distribution function, for (a) O-O and (b) H-O pairs of EG molecules at various concentrations of glucose-EG solutions. Each system is distinctly color-coded

A sharp peak at short distance is observed in all these cases indicating strong characteristic H-bonding features. For both type of RDFs, a weak second peak is also detected. Each EG molecule has two oxygen and two hydroxyl hydrogen atoms. The first peak is the result of H-bonding interactions. The second peak may have originated from the interactions of the corresponding atoms which are not taking part in the formation of H-bonds.

At a first glance it may be assumed from the peak height that correlations between respective atoms are increasing upon addition of glucose in the solution. This interpretation can be misleading as peak intensity does not give the complete population picture, especially for multi-component mixtures. To better understand the molecular arrangements, it was proposed to analyze number density (ρ) times RDF ($g(r)$) instead of only $g(r)$ [77–82]. The modified plots are shown in Figure 7.2. Now, the concentration effect is vivid and with increasing amount of glucose in solution, EG-EG interaction diminishes. Although the peak intensity decreases, peak positions remain almost the same. This implies that EG-EG correlation is mitigated in the presence of glucose but the inherent liquid structure remains unaltered. The number of observed atoms in the first solvation shell of a reference atom can be calculated by integrating up to the first minimum of the calculated RDF. Positions of the first extrema and coordination numbers are listed in Table 7.A.3 (Appendix 7.A). Coordination numbers decrease with increasing glucose concentration, that is, population of observed atoms around one reference atom is gradually reduced.

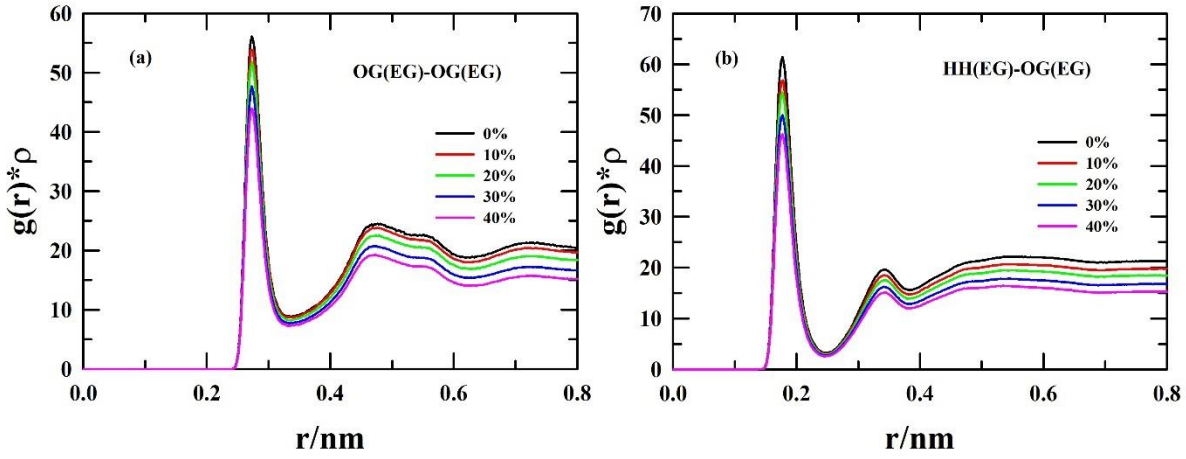

Figure 7.2: Intermolecular radial distribution functions multiplied by number density (ρ*$g(r)$), for (a) O-O and (b) H-O atom pairs of ethylene glycol at various concentrations of glucose-EG solutions. Each system is distinctly color-defined.

Now, we see how the possible H-bonding sites of glucose stack around each other. Figure 7.3 shows the density normalized RDFs, $g(r)$*ρ, for the mutual interaction between oxygen, and hydroxyl hydrogen atoms of glucose. A sharp principal peak is observed for both cases which suggests presence of H-bonding interaction between the corresponding atoms.

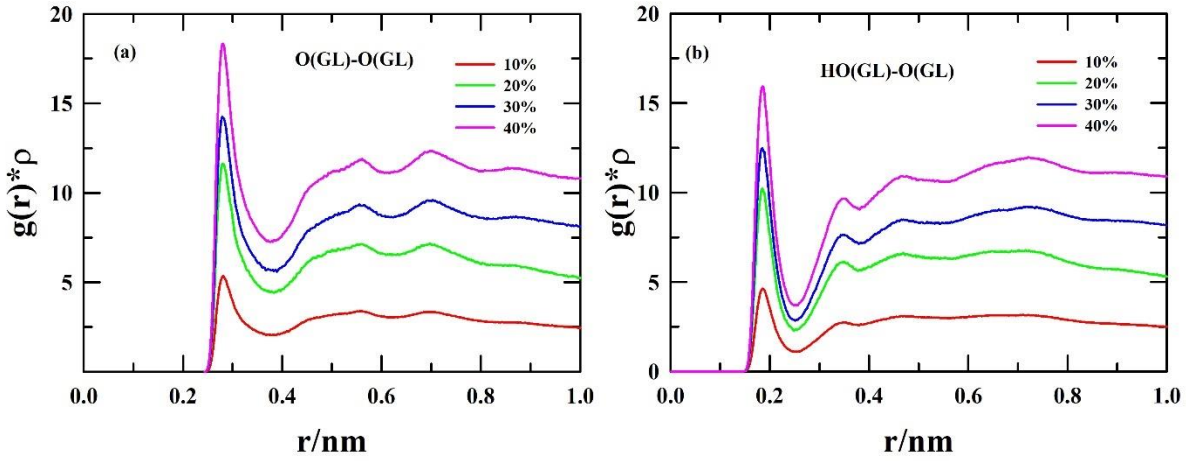

Figure 7.3: Intermolecular radial distribution multiplied by number density ($g(r)$*ρ) for (a) O-O and (b) H-O atom pairs of glucose at various concentrations of glucose-EG solutions. Each system is uniquely color-defined

The peak intensity increases with increasing glucose content in the system. Hence, glucose molecules preferentially interact with other glucose molecules and gradual addition of glucose favors the process. Like EG, here also the peak position does not change much. This indicates

similar type of correlation between glucose molecules present in these solutions. Coordination numbers reflect the gradual accumulation of O atoms around one reference oxygen or hydrogen atom (see Table 7.A.3).

Along with intraspecies interactions, interspecies interactions play crucial role in determining the solution properties. Here two types of EG-glucose interactions are considered. First, we monitor the arrangement of O atoms of glucose around hydroxyl hydrogen of EG, and then distribution of O atoms of EG in the vicinity of hydroxyl hydrogens of glucose. Figure 7.4 shows the corresponding $g(r)*\rho$ plots. The peak positions and coordination numbers are summarized in Table 7.A.4.

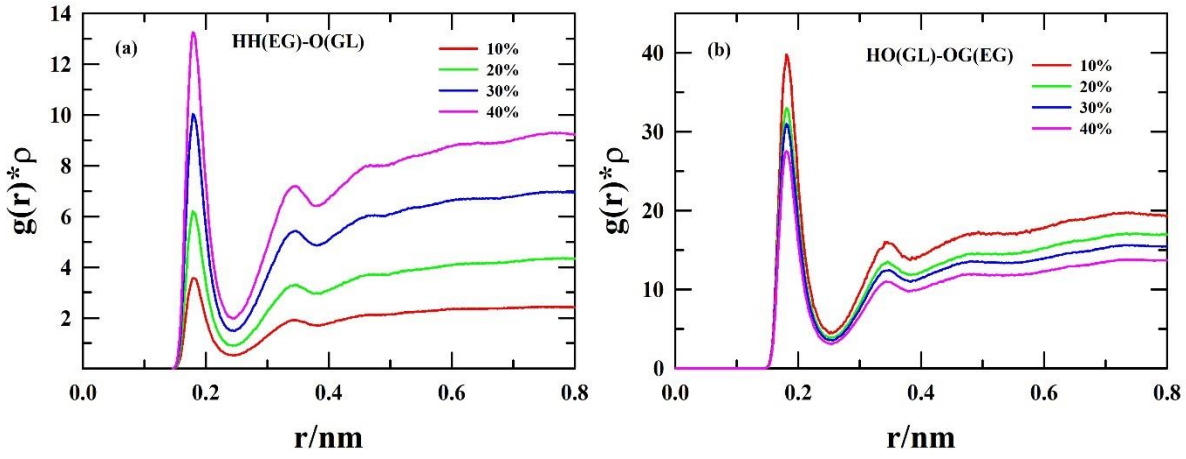

Figure 7.4: Intermolecular radial distribution multiplied by number density ($g(r)*\rho$) for H-O atom pairs of glucose and ethylene glycol respectively at various concentrations of glucose-EG solutions. Each system is color-coded.

Concentration dependent probability distributions of finding O atoms of glucose around HH-type atoms EG are shown in Figure 7.4(a). The same for O atoms of EG around hydroxyl hydrogens of glucose are represented in Figure 7.4(b). In both the cases, the presence of intense first peaks depict the possibility of formation of strong H-bonds between EG and glucose. As the concentration increases, more O atoms of glucose are arriving in the vicinity of hydroxyl hydrogens of EG. In Figure 7.2(b), we have seen gradual reduction of O atom population around HH-hydrogens. Combining these two findings, it can be said that in the vicinity of a given EG molecule, other EG molecules are increasingly replaced by the added glucose molecules. In Figure 7.4(b) it can be observed that number of O atoms of EG around HO unit of glucose decreases with increasing number of glucose molecules in the solution. From Figure 7.3(b) it is already established that incoming glucose molecules prefer to stack around another

glucose molecule. Therefore, in the solvation shells of HO units, O atoms of EG are substituted by O atoms of the added glucose molecules.

We next discuss about how the centers-of-mass (COM) of different molecules align with each other. Intra and interspecies density normalized COM-COM RDFs are shown in Figure 7.5 and the corresponding numerical values of peak positions and coordination numbers are listed in Table 7.A.5. In all the cases a strong principal peak arises which is analogous to the main peaks obtained in atom-atom RDFs indicating the presence of H-bonds. Therefore, this peak is assigned as the manifestation of extensive intra and interspecies H-bonding. This peak occurs at a greater distance for glucose-glucose interactions compared to EG-EG interactions. This could be attributed to the larger size of glucose molecules.

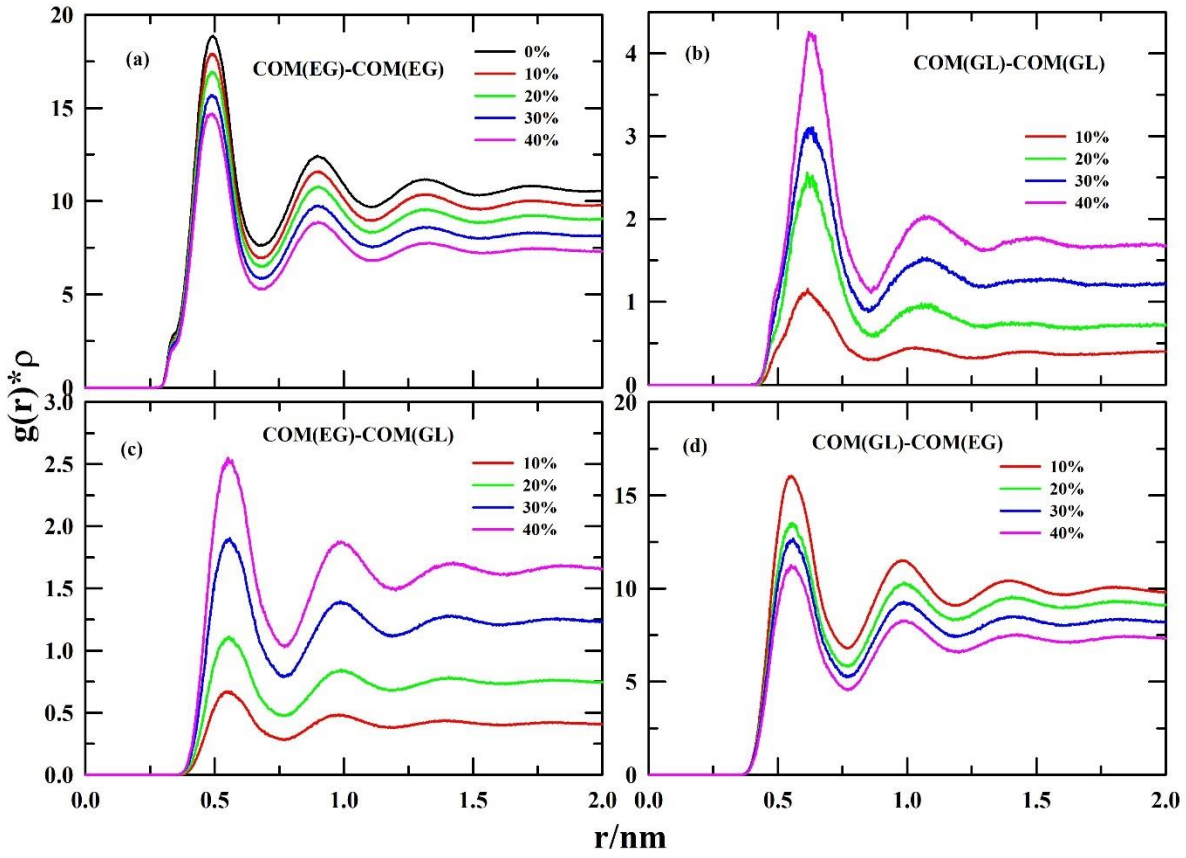

Figure 7.5: COM-COM (COM: center-of-mass) ($g(r)*\rho$) for (a) EG around EG, (b) glucose around glucose, (c) glucose around EG, and (d) EG around glucose. Results are shown for solutions of varying concentrations and each solution is indicated by distinct colors

Moving from lower to higher concentrations significant variation in population distribution is observed. In line with our previous observations, EG-EG correlations diminish in the presence

of glucose molecules (Figure 7.5(a)). On the other hand, glucose molecules tend to come into the solvation shells of other glucose molecules, and this is visible in Figure 7.5(b). Figure 7.5(c) shows number of glucose molecules around EG sharply increases from 10% to 40% concentrations but the reverse trend is found when EG molecules are considered around glucose (Figure 7.5(d)).

From the above observations, we can infer the change in self and cross correlations between EG and glucose molecules with changing the glucose concentration in the solution. At 0% concentration, strong EG-EG interaction is observed which is mainly the result of extensive H-bonding network. As glucose molecules are gradually introduced into the system, this correlation starts to decrease. On the other hand, population of glucose molecules successively increases around a reference glucose molecule indicating strong affinity towards their own type. Incoming glucose molecules start to fill the coordination spheres around a reference EG molecule by replacing other EG molecules. As glucose molecules prefer glucose as their neighbor, number of EG molecules around a reference glucose molecule decreases with increasing glucose concentration. A visual representation of corresponding coordination numbers is shown in Figure 7.6.

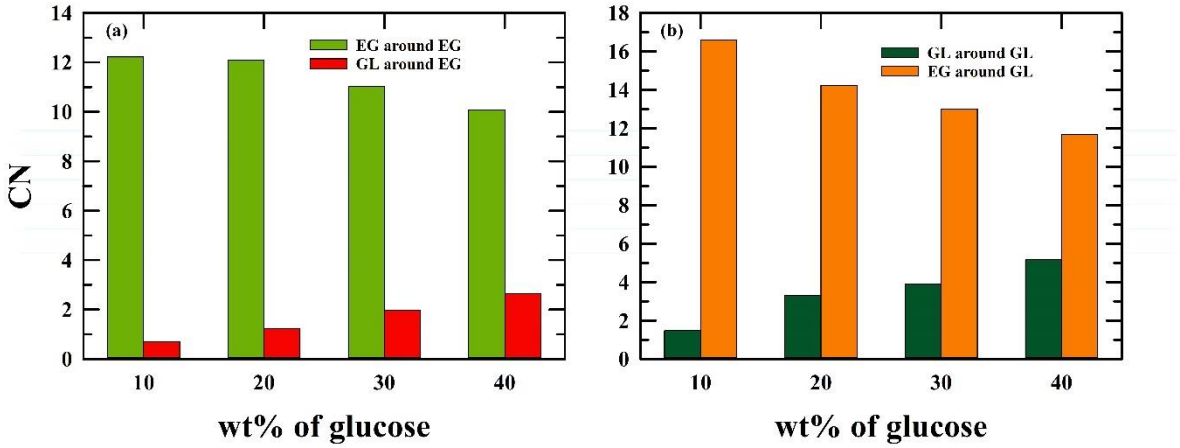

Figure 7.6: Coordination numbers obtained from COM-COM RDFs: (a) around EG, and (b) around glucose at solutions containing different wt% of glucose

7.3.2 Hydrogen bond network

From previous analyses, we have found strong signature of extensive H-bond network. One EG molecule has two donor and two acceptor sites whereas one glucose molecule has five

donor and six acceptor sites. Hence, it is necessary to analyze their H-bonding ability to completely comprehend the structure and dynamics of these potential cryoprotectant solutions. Both EG, and glucose molecules are capable of forming intra as well as intermolecular H-bonds. H-bonds are calculated as per the scheme discussed in Sec. 7.2.1. The cut-off distances are taken from Table 7.A.3 (the r_{min} values). We have calculated average number of H-bonds per molecule for both intra and interspecies cases. Concentration dependent average number of H-bonds per molecule considering different types of interactions are shown in Figure 7.7. We have obtained average number of H-bonds per ethylene glycol molecule in pure state at 298.15 as 3.63 which is in well-agreement with previous results [71,83–85]. Change of number of H-bonds per EG molecule with increasing glucose concentration is shown in Figure 7.7(a): number of intramolecular bonds remains more or less constant but intermolecular H-bonds decreases from 0% to 40% solution. In structural analyses, we have seen how infiltration of glucose molecules weakens the EG-EG pair correlations. The glucose-induced decrease of EG-EG H-bonds offers a possible explanation of this reduced EG-EG interactions. The intramolecular H-bonds are found only in *gauche* conformers of EG and the constant values depict that the ratio between the *gauche* and the *trans* isomers is not altered in the presence of glucose. Similar H-bonding analysis for glucose is shown in Figure 7.7(b). Here too the number of intramolecular H-bonds are not changing much, indicating almost no conformational change of glucose molecules. The number of intermolecular H-bonds increases with glucose concentration and so does the total number of H-bonds. Therefore, glucose molecules favorably bind with themselves and increased concentration leads to enhanced correlation. Again, this is well accordance with previously discussed microscopic arrangements of glucose molecules where more and more glucose molecules are coming into the solvation shells of a reference glucose molecule with rising glucose concentration.

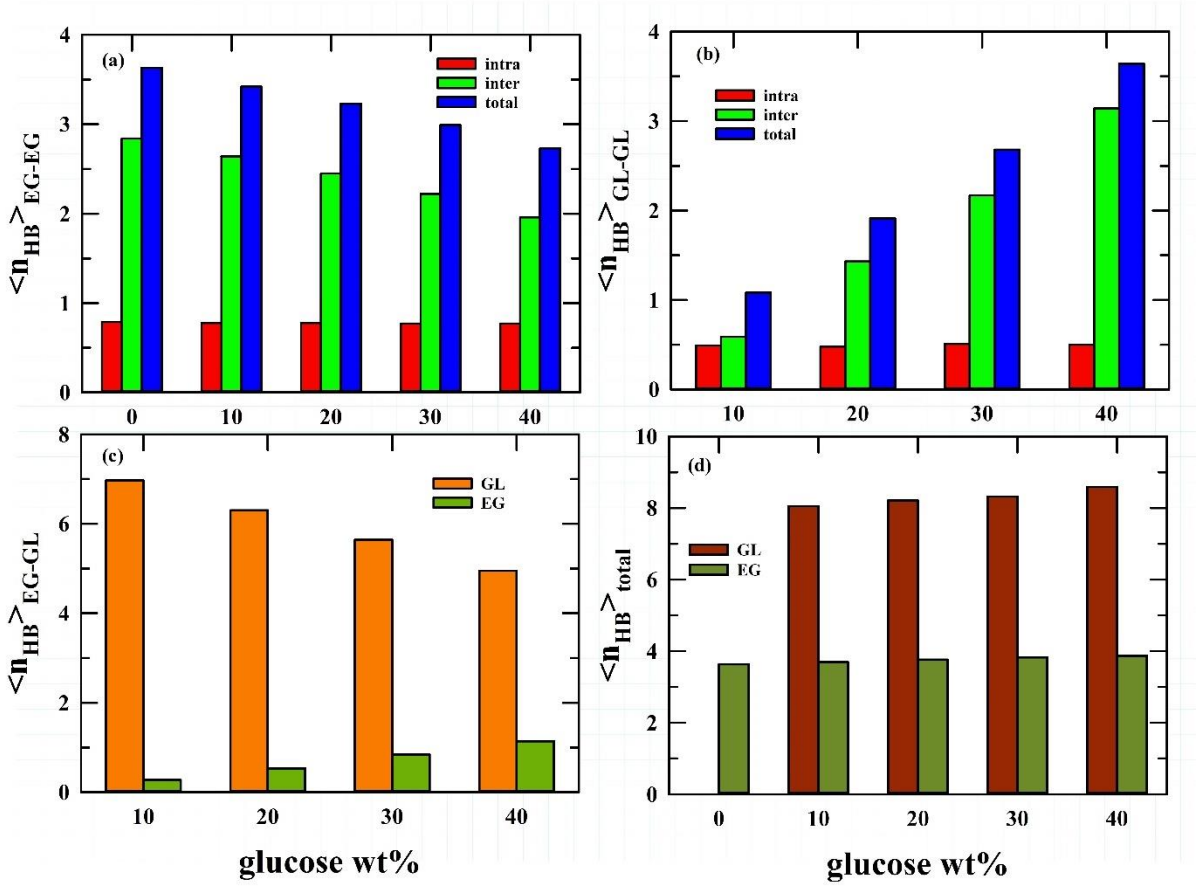

Figure 7.7: Average number of H-bonds ($<n_{HB}>$) per molecule at various concentrations of glucose/EG solutions: (a) H-bond between EG molecules, (b) H-bond between GL molecules, (c) H-bond between EG and glucose, and (d) total number of H-bonds considering all interactions

Now we will see what happens to the interspecies H-bonds as we increase the amount of glucose in solution. Average number of H-bonds between EG, and glucose are represented in Figure 7.7(c) where the orange bars indicate number of H-bonds per glucose molecule with EG, and green bars denote the number of H-bonds per EG molecule with glucose. The average number of H-bonds with glucose per EG increases from ~0.3 to ~1.1 as we move from 10% solution to 40% solution. Moreover, the number of H-bonds on glucose with EG decreases from ~7 to ~5. Hence, at a particular concentration number of H-bonds for glucose with EG is always greater than that for EG with glucose. This observation may be attributed to the number of donor and acceptor sites of the respective molecules. As mentioned earlier, EG has only two donor, and two acceptor sites whereas one glucose molecule contains five donor and six acceptor sites. Consequently, one glucose molecule always binds with a greater number of EG molecules than what one EG molecule can with glucose. The total number of H-bonds per

EG/GL molecules are shown in Figure 7.7(d). For both the molecules, the number slightly enhances with rising the concentration.

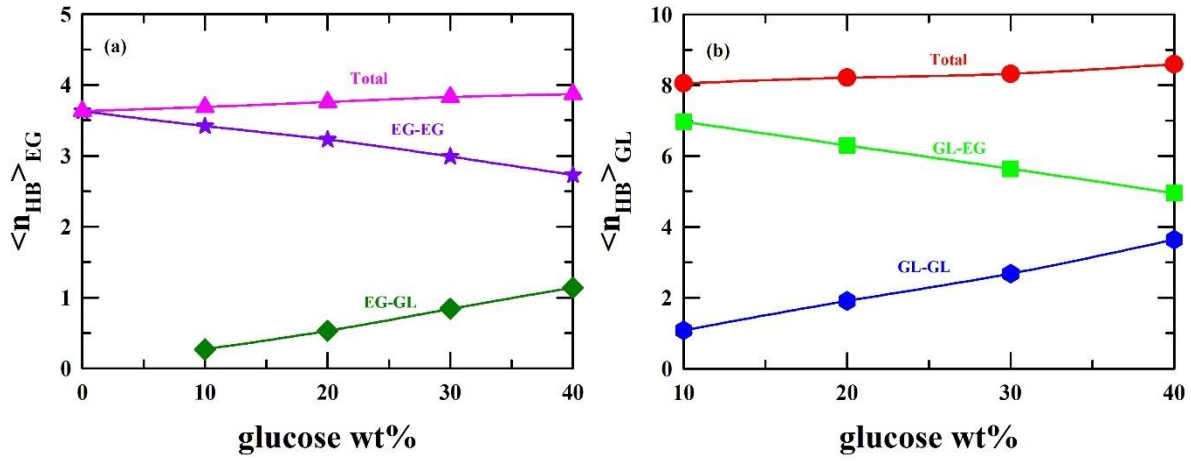

Figure 7.8: Concentration-dependent average number of intraspecies, interspecies, and total H-bonds per (a) EG, and (b) glucose. The lines going through the symbols are only a guide to bare eyes.

Individual contributions from inter and intraspecies H-bonding are analyzed in Figure 7.8. For EG molecules numbers of inter, and intraspecies H-bonds change in opposite direction resulting slight increment in total number of bonds from 0% to 40% solutions. As glucose molecules gradually invade into EG molecules, EG-EG correlations diminish and hence number of intraspecies bonds decrease. On the other hand, with increasing number of glucose molecules in the solution, one EG molecule find more glucose around itself and consequently number of interspecies H-bonds increase. For glucose molecules, total number of H-bonds per molecules enhances too but the intraspecies and interspecies interactions are completely opposite to that of EG. Here, intraspecies bonds increase, and interspecies bonds decrease from low to high concentration. All these simulated RDFs, therefore, indicate that H-bonds play a critical role in determining the solution structure of these cryoprotectant mixtures.

7.3.3 Thermo-physical properties

Density, and viscosity were obtained from both simulations, and experiments. Detailed procedures of measurements are provided in Sec. 7.2.2. A Comparison between the simulated and the experimental results then validate applicability of the force field models employed in the present study.

7.3.3.1 Density

We have calculated density of solutions containing 0% to 40% glucose from MD simulation. Density values are extracted from a 25 ns simulation run in NPT condition. The simulated, and experimental values are displayed in Figure 7.A.5 and a monotonic increment in density is observed with increasing concentration. Simulated densities match excellently with experimentally measured values with a maximum deviation of 0.6%.

7.3.3.2 Viscosity

Viscosity is an important property of liquids to get idea about the dynamics of the system as it severely affects the movement of molecules, e.g., rotation, and translation. The methodology for shear viscosity calculation was briefly discussed in Sec. 7.2.1. For each system, we have performed five independent MD runs in NVT conditions for 5 ns. We follow the protocol for calculation of viscosity, described elsewhere [86].

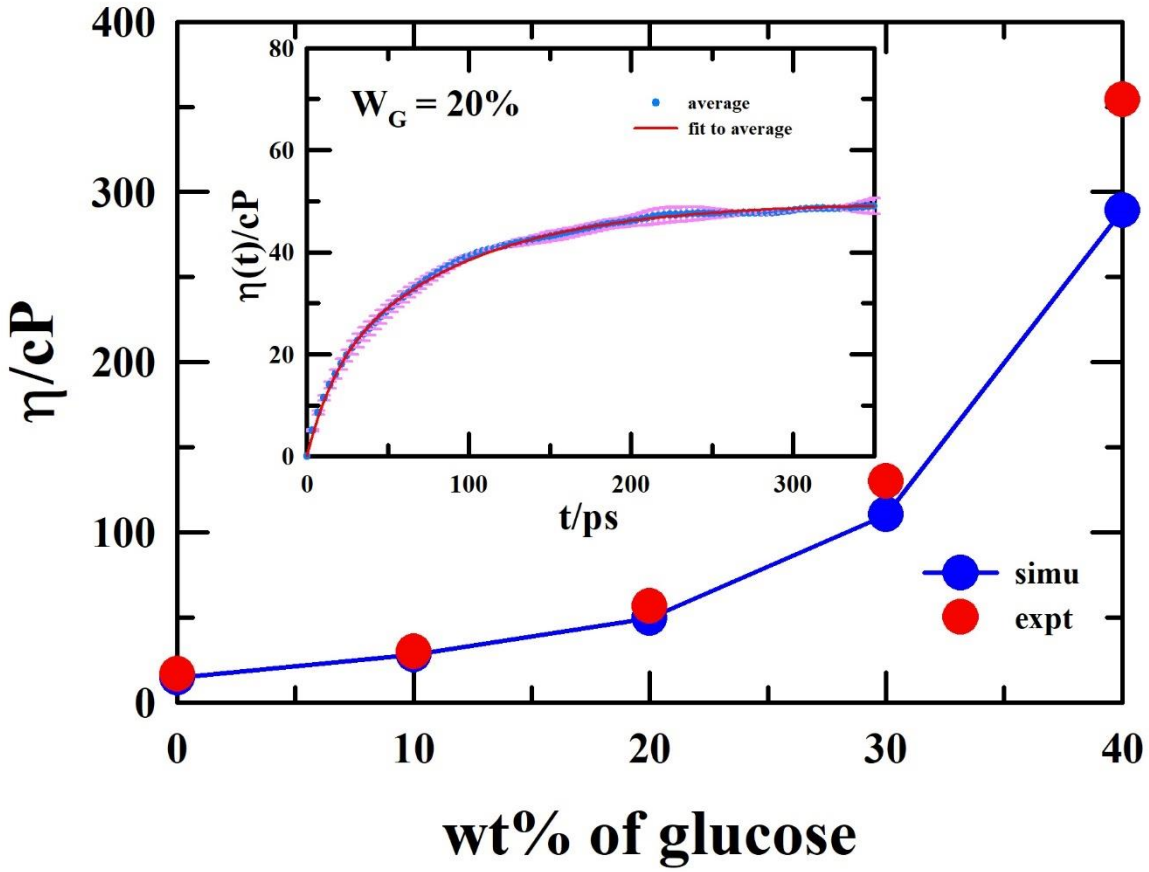

Figure 7.9: Concentration-dependent shear viscosity for glucose/EG solutions at 298.15 K. Blue and red solid spheres denote simulated and experimentally measured viscosity values, respectively. The blue line going through the simulated data points is only a guide to bare eyes. Inset, a representative case of 20 wt% solution is displayed. the simulated data (green points) indicate the dynamical average value of $\eta(t)$ where the upper limit of the integration changes, error bars calculated from different simulation runs are shown in pink color, and the black line going through the points indicates a bi-exponential type fit to the average data points.

Calculated concentration-dependent shear viscosities along with experimentally measured values are shown in Figure 7.9. In the inset of Figure 7.9, the convergence of simulated dynamical viscosity ($\eta(t)$) is shown. Like density, viscosity also increases with concentration. Simulated viscosities are quite close to those from experiments except at the highest glucose concentration. It's worth noting that the simulation technique tends to slightly underestimate

measured viscosity values. The reason for this discrepancy could be the utilization of non-polarizable force field parameters. The structural and dynamical properties can be significantly affected by polarizability. Although polarizability can improve simulated results, its incorporation typically incurs a substantial computational expense. Hence, we chose to use non-polarizable force field parameters for our present study. The increase of viscosity with glucose concentration can be explained in terms of large solute size and the enhanced solute-solute H-bonding interactions in such binary mixtures.

7.3.4 Diffusion

Following methods described in in Sec. 7.2.1, we have calculated mean-square displacements as well as $\beta(t)$. MSD, and $\beta(t)$ values of EG, and glucose are shown in Figures 7.A.6 and 7.A.7, respectively. In Figure 7.A.6, MSD values of EG rapidly decreases upon addition of glucose in the solution. This trend is also observed in Figure 7.A.7 where the glucose molecules are considered. One may assume that the diffusive limit sets in when $\beta(t) \sim 1$. Figure 7.10 shows calculated self-diffusion coefficients values for EG and glucose at different concentrations. The numerical values and their ratio are summarized in Table 7.A.6. With increasing glucose concentration, the translational mobility of both EG, and glucose are decreased. This can be attributed to the effects of viscosity on molecular motions in condensed phases. It is expected that glucose molecules will move slowly due to their larger effective size, and extensive H-bonding network ($<n_{HB}> \sim 8$). The ratio of self-diffusion constants of EG and glucose increase with increasing glucose concentration. Hence, addition of glucose molecules retards translational mobility of glucose to a greater extent compared to that of EG.

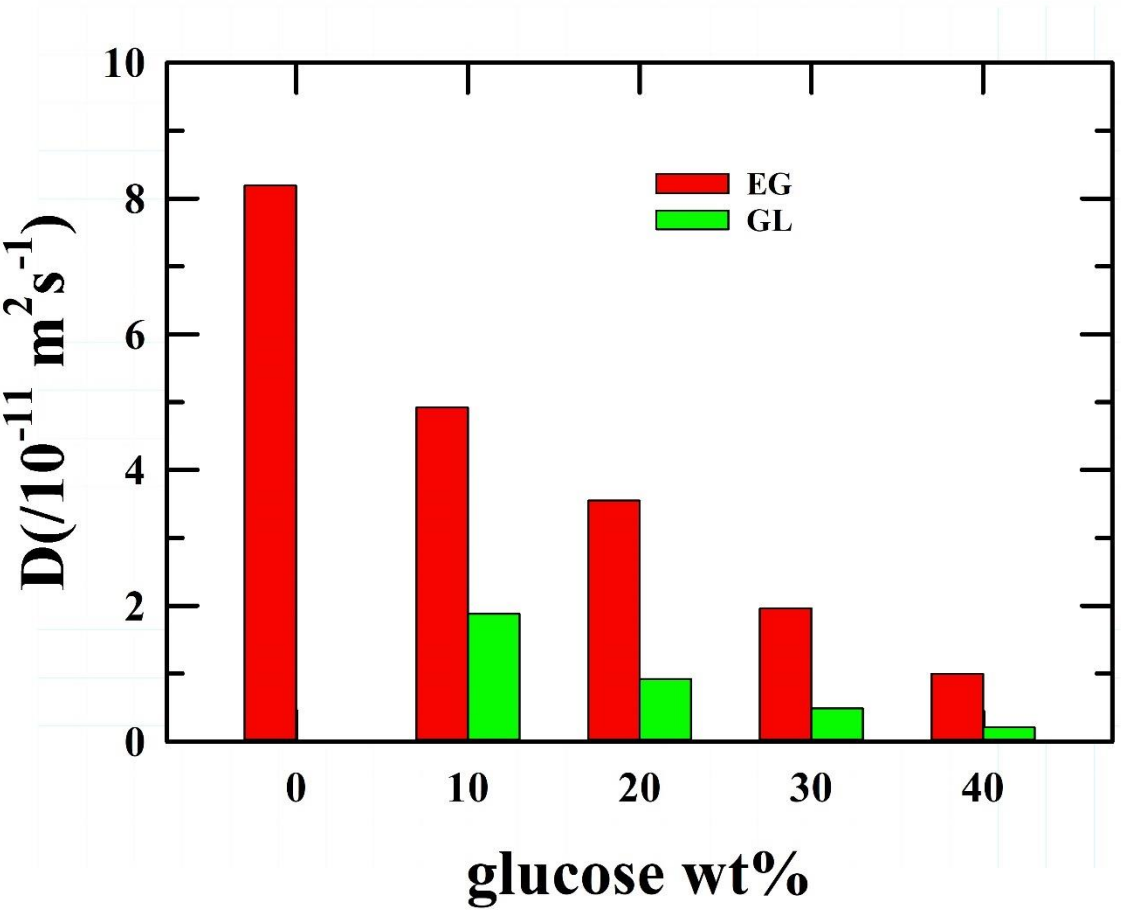

Figure 7.10: Concentration-dependent self-diffusion coefficients of EG (red), and glucose (green) at 298.15 K for 0-40 wt% of glucose/EG solutions.

7.3.5 Molecular vector reorientation dynamics ($C_1(t)$)

Reorientation of molecules in liquid phase is an important factor to understand inherent dynamics. The commonly known reorientational time correlation function of rank 1 for molecular vectors of EG, and glucose are calculated. For EG, the bond connecting two carbon atoms (C1-C2) was considered as the molecular vector. The vector connecting C2, and C5 atoms of a glucose molecule was assigned as molecular vector for glucose (see Figure 7.A.1 of Appendix 7.A) The change of direction of these molecular vectors with time were tracked by simulating the corresponding autocorrelation functions as per the protocol discussed in Sec. 7.2.1. Decay of these autocorrelation functions for EG, and glucose are displayed in Figure 7.11. Multi-exponential functions of time were used to extract the corresponding amplitudes and timescales, and these are provided in Tables 7.A.7 and 7.A.8. Decay functions are modelled as combination of exponential functions as $C_1(t) = \sum_k a_k e^{-t/\tau_k}$ where $\sum_k a_k = 1$.

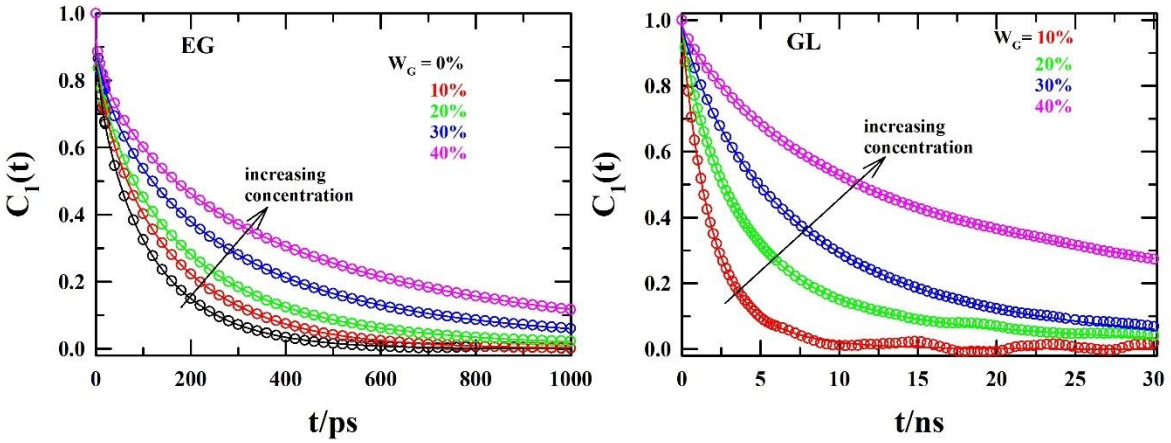

Figure 7.11: Concentration-dependent decay of reorinetational time correlation functions, $C_1(t)$ for EG (left panel), and glucose (right panel) at different concentrations of glucose/EG solution. Different solutions are defined with unique colors. The solid lines going through the symbols represent multi-exponential fitting. The fit parameters are shown in Table 7.A.7-8 of Appendix 7.A.

Effects of glucose concentration on relaxation times of EG is clearly visible from the simulated $C_1(t)$ decays represented in left panel of Figure 7.11. From Table 7.A.7 we can see that at lower concentrations, four timescales are required to adequately describe the behavior of correlation functions whereas from 20% onwards an extra slow timescale arises. Note that going from 30% to 40% solution, this timescale abruptly changes from ~0.7 ns to ~2.5 ns. Increase of viscosity increases relaxation time but the change in individual time components is not monotonic for all the cases studied here. From the amplitude, τ_2 could be considered as the main relaxation time. A ~40 ps timescale is observed for 0-30% solutions but it suddenly goes up to 100 ps in 40% solutions. Moving from 0% to 40% solution, many solution parameters alter; for example, viscosity increases and the interspecies interaction decreases but is compensated by the increased intraspecies interactions. In addition, we do not know the number distribution of H-bonds with glucose concentration. Therefore, it is not straightforward to comment on the origin of individual timescales. Therefore, τ_2 may be considered as a timescale associated with the rotation of those EG molecules which have similar H-bond population like that in pure EG. The slowest timescale, τ_1, may be considered as arising from the rotation of EG molecules which are bound to glucose. Rotation of that EG molecules which have lesser number of (EG-EG) H-bonds may result the ~40 ps timescale. The ~10 ps timescale may arise due to partial rotation of EG molecules.

Now, we explore the rotation of glucose molecules in this solution. The concentration-dependent correlation functions are shown in the right panel of Figure 7.11 and the corresponding fit parameters are summarized in Table 7.A.8. Here also the average reorientation time increases with glucose concentration but individual time components do not change monotonically. Like EG molecules, the abrupt change in the slowest timescale in 40% solution is also visible. These data clearly show that overall rotational dynamics of both EG, and glucose molecules slows down upon increasing glucose concentration, the extent of slowing down being sudden and high at 40%.

7.3.6 Structural hydrogen bond autocorrelation function ($C_{HB}(t)$)

We next present glucose concentration dependent structural H-bond autocorrelation functions. Results are shown in Figure 7.12. Like $C_1(t)$, these correlation functions were fitted to multi-exponential functions of time. The corresponding fit parameters are summarized in Tables 7.A.9 (for EG), and 7.A.10 (for glucose). Note that for the calculations of H-bond correlations, only the *intraspecies* H-bonds were taken into account.

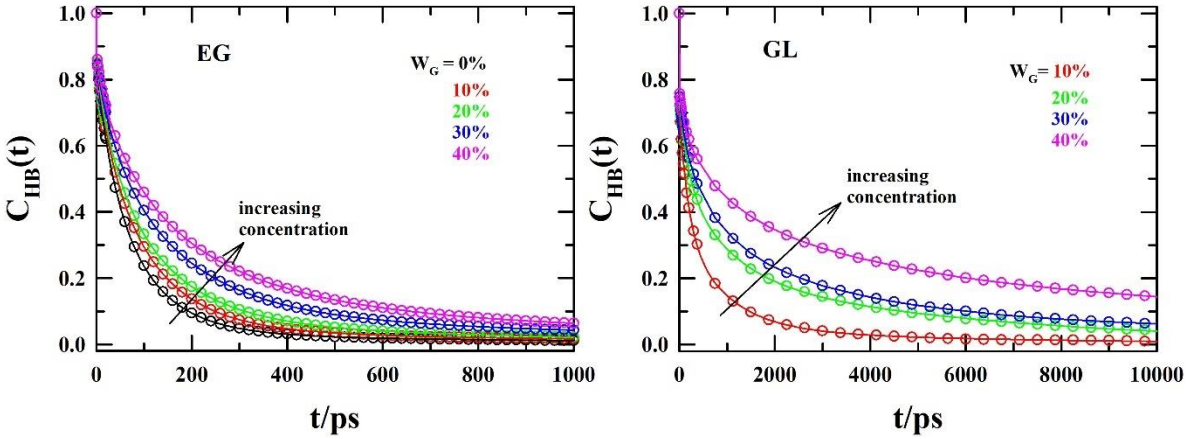

Figure 7.12: Structural hydrogen bond autocorrelation function, $C_{HB}(t)$ for EG (left panel), and glucose (right panel) across all concentrations of glucose/EG solutions. Different solutions are defined with unique colors. The solid lines going through the symbols represent multi-exponential fitting. The fit parameters are shown in Table 7.A.9-10 of Appendix 7.A.

Much like rotation times, structural H-bond relaxation times also increase with concentration. Glucose concentration dependent decay of $C_{HB}(t)$ for EG are shown in the left panel of Figure 7.12. The multi-exponential fit parameters are provided in Table 7.A.9. Here too, slower dynamics is detected but unlike $C_1(t)$, no abrupt change is observed. The average timescale

obtained from $C_{HB}(t)$ decay is very similar to that of $C_1(t)$ indicating close connection between these two processes. In addition, striking similarity is observed in τ_2, τ_3, and τ_4 timescales obtained via fits to these different correlation functions, $C_{HB}(t)$ and $C_1(t)$. $C_{HB}(t)$ decay functions for glucose at different concentrations are presented in the right panel of Figure 7.12, and multiexponential fit parameters for these decays are summarized in Table 7.A.10.

Four distinct timescales are obtained for the structural H-bond dynamics involving glucose molecules. The slowest timescale changes from ~6 ns to ~12 ns. The amplitude also increases from 5% to 32%. Like previous observations, timescales are getting slower with increasing glucose concentration. Unlike EG, reorientation timescales of glucose are much slower than H-bond relaxation times. This can be attributed to the number of H-bonds associated with a given glucose molecule. One glucose molecule contains six donor, and five acceptor sites. Therefore, when two glucose molecules form H-bonds between themselves they can do so without rotating too much. As only partial rotation is enough for making new H-bonds, the structural H-bond relaxation occurs at a faster rate compared to the complete rotation of a glucose molecule.

7.4 Conclusion

In this paper, we have investigated structural, and dynamical properties of a glucose-based potential cryoprotectant system at different glucose concentrations. Strong inter and intraspecies interactions between EG and glucose molecules are found. As number of glucose molecules increase in the binary mixture, EG-EG correlation diminishes. Incoming glucose molecules replace EG molecules in solvation shells around EG. Glucose-glucose correlation gradually increases as glucose concentration rises. Hence, glucose molecules self-aggregate by successively replacing neighboring EG molecules. Extensive H-bond analysis also shows this affinity of glucose molecules to interact with themselves rather than with EG. On the one hand, number of EG-EG H-bonds per EG molecule decreases, and on the other hand, the same within glucose molecules increases. The H-bonding network plays a key role in governing the dynamics of these cryoprotectant mixtures. Viscosity increases with glucose concentration and this leads to slower mobility of both EG and glucose molecules in concentrated solutions. EG molecules have been found to be more mobile than glucose molecules at every glucose concentration studied here than glucose. Reorientation time of glucose molecules is much slower than that of EG. Like translation, rotation of molecules also becomes slow with glucose concentration. Structural H-bond analysis shows good agreement with the simulated

reorientational dynamics for EG. Qualitatively similar trend has been found for glucose as well. These results provide insight into the microscopic structure and dynamics of this cryoprotectant system and may be helpful in designing model cryoprotectant systems for targeted use.

The formation of glucose-domain via a novel interplay between the inter and intraspecies H-bonding may lead to alter plasticity of these media, and may serve as a key factor for understanding the cryoprotection ability of the systems. Cryoprotectant agents can have variations in their physical and chemical properties, such as their size, shape, and chemical composition, which can impact their ability to penetrate the sample and protect it during freezing and thawing. Experimental studies have shown considerable impact of heterogeneous distribution of cryoprotecting agent in the vicinity of biomolecules [87]. Further simulation and experimental studies are required to fully explore the heterogeneous aspects of the media in order to correlate the cryopreserving ability to the spatio-temporal heterogeneity of these systems.

Appendix 7.A

Table 7.A.1: Number of glucose and ethylene glycol molecules and cubic box length of different simulated systems.

Wt.% of glucose	No. of EG molecules	No. of glucose molecules	Box length (nm)
0	1500	0	5.20634
10	1440	60	5.26644
20	1382	118	5.33489
30	1304	196	5.41705
40	1223	277	5.50105

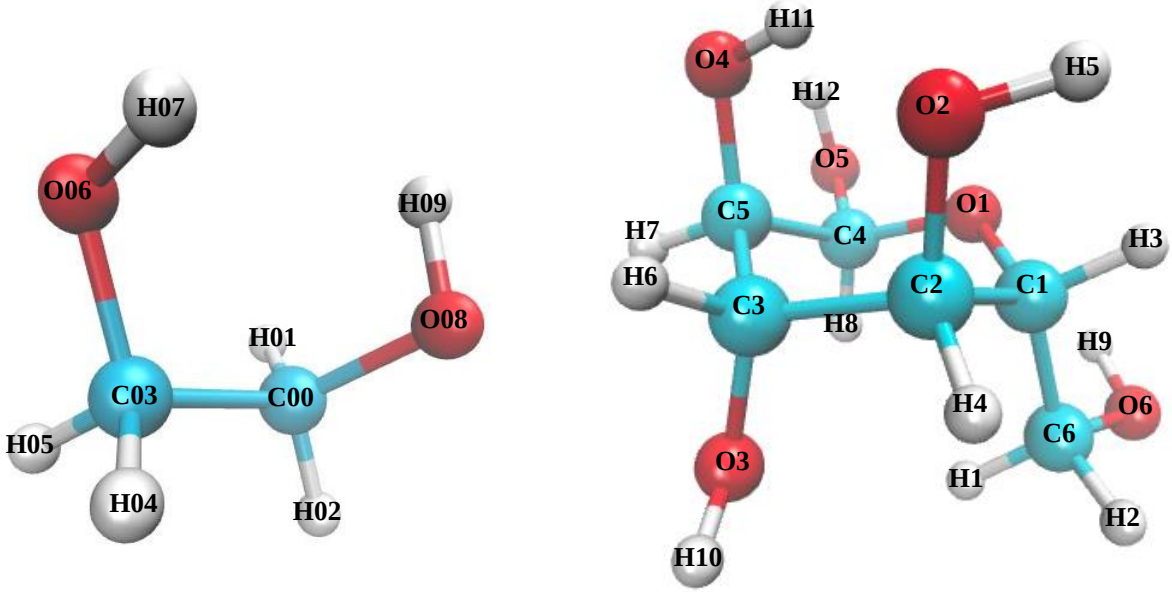

(a) Ethylene glycol **(b) Glucose**

Figure 7.A.1: Structure of ethylene glycol (EG), and glucose (GL) molecules.

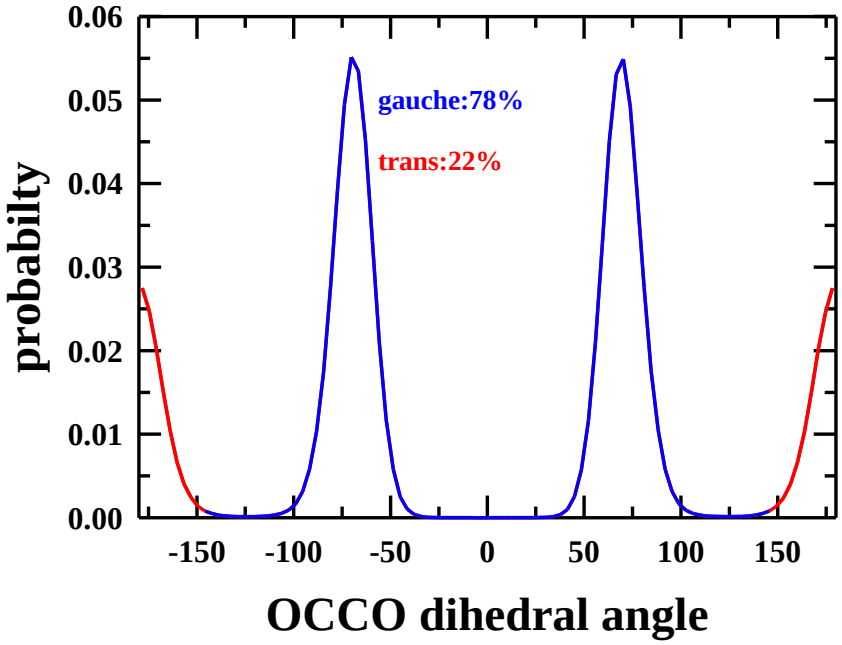

Figure 7.A.2: Probability distribution of -OCCO- dihedral angle of liquid EG at 298.15 K. Blue and red lines denote *gauche* and *trans* isomers, respectively. The *gauche* isomers are defined as the dihedral angle ranging between $\pm 150^{\circ}$.

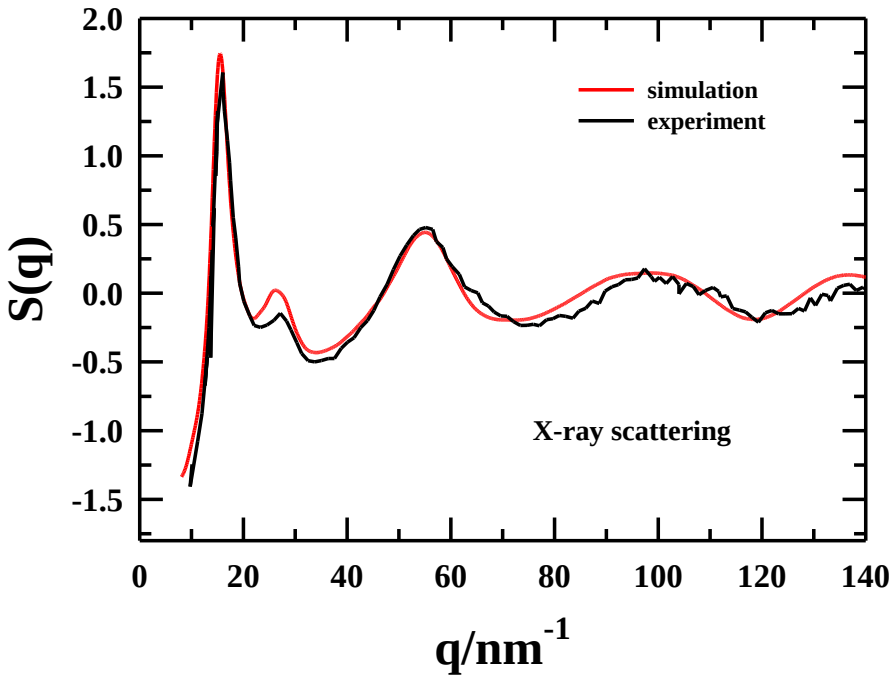

Figure 7.A.3: X-ray scattering structure functions ($S(q)$) for pure ethylene glycol at 298.15 K. The simulated, and experimental results are shown in red, and black curves, respectively. The experimental data are taken from the work of Bako et al [88].

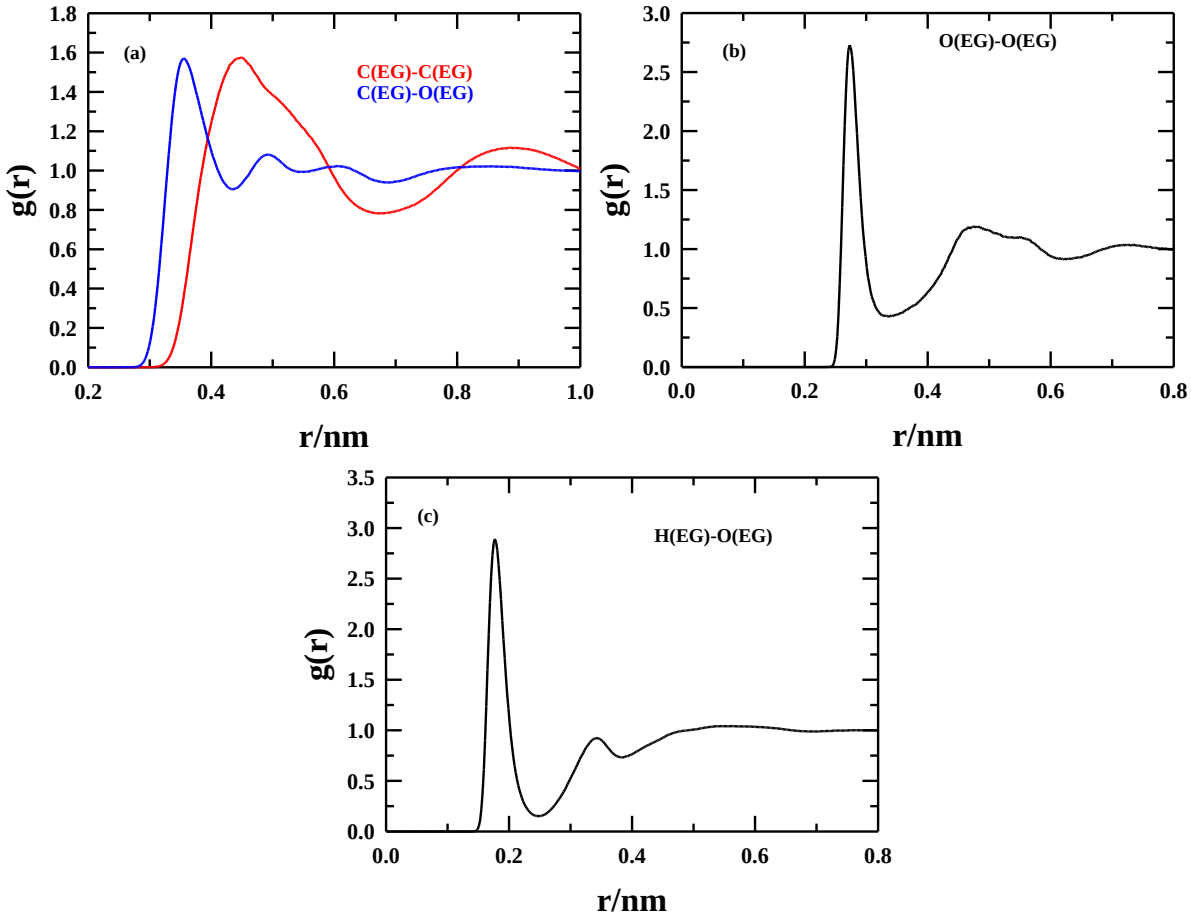

Figure 7.A.4: Intermolecular radial distribution functions between different types of atoms in pure EG at 298.15 K, (a) RDFs for C-C and C-O interactions, (b) RDFs between O atoms, (c) RDFs between hydroxyl hydrogen and oxygen atoms.

Table 7.A.2: Density, viscosity, and self-diffusion coefficient of pure EG at 298.15 K. Experimental data are taken from corresponding articles.

Simulated	**Experimental**	**Deviation (%)**
Density (g/cc)		
1.097	1.110[72]	1.17
Viscosity (cP)		
14.46	17.40[73]	16.89
Self-diffusion coefficient (/10^{-11} m^2s^{-1})		
8.19	8.34[74]	1.80

Table 7.A.3: Positions (in nm) of first maximum, minimum, and coordination number of different atom-atom RDFs (self-interactions) for glucose/EG solutions at various concentrations.

Intermolecular RDF pair	**Wt% of glucose**	r_{max}	r_{min}	N_{coord}
H(EG)-O (EG)	0	0.177	0.249	0.98
	10	0.178	0.248	0.92
	20	0.177	0.247	0.86
	30	0.177	0.245	0.79
	40	0.177	0.245	0.73
O(EG)-O(EG)	0	0.273	0.337	2.24
	10	0.275	0.338	2.13
	20	0.273	0.337	2.00
	30	0.273	0.333	1.80
	40	0.273	0.333	1.67
H(GL)-O(GL)	10	0.185	0.251	0.12
	20	0.185	0.249	0.26
	30	0.185	0.251	0.31
	40	0.185	0.249	0.38
O(GL)-O(GL)	10	0.281	0.385	0.41
	20	0.281	0.383	1.09
	30	0.279	0.389	1.37
	40	0.281	0.381	1.64

Table 7.A.4: Positions (in nm) of first maximum, minimum, and coordination number of different atom-atom RDFs (cross-interactions) for glucose/EG solutions at various concentrations.

Intermolecular RDF pair	**Wt% of glucose**	r_{max}	r_{min}	N_{coord}	
				EG	**GL**
H(EG)-O(GL)	10	0.181	0.245		0.07
	20	0.179	0.243		0.12
	30	0.179	0.247		0.20
	40	0.179	0.247		0.26
H(GL)-O(EG)	10	0.181	0.251	0.80	
	20	0.181	0.251	0.67	
	30	0.185	0.251	0.64	
	40	0.181	0.255	0.56	

Table 7.A.5: Positions (in nm) of first maximum, minimum, and coordination number of different centre-of-mass (COM)-centre-of-mass (COM) RDFs for glucose/EG solutions at various concentrations.

Intermolecular RDF pair between centres-of-mass	**Wt% of glucose**	r_{max}	r_{min}	N_{coord}	
				EG	**GL**
EG-EG	0	0.495	0.672	13.17	
	10	0.489	0.669	12.22	
	20	0.489	0.683	12.09	
	30	0.487	0.681	11.03	
	40	0.491	0.677	10.08	
GL-GL	10	0.615	0.873		1.48
	20	0.613	0.871		3.31
	30	0.629	0.849		3.90
	40	0.619	0.861		5.16
EG-GL	10	0.545	0.771		0.70
	20	0.557	0.771		1.22
	30	0.559	0.765		1.96
	40	0.551	0.771		2.64
GL-EG	10	0.553	0.767	16.58	
	20	0.555	0.771	14.24	
	30	0.559	0.765	13.00	
	40	0.551	0.771	11.67	

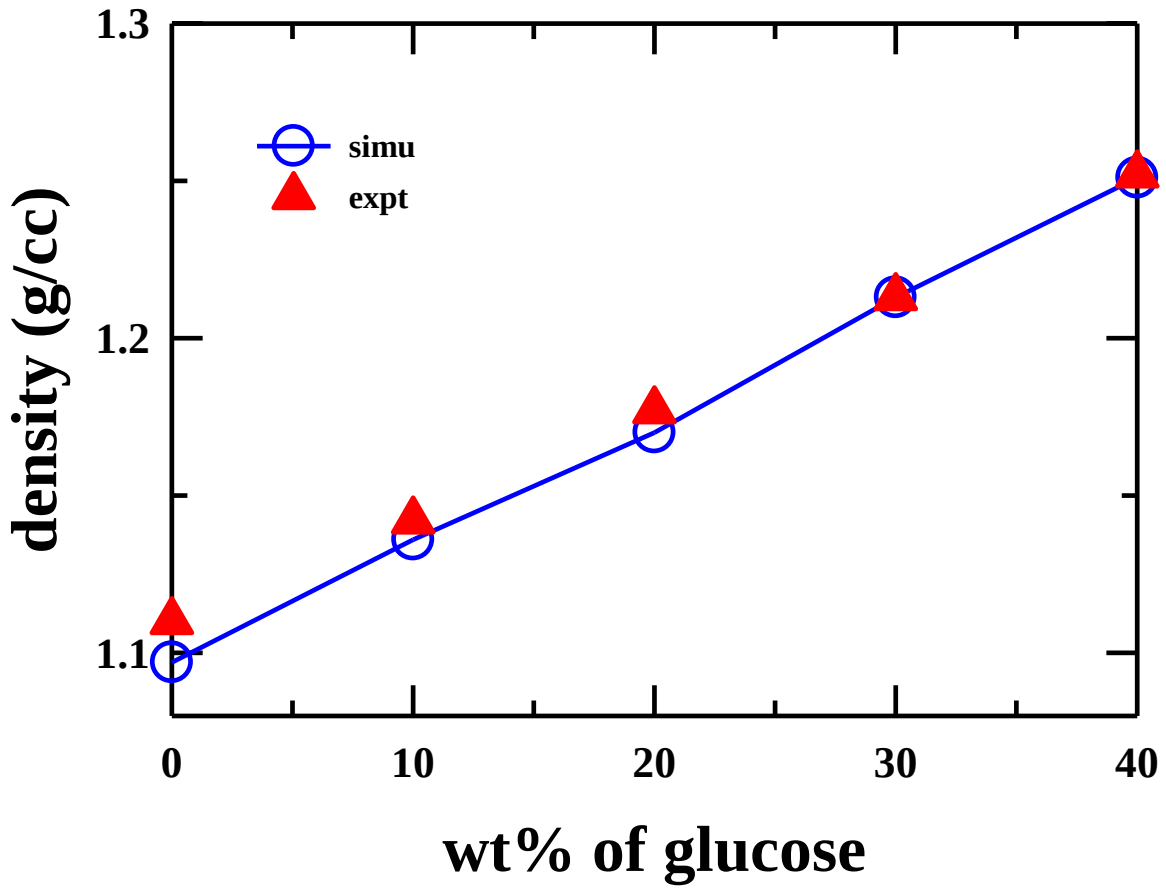

Figure 7.A.5: Concentration-dependent density values calculated from MD simulations, and experimental measurements for glucose/EG solutions at ~298 K. The line going through the data points is only a guide to bare eyes.

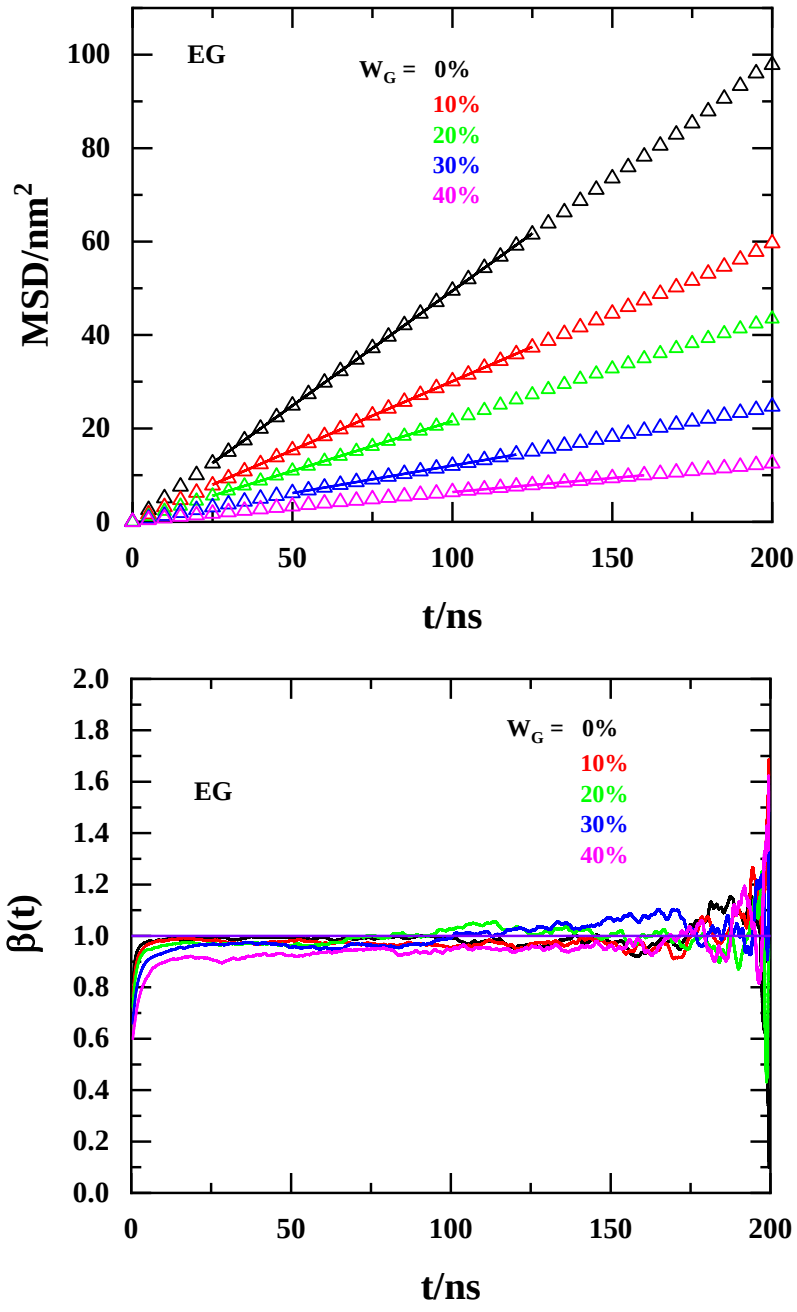

Figure 7.A.6: Concentration-dependent MSD (upper panel), and $\beta(t)$ (lower panel) for EG at pure form as well as in glucose/EG solutions at 298.15 K. The diffusive regimes in MSD curves are defined when corresponding β value is around unity. This region is fitted with linear polynomial and the slope is taken as self-diffusion coefficient. In upper panel, the open symbols represent MSD points, and the straight lines are linear fits. Each solution is uniquely color-defined.

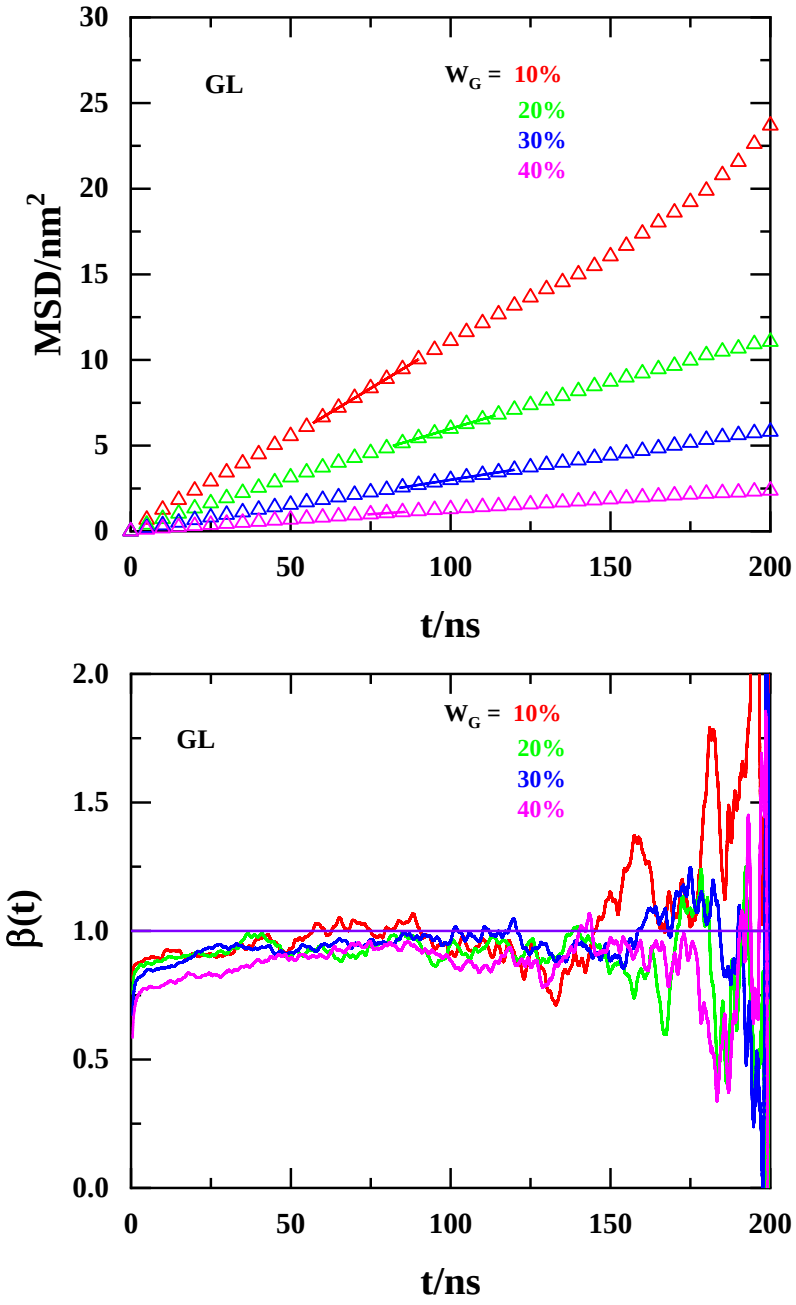

Figure 7.A.7: Concentration-dependent MSD (upper panel), and $\beta(t)$ (lower panel) for glucose for various concentrations of glucose/EG solutions at 298.15 K. The diffusive regimes in MSD curves are defined when corresponding β value is around unity. This region is fitted with linear polynomial and the slope is taken as self-diffusion coefficient. In upper panel, the open symbols represent MSD points, and the straight lines are linear fits. Each solution is uniquely color-defined.

Table 7.A.6: Concentration dependent self-diffusion coefficients of EG, glucose, and their ratio.

Wt% of glucose	D (/10^{-11} m^2s^{-1})		D_{EG}/D_{GL}
	EG	GL	
0	8.19		
10	4.92	1.88	2.62
20	3.55	0.923	3.85
30	1.96	0.490	4.00
40	0.998	0.207	4.82

Table 7.A.7: Multi-exponential fitting parameters for reorientational correlation functions, $C_1(t)$ of EG at various concentrations. Time constants are better within $\pm$5% of the reported values.

Wt% of glucose	a_1	τ_1 (ps)	a_2	τ_2 (ps)	a_3	τ_3 (ps)	a_4	τ_4 (ps)	a_5	τ_5 (ps)	$\langle\tau\rangle$ (ps)
0			0.64	137	0.18	43	0.10	7.2	0.08	0.4	96
10			0.66	182	0.18	45	0.08	6	0.08	0.3	129
20	0.15	477	0.56	176	0.15	36	0.07	4.9	0.07	0.3	176
30	0.23	701	0.51	222	0.12	47	0.07	6.8	0.07	0.3	281
40	0.08	2416	0.55	461	0.21	100	0.08	12.4	0.07	0.5	469

Table 7.A.8: Multi-exponential fitting parameters for reorientational correlation functions, $C_1(t)$ of glucose at various concentrations. Time constants are better within $\pm$5% of the reported values.

Wt% of glucose	a_1	τ_1 (ps)	a_2	τ_2 (ps)	a_3	τ_3 (ps)	a_4	τ_4 (ps)	$\langle\tau\rangle$ (ps)
10	0.28	3746	0.69	1526			0.03	20	2102
20	0.17	18664	0.68	3856	0.13	917	0.02	8	5914
30	0.32	17110	0.56	6294	0.10	1458	0.02	21	9146
40	0.55	42386	0.41	6866	0.03	733	0.01	5	26149

Table 7.A.9: Multi-exponential fit parameters for the structural H-bond correlation functions, $C_{HB}(t)$ for EG across various concentrations. Time constants are better within $\pm 5\%$ of the reported values.

Wt% of glucose	a_1	τ_1 **(ps)**	a_2	τ_2 **(ps)**	a_3	τ_3 **(ps)**	a_4	τ_4 **(ps)**	a_5	τ_5 **(ps)**	$\langle\tau\rangle$ **(ps)**
0	0.04	856	0.52	95	0.26	39	0.08	5.9	0.10	0.2	94
10	0.05	956	0.58	112	0.20	36	0.07	5.6	0.10	0.2	120
20	0.07	860	0.50	137	0.25	46	0.08	6.7	0.10	0.2	141
30	0.10	1133	0.54	164	0.19	44	0.07	6	0.09	0.2	211
40	0.13	1249	0.45	219	0.22	68	0.08	9.6	0.12	0.2	277

Table 7.A.10: Multi-exponential fit parameters for the structural H-bond correlation functions, $C_{HB}(t)$ for glucose across various concentrations. Time constants are better within $\pm 5\%$ of the reported values.

Wt% of glucose	a_1	τ_1 **(ps)**	a_2	τ_2 **(ps)**	a_3	τ_3 **(ps)**	a_4	τ_4 **(ps)**	$\langle\tau\rangle$ **(ps)**
10	0.05	6007	0.32	902	0.34	180	0.29	1	650
20	0.21	5960	0.30	961	0.22	185	0.27	1	1581
30	0.20	8188	0.33	1354	0.21	230	0.24	1	2133
40	0.32	12111	0.28	1482	0.15	221	0.25	1	4324

References

1 C. Krembs, H. Eicken, K. Junge and J. W. Deming, *Deep-Sea Res. I: Oceanogr. Res. Pap.*, 2002, **49**, 2163–2181.

2 G. N. Somero and A. L. DeVries, *Science (1979)*, 1967, **156**, 257–258.

3 K. B. Storey and J. M. Storey, *Annu. Rev. Physiol.*, 1992, **54**, 619–637.

4 R. Gupta and R. Deswal, *J. Biosci.*, 2014, **39**, 931–944.

5 U. Bechtold, *Front. Plant. Sci.*, 2018, **9**, 1-8.

6 M. S. Clark and M. R. Worland, *J. Comp. Physiol. B*, 2008, **178**, 917–933.

7 J. P. Costanzo, R. E. Lee and P. H. Lortz, *J. Exp. Biol.*, 1993, **181**, 245–255.

8 O. Kandror, A. DeLeon and A. L. Goldberg, *PNAS*, 2002, **99**, 9727–9732.

9 K. B. Storey and J. M. Storey, *Physiol. Rev.*, 2017, **97**, 623–665.

10 K. B. Storey, *Comp. Biochem. Physiol. A Physiol.*, 1997, **117**, 319–326.

11 M. R. Michaud and D. L. Denlinger, *J. Comp. Physiol. B*, 2007, **177**, 753–763.

12 D. E. Pegg, *Semin. Reprod. Med.*, 2002, **20**, 005–014.

13 J. Donnez, B. Martinez-Madrid, P. Jadoul, A. van Langendonckt, D. Demylle and M.-M. Dolmans, *Hum. Reprod. Update*, 2006, **12**, 519–535.

14 J. K. Lewis, J. C. Bischof, I. Braslavsky, K. G. M. Brockbank, G. M. Fahy, B. J. Fuller, Y. Rabin, A. Tocchio, E. J. Woods, B. G. Wowk, J. P. Acker and S. Giwa, *Cryobiology*, 2016, **72**, 169–182.

15 C. Olsson, H. Jansson and J. Swenson, *J. Phys. Chem. B*, 2016, **120**, 4723–4731.

16 S. D. Rowley, W. I. Bensinger, T. A. Gooley and C. D. Buckner, *Blood*, 1994, **83**, 2731–6.

17 Y. Xin, C. Kielar, S. Zhu, C. Sikeler, X. Xu, C. Möser, G. Grundmeier, T. Liedl, A. Heuer-Jungemann, D. M. Smith and A. Keller, *Small*, 2020, **16**, 1905959.

18 J. H. Crowe, L. M. Crowe and D. Chapman, *Science (1979)*, 1984, **223**, 701–703.

19 J. H. Crowe, J. F. Carpenter and L. M. Crowe, *Annu. Rev. Physiol.*, 1998, **60**, 73–103.

20 P. S. Belton and A. M. Gil, *Biopolymers*, 1994, **34**, 957–961.

21 G. Yu, R. Li and A. Hubel, *Langmuir*, 2019, **35**, 7388–7395.

22 L. Weng, C. Chen, J. Zuo and W. Li, *J. Phys. Chem. A*, 2011, **115**, 4729–4737.

23 J. P. R. Motta, F. H. Paraguassú-Braga, L. F. Bouzas and L. C. Porto, *Cryobiology*, 2014, **68**, 343–348.

24 S. Indra and R. Biswas, *J. Phys. Chem. B*, 2016, **120**, 11214–11228.

25 P. A. King, M. N. Rosholt and K. B. Storey, *Am. J. Physiol. Regul. Integr. Comp. Physiol.*, 1993, **265**, R1036–R1042.

26 G. M. Volk, J. L. Harris and K. E. Rotindo, *Cryobiology*, 2006, **52**, 305–308.

27 L. Zhang, L. Liu, Y. Qian and Y. Chen, *Eur. J. Pharm. Biopharm.* 2008, **69**, 750–759.

28 A. P. R. Rodrigues, C. A. Amorim, S. H. F. Costa, M. H. T. Matos, R. R. Santos, C. M. Lucci, S. N. Báo, O. M. Ohashi and J. R. Figueiredo, *Theriogenology*, 2004, **61**, 1009–1024.

29 F. Chauvigné, E. Lubzens and J. Cerdà, *BMC Biotechnol.*, 2011, **11**, 34.

30 Y. Q. A'yun, N. Anita, A. Abinawanto, A. A. Jusuf, A. Awanis, I. Muhiardi and M. A. Rosvita, *AIP Conf. Proc.*, 2019, **2168**, 020098.

31 É. C. G. Praxedes, G. L. Lima, A. M. Silva, L. B. Campos, C. M. P. Souza, S. S. J. Moreira, M. F. Oliveira and A. R. Silva, *Reprod. Domest. Anim.*, 2020, **55**, 154–161.

32 M. de los Reyes, L. Saenz, L. Lapierre, J. Crosby and C. Barros, *Vet. Rec.*, 2002, **151**, 477–480.

33 M. T. Cicerone and C. L. Soles, *Biophys. J.*, 2004, **86**, 3836–3845.

34 D. C. C. Brito, S. F. S. Domingues, A. P. R. Rodrigues, J. R. Figueiredo, R. R. Santos and J. C. Pieczarka, *Cryobiology*, 2018, **83**, 97–99.

35 L. L. Kuleshova, D. R. MacFarlane, A. O. Trounson and J. M. Shaw, *Cryobiology*, 1999, **38**, 119–130.

36 R. R. Santos, T. Tharasanit, J. R. Figueiredo, T. van Haeften and R. van den Hurk, *Cell Tissue Res.*, 2006, **325**, 523–531.

37 A. M. da Silva, L. G. P. Bezerra, E. C. G. Praxedes, S. S. J. Moreira, C. M. P. de Souza, M. F. de Oliveira, A. F. Pereira, P. Comizzoli and A. R. Silva, *Cryobiology*, 2019, **91**, 53–60.

38 A. Dhali, R. S. Manik, S. K. Das, S. K. Singla and P. Palta, *Anim. Reprod. Sci.*, 2000, **63**, 159–165.

39 W.-X. Fan, X.-H. Ma, D. Ge, T.-Q. Liu and Z.-F. Cui, *Cryobiology*, 2009, **58**, 28–36.

40 P. S. Almeida-Monteiro, R. R. R. Pinheiro, M. S. Oliveira-Araújo, Y. S. Sales, R. V. Nascimento, L. T. Nunes, V. A. Pereira, A. R. Montenegro, M. A. P. Melo-Maciel and C. S. B. Salmito-Vanderley, *Aquac. Res.*, 2020, **51**, 4565–4574.

41 M.J. Abraham, D. van der Spoel, E. Lindahl, B. Hess, and the GROMACS development team, GROMACS User Manual version 2018.

42 L. Martínez, R. Andrade, E. G. Birgin and J. M. Martínez, *J. Comput. Chem.*, 2009, **30**, 2157–2164.

43 S. Nosé, *Mol. Phys.*, 1984, **52**, 255–268.

44 W. G. Hoover, *Phys. Rev. A (Coll Park)*, 1985, **31**, 1695.

45 M. Parrinello and A. Rahman, *J. App. Phys.*, 1981, **52**, 7182–7190.

46 S. Nosé and M. L. Klein, *Mol. Phys.*, 1983, **50**, 1055–1076.

47 J. Wang, R. M. Wolf, J. W. Caldwell, P. A. Kollman and D. A. Case, *J. Comput. Chem.*, 2004, **25**, 1157–1174.

48 A. Gaur and S. Balasubramanian, *Phys. Chem. Chem. Phys.*, 2022, **24**, 10985–10992.

49 B. Hess, H. Bekker, H. J. C. Berendsen and J. G. E. M. Fraaije, *J. Comput. Chem.*, 1997, **18**, 14631472.

50 C. S. Santos, H. V. R. Annapureddy, N. S. Murthy, H. K. Kashyap, E. W. Castner and C. J. Margulis, *J Chem Phys*, 2011, **134**, 064501.

51 H. K. Kashyap, C. S. Santos, H. V. R. Annapureddy, N. S. Murthy, C. J. Margulis and J. E. W. Castner, *Faraday Discuss.*, 2012, **154**, 133–143.

52 H. V. R. Annapureddy, H. K. Kashyap, P. M. de Biase and C. J. Margulis, *J. Phys. Chem. B*, 2010, **114**, 16838–16846.

53 E. Prince, Ed., *International Tables for Crystallography*, International Union of Crystallography, Chester, England, 2006, vol. C.

54 J. Du, C. J. Benmore, R. Corrales, R. T. Hart and J. K. R. Weber, *J. Condens. Matter Phys.*, 2009, **21**, 205102.

55 E. Lorch, *J. Phys. C: Solid State Phys.*, 1969, **2**, 305.

56 J. P. Hansen and I. R. McDonald, *Theory of Simple Liquids*, Academic Press, 3rd edn., 2006.

57 A. Einstein, *Ann. Phys.*, 1905, **322**, 549–560.

58 A. Luzar and D. Chandler, *Nature*, 1996, **379**, 55–57.

59 D. C. Rapaport, *Mol. Phy.s*, 1983, **50**, 1151–1162.

60 M. P. Allen and D. J. Tildesley, *Computer Simulations of Liquids*, Oxford University Press, New York, 1987.

61 E. F. Pettersen, T. D. Goddard, C. C. Huang, G. S. Couch, D. M. Greenblatt, E. C. Meng and T. E. Ferrin, *J. Comput. Chem.*, 2004, **25**, 1605–1612.

62 M. Brehm and B. Kirchner, *J. Chem. Inf. Model*, 2011, **51**, 2007–2023.

63 M. Brehm, M. Thomas, S. Gehrke and B. Kirchner, *J. Chem. Phys.*, 2020, **152**, 164105.

64 O. Hollóczki, M. Macchiagodena, H. Weber, M. Thomas, M. Brehm, A. Stark, O. Russina, A. Triolo and B. Kirchner, *ChemPhysChem*, 2015, **16**, 3325–3333.

65 S. Gehrke, M. von Domaros, R. Clark, O. Hollóczki, M. Brehm, T. Welton, A. Luzar and B. Kirchner, *Faraday Discuss.*, 2018, **206**, 219–245.

66 S. Gehrke and B. Kirchner, *J. Chem. Eng. Data*, 2020, **65**, 1146–1158.

67 K. G. R. Pachler and P. L. Wessels, *J. Mol. Struct.*, 1970, **6**, 471–478.

68 C. Murli, N. Lu, Z. Dong and Y. Song, *J. Phys. Chem. B*, 2012, **116**, 12574–12580.

69 R. Ghanghas, A. Jindal and S. Vasudevan, *J. Phys. Chem. B*, 2018, **122**, 9757–9762.

70 A. Jindal and S. Vasudevan, *J. Phys. Chem. B*, 2017, **121**, 5595–5600.

71 S. Kaur, Shobhna and H. K. Kashyap, *J. Phys. Chem. B*, 2019, **123**, 6543–6553.

72 W. Y. Tawfik and A. S. Teja, *Chem. Eng. Sci.*, 1989, **44**, 921–923.

73 M.-L. Ge, J.-L. Ma and B. Chu, *J. Chem. Eng. Data*, 2010, **55**, 2649–2651.

74 M. N. Rodnikova, Z. Sh. Idiyatullin and I. A. Solonina, *Russ. J. Phys. Chem. A*, 2014, **88**, 1442–1444.

75 A. Das and R. Biswas, *J. Phys. Chem. B*, 2015, **119**, 10102–10113.

76 K. Kumbhakar, E. Tarif, K. Mukherjee and R. Biswas, *J. Mol. Liq.*, 2019, **290**, 111225.

77 P. D'Angelo, A. Serva, G. Aquilanti, S. Pascarelli and V. Migliorati, *J. Phys. Chem. B*, 2015, **119**, 14515–14526.

78 M. Busato, A. Lapi, P. D'Angelo and A. Melchior, *J. Phys. Chem. B*, 2021, **125**, 6639–6648.

79 F. Sessa, V. Migliorati, A. Serva, A. Lapi, G. Aquilanti, G. Mancini and P. D'Angelo, *Phys. Chem. Chem. Phys.*, 2018, **20**, 2662–2675.

80 A. Serva, V. Migliorati, A. Lapi, G. Aquilanti, A. Arcovito and P. D'Angelo, *Phys Chem. Chem. Phys.*, 2016, **18**, 16544–16554.

81 V. Migliorati, A. Serva, G. Aquilanti, S. Pascarelli and P. D'Angelo, *Phys. Chem. Chem. Phys.*, 2015, **17**, 16443–16453.

82 V. Migliorati, A. Serva, F. Sessa, A. Lapi and P. D'Angelo, *J. Phys. Chem. B*, 2018, **122**, 2779–2791.

83 A. Kaiser, O. Ismailova, A. Koskela, S. E. Huber, M. Ritter, B. Cosenza, W. Benger, R. Nazmutdinov and M. Probst, *J. Mol. Liq.*, 2014, **189**, 20–29.

84 A. Jindal and S. Vasudevan, *J. Phys. Chem. B*, 2017, **121**, 5595–5600.

85 J. A. Padró, L. Saiz and E. Guàrdia, *J. Mol. Struct.*, 1997, **416**, 243–248.

86 Y. Zhang, A. Otani and E. J. Maginn, *J. Chem. Theory Comput.*, 2015, **11**, 3537–3546.

87 G. Yu, R. Li and A. Hubel, *Langmuir*, 2019, **35**, 7388–7395.

88 I. Bakó, T. Grósz, G. Pálinkás and M. C. Bellissent-Funel, *J. Chem. Phys.*, 2003, **118**, 3215–3221.

Chapter 8

Concluding remarks and future problems

8.1 Concluding remarks

In this thesis we focus to unravel the structure and dynamics of various complex liquids, including deep eutectic solvents (DESs) and cryoprotectant solutions. Molecular dynamics (MD) simulation technique was employed to explore the molecular level interactions. The dielectric relaxation (DR) process in acetamide-based ionic DESs has been studied via MD simulation. This study sheds light on the conundrum of exact static dielectric constant as different set of experiments reports totally different results. The decrement in static dielectric constant is explained in terms of local orientational frustration of acetamide molecules which is essentially governed by hydrogen bonding network. The total dielectric response is decomposed into rotational, translational and ro-translational contributions showing the total response is almost entirely dominated by rotational dynamics. This computational approach to calculate dielectric relaxation spectroscopy (DRS) is further extended for a non-ionic glucose-based naturally abundant DES (NADES). This NADES contains glucose, urea and water, and shows complex dynamics. Dielectric relaxation properties are calculated and total response is dissected into contributions from self- and cross-interactions of each species. Moreover, effect of structural hydrogen bond dynamics on system relaxation is also discussed. In each case the effect of temperature is explored by performing simulations in a broad temperature range. Effectiveness of DES to solubilize drug molecules are investigated using paracetamol and two choline chloride DESs where ethylene glycol and propylene glycol are used as hydrogen bond donor, respectively. The solubility of paracetamol in these two DESs are determined by coordination number analysis and interaction energy calculation. Theoretical predictions of solubility are close to experimental results. Analyses of hydrogen bond and non-polar interactions reveal their pivotal role in solubilizing paracetamol. Also, the higher solubility of paracetamol in ChCl-PG DES is somewhat governed by the enhanced non-polar interactions due to presence of an extra methyl group in PG. We have studied ChCl-EG mixtures at different compositions to find a ‘magic composition’ which may be considered as deep eutectic composition. We could not detect such a composition; our structural and dynamical analyses

only indicate the concentration effect of gradual addition of ChCl in EG. Beyond DESs, we have explored a possible cryoprotectant system consisting glucose and EG. Our analyses show how the thermodynamic, structural and dynamical properties of such mixtures change as glucose is gradually added to EG.

The chapter-wise conclusions are given at the end of the respective chapters. Therefore, we opt not to iterate them here. Instead, we choose to discuss about some intriguing problems which can be explored in the near future.

8.2 Future problems

8.2.1 Decrement of static dielectric constant of alcohol-water mixtures: A molecular level insight

Several studies have investigated how the static dielectric constant (ε_s) changes in alcohol-water mixtures as their concentrations.[1–3] Normally, adding water to alcohols should increase the ε_s of the mixture, given that water has a much higher ε_s than alcohols. This holds true for small, linear alcohols like methanol, ethanol, propanol, and butanol. However, for larger alcohols like pentanol, hexanol and, branched alcohols like *t*-butanol, this increment is not straightforward. In the region where there is a higher concentration of alcohol and less amount of water, ε_s first decreases, reaches a minimum, and then increases with the addition of water. While there are explanations involving the self-association of water molecules or complex interactions between alcohol and water, the exact molecular-level details still remain unknown. Molecular dynamics (MD) simulation presents a promising approach to study these systems, offering insights into the molecular interactions that might explain the initial decrease in ε_s in long-chain or branched alcohol-water mixtures.

8.2.2 Ternary DESs are better solvents for drug solubilization: A molecular dynamics study

In chapter 5, we extensively explored how two-component deep eutectic solvents (DESs) outperform water in dissolving a drug, paracetamol. Now, this investigation can be broadened to ternary DESs using the same method. An interesting study by Li et al.[4] demonstrated a significant increase in the solubility of itraconazole in choline chloride (ChCl): glycolic acid (GA) DES (in a 1:2 mole ratio) compared to water (less than 0.001 mg/mL in water versus about 7 mg/mL in DES). Intriguingly, by thoughtfully introducing a third component to the DES, the solubility can be further enhanced. For instance, ChCl: GA: α-ketoglutaric acid (in a

1:1.6:0.4 ratio) DES can dissolve around 30 mg of itraconazole per mL, while ChCl: GA: oxalic acid (in a 1:1.6:0.4 ratio) DES shows a solubility of about 54 mg/mL.[4] These kind of increments in solubility in ternary DESs compared to binary DESs holds potential significance in pharmaceutical research. The molecular dynamics simulation method can be applied to unveil the interactions and understand the role of the third component in dissolving drug molecules. This knowledge can be valuable in designing a framework for drug molecules.

References

1 S. Mashimo, S. Kuwabara, S. Yagihara, and K. Higasi, *J. Chem. Phys.*, 1989, **90**(6), 3292–3294.

2 A. D'Aprano, D.I. Donato, and E. Caponetti, *J. Sol. Chem*., 1979, **8**(2), 135–146.

3 D. Bertolini, M. Cassettari, and G. Salvetti, *J. Chem. Phys*., 1983, **78**(1), 365–372.

4 Z. Li, and P.I. Lee, *Int. J. Pharm*. 2016, **505**(1–2), 283–288.